
**SU(N) chiral spin liquids and
spin-1/2 plaquette phases
in 2D Mott insulators**

Der Naturwissenschaftlichen Fakultät
der Friedrich-Alexander Universität Erlangen-Nürnberg

zur

Erlangung des Doktorgrades Dr. rer. nat.

vorgelegt von
Carolin Boos

Als Dissertation genehmigt von der Naturwissen-
schaftlichen Fakultät der Universität Erlangen-Nürnberg.

Tag der mündlichen Prüfung: 5. Mai 2020

Vorsitzender des Promotionsorgans: Prof. Dr. Martin Eckstein

Gutachter: Prof. Dr. Kai P. Schmidt
Dr. Claudiu Genes

Abstract

In this thesis, the Hubbard model with hopping amplitude, t , and on-site interaction, U , in the Mott-insulating regime is explored for unconventional magnetic phases at $T = 0$ K. These phases are captured within effective low-energy descriptions, and are triggered by quantum fluctuations due to finite hopping. We aim for unconventional phases from two mechanisms, an increased symmetry $SU(N)$ with $N > 2$ compared to the most common $SU(2)$, and highly frustrated interactions.

For $SU(N)$ -symmetric fermions in artificial gauge fields, chiral spin liquid phases (CSLs) are investigated. They are determined within effective spin models, which we derive in order six in t/U for the honeycomb lattice for general values of N , and study in detail for the triangular lattice up to order five in t/U for $SU(3)$ and $SU(7)$ by exact diagonalisations and variational Monte Carlo simulations. On the triangular lattice, the third-order effective model is the J - K model with nearest-neighbour coupling, $J \in \mathbb{R}$, and ring exchange, $K \in \mathbb{C}$. For $SU(3)$ and $\text{Im} K = 0$, the three-sublattice long-range ordered phase is ruled out by a spontaneously time-reversal symmetry breaking $\pi/3$ -flux CSL through finite hopping. Further, for $\text{Im} K = 0$, a lattice nematic, a 120° long-ranged ordered, and the ferromagnetically ordered phase occur. The CSL is found to be extended to $\text{Re} K = 0$. It is also present in the fourth- and fifth-order model in the most relevant π -flux case, where time-reversal symmetry is spontaneously broken. Together with the estimated metal-insulator transition point at larger hoppings, this CSL is therefore expected to be realised in the $SU(3)$ Hubbard model. The analogous CSL is also predicted for $SU(7)$ -symmetric fermions. Experimental realisations with ultra-cold atoms in optical lattices are described.

$\text{SrCu}_2(\text{BO}_3)_2$ is a highly frustrated quantum magnet. At ambient pressure it is captured by the spin-1/2 Shastry-Sutherland model, which yields the effective strong-coupling description of the associated $SU(2)$ Hubbard model. To describe $\text{SrCu}_2(\text{BO}_3)_2$ under higher pressure, we extend the Shastry-Sutherland model by asymmetric coupling strengths, and find that asymmetries of a few percent are sufficient to replace the empty plaquette singlet phase (EPP) of the Shastry-Sutherland model with the filled plaquette singlet phase (FPP) that is found to be identical to a quasi one-dimensional Haldane phase. These results are achieved by series expansions and infinite projected entangled-pair states. The dispersions and dynamic structure factors of both plaquette phases are derived. The EPP naturally hosts one low-lying triplon, whereas the FPP has two. Therefore, the FPP appears to be the likely candidate for $\text{SrCu}_2(\text{BO}_3)_2$ under pressure. The excitations of both phases show some agreement with experimental data if the exchange amplitudes change more than expected. Further measurements are suggested. At last, an orthogonal-plaquette model of spins-1/2 is introduced and proven to host two exact valence bond crystals based on plaquette singlets with an extensive degeneracy at the phase transition. This model exhibits an extensive number of conserved quantities, which is used for further investigations of the phase diagram.

Zusammenfassung

In dieser Dissertationsarbeit „SU(N) chirale Spinflüssigkeiten und spin-1/2 Plakettphasen in 2D Mottisolatoren“ wird das Hubbardmodell mit Hüpfamplitude t und Wechselwirkung U im Mott-isolierenden Bereich nach unkonventionellen magnetischen Phasen bei $T = 0$ K ergründet. Diese Phasen sind in effektiven Niederenergie-Modellen enthalten und werden von Quantenfluktuationen durch eine endliche Hüpfamplitude getrieben. Wir betrachten unkonventionelle Phasen, die entweder durch eine erhöhte Symmetrie SU(N) mit $N > 2$ im Vergleich zur üblichen SU(2) oder durch hochgradig frustrierte Wechselwirkungen hervorgerufen werden.

Wir erforschen SU(N)-symmetrische Fermionen in Eichfeldern und untersuchen chirale Spinflüssigkeiten (CSF). Für das Bienenwabengitter wird das effektive Spinmodell in sechster Ordnung in t/U für allgemeines N abgeleitet. Die effektiven Spinmodelle des Dreiecksgitters werden bis zur fünften Ordnung in t/U für SU(3) und SU(7) mit exakter Diagonalisierung und variationellen Monte Carlo Simulationen untersucht. Auf dem Dreiecksgitter ist das effektive Modell in dritter Ordnung das J - K Modell, welches Nächste-Nachbar-Wechselwirkungen $J \in \mathbb{R}$ und Ringaustausch $K \in \mathbb{C}$ umfasst. Für SU(3) und $\text{Im } K = 0$ wird die lang-reichweitige Ordnung auf drei Untergittern durch endliches Hüpfen t von einer CSF mit $\pi/3$ -Fluss und spontaner Brechung der Zeitumkehrinvarianz abgelöst. Weiterhin folgen eine nematische, eine 120° lang-reichweitig geordnete und eine ferromagnetische Phase. Die CSF erstreckt sich über den gesamten Bereich bis hin zu $\text{Re } K = 0$. Insbesondere tritt sie auch im effektiven Modell in vierter und fünfter Ordnung für den relevanten π -Fluss Fall auf, bei dem die Zeitumkehrinvarianz spontan gebrochen wird. Da der Metall-Isolator Übergang für noch stärkeres Hüpfen abgeschätzt wird, kann diese CSF auch im SU(3) Hubbardmodell erwartet werden. Für SU(7) symmetrische Fermionen liegt eine analoge CSF vor. Experimentelle Realisierungen mit ultra-kalten Atomen in optischen Gittern werden beschrieben.

SrCu₂(BO₃)₂ ist ein hoch frustrierter Quantenmagnet. Bei Atmosphärendruck wird das Material durch das Shastry-Sutherland Modell mit Spin-1/2 beschrieben. Dieses liefert die effektive Beschreibung des dazugehörigen SU(2) Hubbardmodells. Um das Material SrCu₂(BO₃)₂ unter höherem Druck zu beschreiben, erweitern wir das Shastry-Sutherland Modell durch asymmetrische Kopplungskonstanten. Asymmetrien von wenigen Prozent reichen aus, um die Zwischenphase des Shastry-Sutherland Modells, eine verschränkte Phase mit Singulettts auf leeren Plaketten (LPP), durch eine ähnliche Phase auf gefüllten Plaketten (FPP) zu ersetzen. Die FPP ist identisch zur quasi-eindimensionalen Haldanephase. Diese Ergebnisse werden durch Reihenentwicklungen und eine Methode, die auf unendlichen projizierten verschränkten gepaarten Zuständen basiert, erzielt. Die Dispersionen und dynamischen Strukturfaktoren beider Plakettphasen werden abgeleitet. Die LPP hat ein innewohnendes niedrigerenergetisches Triplon, wohingegen die FPP zwei hat. Deswegen ist die FPP die natürliche Kandidatin für SrCu₂(BO₃)₂ unter Druck. Die Anregungen beider Phasen zeigen Ähnlichkeiten

mit experimentellen Daten, wobei die Austauschwechselwirkungen sich stärker ändern als erwartet. Weiterführende Messungen werden vorgeschlagen. Zuletzt führen wir ein Spin-1/2 Modell auf orthogonalen Plaketten ein und zeigen, dass es zwei exakte Valenzbindungs-Kristalle bildet, wobei die Grundzustandsentartung am Phasenübergang extensiv ist. Dieses Modell hat eine extensive Anzahl von Erhaltungsgrößen, die wir zur weiteren Untersuchung des Phasendiagramms nutzen.

Contents

| | |
|--|------------|
| Abstract | i |
| Zusammenfassung | iii |
| 1. Introduction | 1 |
| 2. Methods | 7 |
| 2.1. Perturbation theory | 7 |
| 2.1.1. Linked-cluster expansions | 8 |
| 2.1.2. Takahashi algorithm | 11 |
| 2.1.3. Löwdin formalism | 12 |
| 2.1.4. Perturbative continuous unitary transformations | 13 |
| 2.1.5. Padé extrapolations | 15 |
| 2.2. Exact diagonalisation | 16 |
| | |
| I. Fermionic $SU(N)$ Hubbard models with artificial gauge fields in the strong-coupling regime | 19 |
| | |
| 3. Introduction: Crystals of $SU(N)$-symmetric fermions | 21 |
| 3.1. Theoretical basis | 21 |
| 3.2. Experimental realisations | 27 |
| 3.3. Models and phases | 29 |
| | |
| 4. Derivation of effective models | 33 |
| 4.1. Small clusters | 33 |
| 4.2. Linked-cluster expansions | 36 |
| 4.2.1. Honeycomb lattice | 36 |
| 4.2.2. Triangular lattice | 41 |
| 4.2.3. 12-site triangular cluster with periodic boundary conditions | 46 |
| 4.3. Verification and metal-insulator transition | 49 |
| | |
| 5. $SU(7)$-symmetric fermions on the triangular lattice | 53 |
| 5.1. J - K model | 53 |
| 5.1.1. Chiral phase on systems with periodic boundary conditions | 53 |
| 5.1.2. Chiral edge states | 55 |
| | |
| 6. $SU(3)$-symmetric fermions on the triangular lattice | 61 |
| 6.1. J - K model | 61 |
| 6.1.1. Full phase diagram without fluxes | 63 |
| 6.1.2. Chiral phases at moderate values of K | 68 |

| | |
|---|------------|
| 6.2. Chiral phases in the Hubbard model | 71 |
| II. Plaquette phases in extended Shastry-Sutherland models and $\text{SrCu}_2(\text{BO}_3)_2$ | 75 |
| 7. Introduction: Shastry-Sutherland model and $\text{SrCu}_2(\text{BO}_3)_2$ | 77 |
| 7.1. $\text{SrCu}_2(\text{BO}_3)_2$ under hydrostatic pressure | 81 |
| 7.2. 4-spin-1/2 plaquettes | 86 |
| 7.3. Extended Shastry-Sutherland models | 90 |
| 8. Series expansion approaches for plaquette singlet phases | 97 |
| 8.1. Models | 97 |
| 8.2. Quantities | 101 |
| 8.3. Convergence | 105 |
| 9. Asymmetric orthogonal-dimer spin chain | 113 |
| 9.1. Phase diagram | 113 |
| 9.2. Excitations | 116 |
| 10. Extended Shastry-Sutherland models | 121 |
| 10.1. Phase diagrams | 121 |
| 10.1.1. Distinct dimer couplings | 121 |
| 10.1.2. Distinct nearest-neighbour couplings | 124 |
| 10.1.3. Completely distorted | 126 |
| 10.2. Excitations of plaquette phases | 130 |
| 10.2.1. Empty plaquette singlet phase | 131 |
| 10.2.2. Filled plaquette singlet phase | 133 |
| 10.3. Dynamic structure factor | 138 |
| 10.3.1. Empty plaquette singlet phase | 139 |
| 10.3.2. Filled plaquette singlet phase | 140 |
| 10.4. Comparison with experiments | 141 |
| 11. Orthogonal-plaquette model | 147 |
| 11.1. Exact plaquette singlet phases | 149 |
| 11.2. Phase diagrams | 151 |
| 11.2.1. $J_h = J_v$ | 152 |
| 11.2.2. $J_h = 0$ | 154 |
| 12. Conclusion and outlook | 159 |
| Appendix | 165 |
| A. Effective $\text{SU}(N)$ models on small clusters | 165 |
| Bibliography | 169 |

| | |
|------------------------------|------------|
| List of publications | 185 |
| List of abbreviations | 187 |
| Acknowledgements | 189 |

1. Introduction

Our current understanding of nature is mainly based on a reductionist approach, in which everything is divided into smaller and smaller units down to the subatomic level. The behaviour of small individual constituents is captured by fundamental laws of physics. However, the behaviour of a macroscopic system does not necessarily follow from these laws in a direct way. In fact, the presence of many constituents often leads to completely new features, which relate non-trivially to the properties of individual constituents and only arise from their interplay. These emergent phenomena result into further fundamental properties of nature. The underlying theories depend on the properties of the dominant units, so the degrees of freedom as well as the scale. Systems governed by large units can be described fully classical, and examples of emergent phenomena are given by crystals, quasi-crystals, or ferromagnets. On small scales in the range of atoms $\approx 10^{-10}\text{m} = 1\text{\AA}$, or smaller, the underlying theory is quantum mechanics, and the relevant constituents are electrons, protons, and neutrons. A unique property in quantum mechanical systems is quantum entanglement, which means that a state of a system cannot be separated into the states of its parts. The individual constituents are entangled, and measuring one part modifies the states of other parts. If a quantum mechanical system is not entangled, emergent phenomena resemble classical ones, like the ferromagnet. Otherwise, quantum entanglement plays a crucial role and can lead to emergent phenomena, which are even more striking than in classical systems. In the last decades, strenuous efforts have been made to gain insights into these systems, and unconventional physical properties have been found to arise as emergent phenomena. This opened many new perspectives and yields the motivation for a tremendous amount of research on many-body quantum systems done today.

In equilibrium, the determining property of many-body quantum systems are quantum phases, i.e. phases of matter stabilised by quantum effects such as quantum entanglement. An essential condition for the presence of these quantum phases is that thermal fluctuations are small, so the temperature must be in a regime where the number of thermodynamic excitations mixed into the system is negligible. Then, the system is not governed by an ensemble of states, but rather by the state with the lowest energy, the ground state, which determines the phase of the system. Theoretically, the suppression of thermal fluctuations can be achieved by studying zero temperature. In experiments the temperature must be lowered sufficiently. Quantum effects are enhanced in systems of particles with smaller quantum numbers in contrast to larger quantum numbers, as well as in more symmetrical systems. Systems with small coordination numbers show stronger quantum effects than systems with large coordination numbers, which often relates to lower-dimensional systems compared to higher-dimensional ones. Another route to enhance quantum effects is given by frustration. This occurs in systems where the energy of all constituents cannot be minimised simultaneously. In this thesis, we follow all of these routes to reveal unconventional emergent phenomena in many-body

quantum magnetism.

Before 1973, phases were grouped into two major categories, ordered and disordered phases. Following Landau's theory from 1937, an ordered phase is related to an order parameter, which signals a spontaneously broken symmetry [1, 2]. Different ordered phases are distinguished by distinct broken symmetries. Spontaneous symmetry breaking occurs if the symmetry of the state is lower than the one of the system. This is an excellent example for an emergent phenomenon. In contrast, if a symmetry is already violated within the model, it is called an explicitly broken symmetry. An ordered state of matter is given by a periodic crystal, where the continuous translational symmetry is broken, and reduced to a discrete one. Distinct lattice structures are invariant under different translations. If the lattice structure is fixed, further symmetries can be spontaneously broken by localised degrees of freedom. A famous example for a phase with a broken continuous symmetry is the antiferromagnetic Néel phase for particles with a spin $s = 1/2$, like electrons [3]. Throughout this thesis, the reduced Planck constant, \hbar , is set to unity. The long-range ordered Néel phase shows a finite staggered susceptibility and arises for a Heisenberg model with antiferromagnetic couplings on the square lattice [4]. In this framework, disordered phases occur if no symmetry is spontaneously broken. For instance, an ideal gas where particles are distributed homogeneously in space, or, once a lattice structure is fixed, disordered phases include paramagnetic phases or a polarised phase within an external magnetic field.

However, in 1973, Anderson suggested phases that do not break any symmetry spontaneously and are not disordered [5]. These types of long-range entangled phases are called quantum spin liquids and are more difficult to define and to classify than the previously known conventional phases. Reviews on the topic are given in Refs. [6–8]. The common feature of spin liquids is that no long-range order in local order parameters occurs. Still, these phases are not disordered and a new type of order, topological order, was introduced by Wen in 1989 [9]. This was also motivated by the discovery of the fractional Quantum-Hall effect, which can be understood in terms of topological invariants and long-range entanglement [10, 11]. It is closely related to topological (opposing algebraic) spin liquids, where the topological order is signalled, for instance, by the ground-state degeneracy that depends on the topology of the system. Even though a spin liquid state is not conducting and can be topologically ordered, topological spin liquids are not referred to as topological insulators. This term is used for weakly or non-interacting particles, where the topological order arises as a property in momentum space [12, 13]. In contrast, topological spin liquids occur in strongly-interacting systems. In two-dimensions, they host anyonic excitations, which can show "any" phase while interchanging with another excitation [14–16], unlike bosons and fermions. The properties of non-Abelian anyons could potentially be employed in topological quantum computers [17–19]. Therefore, quantum spin liquid phases are at the forefront of current research.

Phase transitions from everyday life experiences are mostly triggered by thermal fluctuations. In quantum systems, phase transitions occur at zero temperature and are induced by some other control parameter, like magnetic field, pressure, or chemical potential. A first-order phase transition is characterised by an energetic level crossing between two states. At the transition point, where both states yield the ground state simultaneously, the phases coexist and a potential order parameter shows a disconti-

nuity. A second-order phase transition conventionally occurs if one of the phases is invariant under the operation of a symmetry group, which is a subgroup of the other phase. At the phase transition point, the critical point, both states constitute the same phase, which is why these transitions are also called continuous. In the critical regime, quantum fluctuations and correlation lengths diverge, and such systems behave universal. A review on quantum phase transitions can be found in Ref. [20]. An example for a second-order quantum phase transition is given by the metal-insulator transition in the SU(2) Hubbard model [21] from the metallic to a symmetry-broken phase [22]. The model describes interacting electrons on crystal structures. The electrons can hop between neighbouring sites, which captures the tunnelling between different minima in the energy potential, and the Coulomb repulsion is approximated by repulsive on-site interactions. From these two properties, it is clear that the system for dominant hopping is metallic, whereas for dominant coupling it is insulating. In order to better understand the insulating phase and the phase transition to the metallic phase, we need to be more precise. The Hamiltonian of the SU(2) spin-1/2 Hubbard model reads

$$H = -t \sum_{\substack{\langle i,j \rangle \\ \sigma \in \{\uparrow, \downarrow\}}} \left(c_{i\sigma}^\dagger c_{j\sigma} + \text{h.c.} \right) + U \sum_i n_{i\uparrow} n_{i\downarrow}. \quad (1.0.1)$$

The first sum, scaling with the hopping amplitude, t , runs over all nearest-neighbour sites of the lattice, $\langle i, j \rangle$, and the z -component of the spin, m , is included in σ . Spin up, \uparrow , stands for $m = 1/2$ and spin down, \downarrow , for $m = -1/2$. The fermionic creation and annihilation operators, $c_{i\sigma}^\dagger$ and $c_{i\sigma}$, create or annihilate a fermion with σ on lattice site i . The second sum runs over all sites of the lattice and the occupation number operators, $n_{i\uparrow}$ and $n_{i\downarrow}$, yield the number of particles with spin \uparrow and \downarrow on site i , respectively. Only if a lattice site is occupied by two fermions, this term contributes with the interaction constant, U . In the tight-binding limit without interactions, $U = 0$, the system is metallic. In the strong-coupling regime, $U \gg t$, an insulating phase occurs for a commensurate filling. Let the average filling be one electron per site. Then, in the insulating phase all states with doubly occupied sites are separated from the ground state by an energy gap, and therefore no current is possible. In contrast to common insulators, this does not stem from the electronic band structure, but from the strong coupling. This difference is stressed by calling it the Mott-insulating phase. Within the Mott-insulating phase, the magnetic degrees of freedom determine the properties of the system, and the Hubbard model can be described in terms of localised interacting spins. Besides conventional magnetic phases also unconventional ones, like spin liquids, have been found [23–33]. The magnetic nature of the system breaks down, where the particle-hole gap of the Mott-insulating phase closes. It is determined by the energy difference between the ground state with no doubly occupied site and the state of lowest energy with a single doubly occupied site and one empty site. At the critical point the former excitation of the Mott-insulating phase becomes part of the metallic ground state, as described above for a second-order phase transition.

The name "particle-hole gap" illustrates that physicists preferably play with particles. A doubly occupied site is considered as a particle, named a doublon, and an empty site is considered as a hole. Clearly, these are not real particles, like the electrons, but quasiparticles, which are mainly useful in situations with many real particles. The quantum

entanglement is already contained in the notion of quasi-particles. Thus, a quasi-particle relates to an entangled state including many product states with the associated features (like a double occupancy). Usually, a quasi-particle is associated with the eigenstate with the lowest energy from the specific subspace. We already mentioned one other example of quasi-particles, anyons, the excitations of topological spin liquids. In this terminology, the ground state is considered as a non-trivial vacuum. The vacuum most commonly describes an entangled quantum state. One of the best known types of quasi-particles are phonons describing atomic vibrations in crystalline lattices. In this work, the relevant excitations are doublon-hole pairs as well as triplons [34]. The latter are defined as a dressed triplet, here on top of a vacuum set up from singlets. The terminology of a "dressed" triplet signals again the entanglement of the state.

Quasi-particles are often used in perturbation theory, which yields a successful way to study many-body quantum systems. Generally, the inclusion of the perturbation can be seen as a basis transformation of the unperturbed problem. For instance, the triplet, present without inter-triplet interactions, becomes the triplon under the basis transformation. Because of this correspondence, the notion of quasi-particles has proven to be extremely successful in perturbative approaches. Excitations can be understood in a simple limit, and are then adiabatically connected to the model of interest. This allows the derivation of energies, observables, or other quantities with an intrinsic knowledge about the related quantum state. With other methods the physical interpretation of the results is often missing, for example in exact diagonalisation (ED). Further common methods in quantum magnetism are the density-matrix renormalization group, quantum Monte-Carlo, variational Monte-Carlo (VMC) and infinite projected entangled-pair states (iPEPS). The performance of each individual method strongly depends on the model under study. ED works only for small systems since it suffers from the exponential scaling of the Hilbert space with the number of particles. Quantum Monte-Carlo works for much larger systems, but fails for frustrated models possessing a sign problem. VMC as well as partly perturbation theory rely on an intrinsic understanding of the model. iPEPS solves most of these problems, but only works for states fulfilling an area law and remains to be very costly computationally. An overview of common numerical methods is given in Ref. [35].

In order to discover unconventional emergent phenomena in quantum magnetism, the most promising route is to study frustrated systems. Frustration often leads to strongly entangled states and has been found to induce exotic properties ranging from quantum spin liquids [5, 25–28] via exact ground states [36–40] to magnetization plateaux [41–49]. Within the Mott-insulating phase of the Hubbard model in Eq. (1.0.1) on the triangular lattice, an exotic disordered phase is realised. The precise nature of this phase is still under debate [23–25, 28–33]. This is similar for the Hubbard model in the strong-coupling limit on the frustrated Kagomé lattice where a gapped spin liquid with topological order was identified [26, 27], but also evidence for a gapless spin liquid was found [50, 51]. Besides varying the lattice structure, the Hubbard model in Eq. (1.0.1) can be modified by changing the properties of the particles. Instead of the quantum mechanically most relevant spin-1/2, other instances of SU(2)-symmetric spins can be studied, like $s = 3/2$. However, the larger the value of the spin is, the fewer quantum effects occur, and this route leads to rather conventional ordered phases. Completely different sets of spins are reached by enlarging the spin rotation symmetry to SU(N) with $N > 2$. This does not

only increase the number of quantum states, but also enhances quantum fluctuations in comparison to $SU(2)$ -symmetric particles. Spin liquid phases were observed in a very specific strong-coupling and large- N limit [52, 53]. Experimentally, $SU(N)$ Hubbard models in the strong-coupling regime, $t/U \ll 1$, can be realised with cold atoms in optical lattices for $SU(N)$ -symmetric particles with N as large as 10 [54–61], which yields an opportunity to test theoretical findings. The question arises whether the Hubbard model for these values of $N \leq 10$ also exhibits exotic behaviour. On the triangular lattice, chiral spin liquids (CSLs) were discovered for $3 \leq N \leq 9$ in a strong-coupling description of the Hubbard model, the J - K model, with an artificial gauge field [62]. There is also evidence for spin liquids in the J - K model for $N = 3$ without artificial gauge fields [63–65]. The model yields the effective low-energy description in third-order of t/U , and it remains open if the discovered phases also occur in the experimentally relevant Hubbard model. In this thesis, we derive the effective model in order 6 for the honeycomb lattice, and in order 4 for a 12-site triangular cluster with periodic boundary conditions (PBCs). The effective model for the triangular lattice in the thermodynamic limit from Ref. [66] is then studied for the cases $N = 7$ and $N = 3$. We find strong evidence for a $\pi/3$ -flux CSL in the $SU(3)$ Hubbard model with spontaneous breaking of time-reversal symmetry.

Another speciality occurring in frustrated quantum spin models are exact ground states. This was found in the highly-frustrated Shastry-Sutherland model constituted of spins-1/2 [38], which can be seen as the effective description within the Mott-insulating phase of a related Hubbard model [67]. The Shastry-Sutherland model realises an exact ground state of singlets on dimers, a pair of coupled spins, and at the same time yields an accurate description of the quantum magnet $SrCu_2(BO_3)_2$ [44, 68]. This model has been studied a lot over the last nearly 40 years. In particular, the nature of the phase at intermediate coupling ratios was under debate and was only resolved recently [69–74]. The related intermediate phase in $SrCu_2(BO_3)_2$ under the application of pressure has just started to be understood [75–80]. This issue is linked to entangled 4-spin plaquette phases, which we study extensively in this thesis. Apart from deriving ground-state phase diagrams, we determine experimentally relevant quantities, like dispersions and dynamic structure factors, and compare with experimental data. The Shastry-Sutherland model is one of the rare examples where a model hosts an exact ground state. Such systems have been discovered in one [36, 37, 81–87], two [38, 88–91], and three dimensions [39, 40], but overall the number of models with an exact ground state is limited and the majority of systems in many-body quantum magnetism is extremely difficult to solve. Most known exact ground states in frustrated models are dimer singlet product states. In this thesis, we search for new models hosting exactly solvable ground states and introduce the orthogonal-plaquette model with an exact ground state of singlets on 4-spin plaquettes in an extended region of parameter space, and an extended phase transition to the exact dimer phase.

The thesis is structured into two main parts. They are preceded by Chapter 2 where the main methods employed further on are introduced. Namely, various approaches in perturbation theory including linked-cluster expansions and ED in particular for $SU(N)$ -symmetric spin models. Then, in Part I we discuss the Mott-insulating phase of the $SU(N)$ Hubbard model with artificial gauge fields in the strong-coupling regime. A separate introduction into this more specialised field is given in Chapter 3. First, we

derive the low-energy effective description for general values of N , and then analyse it with numerical methods. In Part II, extended Shastry-Sutherland models are investigated with a focus on plaquette phases. The topic is introduced in detail in Chapter 7. Phase diagrams, excitation spectra, and dynamic structure factors are derived and finally compared with experimental data. At the end of this part in Chapter 11, we introduce a general scheme to create spin models with exact singlet ground states and investigate the new orthogonal-plaquette model. A conclusion and an outlook are given in Chapter 12.

2. Methods

The study of many-body quantum systems, and in particular of strongly-correlated particles, triggered the development of a whole set of new methods. Every one of them has certain strengths and bottlenecks. We mainly apply perturbation theory and EDs, that are introduced in Section 2.1 and Section 2.2, respectively. On a fundamental level, both techniques are complementary. Perturbative approaches are only reliable within certain limits, but provide a direct understanding of the involved phases in the thermodynamic limit, whereas ED gives unbiased numerical results, which then need to be interpreted. Our collaborators worked with VMC, ED, and iPEPS. The VMC is briefly motivated in Chapter 6. For details on iPEPS see the Supplemental Material of Ref. [79] and references therein.

2.1. Perturbation theory

The first time-independent perturbation theory in quantum mechanics was introduced by Schrödinger, known as Rayleigh-Schrödinger perturbation theory, in 1926 [92]. The general idea is to separate a problem into a part with an analytic solution and the rest, which is reflected in the Hamiltonian

$$H = H_0 + \lambda V . \quad (2.1.1)$$

The first term, H_0 , has exactly known solutions and the second term, V , is handled perturbatively in orders of the perturbation parameter, $\lambda \in \mathbb{R}$. The results for studied scalar quantities F are polynomial series in some order o in λ of the form

$$F(\lambda) = \sum_{n=0}^o a_n \lambda^n . \quad (2.1.2)$$

Perturbative approaches potentially yield valid results within a range of the perturbation parameter, λ , where the properties of H are not fundamentally changed in respect to H_0 , i.e. the ground state of the system at $\lambda > 0$ is adiabatically connected to the one at $\lambda = 0$. This condition eventually breaks down in the relevant case where $[H_0, V] \neq 0$, since a phase transition must occur for some value of λ , although it might be $\lambda \rightarrow \infty$. Even in infinite order, the perturbative results become unphysical after the phase transition.

In Schrödinger's approach, eigenenergies and eigenstates can be studied, which is possible for both - non-degenerate and degenerate - levels. However, there are many ways to continue from the fundamental setting in Eq. (2.1.1). The resulting methods yield equivalent results, meaning that effective descriptions in the same order of λ are connected by unitary transformations, and that the physically relevant properties are identical [93,94]. The perturbative results are often phrased as effective Hamiltonians, H_{eff} . These can be written as a matrix in the number basis of quasi-particles, which we

employ in this thesis. To this end, the counting operator, Q , is defined that counts the number of excitations, or quasi-particles, in a state

$$Q|\nu\rangle = q|\nu\rangle, \quad (2.1.3)$$

so the eigenstate $|\nu\rangle$ contains q quasi-particles. These number states yield a valid eigenbasis for $\lambda = 0$ if $[H_0, Q] = 0$. The effective Hamiltonian for $\lambda > 0$ is reached by some basis transformation leading to transformed or dressed states. A non-degenerate ground state at $\lambda = 0$ is associated with the vacuum, $q = 0$, throughout the valid range of the perturbative calculation. The effective Hamiltonian contains a single diagonal entry identical to the ground-state energy. The excitations are seen as quasi-particles. The first excitations present at $\lambda = 0$ belong to the one-quasi-particle block, the second excitations to the two-quasi-particle block, and so on. Similarly, if at $\lambda = 0$ degenerate ground states are present that remain degenerate under the inclusion of the perturbation, these degenerate ground states can be taken as the vacuum and the effective Hamiltonian in the zero-quasi-particle block is diagonal. Excited states in H_0 are usually degenerate, since a local quasi-particle can be placed on different positions of the lattice. Generally, the corresponding effective Hamiltonian is not diagonal and needs to be studied additionally. This is also required for the zero-quasi-particle block if the ground state is degenerate at $\lambda = 0$ and this degeneracy is lifted under the perturbation. Here, the low-lying excitations at $\lambda > 0$ arise from the unperturbed ground-state manifold of H_0 . A quasi-particle picture can be introduced, where the non-degenerate ground state is again seen as a vacuum. The corresponding quasi-particles are from the same subsector of degenerate eigenstates in (the initial) H_0 . Further quasi-particles from subsectors distinct from the one containing the degenerate ground state in H_0 can exist, for instance doublons and holons as charge excitations on top of triplons. Evidently, if the ground state of the system changes the quasi-particle picture has to be redefined.

In this thesis, we use several perturbative methods. Degenerate perturbation theory derived by Kato [95] and known from Takahashi's work [96] is introduced in Subsection 2.1.2. A projective formalism from Löwdin [97] is discussed in Subsection 2.1.3, and a method based on unitary transformations [98] is described in Subsection 2.1.4. In comparison to the most conventional Rayleigh-Schrödinger perturbation theory, where the eigenvectors in order $o - 1$ must be known to generate the eigenenergies in order o for $o > 1$, this is not necessary with our approaches. The derivation of eigenenergies and eigenstates is decoupled. The application of these techniques for high orders was done with an algebraic computer code written by Daniel Klagges, known as "Solver" [99].

For all perturbative methods linked-cluster expansions are applied, in order to derive series valid in the thermodynamic limit. The basics of linked-cluster expansions are introduced in the next subsection. Once the series are derived, they can be studied using Padé extrapolation, which is explained in Subsection 2.1.5.

2.1.1. Linked-cluster expansions

Undergraduate studies usually capture perturbation theory applied on finite systems. For solid state systems with many particles, mostly approximated by the thermodynamic limit, the technique of linked-cluster expansions is established. These expansions

allow to extend perturbative calculations on small finite clusters to large or infinite systems based on cluster additivity. Linked-cluster expansions are also briefly introduced in Ref. [100]. A cluster is defined by a part of the full lattice. If all sites within a cluster are connected by bonds, it is called a linked cluster. Two linked clusters A and B not sharing any common sites and without a connecting bond between them are disconnected. If one of these conditions is not fulfilled, they are connected and form a single linked cluster. Cluster additivity is given for a quantity M^C on cluster $C = A \cup B$ if

$$M^C = M^A \otimes \mathbb{1}^B + \mathbb{1}^A \otimes M^B \quad (2.1.4)$$

is fulfilled, where M^A and M^B give the quantity M on the apparent disconnected clusters A and B . This clearly holds for the Hamiltonian and all extensive quantities. It was first exploited for the ground-state energy in 1981 [101]. The application of the idea to intensive quantities is less obvious and was only achieved in 1996, when Gelfand discovered a way to perform linked-cluster expansions for excitation energies by subtracting the ground-state energies on every cluster. He applied similarity transformations [102]. However, these transformations are only valid for a linked-cluster expansion if the ground and excited state belong to different symmetry sectors, such that excitations can not hop between disconnected clusters. This limitation was overcome by orthogonal transformations [103–105] and perturbative continuous unitary transformations (pCUTs) [98, 106], which always fulfil cluster additivity for multi-particle properties. So, whether linked-cluster expansions are applicable depends on the quantity and the model of interest, as well as the perturbative approach on the finite clusters. In the following, we sketch the general concept of linked-cluster expansions. More details can be found in Refs. [93, 105, 107]. The individual approaches used in this thesis and their validity for the linked-cluster theorem are discussed in the following Subsections 2.1.2, 2.1.3, and 2.1.4. Later on, we employ them to calculate low-energy effective Hamiltonians in Part I, and ground-state energies, dispersion relations, and structure factors in Part II.

The idea of a linked-cluster expansion is to add reduced contributions of finite linked clusters in order to reach results for large systems. For many expansions, it is useful to introduce super-sites consisting of several sites as the building blocks of the linked clusters. This makes sense if the local units of the eigenstates of H_0 consist of several sites, and also because they are really totally super. Bonds between super-sites represent all interactions between the included sites.

At first, we consider the case of an extensive quantity, P . On a system of N_s sites this quantity normalised on the number of sites is given by the linked-cluster expansion as

$$\frac{P}{N_s} = \sum_c L(c) W_P(c) . \quad (2.1.5)$$

The sum runs over all topologically different linked clusters c . It contains the weights of the apparent quantity on every cluster, $W_P(c)$, multiplied by the embedding factor, $L(c)$, determining the impact of the cluster. The latter is given by the number of ways in which a cluster can be embedded on the full lattice. The weight, $W_P(c)$, contains all processes, which are specific to the apparent cluster c . They can be derived in (at

least) two ways. The standard approach is the inclusion-exclusion principle

$$W_P(c) = P(c) - \sum_{s \subset c} W_P(s) . \quad (2.1.6)$$

At first, the extensive quantities $P(c)$ on all relevant clusters are derived. Then, the inclusion-exclusion principle requires that from the quantity $P(c)$ on cluster c all weights $P(s)$ of all sub-clusters are subtracted, including cases where a sub-cluster s can be placed on cluster c in several ways. If the subtraction is performed on a disconnected cluster, the weight is identical to the sum of the sub-clusters and vanishes, which justifies the name linked-cluster expansion. Another route to determine the weights, $W_P(c)$, is a bookkeeping technique during the derivation of $P(c)$, where all bonds are labelled with an individual interaction parameter [108]. This allows to take only terms into account, which act on every bond at least once and are therefore specific to the cluster directly.

Let us phrase the steps of a linked-cluster expansion for the ground-state energies in a hands-on way. The derivation of a non-degenerate ground-state energy is the most straight forward. At first, one has to determine all reduced contributions, $W_P(c)$. To this end, one should iterate from small to large cluster sizes. For the smallest cluster, no sub-clusters exist. Then, to find the reduced contribution $W_P(c)$ of a larger linked-cluster c in the standard way, the reduced results $W_P(s)$ on all sub-graphs s multiplied by the number of ways they can be placed on the linked-cluster c must be subtracted from the full result on c . These results get embedded on the full lattice with the proper embedding factors $L(c)$. They are determined by fixing a single site of the lattice and counting the number of distinct ways how every cluster can be placed on the lattice divided by the number of sites of the cluster. The sum in Eq. (2.1.5) gives the final result. If the ground state of H_0 is degenerate the linked-cluster expansion gives an effective Hamiltonian, which consists of a constant part and multi-quasi-particle interactions. The constant part is calculated exactly as the ground-state energy in the non-degenerate case. In order to derive the interaction amplitudes, one also has to first find the reduced interactions on clusters. To this end, it is again best to go from simple to more complicated interactions, or from small to large clusters. For every cluster, the number of distinct ways in which every smaller cluster can be placed on the original cluster yielding the investigated interaction has to be determined. This gives the number of times the reduced exchange parameter of the sub-cluster needs to be subtracted from the original parameter. The embedding of interactions is trivial. Wherever the full lattice hosts a fitting set of sites and bonds, they are present.

Excitation energies are not extensive. Nevertheless, the calculations at least for the one-quasi-particle sector are only slightly more involved than the ones for a degenerate ground state [98, 106]. For simplicity, let us consider a single quasi-particle as the first excitation. The mobility of the quasi-particle leads to a large or infinitely large block in the effective real-space Hamiltonian, H_{eff} , depending on the lattice under study. This is similar to the expansion of a degenerate ground-state energy. Here, however, the basis states are associated with the quasi-particle located on different super-sites. The only real difference in the linked-cluster expansions is then given by the necessity to subtract the vacuum energies of static hopping processes

$$(H_{\text{eff}} - E\mathbf{1})_C = (H_{\text{eff}} - E\mathbf{1})_A \oplus (H_{\text{eff}} - E\mathbf{1})_B . \quad (2.1.7)$$

So for every linked-cluster not only the hopping processes of excitations but also the vacuum energies need to be derived. Usually, the series is truncated, and for translational invariant local Hamiltonians a Fourier-transformation yields the dispersion relation, $\omega(\vec{k})$. If there are several species of quasi-particles, that are not protected by symmetry, the effective Hamiltonian in momentum space needs to be diagonalised. This can introduce higher-order effects and a Taylor expansion has to be performed to achieve the valid dispersions.

The linked-cluster expansion in Eq. (2.1.5) includes clusters up to the same size as the system under study. It is therefore exact, if infinite orders are achieved on the clusters. However, the number of clusters grows exponentially with the order as well as with the number of distinct couplings, and usually in the concrete application, the series have to be truncated. We choose a scheme, where all clusters contributing in a specific order of perturbation theory are taken into account. Computationally, linked-cluster expansions are powerful if one performs a full graph decomposition, in particular compared to the performance of other methods in dimensions larger than one. The linked-clusters, subgraph subtractions, and embeddings required for the high-order expansions in Part II were calculated with the computer code written by Dominik Ixert [109]. In the following subsections, the specific perturbative approaches applied on the clusters are explained.

2.1.2. Takahashi algorithm

This type of degenerate perturbation theory is based on Kato's work from 1949 [95]. It is widely known as Takahashi's perturbation theory though, since he used Kato's basis to perform perturbation theory on the half-filled SU(2) Hubbard model (1.0.1), where he investigated amongst other quantities the ground-state energy, E_0 , from the atomic limit in 1977 [96]. In Part I, this perturbation theory is applied to the SU(N) Hubbard model with an average filling of one particle per site, which generalises and extends the calculations done by Takahashi, and others [25, 62, 64, 110]. A review chapter with many examples for the application of the method can be found in Ref. [111]. It is also briefly introduced in Ref. [100].

Let us consider the m -fold degenerate eigenstates of some eigenenergy $E_i^{(0)}$ of H_0 . The subspace spanned by these eigenstates is denoted with \mathcal{U}_0 and the operator P_0 is the projector onto this space. The space of the according perturbed eigenstates is \mathcal{U} and the related projector P . These two spaces usually overlap. Kato showed that

$$P = P_0 - \sum_{n=1}^{\infty} \lambda^n \sum_{\substack{k_1+k_2+\dots+k_{n+1} \\ k_i \geq 0}} S^{k_1} V S^{k_2} V \dots V S^{k_{n+1}} \quad \text{with} \quad (2.1.8)$$

$$S^0 \equiv -P_0 \quad \text{and} \quad S^k \equiv \left[\frac{1 - P_0}{E_i^{(0)} - H_0} \right]^k \quad \text{for } k \geq 1. \quad (2.1.9)$$

Takahashi then found a basis transformation, Γ , which is linear and conserves the scalar product, but is not necessarily orthogonal, reducing the eigenvalue problem of the degenerate level in the full Hilbert space \mathcal{U} to one in \mathcal{U}_0 by an effective Hamiltonian

$$H_{\text{eff}} = \Gamma^\dagger H \Gamma \quad \text{with} \quad \Gamma = P P_0 (P_0 P P_0)^{-1/2}. \quad (2.1.10)$$

Up to this point, the calculation is exact. The series expansion is done by expressing $(P_0 P P_0)^{-1/2}$ as a series and truncating the transformation in some order of interest. A formal representation of the infinite order is known. However, the number of terms grows exponentially with the order. For the effective Hamiltonian operator sequences of projection, perturbation, and resolvent operator, $S = (1 - P_0)/(H_0 - E_0)$, occur. In third order, the effective Hamiltonian reads

$$H_{\text{eff}}^{\mathcal{O}(3)} = P_0 H_0 P_0 + P_0 V P_0 + P_0 V S V P_0 + P_0 V S V S V P_0 - \frac{1}{2} P_0 V P_0 V S^2 V P_0 - \frac{1}{2} P_0 V S^2 V P_0 V P_0 . \quad (2.1.11)$$

Every term is embraced by projection operators, which ensure that the effective model is only acting in \mathcal{U}_0 . The dimension of the problem is significantly reduced, and all states from outside the manifold might seem to be neglected. This is not the case, since the basis transformation mixes states and hence includes quantum fluctuations due to virtual processes with apparently abandoned states.

The linked-cluster expansion is always valid for extensive ground-state properties regardless of the perturbation theory applied on the clusters, so linked-cluster expansions combined with Takahashi's perturbation theory form a valid approach if $E_i^{(0)} = E_0^{(0)}$. Whether Takahashi's perturbation theory is applicable for excitations within a linked-cluster expansion is model and phase dependent, since the transformation matrix is not necessarily orthogonal. Only if the excitations are protected by symmetry from the ground state it can be applied, i.e. the ground and excited state must differ by some conserved quantum number in order to fulfil cluster additivity.

2.1.3. Löwdin formalism

This formalism was originally derived by Löwdin in 1962 [97]. A review is given in Ref. [112]. The formalism is applicable for both non-degenerate and degenerate levels. It is based on projection operators, somewhat similar to Takahashi's perturbation theory. Again, the Hilbert space is split into one part \mathcal{H}_0 containing the eigenstate or degenerate eigenstates under consideration in the unperturbed case and the orthogonal space, $\bar{\mathcal{H}}_0$. The projection operator on \mathcal{H}_0 is P , and on $\bar{\mathcal{H}}_0$ is $Q = 1 - P$. The first projection is the same as P_0 in Takahashi's perturbation theory, however, the second subspace is defined differently. An eigenstate $|\Psi_i\rangle$ of the full system H is decomposed into

$$|\Psi_i\rangle = P |\Psi_i\rangle + Q |\Psi_i\rangle \equiv |\Psi_i\rangle_{\mathcal{H}_0} + |\Psi_i\rangle_{\bar{\mathcal{H}}_0} , \quad (2.1.12)$$

yielding together with the Schrödinger equation an exact eigenvalue problem of the dimension of the degeneracy of the considered energy level

$$\Theta_i |\Psi_i\rangle_{\mathcal{H}_0} = (E_i - E_i^{(0)}) |\Psi_i\rangle_{\mathcal{H}_0} . \quad (2.1.13)$$

The energy E_i is the eigenenergy of H , and the energy $E_i^{(0)}$ is the known eigenvalue of H_0 . The operator Θ_i also contains the eigenenergy E_i , and therefore Eq. (2.1.13) is self-consistent. At this point, the exact calculation is expanded in a series for the

operator Θ_i and for the eigenenergy E_i . This is expressed by

$$\sum_{k=1}^o \Theta_i^{(k)} |\Psi_i\rangle_{\mathcal{H}_0} = \sum_{k=1}^o E_i^{(k)} |\Psi_i\rangle_{\mathcal{H}_0} , \quad (2.1.14)$$

where the series is truncated in order o . The relevant operators $\Theta_i^{(k)}$ in order k are mainly determined by sequences of perturbations and projections. They also depend on eigenenergies $E_i^{(l)}$ with $l < k - 2$, so if an iterative algorithm is applied these are known automatically.

2.1.4. Perturbative continuous unitary transformations

A more recent approach in perturbation theory is given by pCUTs [98], which in contrast to Takahashi's and Löwdin's approaches does not require projections. The original work focused on effective Hamiltonians describing ground and excited states, and was then extended to study observables [106]. Detailed discussions are given in the PhD theses [113, 114].

In order to understand the pCUT approach, we first introduce continuous unitary transformations (CUTs). They were proposed in 1994 independently by Wegner [115], and Głazek and Wilson [116, 117]. Review articles are given in Refs. [118, 119]. The overall idea is to perform a unitary transformation $U(l)$ on the initial Hamiltonian

$$H(l) = U^\dagger(l) H U(l) , \quad (2.1.15)$$

which brings it into a more comprehensive form, like a diagonal or block-diagonal structure. In contrast to standard unitary transformations, for CUTs the unitary matrix $U(l)$ depends on a continuous flow parameter $l \in [0, \infty)$. At $l = 0$ the Hamiltonian $H(l = 0)$ is identical to the non-transformed Hamiltonian, whereas at $l = \infty$ the final transformed Hamiltonian in some ideal basis is given. Differentiating Eq. (2.1.15) by l yields the flow equation

$$\begin{aligned} \partial_l H(l) &= \partial_l (U^\dagger(l)) H(0) U(l) + U^\dagger(l) H(0) \partial_l (U(l)) \\ &= \partial_l (U^\dagger(l)) U(l) H(l) + H(l) U^\dagger(l) \partial_l (U(l)) \\ &= [\eta(l), H(l)] , \end{aligned} \quad (2.1.16)$$

where in the first step the unitarity of the transformation $U U^\dagger = \mathbb{1}$ is used together with Eq. (2.1.15), and in the second step the anti-Hermitian generator of the transformation $\eta(l)$ as $\partial_l U(l) = \eta(l) U(l)$ is introduced. The flow equation is a differential equation for $H(l)$ and the choice of generator is the crucial point of the approach. The most common generators are the one introduced by Wegner [115], and a quasi-particle conserving one, also known as MKU-generator, based on work by Mielke [120], and Knetter and Uhrig [98]. The matrix elements in the quasi-particle basis are given by

$$\eta_{ij}^{\text{MKU}}(l) = \text{sgn}(q_i(l) - q_j(l)) H_{ij}(l) . \quad (2.1.17)$$

This generator leads to a block-diagonal Hamiltonian, where every block belongs to a set of states with the same number of quasi-particles. For most problems, the flow equation

represents an infinite equation system due to the appearing operators. Several ways of overcoming this challenge by truncation have been applied [121, 122]. However, the choice of truncation is difficult to justify and usually model dependent. This problem was solved consistently by pCUTs, briefly explained in the following.

Again, for a perturbative approach the Hamiltonian has to be written as in Eq. (2.1.1). For pCUTs to be applicable the unperturbed diagonal part of the Hamiltonian, H_0 , must have an equidistant spectrum that is bounded from below. The dressed energy quanta are identical to quasi-particles. Furthermore, the perturbation must be expressible as

$$V = \sum_{m=-N}^N T_m \quad \text{with} \quad [H_0, T_m] = mT_m . \quad (2.1.18)$$

The operators T_m change the number of quasi-particles in the system by a finite number m and are defined for $m \in \{-N, \dots, N-1, N\}$ with the number of maximally created or annihilated quasi-particles from a single perturbation N . The idea is to expand the Hamiltonian in a series such that in order k all combinations of k operators T_m are considered. It reads

$$H(l) = E_0 + Q + \sum_{k=1}^{\infty} \lambda^k \sum_{|\mathbf{m}|=k} F(l, \mathbf{m}) T(\mathbf{m}) . \quad (2.1.19)$$

The first two terms give the unperturbed Hamiltonian $H_0 = E_0 + Q$ with the counting operator Q as introduced in Eq. (2.1.3) for quasi-particles defined by the spectrum of H_0 . The first sum runs over all orders k and the second sum over all possible combinations of k operators T_m . This is represented by $|\mathbf{m}| = k$, where \mathbf{m} encodes the specific choice of T_m operators and the absolute value $|\mathbf{m}|$ gives the total number of operators T_m in the sequence. Note, that only the according coefficients $F(l, \mathbf{m})$ depend on the flow parameter, l . They are calculated under the use of a series representation of the MKU-generator (2.1.17) in the flow equation, and are model independent. The coefficients for the effective Hamiltonian with $l \rightarrow \infty$ are defined as $C(\mathbf{m}) = F(l = \infty, \mathbf{m})$, and the final expansion is determined by

$$H_{\text{eff}} = E_0 + Q + \sum_{k=1}^{\infty} \lambda^k \sum_{\substack{|\mathbf{m}|=k \\ M(\mathbf{m})=0}} C(\mathbf{m}) T(\mathbf{m}) \quad (2.1.20)$$

with the number of created or annihilated quasi-particles $M(\mathbf{m})$. The coefficients $C(\mathbf{m})$ are exact rational numbers, depending only on the number N of maximally created or annihilated quasi-particles during one perturbation and are otherwise model independent. The condition $M(\mathbf{m}) = 0$ reflects, that the final effective Hamiltonian is block diagonal in the number of quasi-particles, so it is decomposed into

$$H_{\text{eff}} = H_{0\text{QP}} + H_{1\text{QP}} + H_{2\text{QP}} + H_{3\text{QP}} + \dots , \quad (2.1.21)$$

which allows to study different quasi-particle blocks individually. The calculation costs are determined by the number of combinations of operators T_m , which grows exponen-

tially with the order o . The other relevant factor is the number of different T_m operators of the model, determined by N .

The pCUT can also be applied for observables [106]. To this end, the same transformation as for the Hamiltonian has to be applied. Here, however, this does not lead to a quasi-particle-conserving structure of the observable in relevant cases, where it does not commute with the Hamiltonian. Let the system be in the ground state. Then, the application of the effective observable creates quasi-particles and can be written as

$$\mathcal{O}_{\text{eff}} = \mathcal{O}_{0\text{QP},0} + \mathcal{O}_{1\text{QP},0} + \mathcal{O}_{2\text{QP},0} + \dots, \quad (2.1.22)$$

where the indices denote the subsectors. The first one gives the number of created quasi-particles, and the second one signals that the observable only acts on the vacuum. The pCUT expansion is determined from the flow equation by

$$\mathcal{O}_{\text{eff}} = \sum_{k=1}^o \sum_{i=1}^{k+1} \sum_{M(\mathbf{m})=k} \tilde{C}(\mathbf{m}, i) \mathcal{O}(\mathbf{m}, i) \quad (2.1.23)$$

with model independent coefficients $\tilde{C}(\mathbf{m}, i)$ and operator products

$$\mathcal{O}(\mathbf{m}, i) = T_{m_1} \dots T_{m_{i-1}} \mathcal{O} T_{m_i} \dots T_{m_k}. \quad (2.1.24)$$

From this it becomes clear, that the effective observable does not conserve the number of quasi-particles, since the sum is not restricted to $M(\mathbf{m}) = 0$, in contrast to the effective Hamiltonian in Eq. (2.1.20). The coefficients $\tilde{C}(\mathbf{m}, i)$ were calculated with a computer program provided by Matthias Mühlhauser. The pCUT as a unitary transformation is applicable in a linked-cluster expansion for all quantities of interest.

2.1.5. Padé extrapolations

This subsection yields an extended version of the discussion of Padé extrapolants given in the Supplemental Material of Ref. [79]. By performing a linked-cluster expansion together with one of the perturbative approaches described in Subsections 2.1.2, 2.1.3, and 2.1.4 one reaches a polynomial series $F(\lambda)$, as given in Eq. (2.1.2). For small values of λ different orders give identical or very similar results. At larger values of λ the higher-order terms become dominant and the series eventually diverge. This can be overcome, at least within some range of λ , using extrapolation techniques, which bring the bare series in Eq. (2.1.2) into a different form called extrapolant. The study of various extrapolants also gives insights on the convergence behaviour. Detailed information on various extrapolation techniques can be found in Ref. [123]. For the purposes of the present thesis, Padé extrapolations provide a good framework. They are given by rational functions

$$P[L/M]_F \equiv \frac{p_0 + p_1 \lambda + \dots + p_L \lambda^L}{1 + q_1 \lambda + \dots + q_M \lambda^M} \quad (2.1.25)$$

with $L + M = o$. The Taylor expansion of $P[L/M]_F$ around $\lambda_0 = 0$ uniquely equals the original series $F(\lambda)$ in the prevailing order. The extrapolant is characterised by the degree of the numerator and denominator polynomials by $[L, M]$. For every set of L

and M , a single set of coefficients in Eq. (2.1.25) is defined. Such a rational function of two series is usually better suited than a plain series to describe physical quantities. The closer the form of the extrapolant to the one of the physical quantity, the more reliable it is expected to be. Therefore, often, the extrapolations with identical or nearly identical powers in the numerator and denominator are employed.

Given the rational structure of the Padé extrapolants an important issue is the occurrence of poles. These can either be non-physical or physical and the distinction between both cases is not always clear without further information on the model and phase. Non-physical poles are artefacts of the extrapolation technique and are also referred to as spurious poles. If such a pole arises at values of λ smaller than the value of interest or somewhere close in parameter space, the extrapolant is defective and must be discarded. Physical poles can indicate phase transitions or quasi-particle decay. The series diverges, because the expansion becomes invalid. In order to distinguish between both cases, many extrapolations with various degrees have to be studied. If several extrapolants give similar results and only one or a few show divergent behaviour, it is plausible that the observed poles are non-physical, whereas if the majority of extrapolants diverges it is a sign for the breakdown of the perturbative approach. However, compared with the bare series $F(\lambda)$, which always diverges at large values of λ unless all coefficients for orders $\lambda > 0$ vanish, Padé extrapolants with comparable exponents generally diverge only at larger perturbations. For instance, for $P[L/L]_F$, the behaviour for large values of λ is constant.

Padé extrapolations also provide a useful framework to study the convergence behaviour. To this end, the Padé extrapolants are grouped into families. Members of a family have the same difference between the degrees $L - M$. If the extrapolants within a family converge, the member with the highest order can be taken as the best converged result of this family. A more elaborate way is to fit the results within the family against the inverse order $1/o$ to zero, where the value represents the infinite order result. The specific choice of method depends on the detailed requirements and properties. However, if the results within a family do not converge, the extrapolants have to be discarded. The average about the converged results from different families is considered the most reliable.

2.2. Exact diagonalisation

ED is a straight forward approach to solve quantum mechanical problems. It means exactly what it says, diagonalising the Hamiltonian exactly, in order to solve the time-independent Schrödinger equation. This leads to eigenenergies, eigenstates, degeneracies, and potentially expectation values. Even though, the idea is simple and the outcome is clear, the computational realisation and understanding of the results can be challenging. In principle, ED is applicable to all kinds of problems without prerequisites. The method does not include any biases or systematic errors and is non-perturbative. The computational challenge is given by the exponential scaling of the dimension of the Hilbert space, for example a general spin- S system of N_s particles leads to a dimension $(2S + 1)^{N_s}$. That is why, the available system sizes are small compared to other methods. Finite-size scaling can be applied if several reliable cluster sizes can be solved. Then, the results are plotted against the inverse system size and extrapolated to the

infinite limit. In the following, the main steps of the method are given. For details, excellent reviews can be found in Ref. [124] and in Chapter 18.6 of Ref. [35].

To start with, a finite cluster with a small enough Hilbert space has to be chosen. It should reflect the properties also given in the thermodynamic limit as good as possible. For instance, it is often required that the number of sites allows singlets to form. The possible number of particles can be increased mainly in two ways. Firstly, if not the full energy spectrum is required, but only a small part, like the low-energy states determining the behaviour at low temperatures, specific algorithms can be applied. In this work, the Lanczos algorithm is used, which yields an efficient approach to calculate the extreme eigenvalues of a large sparse matrix [125]. It reduces the full problem to the diagonalisation of a tridiagonal matrix of dimensions ≈ 100 . In order to derive the eigenvectors, the algorithm has to be applied twice, and for the degeneracies at least as many times as the degeneracy of the energy level of interest. Therefore, these properties are more costly to determine. The method is based on matrix vector products and does not require the storage of the Hamiltonian as a matrix. Since the computational memory is the main limitation in ED, this is very helpful. Secondly, usually the Hamiltonian is invariant under symmetry transformations. This allows to split the basis into decoupled symmetry sectors, which can be studied individually. Then, another advantage is the direct knowledge about specific quantities of states within a sector. Often, lattice symmetries are employed, yielding momentum quantum numbers. On top of these for SU(2)-symmetric spin systems, the z -component of the spin, is relatively easy to exploit, whereas the SU(2) symmetry for the total spin is much more challenging and mostly not used. However, for SU(N)-symmetric models an algorithm has been found, which allows to perform ED in the different SU(N)-subspaces independently, whilst not considering all other symmetries. This still reduces the dimensions of the Hilbert spaces, in particular the singlet sectors, under study more than the conventional set of symmetries for $N > 2$ [126]. In this work, we employ the SU(N) symmetry in Part I, where further details are given in Subsection 3.1.

It would be a mistake to believe, that once the exact properties of a finite clusters are found, it becomes obvious which phase the model realises in the thermodynamic limit, since manifolds present in the infinite systems are usually split and energy gaps can be much less pronounced on finite clusters, if visible at all. Also, symmetries can not be broken directly on finite systems. However, if some states are clearly separated from others energetically this may indicate a ground-state manifold and excited states above, or if some correlations show very pronounced features this can be expected to be the case in the phase of an infinite system as well. The signature of an ordered state with a broken continuous symmetry is given by an Anderson tower of states (TOS) [35, 127, 128]. These TOS are sets of low-lying eigenenergies grouped together by their total spin quantum numbers, \vec{S}^2 , for SU(2)-symmetric systems, which generalises to the Casimir operator, C , for SU(N)-symmetric systems [Eq. (3.1.14)]. Together with the spatial symmetries, this yields the symmetry broken state in the thermodynamic limit, where the states collapse onto each other.

Part I.

Fermionic $SU(N)$ Hubbard models
with artificial gauge fields in the
strong-coupling regime

3. Introduction: Crystals of $SU(N)$ -symmetric fermions

The theoretical investigation of $SU(N)$ -symmetric models with $N > 2$ started about 50 years ago [129] and has been an active field of research since then [62–64, 126, 130–142]. A specific point of motivation is that they are likely to host exotic quantum phases [62–64, 137, 138, 140]. This is due to the enhanced symmetry compared to $SU(2)$ -symmetric models, which leads to more quantum fluctuations. A technological perspective is given by phases with non-Abelian anyonic excitations, which have the potential for applications in topological quantum computers [17–19]. Since the start of the millennium, this activity is also triggered by experimental advances, mostly based on experiments with ultra-cold atoms in optical lattices [54–61].

In the following, we first introduce the underlying concepts of $SU(N)$ -invariant spin-systems, before giving a basic understanding of the experimental realisation. Then, the $SU(N)$ Hubbard model, a generalisation of the $SU(2)$ Hubbard model in Eq. (1.0.1), which is the relevant model for the description of these experiments, is introduced, as well as theoretical models allowing to investigate certain limits. At last, we provide some first results, on the extension of the Mott-insulating phase for $N = 3$.

3.1. Theoretical basis

A quantum mechanical system is invariant under a symmetry transformation if the apparent Hamiltonian H does not change under its application. So, let the symmetry transformation be reflected by an operator \mathcal{U} , then the statement is identical to $[H, \mathcal{U}] = 0$. In this case, the energy eigenstates can be grouped together in multiplets, where all states within one multiplet are characterised by the same quantum number of \mathcal{U} , which are represented by the irreducible representations (irreps) of the symmetry group. In the following, we provide a short introduction to $SU(N)$ -symmetric systems, given by particles symmetric under permutations of N colours, along the lines of explicit examples for $SU(2)$ and $SU(3)$.

The special unitary group, $SU(N)$, consists of all N -dimensional unitary matrices with complex matrix elements and a determinant equal to one. The group operation is the matrix product. The associated Lie algebra is written $su(N)$, and usually just called $SU(N)$ algebra. Its basis is given by $(N^2 - 1)$ generators, T_α , and it is defined by

$$[T_\alpha, T_\beta] = if_{\alpha\beta\gamma}T_\gamma, \quad (3.1.1)$$

using the sum convention and the general structure constant, $f_{\alpha\beta\gamma}$. For $N = 2$, $f_{\alpha\beta\gamma}$ is given by the Levi-Civita symbol, whereas for larger N it is more complicated. The $SU(N)$ can be represented in all dimensions that are equal or larger than N . In this work, we focus on the representation with a local Hilbert space of dimension N for a

single particle. The only exception is given by spin-1 ($s = 1$), which is represented by a symmetric combination of two fundamental irreps of the $SU(2)$.

The $SU(2)$ is the most prominent instance of the special unitary groups in solid state physics, yielding the symmetry properties - among others - of electron spins. The group elements in two dimensions are given by

$$SU(2) = \left\{ \begin{pmatrix} \alpha & -\bar{\beta} \\ \beta & \bar{\alpha} \end{pmatrix} : \alpha, \beta \in \mathbb{C}, |\alpha|^2 + |\beta|^2 = 1 \right\}. \quad (3.1.2)$$

The spin operator is defined by $\vec{S} = (S^x, S^y, S^z)^T$. Usually, the total spin quantum number $s = \{1/2, 1, 3/2, 2, \dots\}$ of the squared spin operator, \vec{S}^2 , and the magnetic quantum number, $s_z \in \{-s, -s+1, \dots, s\}$, of the z -component of the spin, S^z , are chosen as good quantum numbers. All states belonging to the same total spin are in the same multiplet of states. These multiplets are given by the irreps of $SU(2)$. Physically, the term "irrep" can be understood such that an eigenstate does not change when the apparent observable is measured. It can not be reduced into other measurable states, just like an irrep that can not be reduced into other representations. For interactions between spins i and j of the form $\vec{S}_i \cdot \vec{S}_j$ a very useful relation reads

$$\vec{S}_i \cdot \vec{S}_j = \frac{1}{2} \left(S_i^+ S_j^- + S_i^- S_j^+ \right) + S_i^z S_j^z. \quad (3.1.3)$$

The ladder operators S_i^+ and S_i^- raise and lower the magnetic quantum number s_z , respectively. An $SU(2)$ -symmetric spin-1/2 particle has two possible values for the magnetic quantum number $s_z = \pm 1/2$ and the fundamental representation of dimension **2** directly describes a single spin. It is given by the Pauli-matrices, σ_x, σ_y , and σ_z , and the spin operator reads $\vec{S} = (\sigma_x, \sigma_y, \sigma_z)^T / 2 = \vec{\sigma} / 2$.

The properties of larger spins with $s = \{1, 3/2, 2, \dots\}$ are also defined by the $SU(2)$. Here, the spin operators are not defined by the Pauli matrices, but by $(2s+1)$ -dimensional representations. These can be derived for example by the angular momentum commutation relations in Eq. (3.1.1). For instance, the spin-1 operators are three 3×3 matrices. Such states, built from a local Hilbert space with a larger dimension than the one of the defining irrep N , are achieved by combinations of the defining irrep. So, an $SU(2)$ -invariant spin-1 is created from two spin-1/2. For later on, we introduce the fundamental time-reversal invariant $SU(2)$ spin-1 states

$$|x\rangle = \frac{i|1\rangle - i|\bar{1}\rangle}{\sqrt{2}}, \quad |y\rangle = \frac{|1\rangle + |\bar{1}\rangle}{\sqrt{2}}, \quad |z\rangle = -i|0\rangle, \quad (3.1.4)$$

where the local states are given by $s_z = \{\pm 1, 0\}$ for $|1\rangle$, $|\bar{1}\rangle$, and $|0\rangle$, respectively [63]. This also gives a fundamental time-reversal invariant representation of $SU(3)$ [143]. The spin-1 states are linked via a single pair of ladder operators, S^\pm . Hence, to get from $|1\rangle$ to $|\bar{1}\rangle$ the annihilation operator needs to be applied twice. This is a significant difference to an $SU(3)$ -invariant system, which also has three fundamental states, however these are all directly connected and the system offers three pairs of ladder operators. That is one of the reasons why $SU(N)$ -symmetric models exhibit more quantum fluctuations with increasing values of N . The degrees of freedom spanning the local Hilbert space of $SU(N)$ -symmetric particles are often called the spin-colours or short colours, and

sometimes referred to as flavours. We stick with the first colourful terminology, thinking about rainbows rather than chocolates. For $SU(2)$ the colour is identical to the spin orientation in z -direction, s_z . The $SU(N)$ product states at a filling of one particle per site are usually written with letters representing the spin-colours, like $|abc\rangle$ for three distinct colours at positions 1, 2, and 3 implicitly indicated by the order. The interactions of such states are most simply given by permutations, interchanging the spin-states between sites. The permutation operator between two sites, i and j , reads

$$P_{ij} = \sum_{\mu, \gamma = \{a, b, c, \dots\}} |\mu_i \gamma_j\rangle \langle \gamma_i \mu_j| . \quad (3.1.5)$$

Up to a constant and scaling this is identical to the interactions for $SU(2)$ in Eq. (3.1.3). Precisely, the operator $(P_{ij} - 1/N)/N$ is the same, but for $SU(N)$ systems the form in Eq. (3.1.5) is more convenient.

The symmetry transformation arising from the $SU(N)$ is a global rotation of the spin-colours. The generators are

$$S_\gamma^\mu = \sum_i c_{i\gamma}^\dagger c_{i\mu} , \quad (3.1.6)$$

where the operator $c_{i\gamma}^\dagger$ creates a particle of colour γ on site i , and $c_{i\mu}$ destroys a particle of colour μ on site i . They are the ladder operators of $SU(N)$, fulfilling the $SU(N)$ algebra, which yields the associated irreps. A system is therefore symmetric under $SU(N)$, if the Hamiltonian commutes with all generators, i.e. $[H, S_\gamma^\mu] = 0$ for all γ, μ . For $SU(2)$ the transformation can be written as, $\exp(-i\alpha \vec{n} \cdot \vec{\sigma}/2)$, a rotation around a vector, \vec{n} , by an angle, α . Therefore, the symmetry is explicitly broken under the application of a non-isotropic magnetic field. Crystals - without magnetic fields - are mostly well described by $SU(2)$ -invariant Hamiltonians. However, there can be special points where the symmetry of the Hamiltonian is enhanced. Such a case arises in the bilinear-biquadratic spin-1 model, where the $SU(2)$ symmetry is enlarged to $SU(3)$ for identical interaction strengths [143]. The special unitary group of dimension $N = 3$, the $SU(3)$, has 8 fundamental representation matrices called the Gell-Mann matrices. In the $SU(2)$ spin-1 notation these arise from three bilinear and five quadrupolar spin operators.

For the further discussion, we introduce Young tableaux, which correspond one-to-one to the irreps of $SU(N)$. This connection offers an illustrative way of dealing with the irreps and yields a substantial improvement for performing EDs. Young tableaux were first introduced by Young in 1900 [144]. They represent irreps of the symmetric group, S_n , of n permutations as well as of the special unitary group, $SU(N)$. A Young tableau yields all states within one irrep of $SU(N)$. In terms of a multiplet a certain Young tableau is equivalent to the quantum number grouping the states together, but Young tableaux are actually much more powerful than that.

Young tableaux can be defined in the notion of boxes \square . A finite number, n , of these boxes is arranged in at most N rows with the condition that the number of boxes in every row does not increase from top to bottom. The form of a Young tableau, α , is

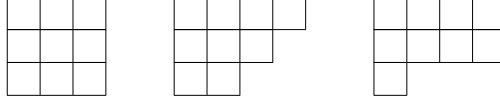


Fig. 3.1.: Young tableaux for $n = 9$ particles with three colours, $N = 3$, $\alpha_1 = [3, 3, 3]$, $\alpha_2 = [4, 3, 2]$, and $\alpha_3 = [4, 4, 1]$.

defined by the number of boxes, α_i , in every row, i , as

$$\alpha = [\alpha_1, \alpha_2, \dots, \alpha_k], \quad k \leq N, \quad \alpha_1 \geq \alpha_2 \geq \dots \geq \alpha_k. \quad (3.1.7)$$

Examples of Young tableaux are shown in Fig. 3.1. These are valid for all $N \geq 3$. Every Young tableau with n boxes is related to invariant sectors of states from n particles with N colours in the fundamental representation \square . The states belonging to one Young tableau are characterised by their permutation symmetry properties. The rows in the tableaux relate to symmetric properties, whilst columns account for the antisymmetric properties of the wave function [139]. A totally symmetric wave function does not change the sign under a permutation of two elements, a totally antisymmetric one does, and a mixed one behaves differently depending on the elements. In order to generate the associated symmetrising operators, one uses standard Young tableaux, which define projectors on symmetrised states. Standard Young tableaux are Young tableaux, which are labelled by natural numbers from 1 to n in every box. Every label must be larger than the one in the boxes above and on the left. As an example, the two tableaux for two $SU(2)$ -symmetric particles each given by the fundamental representation \square of dimension **2** are

$$\text{i) } \begin{array}{|c|} \hline 1 \\ \hline 2 \\ \hline \end{array} \quad \text{and} \quad \text{ii) } \begin{array}{|c|c|} \hline 1 & 2 \\ \hline \end{array}.$$

The first one i) represents the antisymmetric state, the second one ii) the symmetric states. The explicit states can be generated by antisymmetrising and symmetrising operators, A and S , respectively. For two particles the operators read

$$A_{12} = \mathbb{1} - P_{12} \quad \text{and} \quad S_{12} = \mathbb{1} + P_{12} \quad (3.1.8)$$

with the identity, $\mathbb{1}$. If they are employed on the product states of two spins-1/2, one finds the well known singlet state with $s = 0$ and triplet states with $s = 1$. In order to consider spin-1 particles, one has to take a local basis of two combined spins-1/2 in the symmetric representation $\square\square$. For three $SU(3)$ -symmetric particles given by the fundamental representation \square of dimension **3**, the standard Young tableaux are

$$\text{i) } \begin{array}{|c|} \hline 1 \\ \hline 2 \\ \hline 3 \\ \hline \end{array}, \quad \text{ii) } \begin{array}{|c|c|} \hline 1 & 2 \\ \hline 3 & \\ \hline \end{array}, \quad \text{iii) } \begin{array}{|c|c|} \hline 1 & 3 \\ \hline 2 & \\ \hline \end{array}, \quad \text{and} \quad \text{iv) } \begin{array}{|c|c|c|} \hline 1 & 2 & 3 \\ \hline \end{array}.$$

The first one i) yields the totally antisymmetric, the last one iv) the totally symmetric

state. The totally antisymmetric state is determined by

$$\begin{aligned} A_{123} &= \mathbf{1} - P_{12} - P_{23} - P_{31} + P_{123} + P_{321} , \quad \text{to} \\ A_{123} |abc\rangle &= |abc\rangle - |bac\rangle - |cba\rangle - |acb\rangle + |bca\rangle + |cab\rangle = \sqrt{6} |\Psi_1\rangle . \end{aligned} \quad (3.1.9)$$

The totally symmetric state with three colours can be determined analogously

$$\begin{aligned} S_{123} &= \mathbf{1} + P_{12} + P_{23} + P_{31} + P_{123} + P_{321} , \quad \text{to} \\ S_{123} |abc\rangle &= |abc\rangle + |bac\rangle + |cba\rangle + |acb\rangle + |bca\rangle + |cab\rangle = \sqrt{6} |\Psi_2\rangle . \end{aligned} \quad (3.1.10)$$

The other standard Young tableaux ii) and iii) represent mixed-symmetry states. They belong to the same Young tableau, and therefore, the apparent multiplet is still of dimension larger than one and includes several permutation symmetry sectors. The states are generated by a product of symmetrising and antisymmetrising operators. These do not directly lead to an orthonormal set of states. However, through linear combinations and normalisation one finds

$$\begin{aligned} |\Psi_3\rangle &= -\frac{1}{\sqrt{12}} (2|abc\rangle + 2|bac\rangle - |cba\rangle - |cab\rangle - |acb\rangle - |bca\rangle) , \\ |\Psi_4\rangle &= \frac{1}{2} (-|cba\rangle + |cab\rangle + |acb\rangle - |bca\rangle) , \\ |\Psi_5\rangle &= \frac{1}{\sqrt{12}} (2|abc\rangle - 2|bac\rangle + |cba\rangle - |cab\rangle + |acb\rangle - |bca\rangle) , \\ |\Psi_6\rangle &= -\frac{1}{2} (|acb\rangle + |bca\rangle - |cba\rangle - |cab\rangle) . \end{aligned} \quad (3.1.11)$$

The first two states belong to the standard Young tableau ii) and are symmetric under permutations of the elements 1 and 2, the latter two belong to iii) and are antisymmetric under permutations of the elements 1 and 2. These are not yet all states of the system, since also states with two colours and states with a single colour exist. Overall, there are $3^3 = 27$ states. All one- and two-colour states can be obtained by replacing particles with one colour by particles of another colour within the three-colour states, i.e. the application of a single ladder operator given in Eq. (3.1.6). This procedure generates twelve more states of mixed symmetry, and nine totally symmetric states. So, together the standard Young tableaux account for i) **1**, ii) **8**, iii) **8**, and iv) **10** states. The number of states linked to a standard Young tableau is called the *dimension*, d^α , of the irrep that is associated with the Young tableau α . The dimension is identical for all standard Young tableaux of the same Young tableau and physically gives the number of states within the symmetry sector of permutations. It is

$$d^\alpha = \frac{H}{\prod_{i=1}^n l_i} , \quad (3.1.12)$$

where the constant H is defined by a product over natural numbers assigned to the boxes in the Young tableau as follows. The top left box is labelled with N . For every box on the right this number is increased by one, whereas it is decreased by one for boxes below. Another set of integers needs to be assigned to every box for the product in the denominator, the hook length, l_i . For every box it is determined by the number

of boxes on the right and below plus one. The name "hook" stems from the fact, that the hook length can also be found by counting all boxes along a line going from the considered box to the right and to the bottom of the tableau with the shape of a hook. The dimension is commonly used to label the Young tableaux for which the value is written as a bold number as already done above.

Another useful quantity is the *multiplicity*, f^α , which yields how many times the irrep associated with the Young tableau α appears in the full Hilbertspace under the decomposition. This is identical to the total number of standard Young tableaux belonging to α . It can be determined by

$$f^\alpha = \frac{n!}{\prod_{i=1}^n l_i}. \quad (3.1.13)$$

In the example of three $SU(3)$ -symmetric particles, one finds $f^{[1,1,1]} = \frac{3!}{3 \cdot 2 \cdot 1} = 1$, $f^{[2,1]} = \frac{3!}{1 \cdot 1 \cdot 3} = 2$, and $f^{[3]} = \frac{3!}{3 \cdot 2 \cdot 1} = 1$. For two spin-1/2 particles both irreps have a multiplicity of one, so the multiplicity in Eq. (3.1.13) should not be confused with the total number of states within a multiplet, which are one and three for singlet and triplet. These are reflected by the dimension. In this specific case, all states within every multiplet belong to the same pair of quantum numbers for permutation and total spin. The multiplicity, f^α , can be non-trivial for $SU(2)$ -symmetric spin-1/2 particles as well. For instance for three particles in the irrep with mixed symmetry, or for four spin-1/2 particles in the singlet sector as can be seen in Fig. 3.2. Overall, the multiplicity, f^α , gives the dimension of the subspace of distinct permutation symmetries, without including the number of degenerate states within these subspaces, which is given by d^α . More technically, the multiplicity gives the dimension of the subspace that needs to be diagonalised in ED for an $SU(N)$ -invariant Hamiltonian, if one performs it in the $SU(N)$ -symmetric basis. This is due to the fact that all states belonging to the same standard Young tableau are degenerate in energy.

An extremely insightful property is determined by the Casimir operator, which is generally defined as an operator that commutes with all generators of a group. Therefore, it allows to assign a quantum number to every irrep and different irreps can share the same Casimir quantum number. For $SU(2)$, the only Casimir operator is \vec{S}^2 , which yields the total spin quantum number, s . For a given Young tableau, the quadratic Casimir operator is defined by

$$C = \frac{1}{2} \left(n \left(N - \frac{n}{N} \right) + \sum_{i=1}^k \alpha_i^2 - \sum_{j=1}^{\alpha_1} c_j^2 \right). \quad (3.1.14)$$

The number of boxes in a column j of the examined tableau α is denoted with c_j . The lowest Casimir emerges for the singlet sector, which yields the low-energy regime for antiferromagnetic interactions.

Let us now turn to some additional properties, allowing to employ the $SU(N)$ -

| | | | |
|---|---|---|---|
| 1 | 2 | 1 | 3 |
| 3 | 4 | 2 | 4 |

Fig. 3.2.: Both standard Young tableaux for $n = 4$ $SU(2)$ -symmetric particles of the fundamental representation in the singlet sector, $\alpha = [2, 2]$.

symmetry in ED. This is advantageous, since the use of the $SU(N)$ -symmetry reduces the required basis dimension for $N > 2$ more than other symmetries like magnetisation or lattice symmetries, and often allows to focus the investigation on low-energy states by studying certain irreps. For these reasons, the use of standard Young tableaux as basis states has recently been investigated and established [139]. It allows to perform ED for $SU(N)$ -symmetric systems basically on the same cluster sizes as for $SU(2)$ -symmetric spin-1/2 models. In order to perform ED, the Hamiltonian should be written in an orthonormal basis. However, the scheme employing simple symmetrisers and antisymmetrisers exemplified in Eqs. (3.1.9) and (3.1.10) does not generically lead to orthonormal states. This is achieved by a set of operators called orthogonal units [139, 145]. These are more complicated than products of A and S , if one writes them down explicitly. However, for ED this is not necessary, since the Hamiltonian can be expressed in the apparent orthonormal basis directly, in which it takes a rather simple form. To this end, one employs transposition operators, $\tau_{k,k+1}$, for the spins on sites k and $k+1$ to construct permutations, P_{ij} , between the spins on sites i and j . Consider two standard Young tableaux S_r and S_q of the same Young tableau α in the basis $\{S_r, S_q\}$ for which the transposition of k and $k+1$ is possible. Then, the transposition operator reads

$$\tau_{k,k+1} = \begin{pmatrix} -\rho & \sqrt{1-\rho^2} \\ \sqrt{1-\rho^2} & \rho \end{pmatrix}. \quad (3.1.15)$$

The axial distance, ρ , follows from the shape of the Young tableau α in a very easy manner, for details see Ref. [139]. The transpositions are sparse matrices with at most two entries per column and row and are only possible for consecutive numbers. So, $n-1$ transposition operators exist for a tableau with n boxes. The permutation operator between spins i and j with $i \leq j$ follows from

$$P_{ij} = \tau_{i,i+1}\tau_{i+1,i+2}\dots\tau_{j-1,j}\tau_{j-2,j-1}\dots\tau_{i,i+1}. \quad (3.1.16)$$

3.2. Experimental realisations

In the last decades, substantial progress was made in experiments with optical lattices as well as with ultra-cold atomic quantum-gases. Their combination yields the possibility to build quantum simulators, which are able - among other applications - to probe theoretical models that are otherwise lacking in materialised counterparts. Here, we only briefly describe how $SU(N)$ -symmetric systems can be realised experimentally with these techniques. Articles and reviews on crystals of light and matter are given in Refs. [146–148], for the specific realisation of $SU(N)$ -symmetric models see Refs. [54–61].

Optical lattices are basically periodic potentials created by the interference patterns of laser light. They can be employed to simulate the periodic potential of a crystal. The simplest set-up is given by two opposing laser beams of the same wavelength, interfering and creating a standing wave. In places of either maximal or minimal intensity of the periodic potential, particles can be confined and these points correspond to lattice sites [148]. The use of several lasers extends this setting to more-dimensional structures, e.g. six lasers can generate a cubic lattice. It is also possible to create more complicated lattices, like the honeycomb and triangular lattice [149–151]. Another feature of optical

lattices is that the depth of the confining areas is controlled by the laser intensity and can be tuned easily. Experiments are never perfect though and the potential shows an inhomogeneity due to the Gaussian profile of the laser beams. However, this effect is weak in comparison to the desired periodic potential [148].

The second necessity is the preparation of an ultra-cold quantum gas, where the atoms are present in certain ratios of distinct single-particle quantum states. This can be done with bosonic and fermionic particles as well as with mixtures of particles. For the optical crystals, we focus on *strongly-correlated neutral fermions*. These particles can be loaded into the optical lattice, where the kinetics arise from tunneling processes between the sites [146, 148, 152–154]. These occur mainly between nearest-neighbour sites for reasonably deep potentials and the strength of motion is set by the tunneling rate [146, 154]. The atoms mainly interact via inter-atomic collisions on single sites, i.e. the interactions only occur when several atoms occupy the same site [56, 152, 155]. The repulsion between atoms on nearest- and next-nearest-neighbour sites is two orders of magnitude smaller than on a single site [152]. These interactions are repulsive and can be adjusted by the potential depth of the light-field, hence by the laser intensity. A strong potential localises the particles such that the repulsive interactions are large and the kinetics are small, whereas a weak potential leads to weak repulsion and strong kinetics [152].

We see, that this setting is quite well captured by the Hubbard model in Eq. (1.0.1), and it is indeed possible to enlarge the repulsion sufficiently to enter the Mott-insulating phase [156–158]. In order to measure this, the temperature must be small in comparison to the particle-hole gap, such that thermally excited doublons are neglectable. This was first achieved with bosons in 2002 [156] and with fermions in 2008 [157]. In the latter experiment, a quantum gas of ^{40}K atoms in two magnetic levels of the total angular momentum was used. These were loaded in a cubic optical lattice and various interaction strengths were applied. Then, the suppression of double occupancies with increasing interaction was measured, indicating the Mott-insulating phase. A second group published similar results in the same year [158]. Furthermore, it was demonstrated that artificial gauge fields can be applied, creating magnetic fluxes through plaquettes. The particles accumulate complex phase factors whilst encircling plaquettes [159]. Given that the standard mechanism for such behaviour - the Aharonov-Bohm effect - only works for charged particles, this achievement illustrates well how powerful the control of the laser fields over the optical lattice is.

The use of ultra-cold fermionic alkaline earth-like atoms, i.e. alkaline earths or Ytterbium, as the constituents confined in the optical lattice leads to almost perfect $SU(N)$ -invariant systems. The enhanced symmetry arises, because the nuclear spin, I , is nearly completely decoupled from the electronic angular momentum, J , in the alkaline earth-like atoms. Therefore, the scattering parameters, which determine the exchange interactions in the Hamiltonian, do not depend on the nuclear spin. This was measured for Y in Ref. [56]. Indications were found for Sr in Refs. [160]. The first direct spectroscopic observation of the $SU(N = 10)$ -symmetry in ^{87}Sr at temperatures in the order of mK was done in 2012 [58], where the atoms were confined in a two-dimensional optical trap. The number of nuclear Zeeman states, $m = \{-I, \dots, I\}$, sets the number $N = 2I + 1$ of the $SU(N)$ -symmetry of the system. The distinct nuclear Zeeman states correspond to the N spin-colours described in Section 3.1. The experimental systems can also be

prepared such that $N < 2I + 1$ [55]. For instance, ^{87}Sr has a nuclear spin $I = \frac{9}{2}$ and nuclear Zeeman states with $m = \{-\frac{9}{2}, -\frac{7}{2}, \dots, \frac{9}{2}\}$. Therefore, $\text{SU}(N)$ -symmetries with $N \leq 10$ can be build.

In 2012, the first purely fermionic Mott-insulating phase for an $\text{SU}(6)$ -invariant system was demonstrated using ^{173}Y atoms [56]. Again, the double occupancy was measured in order to determine the insulating phase. The ^{173}Y atoms were also used to realise a Mott-insulating phase in $\text{SU}(3)$ -symmetric systems [61]. These recent experimental developments set a strong motivation for further theoretical investigations in order to predict phase diagrams and discover parameter regimes of unconventional quantum phases.

3.3. Models and phases

The experimental set-up with ultra-cold alkaline rare-earth atoms trapped in an optical lattice is overall well captured by the Hubbard model for $\text{SU}(N)$ -symmetric fermions. Usually, if one talks about the Hubbard model, the $\text{SU}(2)$ -symmetric Hubbard model, Eq. (1.0.1), is meant. The only difference lies in the symmetry of the local quantum states of a spin and the interactions. Originally, the Hubbard model was introduced in solid state quantum mechanics to describe electrons in correlated crystals [21]. However, the model works even better for atoms in optical lattices, where no additional longer-range interactions, like Coulomb interactions, occur. Also, the nearest-neighbour approximation works better, due to the low density of particles [146, 148, 152, 153, 157]. In such experiments, it is possible to add a uniform magnetic-flux on plaquettes of the light crystal leading to non-trivial phases by the same mechanism as in the Aharonov-Bohm effect. The Hamiltonian of the $\text{SU}(N)$ Hubbard model with fluxes reads

$$H = -t \sum_{\langle i,j \rangle} \sum_{\alpha=1}^N (e^{i\phi_{ij}} c_{i\alpha}^\dagger c_{j\alpha} + \text{h.c.}) + U \sum_{i,\alpha < \beta} n_{i\alpha} n_{i\beta} . \quad (3.3.1)$$

It can be understood in analogy to the Hamiltonian of the $\text{SU}(2)$ Hubbard model in Eq. (1.0.1). The first term with the hopping amplitude $t \geq 0$ represents the kinetics given by the fermionic creation, $c_{i\alpha}^\dagger$, and annihilation operator, $c_{i\alpha}$, creating and annihilating a fermion of colour α on site i . A particle hopping between sites i and j accumulates a phase ϕ_{ij} , which adds up to the flux Φ uniformly for all plaquettes of the lattice. The Pauli principle needs to be fulfilled and no particles of the same colour are allowed on the same site. The second term represents the on-site coupling of strength U between the fermions. The counting operator, $n_{i\alpha}$, vanishes if on site i no particle of colour α is present and otherwise is unity.

If the coupling between the fermions is strong in comparison to their kinetic energy, the system realises the Mott-insulating phase. A basic effective theoretical description is given by a model with localised spins on sites. For a filling of one particle per site the simplest description is the Heisenberg model

$$H = J \sum_{\langle i,j \rangle} P_{ij} . \quad (3.3.2)$$

In the following, two phases are most relevant: 3-SL LRO phases and CSL phases. A 3-SL LRO phase in the $SU(3)$ -symmetric Heisenberg model was discovered by Papanicolaou in 1988 using a first version of linear flavour-wave theory in the context of the spin-1 bilinear-biquadratic model [161]. This type of order is characterised by a continuous symmetry breaking of the colour-rotation symmetry, $SU(3)$. It can be sketched by diagonal stripes of the same colour with neighbouring stripes in different colours as illustrated in Fig. 3.3. It is further discussed in Chapter 6. The $SU(N)$ Heisenberg model was also found to exhibit CSL phases. These were discovered in 2009 for $m = N/k$ particles per site with integer values of $k \geq 2$ in the limit of large N at fixed k on the square lattice [52, 53]. These phases break time-reversal symmetry and parity, but not their product. On systems with open boundary conditions they exhibit gapless chiral edge modes.

The Heisenberg model in Eq. (3.3.2) offers a valid description for the strong-coupling limit, $U \rightarrow \infty$. If the coupling U is decreased within the range of the Mott-insulating phase, the increasing quantum fluctuations potentially trigger other phases. Within the effective description of localised spins these fluctuations are captured by further interactions, which depend on the lattice structure, compare Subsection 4.2.1 and Subsection 4.2.2. For the triangular lattice, a perturbative treatment of the Hubbard model around the limit $t/U \ll 1$ to subleading third order yields the J - K model. The occurrence of an effective interaction in third-order is unique to lattices including triangles, and suggests strong quantum fluctuations at relatively small values of t/U in comparison to other lattices with smaller coordination numbers. Therefore, the triangular lattice is more likely to exhibit unconventional quantum phases than other geometries and we mostly focus on it in this part.

The J - K model includes nearest-neighbour Heisenberg interactions, J , as well as three-site ring exchanges, K , on every triangle. The Hamiltonian reads

$$H = J \sum_{\langle i,j \rangle} P_{ij} + K \sum_{(i,j,k)} P_{ijk}, \quad (3.3.3)$$

where the first sum runs over nearest-neighbours and the second sum over all triangles. A permutation operator acting on several sites is defined by $P_{ijk} = P_{ij}P_{jk}$. The coupling constants are $J = 2t^2/U - 12 \cos(\Phi) t^3/U^2$ and $K = -6e^{i\Phi} t^3/U^2$ with the flux Φ per triangular plaquette. Instead of J and K , it is commonly phrased in terms of the

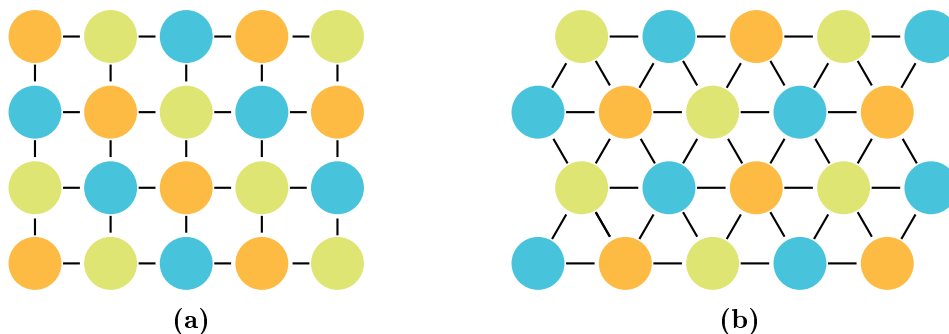


Fig. 3.3.: Sketch of the 3-SL LRO phases for the $SU(3)$ Heisenberg model on the square (a) and triangular (b) lattices, taken from Ref. [66].

parameter α by $J = \cos \alpha$ and $K = \sin \alpha$. For the J - K model with purely imaginary ring exchange K , hence explicitly broken time-reversal symmetry, the presence of CSL phases was discovered for all $2 < N < 10$ by ED and VMC [62]. These phases have a topological ground-state degeneracy of N on the torus and exhibit N different Abelian anyons if time-reversal symmetry is explicitly broken [53]. If time-reversal symmetry is not explicitly broken the degeneracy is $2 \cdot N$. Their Chern number is one, and the chiral edge states on open systems can be described by an $SU(N)$ Wess-Zumino-Novikov-Witten (WZNW) theory. We study the J - K model for $N = 7$ and $N = 3$ in Chapter 5 and Chapter 6, respectively. The literature for $N = 3$ is discussed further in Section 6.1.

The previous findings lead to three open points, which are the motivation for our investigations. Firstly, it is not clear if the effective description of the Hubbard model in subleading order is still accurate enough at the coupling strengths where the CSL phases occur. Secondly, only specific fluxes have been studied so far and an understanding of the extension of the CSL is in demand. And thirdly, one also has to ask whether the coupling strengths, where the CSLs appear, lie within the Mott-insulating phase, since otherwise the effective description breaks down.

4. Derivation of effective models

In this chapter, it is our goal to derive effective models for the Mott phase of a general $SU(N)$ Hubbard model at a commensurate $1/N$ -filling for arbitrary uniform fluxes, Φ . We perform perturbation theory about the strong-coupling limit $t/U \ll 1$ in Eq. (3.3.1), where the ground-state subspace \mathcal{H}_0 is spanned by all states with exactly one fermion per site. At first, we perform degenerate perturbation theory on finite linked clusters [25, 95, 96, 162, 163] using Takahashi’s perturbation theory briefly discussed in Subsection 2.1.2. Second, we exploit the linked-cluster theorem using white graphs [108] as explained in Section 2.1.1. We derive the effective model for the honeycomb lattice in order six in t/U in the thermodynamic limit. For the triangular lattice the effective model in order five was already derived in Ref. [66], where also the effective model for the square lattice is given. The effective model of the triangular lattice is published in Ref. [100]. These lattices with various $SU(N)$ fermions were found to host quantum phases, such as plaquette order and unconventional CSLs [62–64, 164–166]. Furthermore, the effective model of a 12-site cluster with PBCs is calculated up to order four to validate the effective models. To this end, ED is performed for $SU(3)$ at the end of the chapter. These results are also published in Ref. [100], and the according content in this chapter is taken from there, and adapted for the additional inclusion of the honeycomb lattice.

In their generic form the effective Hamiltonians can be expressed as

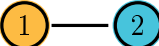

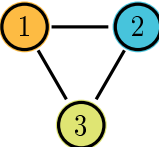
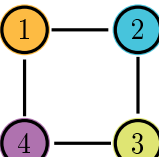
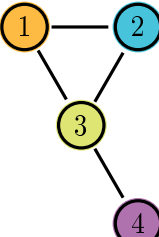
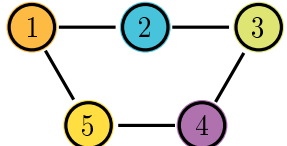

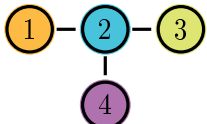
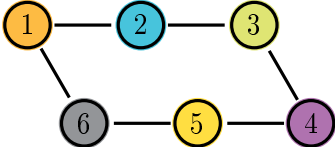
$$\mathcal{H}_{\text{eff}}(t/U, \Phi) = \sum_{(i,j)} A_{ij} P_{ij} + \sum_{(i,j,k)} B_{ijk} P_{ijk} + \dots, \quad (4.0.1)$$

where the coupling constants A_{ij}, B_{ijk}, \dots depend on t/U and Φ . In the following, all effective Hamiltonians and effective couplings are given in units of U .

4.1. Small clusters

In a linked-cluster expansion, a link is created by the perturbative hopping of a fermion between two sites. We find that in order k only linked clusters with up to k sites contribute. Precisely, a linked cluster yields a non-vanishing contribution, if the number of links that are part of a loop plus twice the number of links that are not part of a loop is smaller or equal to the order. The factor two arises because a single hopping on a bond that is not part of a loop leads to an excited state and the term vanishes after projection, P . All linked-clusters, g_i , that are relevant for the linked-cluster expansions are summarised in Tab. 4.1. The linked-cluster expansion for the honeycomb lattice requires the dimer, g_1 , the trimer, g_2 , a 4-site chain, g_7 , a 4-site T graph, g_8 and a 6-site loop, g_9 . The effective model for the triangular lattice in fifth-order also has contributions from a triangle, g_3 , a triangle plus an additional site, g_5 and a 5-site loop, g_6 . In sixth-order, all graphs shown in Tab. 4.1 contribute to the effective model on the

triangular lattice, as well as a 4-site plaquette including a diagonal bond, which is not studied here.

| name | index | graph | contributing order |
|------------------------|-------|--|-------------------------------------|
| dimer | g_1 |  | 2 nd and 4 th |
| trimer | g_2 |  | 4 th |
| triangle | g_3 |  | 3 rd and 5 th |
| 4-site plaquette | g_4 |  | 4 th |
| triangle plus one site | g_5 |  | 5 th |
| 5-site loop | g_6 |  | 5 th |
| 4-site chain | g_7 |  | 6 th |
| 4-site T graph | g_8 |  | 6 th |
| 6-site loop | g_9 |  | 6 th |

Tab. 4.1.: Linked-clusters contributing in sixth-order to the effective model on the honeycomb lattice, and in fifth-order to the triangular lattice. The sites are labelled according to the usage in the text. Given are the lowest non-vanishing orders of the associated reduced effective models. The table is extended from Ref. [66].

In Tab. 4.1 the graphs are illustrated with labelled sites as used in the following,

together with the order in which they first contribute. Details of the calculations for the linked clusters can be found in Ref. [66], where also the effective model for the square and triangular lattice in the thermodynamic limit are derived. In the following, we motivate the main steps of the perturbative calculations on the small clusters. The full results on all linked clusters in Tab. 4.1 are given in Appendix A. We employ them for the linked-cluster expansions in Section 4.2.1 and Section 4.2.3.

The unperturbed Hamiltonian, H_0 , is given by the Hubbard interaction, whereas the hopping term is taken as the perturbation, V . When V is applied on a ground state it always leads to an excited state with one doubly occupied site. As a first simple conclusion, all terms containing PVP in the transformation in Eq. (2.1.10) vanish.

On a finite N_s -site cluster for arbitrary N , that is possibly larger than the number of sites, N_s , the basis of spin states consists of all states with maximal N_s different spin colours. The cases where $N < N_s$ are all included within the case $N = N_s$ and one has to consider only a basis of $N!$ states for every linked cluster out of the N^{N_s} degenerate states. Together with the maximal number of sites $N_s = k$, only $N = k$ has to be studied for the derivation of the effective model for all N in order k .

We use a very appealing linked-cluster expansion approach along the lines of a white-graph expansion [108], which originally was set up to reduce the number of separate linked-cluster calculations. We employ it to simplify the subtraction process, as well as to include complex phases. To this end, every bond on a linked cluster is labelled with a different exchange constant during the calculation. For instance, on the triangle, g_3 , we take three exchange constants h_1 , h_2 , and h_3 connecting different sites. The perturbation is written as

$$V^{g_3} = \sum_{\alpha=1}^N \left(h_1 c_{1\alpha}^\dagger c_{2\alpha} + h_2 c_{2\alpha}^\dagger c_{3\alpha} + h_3 c_{3\alpha}^\dagger c_{1\alpha} \right) + \text{h.c.} .$$

The subtraction of the so derived effective Hamiltonian is then achieved by taking only terms that include every exchange constant at least once and hence emerge from perturbations that link the whole cluster. This procedure can be extended to include complex phase factors by splitting up a hopping process on a link into the hopping from site i to j and from site j to i . For the triangle one can choose

$$\begin{aligned} V^{g_3} = & \sum_{\alpha=1}^N \left(h_{1A} c_{1\alpha}^\dagger c_{2\alpha} + h_{1B} c_{1\alpha}^\dagger c_{2\alpha} \right) \\ & + \sum_{\alpha=1}^N \left(h_2 c_{2\alpha}^\dagger c_{3\alpha} + h_3 c_{3\alpha}^\dagger c_{1\alpha} \right) + \text{h.c.}, \end{aligned}$$

with $h_{1A} = h_1 e^{i\Phi_{g_3}} = h_{1B}^*$. In this section, the flux through a closed loop on a graph g_i is Φ_{g_i} . For the linked-cluster expansions the actual fluxes for the whole lattice have to be considered. The results do not depend on how the phases are distributed over the bonds as long as the sum of a loop gives the proper flux. This is clear, since processes where bonds get acted on a single time can only contribute if the perturbation acts on all bonds of a loop, so the phases in such processes always add up to the flux of the loop. A back and forth hopping yields compensating phases. In the following, a

particle encircling a loop clockwise or counter clockwise accumulates a phase, Φ_{g_i} or $-\Phi_{g_i}$, respectively.

For each cluster, one derives the effective Hamiltonian, where we perform the subtraction directly as described above. These Hamiltonians can already be written in a compact form as in Eq. (4.0.1). For the triangle in order three, it is

$$\tilde{H}_{\text{eff}}^{g_3, \mathcal{O}(3)} = \tilde{A}_3 + \tilde{B}_3 (P_{12} + P_{23} + P_{13}) + \tilde{C}_3 P_{12} P_{23} + \tilde{C}_3^* P_{32} P_{21}$$

with the parameters

$$\begin{aligned} \tilde{A}_3 &= -6 \frac{t^3}{U^3} \cos \Phi_{g_3}, & \tilde{B}_3 &= 6 \frac{t^3}{U^3} \cos \Phi_{g_3}, \\ \text{and } \tilde{C}_3 &= -6 e^{i\Phi_{g_3}} \frac{t^3}{U^3}. \end{aligned}$$

The reduced effective models of all linked-clusters g_i named in Tab. 4.1 can be found in Appendix A.

4.2. Linked-cluster expansions

Every linked cluster yields a different set of exchanges that are embedded on the full system. Some of these exchanges are unique to the specific cluster, e.g. the ring-exchange on the six-site loop in order six, where the embedding is trivial. Other interactions emerge from contributions of a variety of linked clusters like the nearest-neighbour exchange in orders larger than two on the triangular lattice, or order three on other lattices. The embedding is performed by a weighted summation. In principle, every exchange existing on the linked clusters is embedded in every possible configuration of the linked cluster on the full lattice. For a better understanding of the technique, we give a few details during the derivation of the effective model on the honeycomb lattice in the next subsection. The derivation of the effective models on the square and the triangular lattice are given in Ref. [66], including a detailed description of the embedding.

4.2.1. Honeycomb lattice

Motivated by experimental advances, the honeycomb lattice has been studied for SU(6)-symmetric spins in a Heisenberg model (3.3.2). It was proposed that the model hosts a CSL phase by mean-field theory [164, 165]. A later study using ED, VMC, and iPEPS showed that it is actually a plaquette phase. A similar plaquette phase was also discovered in a recent study of the SU(3) Hubbard model by iPEPS [167]. The phase transition from the plaquette phase to a dimerised colour-ordered phase is at $(U/t)_c = 7.2 \pm 0.2$ before the Mott phase breaks down at $(U/t)_c^{\text{mi}} = 4.5 \pm 0.5$ (or $(t/U)_c^{\text{mi}} = 0.14$). So, for vanishing flux and SU(3)-symmetric fermions no CSL is expected on the honeycomb lattice.

In Ref. [166], also a complex ring exchange K on the plaquettes was included, which stabilises the SU(6) CSL phase. Precisely, a flux $\Phi = \pi/2$ per plaquette was investigated and the phase transition is at a coupling ratio $K/J \approx 0.2i$. The main motivation for the extension of the Hamiltonian was to stabilise the CSL. Given the experimental

possibilities, where the Hubbard model is realised including fluxes Φ by artificial gauge fields, the question arises if this term is a relevant part of the effective description. In similar cases for the triangular lattice with $SU(3)$ fermions and for the square lattice with spin-1/2 particles, this is the case [62, 163]. However, in these models the ring exchange terms are the subleading contributions, whereas for the honeycomb lattice the ring exchange term is only one of the subsubleading terms, and it is not obvious if it dominates over other processes. We derive the full effective model for general values of N and fluxes Φ up to order six in t/U , and compare the occurring couplings.

All interactions from the linked clusters are embedded onto the lattice in the thermodynamic limit. The effective Hamiltonian on the honeycomb lattice reads

$$\begin{aligned}
H_{\text{hc}}^{\mathcal{O}(6)} = & N_s \cdot \epsilon_0 + J \sum_{i-j} P_{ij} + L_{\text{NNN}}^{2\text{sp}} \sum_{i-j} P_{ij} + L_{4\text{N,p}}^{2\text{sp}} \sum_{i-j} P_{ij} \\
& + L_{4\text{N,dp}}^{2\text{sp}} \sum_{i-j} P_{ij} + \sum_{i-j} \left(L_{\text{NN}}^{3\text{sp}} P_{ijk} + \text{h.c.} \right) \\
& + \sum_{i-j-k} \left(L_{\text{NNN,p}}^{3\text{sp}} P_{ijk} + \text{h.c.} \right) + L_{\text{NNN,dp}}^{3\text{sp}} \sum_{i-j-k} (P_{ijk} + \text{h.c.}) \\
& + \sum_{i-j-k} \left(L_{2\text{NNN,p}}^{3\text{sp}} P_{ijk} + \text{h.c.} \right) + L_{2\text{NNN,dp}}^{3\text{sp}} \sum_{i-j-k} (P_{ijk} + \text{h.c.}) \\
& + \sum_{i-j-k-l} \left(L_{\text{NN,p}}^{4\text{sp}} P_{ijkl} + \text{h.c.} \right) + \sum_{i-j-k-l} \left(L_{\text{NNN,p}}^{4\text{sp}} P_{ijkl} + \text{h.c.} \right) \\
& + L_{\text{NN,dp,1}}^{4\text{sp}} \sum_{i-j-k-l} P_{ijkl} + L_{\text{NN,dp,2}}^{4\text{sp}} \sum_{i-j-k-l} P_{ijkl} + L_{\text{NN,NNN}}^{2\text{sp,2sp}} \sum_{i-j-k-l} P_{ij} P_{kl} \\
& + \sum_{i-j-k-l-m} \left(L_{\text{NN}}^{5\text{sp}} P_{ijklm} + \text{h.c.} \right) + \sum_{i-j-k-l-m-n} (K P_{ijklmn} + \text{h.c.}) .
\end{aligned} \tag{4.2.1}$$

The pictogram underneath every sum indicates, which sites on the full lattice are addressed. This has to be understood as follows. The indicated graphs are not allowed to be changed in the angles between links (e.g. the graph of $L_{4\text{N,p}}^{2\text{sp}}$ cannot be transformed into that of $L_{4\text{N,dp}}^{2\text{sp}}$), however every possibility of rotation has to be included. For instance, the graph of $L_{\text{NN}}^{3\text{sp}}$ can be rotated around the axis defined by i and j by π . Then, every distinct set of sites contributes to the Hamiltonian. The interactions range from simple nearest-neighbour permutations, J , to more involved exchanges like

$L_{\text{NN,dp},1}^{4\text{sp}}$, where four spins from different plaquettes (dp) are permuted. In total, the Hamiltonian includes all possible exchanges of linked-clusters in order six. The coupling constants are determined by the embedding

$$\begin{aligned}
\epsilon_0 &= \frac{3}{2}\tilde{A}_1 + 3\tilde{A}_2 + 8\tilde{A}_7 + \tilde{A}_8 + \frac{1}{2}\tilde{A}_9, \\
J &= \tilde{B}_1 + 4\tilde{B}_2 + 12\tilde{B}_7 + 2\tilde{B}_8 + 2\tilde{B}_9, \\
L_{\text{NNN}}^{2\text{sp}} &= \tilde{C}_2 + 4\tilde{C}_7 + \tilde{C}_8 + \tilde{C}_9, \quad L_{4\text{N,p}}^{2\text{sp}} = \tilde{D}_7 + \tilde{D}_9, \quad L_{4\text{N,dp}}^{2\text{sp}} = \tilde{D}_7, \\
L_{\text{NN}}^{3\text{sp}} &= \tilde{D}_2 + 4\tilde{E}_7 + \tilde{E}_8 + \tilde{E}_9, \quad L_{\text{NNN,p}}^{3\text{sp}} = \tilde{F}_7 + \tilde{F}_9, \quad L_{\text{NNN,dp}}^{3\text{sp}} = \tilde{F}_7, \\
L_{2\text{NNN,p}}^{3\text{sp}} &= \tilde{F}_9, \quad L_{2\text{NNN,dp}}^{3\text{sp}} = \tilde{D}_8, \quad L_{\text{NN,p}}^{4\text{sp}} = \tilde{G}_7 + \tilde{G}_9, \quad L_{\text{NNN,p}}^{4\text{sp}} = \tilde{H}_9, \\
L_{\text{NN,dp},1}^{4\text{sp}} &= \tilde{G}_7, \quad L_{\text{NN,dp},2}^{4\text{sp}} = \tilde{F}_8, \quad L_{\text{NN,NNN}}^{2\text{sp},2\text{sp}} = \tilde{G}_8, \quad L_{\text{NN}}^{5\text{sp}} = \tilde{I}_9, \quad K = \tilde{J}_9,
\end{aligned} \tag{4.2.2}$$

and the coefficients in terms of t/U and Φ are found to be

$$\begin{aligned}
\epsilon_0 &= -3\left(\frac{t}{U}\right)^2 + 2\left(\frac{t}{U}\right)^4 + \left(-\frac{2192}{27} - 6\cos(\Phi)\right)\left(\frac{t}{U}\right)^6, \\
J &= 2\left(\frac{t}{U}\right)^2 - \frac{8}{3}\left(\frac{t}{U}\right)^4 + (-30 + 24\cos(\Phi))\left(\frac{t}{U}\right)^6, \\
L_{\text{NNN}}^{2\text{sp}} &= \frac{10}{3}\left(\frac{t}{U}\right)^4 + \left(\frac{49}{27} + 12\cos(\Phi)\right)\left(\frac{t}{U}\right)^6, \\
L_{4\text{N,p}}^{2\text{sp}} &= \left(\frac{14}{3} + 12\cos(\Phi)\right)\left(\frac{t}{U}\right)^6, \quad L_{4\text{N,dp}}^{2\text{sp}} = \frac{14}{3}\left(\frac{t}{U}\right)^6, \\
L_{\text{NN}}^{3\text{sp}} &= -\frac{4}{3}\left(\frac{t}{U}\right)^4 + \left(\frac{241}{54} - 21e^{i\Phi}\right)\left(\frac{t}{U}\right)^6, \\
L_{\text{NNN,p}}^{3\text{sp}} &= \left(-\frac{4}{3} - 21e^{i\Phi}\right)\left(\frac{t}{U}\right)^6, \quad L_{\text{NNN,dp}}^{3\text{sp}} = -\frac{4}{3}\left(\frac{t}{U}\right)^6, \\
L_{2\text{NNN,p}}^{3\text{sp}} &= -21e^{i\Phi}\left(\frac{t}{U}\right)^6, \quad L_{2\text{NNN,dp}}^{3\text{sp}} = -\frac{79}{6}\left(\frac{t}{U}\right)^6, \\
L_{\text{NN,p}}^{4\text{sp}} &= (2 + 56e^{i\Phi})\left(\frac{t}{U}\right)^6, \quad L_{\text{NNN,p}}^{4\text{sp}} = 56e^{i\Phi}\left(\frac{t}{U}\right)^6, \\
L_{\text{NN,dp},1}^{4\text{sp}} &= 2\left(\frac{t}{U}\right)^6, \quad L_{\text{NN,dp},2}^{4\text{sp}} = \frac{83}{9}\left(\frac{t}{U}\right)^6, \\
L_{\text{NN,NNN}}^{2\text{sp},2\text{sp}} &= -\frac{146}{9}\left(\frac{t}{U}\right)^6, \\
L_{\text{NN,p}}^{5\text{sp}} &= -126e^{i\Phi}\left(\frac{t}{U}\right)^6, \quad \text{and} \quad K = 252e^{i\Phi}\left(\frac{t}{U}\right)^6.
\end{aligned} \tag{4.2.3}$$

For the real exchange constants, i.e. exchanges between two spins where no direction of rotation can be defined (no perturbative loop processes are involved), or on more sites but not confined on a plaquette, the turning direction of rotation is arbitrary, since the cosine is symmetric and the coupling constants are identical under the transformation $\Phi \rightarrow -\Phi$. For the exchanges contributing with a non-trivial phase factor that arises

from rotations around the plaquettes, the proper turning direction has to be chosen.

The representation of the effective model in Eq. (4.2.1) is not unique for real exchange constants if $N < 6$. This is due to the fact that consecutive permutations acting on more sites than spin colours in the model can be rewritten in terms of sums of various other permutation operators. The best known example occurs for the three-site permutation acting on $SU(2)$ spins, which can be expressed by two-site permutations plus a constant. The situation becomes much richer if one considers permutations between more spins. For instance, in the case of $SU(3)$ spins, the four-site permutation can be rewritten in terms of two-spin, three-spin, and various four-spin interactions

$$P_{1234} + P_{4321} = \mathbb{1} - \sum_{(i,j)} P_{ij} + \sum_{(i,j,k)} P_{ijk} + P_{12}P_{34} \\ + P_{14}P_{23} + P_{13}P_{24} - (P_{1243} + P_{1324} + \text{h.c.}), \quad (4.2.4)$$

where the sums include all possible permutations of different sites. If we use this relation to reexpress the four-site ring exchange on a plaquette in the effective Hamiltonian various coupling constants get rescaled. Additionally, new interactions occur which in perturbation theory arise only in higher orders. In this sense the replacement of operators is not helpful and the formulation in Eq. (4.2.1) is the more natural one in terms of perturbation theory. If and how a systematic reduction of higher-order interactions to only already included exchanges is possible remains an open question.

Independent of the formulation of the Hamiltonian, there is a large variety of different interactions. Using the form in Eq. (4.2.1), there are 16 different interactions. The notation is chosen according to the J - K model on the triangular lattice. The leading order interaction is the same for both lattices, so the unique label for the nearest-neighbour exchange is J . The K -term in the J - K model is the subleading term and yields the rotation of all spins on a plaquette. We choose to use the latter feature for the notation, such that the 6-spin ring exchange scales with K . Even though it occurs only in sixth- and not in subleading fourth-order, it seems plausible that it has a large impact, due to the large constant K .

However, we want to determine, if the CSL found at $\Phi = \pi/2$ in Ref. [166] might be a feature of the $SU(6)$ Hubbard model. To this end, we first estimate the phase transition

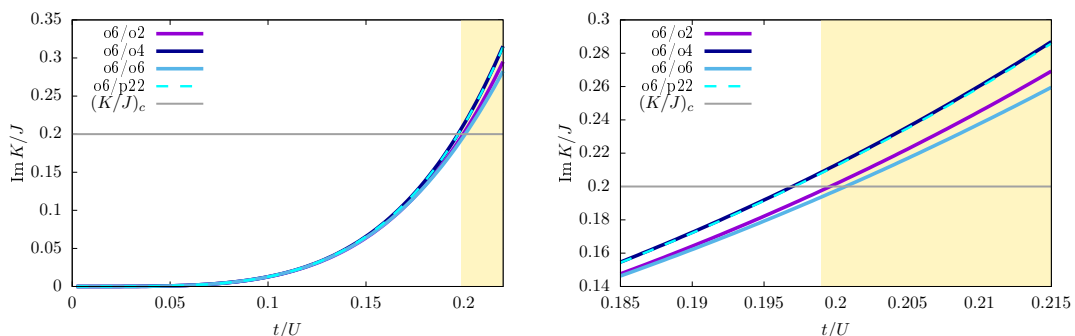


Fig. 4.1.: Ratio between ring exchange and nearest-neighbour coupling at $\Phi = \pi/2$ for the honeycomb lattice. The grey line gives the critical ratio from Ref. [166] and the yellow background indicates the possible area of the CSL phase.

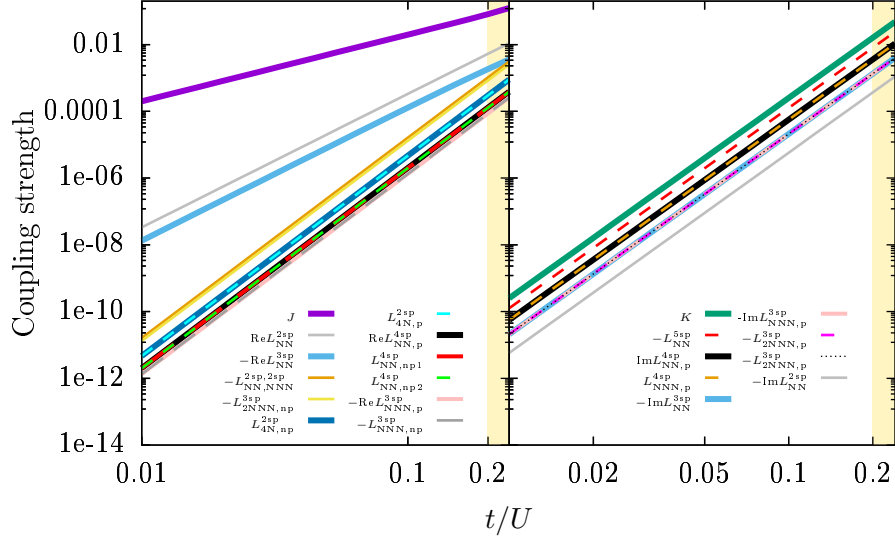


Fig. 4.2.: All coupling strengths at $\Phi = \pi/2$ for the honeycomb lattice. Real parts are plotted on the left, imaginary parts on the right. The background colour can be understood as in Fig. 4.1.

point towards the CSL in the Hubbard model, before we study all interactions and see if the simplification of the effective model is valid.

The convergence of the bare series is improved using Padé extrapolations [123] as discussed in Subsection 2.1.5. They are functions depending on t/U and Φ and can in principle be used for the whole range of parameters including all fluxes. Since they are rational functions though, nonphysical divergencies emerge at certain points. In the area around such a point, one has to use the bare series. Note, that Padé extrapolations of series starting only in higher orders can not be calculated directly, when the exponent of the numerator is smaller than the lowest order of the series. This can be resolved by considering the series in units of (t/U) or (t^2/U^2) for the extrapolation.

If one assumes that all couplings except for J and K are not relevant, it is possible with the effective model and the transition point from Ref. [166] to determine the phase-transition point towards the CSL in the Hubbard model at $\pi/2$ -flux, $(t/U)_c$. The purely imaginary effective coupling ratio K/J is shown in Fig. 4.1. Given are various orders of J as well as the Padé extrapolant with the exponents [2,2]. If one uses the bare sixth-order series and the Padé extrapolant the value $(K/J)_c \approx 0.2i$ translates to $(t/U)_c \approx 0.199 \pm 0.002$. The error is determined from the standard deviation of the ratios with K in bare order six, and J in bare order six and as Padé extrapolant [2, 2]. Other uncertainties from finite-size effects in the ED or from neglected couplings should cause larger errors. It is also not known if the Hubbard model at couplings as small as $(U/t)_c \approx 5$ is still in the Mott-insulating phase.

In order to clarify at least one of these issues, all effective couplings are shown in Fig. 4.2. The six-site ring exchange K is the largest imaginary contribution. However, there is a variety of additional couplings, which might favour different phases, and they may be even more relevant than K , since they occur more often on the lattice. For instance, the five-site ring exchange $L_{NN,p}^{5sp}$ is present six times on every plaquette,

whereas the six-site ring exchange only appears once. The prefactor $L_{\text{NN,p}}^{5\text{sp}}$ is negative in contrast to $L_{\text{NN,p}}^{6\text{sp}}$, so the effects might cancel to some extent. The real fourth-order contributions are of the same magnitude as the sixth-order contributions at the estimated critical value $(t/U)_c$, so in this sense the relevance of the sixth-site ring exchange is given. However, without performing a numerical analysis of the full effective model, it is not clear if the CSL phase or another phase is stabilised.

4.2.2. Triangular lattice

The effective model for the triangular lattice in the thermodynamic limit was derived in Ref. [66]. Parts of this subsection are published in Ref. [100]. In this thesis, we study it extensively in Chapter 5 and Chapter 6, where we also show that it hosts extended CSL phases for SU(7)- and SU(3)-symmetric fermions. Previously, CSL phases were found for all $2 < N < 10$ at $\pi/2$ -flux in the third-order model [62]. In the following, we discuss the effective fifth-order model and investigate the convergence behaviour for all fluxes. This is independent of the number of colours N . In contrast, phase transition points $(t/U)_c$ depend on N . For SU(3)-symmetric fermions a phase transition towards the CSL occurs, as deduced in Chapter 6 for $\Phi = \pi/2$ and $\Phi = \pi$. In this subsection, we already use these values to study the convergence behaviour in the area of interest. For all other values of N at $\pi/2$ -flux in the third-order model the phase transitions occur at comparable ratios $(t/U)_c$ [62], and it is not necessary to study them separately regarding the limitations of the convergence [62].

On the triangular lattice, all possible loops, also with odd numbers of sites, contribute in the linked-cluster expansion. Therefore, the effective model contains a larger variety of exchanges, illustrated in Fig. 4.3, than on the square or honeycomb lattice. In fifth-order perturbation theory, there are 13 different types of exchange interactions involving permutations on up to five sites. The flux through one triangle is chosen to be $\Phi_{g_3} = \Phi$, so the fluxes for the 4-site plaquette and for the 5-site loop are $\Phi_{g_4} = 2\Phi$ and $\Phi_{g_6} = 3\Phi$, respectively.

The effective Hamiltonian on the triangular lattice with the same notation employed for the honeycomb lattice in Eq. (4.2.1), can be written as

$$\begin{aligned}
H_t^{\mathcal{O}(5)} = & N_s \cdot \epsilon_0 + J \sum_{i-j} P_{ij} + \sum_{i \underset{k}{\curvearrowright} j} (K P_{ijk} + \text{h.c.}) + L_s^{2\text{sp}} \sum_{i \bullet j} P_{ij} \\
& + L_d^{2\text{sp}} \sum_{i \bullet j} P_{ij} + L_s^{3\text{sp}} \sum_{i-j-k} (P_{ijk} + \text{h.c.}) + \sum_{i-j \overset{k}{\curvearrowright}} (L_d^{3\text{sp}} P_{ijk} + \text{h.c.}) \\
& + \sum_{i \underset{1-k}{\curvearrowright} j} (L_r^{4\text{sp}} P_{ijkl} + \text{h.c.}) + \sum_{i \underset{k}{\curvearrowright} j} (L_{\text{cr}}^{3\text{sp}} P_{ijk} + \text{h.c.}) \\
& + \sum_{i \underset{1-k}{\curvearrowright} j} (L_{\text{cr}}^{4\text{sp}} (P_{ijk} + P_{kjli}) + \text{h.c.}) + L_{\text{pl}}^{4\text{sp}} \sum_{i \underset{1-k}{\curvearrowright} j} (P_{ikjl} + P_{kijl} + \text{h.c.}) \\
& + L_{\text{Ka}}^{4\text{sp}} \sum_{i \underset{1-k}{\curvearrowright} j} P_{ij} P_{lk} + L_{\text{Kb}}^{4\text{sp}} \sum_{i \underset{1-k}{\curvearrowright} j} P_{il} P_{jk} + \sum_{i \underset{m-l}{\curvearrowright} j} (L_r^{5\text{sp}} P_{ijklm} + \text{h.c.}) .
\end{aligned} \tag{4.2.5}$$

The coupling constants for the Hamiltonian in Eq. (4.2.5) are

$$\begin{aligned}
\epsilon_0 &= -6 \frac{t^2}{U^2} - 12 \cos \Phi \frac{t^3}{U^3} + (-26 - 24 \cos 2\Phi) \frac{t^4}{U^4} \\
&\quad - (92 \cos \Phi + 60 \cos 3\Phi) \frac{t^5}{U^5}, \\
J &= 2 \frac{t^2}{U^2} + 12 \cos \Phi \frac{t^3}{U^3} + (12 + 40 \cos 2\Phi) \frac{t^4}{U^4} \\
&\quad + \left(\frac{820}{9} \cos \Phi + 140 \cos 3\Phi \right) \frac{t^5}{U^5}, \\
K &= -6e^{i\Phi} \frac{t^3}{U^3} + (-4 - 30e^{i2\Phi}) \frac{t^4}{U^4} - \left(\frac{58}{3} e^{i\Phi} - 16e^{-i\Phi} + 135e^{i3\Phi} \right) \frac{t^5}{U^5}, \\
L_s^{2\text{sp}} &= \frac{10}{3} \frac{t^4}{U^4} + \left(\frac{104}{3} \cos \Phi + 20 \cos 3\Phi \right) \frac{t^5}{U^5}, \\
L_d^{2\text{sp}} &= \left(\frac{20}{3} + 8 \cos 2\Phi \right) \frac{t^4}{U^4} - \left(\frac{208}{3} \cos \Phi + 40 \cos 3\Phi \right) \frac{t^5}{U^5}, \\
L_s^{3\text{sp}} &= -\frac{4}{3} \frac{t^4}{U^4} - \left(\frac{32}{3} \cos \Phi + 30 \cos 3\Phi \right) \frac{t^5}{U^5}, \\
L_d^{3\text{sp}} &= \left(-\frac{4}{3} - 10e^{i2\Phi} \right) \frac{t^4}{U^4} - \left(\frac{32}{3} \cos \Phi + \frac{224}{9} e^{i\Phi} + 60e^{i3\Phi} \right) \frac{t^5}{U^5}, \\
L_r^{4\text{sp}} &= 20e^{i2\Phi} \frac{t^4}{U^4} + \left(\frac{232}{9} e^{i\Phi} + 140e^{i3\Phi} \right) \frac{t^5}{U^5}, \\
L_{\text{cr}}^{3\text{sp}} &= -\left(\frac{112}{9} e^{i\Phi} + 15e^{i3\Phi} \right) \frac{t^5}{U^5}, \quad L_{\text{cr}}^{4\text{sp}} = \frac{58}{9} e^{i\Phi} \frac{t^5}{U^5}, \\
L_{\text{pl}}^{4\text{sp}} &= \frac{116}{9} \cos \Phi \frac{t^5}{U^5}, \quad L_{\text{Ka}}^{4\text{sp}} = -\frac{232}{9} \cos \Phi \frac{t^5}{U^5}, \\
L_{\text{Kb}}^{4\text{sp}} &= -\frac{116}{9} \cos \Phi \frac{t^5}{U^5}, \quad \text{and} \quad L_r^{5\text{sp}} = -70e^{i3\Phi} \frac{t^5}{U^5}.
\end{aligned} \tag{4.2.6}$$

The dependence on t/U for the most important coupling constants of every order at $\Phi = \pi$ are illustrated in Fig. 4.4. In all plots the lighter and darker yellow background colours indicate the area, where the SU(3) CSL phase is found in VMC, and in VMC and ED, respectively, in Chapter 6. The Padé extrapolants of the dominant nearest-neighbour coupling, J , and the subleading three-site ring exchange, K , at $\Phi = \pi$ are shown in the insets of Fig. 4.4 and Fig. 4.5, respectively. The most relevant ratio K/J at $\Phi = \pi$ is plotted in Fig. 4.5, where we take the ratio of the extrapolations of J and K . The largest couplings of every order, similar to Fig. 4.4, for $\Phi = \pi$ are shown as bare fifth-, fourth-, and third-order series (solid, long dashes, short dashes) and if possible as Padé extrapolations (mostly diamonds) in a double logarithmic plot in Fig. 4.6. This representation directly indicates the leading orders and allows to extract the ratios of t/U where higher-order contributions become influential. In order to avoid spurious poles, we found a composition of [3, 2]-Padé extrapolations for ϵ_0 , J , and K , [2, 1]-Padé extrapolations for $L_s^{2\text{sp}}$, $L_d^{2\text{sp}}$, $L_s^{3\text{sp}}$, $L_d^{3\text{sp}}$, and $L_r^{4\text{sp}}$, and all other couplings as bare series to work best for the fluxes $\Phi = \pi$ and $\Phi = \pi/2$.

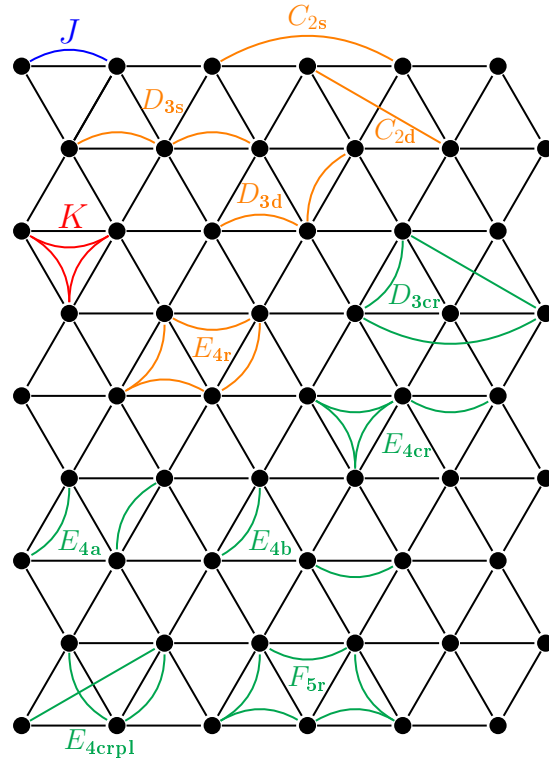


Fig. 4.3.: Sketch of the effective interactions on the triangular lattice in fifth-order of t/U from the strong-coupling limit, taken from Ref. [66].

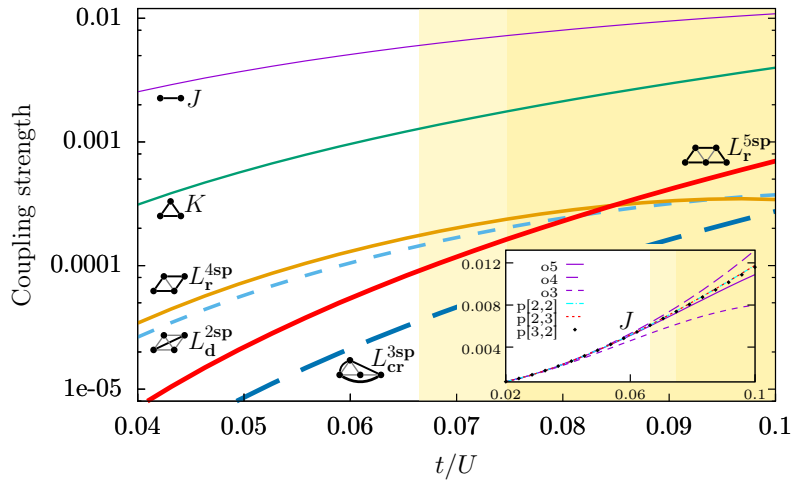


Fig. 4.4.: Effective couplings in units of U of the Hubbard model as a function of t/U for $\Phi = \pi$ using bare fifth-order series. Plotted are the largest contributions in every order with a pictogram sketching the associated permutations. The dark yellow background indicates the area where the $SU(3)$ CSL is observed within ED and VMC in Chapter 6, whereas the light yellow corresponds to its stability according to VMC only. A similar double logarithmic plot can be found in Fig. 4.6. The inset shows the nearest-neighbour exchange in different orders and Padé extrapolations. This figure is published in Ref. [100].

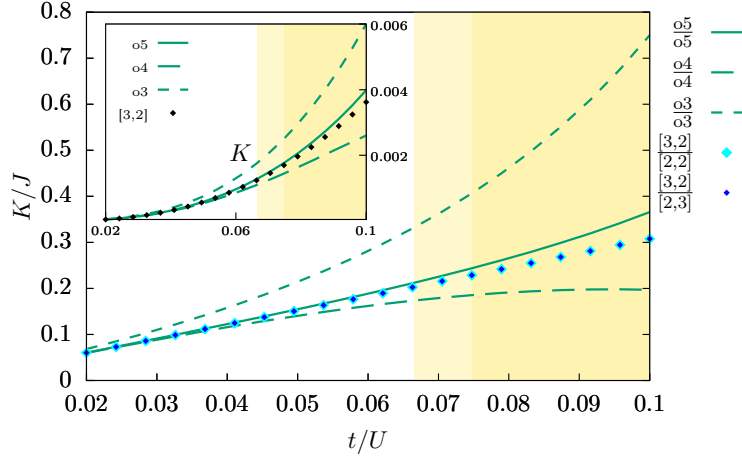


Fig. 4.5.: Ratio of effective coupling constants K/J depending on t/U for $\Phi = \pi$ using bare series up to order five (green) as well as Padé extrapolations (cyan, blue). The inset shows a similar plot for the three-site ring exchange K by itself. The background colours are chosen identical to Fig. 4.4. This figure is published in Ref. [100].

The convergence behaviour for $\Phi = \pi/2$ is shown for all couplings in Fig. 4.7. For this special case, a number of interesting and subtle features of the model become clear. The three-site ring exchange, K , is purely imaginary only in order three. The fourth-order term partly arises from fluctuations around two triangles leading to a flux of 2Φ , therefore a real part is present in higher orders. Similarly, the imaginary part of the fourth-order contribution to the four-site ring exchange vanishes and it effectively becomes an order five term. As a consequence, the model is dominated by a real nearest-neighbour and an imaginary three-site ring exchange. For exactly this subset of

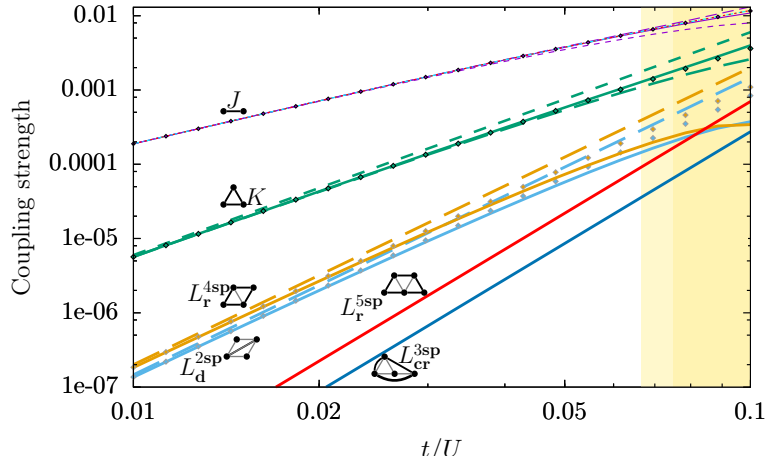


Fig. 4.6.: Same as in Fig. 4.4 in a double logarithmic plot including various orders and extrapolants. The bare fifth- (solid line), fourth- (long dashes), and third-order (short dashes) series as well as $[3, 2]$ - and $[2, 1]$ -Padé extrapolations (diamonds encircled in black and grey respectively) are indicated. For the nearest-neighbour exchange the $[2, 2]$ - and $[2, 3]$ -Padé extrapolations (red and cyan dashed lines) are given as well. This figure is published in Ref. [100].

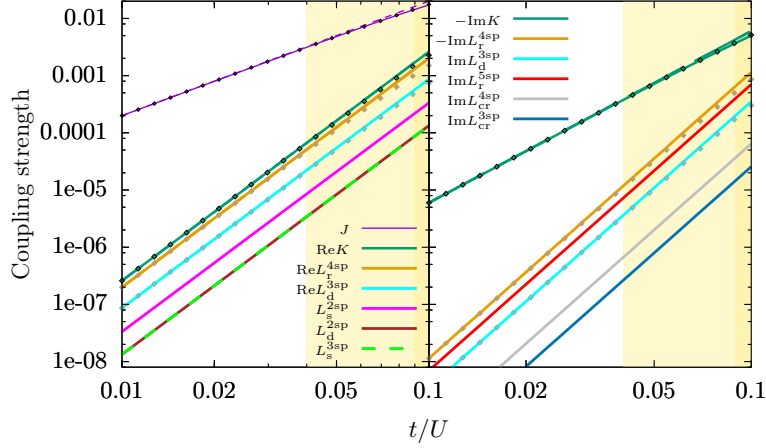


Fig. 4.7.: Effective couplings in units of U of the Hubbard model as a function of t/U for $\Phi = \pi/2$ in a double logarithmic plot. Shown are the non-vanishing real and imaginary contributions in bare orders. The diamonds encircled in black (grey) give the Padé extrapolants with the exponents $[3, 2]$ ($[2, 1]$). Note, that all uneven (even) terms in the real (imaginary) part vanish. The background colours can be understood as in Fig. 4.5. This figure is contained in the Appendix of Ref. [100].

interactions, the CSL phase was found in Ref. [62]. In Fig. 4.8, the ratios of Padé extrapolants for the imaginary part of $-K$ and the real quantity J (green larger diamonds) and the direct Padé extrapolation of the ratio $-\text{Im} K/J$ (black smaller diamonds) are

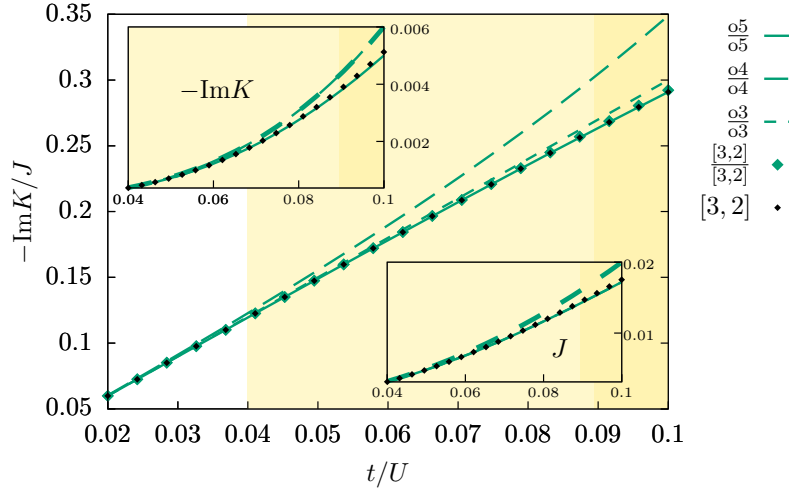


Fig. 4.8.: Imaginary part of the ratio of effective coupling constants $-K/J$ depending on t/U for $\Phi = \pi/2$ using bare series up to order five. The ratios of Padé extrapolants with the exponents $[3, 2]$ as well as the direct Padé extrapolation of the ratio $-\text{Im} K/J$ are indicated. The insets show similar plots for the imaginary part of the negative three-site ring exchange $-\text{Im} K$ and the nearest-neighbour exchange J . Extrapolations of J with different pairs of exponents $[2, 2]$ and $[2, 3]$ are identical at $\Phi = \pi/2$. The background colours can be understood as in Fig. 4.5. This figure is contained in the Appendix of Ref. [100].

shown. In the regime of the SU(3) CSL in t/U not only the extrapolations, but also the bare fifth-order (solid line) series are well converged.

For intermediate values of the flux, Φ , divergencies appear for the coupling constant $L_d^{2\text{sp}}$ around $\Phi \approx 0.6\pi$ and for $L_s^{3\text{sp}}$ around $\Phi \approx 0.55\pi$ and $\Phi \approx 0.75\pi$ depending on t/U . Here, one also has to use the bare series.

4.2.3. 12-site triangular cluster with periodic boundary conditions

In this subsection, we determine the effective strong-coupling description of the Hubbard model on a 12-site triangular cluster with PBCs in order four in t/U . This is published in Ref. [100].

On a cluster consisting of a finite number of sites, the effective model is different to the model for the thermodynamic limit. In the case of PBCs, this is due to the fact that a finite number of fermionic hoppings in one direction leads back to the starting site. For the 12-site torus this becomes relevant in order four in t/U , where the four-site plaquette can be embedded surrounding the cluster via the PBCs. This leads to an additional effective interaction around the 12-site torus, but also to modifications of other coupling constants compared to the infinite lattice. The newly arising exchanges from the loops around the torus partly contribute with a phase. The easiest approach to calculate the effective Hamiltonian for the experimentally most interesting case $\Phi = \pi$ is to consider the model without phases and then perform the transformation $t \rightarrow -t$, which is identical to $\Phi = 0 \rightarrow \Phi = \pi$. Here, we perform the general calculation for all fluxes Φ by choosing a gauge for the 12-site cluster as depicted in Fig. 4.9. Every second line of horizontal bonds in the cluster gets assigned with a phase Φ , whereas the parallel intermediate bonds contribute with a phase $-\Phi$. All non-parallel bonds yield a vanishing phase.

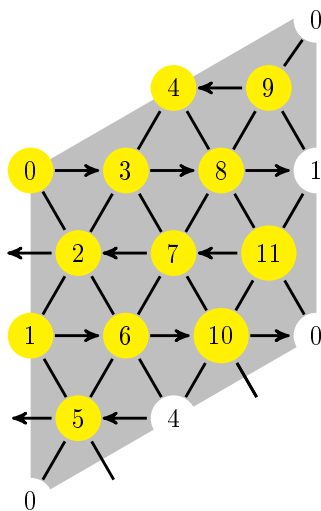


Fig. 4.9.: Triangular lattice cluster with 12 sites and PBCs. The chosen gauge is illustrated by the arrows as bonds. A hopping following the direction of an arrow leads to a positive phase factor $e^{i\Phi}$, whereas it is the complex conjugated for the opposite direction.

The effective Hamiltonian in order five in t/U can be written as

$$\begin{aligned}
H_{\text{triangular,12sites,pbc}}^{\mathcal{O}(4)} &= 12 \cdot \epsilon_0 + J_{\text{diag}} \sum_{\substack{i \quad i \\ j \quad j}} P_{ij} + J_{\text{horiz}} \sum_{i-j} P_{ij} \\
&+ \sum_{\substack{k \\ i-j}} (K P_{ijk} + \text{h.c.}) + \frac{1}{3} L_s^{2\text{sp}} \sum_{i \bullet j} P_{ij} + \frac{1}{2} L_d^{2\text{sp,diag}} \sum_{i \bullet j} P_{ij} \\
&+ \frac{1}{2} L_d^{2\text{sp,vert}} \sum_{\substack{i \quad i \\ \bullet \quad \bullet}} P_{ij} + \sum_{\substack{i \quad i \\ j \quad j}} (L_{s,\text{diag}}^{3\text{sp}} P_{ijk} + \text{h.c.}) \\
&+ \sum_{i-j-k} (L_{s,\text{horiz}}^{3\text{sp}} P_{kji} + \text{h.c.}) + \sum_{\substack{i \quad i \\ k-j \quad j-k}} (L_d^{3\text{sp,diag}} P_{ijk} + \text{h.c.}) \\
&+ \sum_{\substack{j-i \quad i-j \\ k \quad k}} (L_d^{3\text{sp,diag}} P_{kji} + \text{h.c.}) + \sum_{\substack{i \quad i \\ j \quad j \\ k \quad k}} (L_d^{3\text{sp,vert}} P_{kji} + \text{h.c.}) \\
&+ L_r^{4\text{sp},\Phi=0} \sum_{\substack{i \quad i \\ l \quad j \\ k}} (P_{lkji} + \text{h.c.}) + \sum_{\substack{i-j \quad i-j \\ l-k \quad l-k}} (L_r^{4\text{sp},\Phi \neq 0} P_{ijkl} + \text{h.c.}) \\
&+ \sum_{\text{torus loops}} (L_{\text{rpb}}^{4\text{sp}}(\Phi) P_{ijkl} + \text{h.c.}) ,
\end{aligned} \tag{4.2.7}$$

where the depicted graphs under every sum indicate in which orientations the exchanges lie on the cluster. Some of the exchanges in this effective model on 12 sites, which are symmetric on the infinite lattice, take different coupling constants for different directions. For instance, the nearest-neighbour exchange on the bonds with a phase J_{horiz} and the nearest-neighbour exchange on the bonds without a phase J_{diag} differ. From the perspective of a linked-cluster expansion, this relates to the contributions from the four-site plaquette looping around the torus with differing phases for different directions. In order four in t/U , the embeddings read

$$\begin{aligned}
J_{\text{horiz}} &= \tilde{B}_1 + 10\tilde{B}_2 + 2\tilde{C}_2 + \tilde{B}_3^\Phi + \tilde{B}_3^{-\Phi} + 4\tilde{B}_4^{\Phi \neq 0} + 2\tilde{B}_4^{\text{pbc},\Phi=0} \\
&+ 4\tilde{B}_4^{\text{pbc},\Phi \neq 0} + \tilde{C}_4^{\Phi=0} \\
&= 2 \left(\frac{t}{U} \right)^2 + 12 \cos(\Phi) \left(\frac{t}{U} \right)^3 + (60 + 40 \cos(2\Phi)) \left(\frac{t}{U} \right)^4
\end{aligned} \tag{4.2.8}$$

and

$$\begin{aligned}
J_{\text{diag}} &= \tilde{B}_1 + 10\tilde{B}_2 + 2\tilde{C}_2 + \tilde{B}_3^\Phi + \tilde{B}_3^{-\Phi} + 2\tilde{B}_4^{\Phi=0} + 2\tilde{B}_4^{\Phi \neq 0} \\
&\quad + 4\tilde{B}_4^{\text{pbc}, \Phi=0} + 2\tilde{B}_4^{\text{pbc}, \Phi \neq 0} + \tilde{C}_4^{\Phi=0} \\
&= 2 \left(\frac{t}{U} \right)^2 + 12 \cos(\Phi) \left(\frac{t}{U} \right)^3 + (36 + 64 \cos(2\Phi)) \left(\frac{t}{U} \right)^4.
\end{aligned} \tag{4.2.9}$$

The additional terms of the PBCs are marked with an index pbc and if they contribute with or without a phase factor is noted as well.

Again, the three-site ring exchanges K on a triangle contribute all with the same amplitude, which differs compared to the infinite lattice in order four. The embedding is given by

$$\begin{aligned}
K &= \tilde{C}_3 + 3\tilde{D}_2 + \tilde{D}_4^{\Phi=0} + 2\tilde{D}_4^{\Phi \neq 0} \\
&= -6e^{i\Phi} \left(\frac{t}{U} \right)^3 + (-14 - 20e^{2i\Phi}) \left(\frac{t}{U} \right)^4.
\end{aligned} \tag{4.2.10}$$

The newly arising four-site ring exchange around the torus $L_{\text{pbc}}^{4\text{sp}}(\Phi)$ in Eqs. (4.2.8) and (4.2.9) can either host a flux or not, depending on the location of the interaction

$$\begin{aligned}
L_{\text{r,pbc}, \Phi \neq 0}^{4\text{sp}} &= \tilde{E}_4^{\text{pbc}, \Phi \neq 0} = 20e^{2i\Phi} \left(\frac{t}{U} \right)^4, \\
L_{\text{r,pbc}, \Phi=0}^{4\text{sp}} &= \tilde{E}_4^{\text{pbc}, \Phi=0} = 20 \left(\frac{t}{U} \right)^4.
\end{aligned} \tag{4.2.11}$$

In order to find which interactions contribute with a phase, one has to add up the phases of the taken bonds. Overall, there are three directions with 18 loops each hosting the four-site ring exchange around the PBCs. All exchanges along the vertical direction have a zero flux. For the other directions 2/3 of the exchanges contribute with a phase factor, whereas again 1/3 do not host a flux. Therefore, 10 contribute without a phase factor and 8 with a phase factor. In total, these exchanges double due to the Hermitian conjugated exchange, which turns the spins the other way around. Due to the specific gauge also the contributions of the usual 4-site plaquette are modified in respect to the thermodynamic limit, since the vertical orientation does not yield a phase factor. That is why, a four-site ring-exchange $\tilde{C}_4^{\Phi=0}$ with vanishing flux arises.

The other coupling constants of the interactions in Eq. (4.2.7) are determined by

$$\begin{aligned}
L_{\text{s}}^{2\text{sp}} &= 3\tilde{C}_2 + 2\tilde{C}_4^{\text{pbc}, \Phi \neq 0} + \tilde{C}_4^{\text{pbc}, \Phi=0} = (18 + 16 \cos(2\Phi)) \left(\frac{t}{U} \right)^4, \\
L_{\text{d,diag}}^{2\text{sp}} &= 4\tilde{C}_2 + 2\tilde{C}_4 + 2\tilde{C}_4^{\text{pbc}, \Phi \neq 0} + 2\tilde{C}_4^{\text{pbc}, \Phi=0} = \left(\frac{88}{3} + 32 \cos(2\Phi) \right) \left(\frac{t}{U} \right)^4, \\
L_{\text{d,vert}}^{2\text{sp}} &= 4\tilde{C}_2 + 2\tilde{C}_4 + 4\tilde{C}_4^{\text{pbc}, \Phi \neq 0} = \frac{184}{3} \left(\frac{t}{U} \right)^4, \\
L_{\text{s,diag}}^{3\text{sp}} &= \tilde{D}_2 + \tilde{D}_4^{\text{pbc}, \Phi \neq 0} + \tilde{D}_4^{\text{pbc}, \Phi=0} = \left(-\frac{34}{3} - 10e^{2i\Phi} \right) \left(\frac{t}{U} \right)^4,
\end{aligned} \tag{4.2.12}$$

$$\begin{aligned}
L_{s,\text{horiz}}^{3\text{sp}} &= \tilde{D}_2 + 2\tilde{D}_4^{\text{pbc},\Phi\neq 0} = \left(-\frac{4}{3} - 20e^{2i\Phi}\right) \left(\frac{t}{U}\right)^4, \\
L_{d,\text{diag}}^{3\text{sp}} &= \tilde{D}_2 + \tilde{D}_4 + \tilde{D}_4^{\text{pbc},\Phi\neq 0} + 2\tilde{D}_4^{\text{pbc},\Phi=0} = \left(-\frac{34}{3} - 20e^{2i\Phi}\right) \left(\frac{t}{U}\right)^4, \\
L_{d,\text{vert}}^{3\text{sp}} &= \tilde{D}_2 + \tilde{D}_4 + \tilde{D}_4^{\text{pbc},\Phi\neq 0} + 2\tilde{D}_4^{\text{pbc},\Phi=0} = -\frac{94}{3} \left(\frac{t}{U}\right)^4, \quad \text{and} \\
L_r^{4\text{sp}} &= \tilde{E}_4 = 20e^{2i\Phi} \left(\frac{t}{U}\right)^4.
\end{aligned}$$

The exchanges with $L_s^{2\text{sp}}$ and $L_d^{2\text{sp}}$ exist several times around the PBCs of the cluster, e.g. the exchanges between sites $i = 0$ and $j = 8$ go via sites 3, 9, and 11 independently, but lead to the same result. Therefore, if the Hamiltonian is defined as the same set of exchanges starting from every site as given in Eq. (4.2.7), only a fraction of the above coupling strengths has to be taken to avoid double or triple application of these exchanges. For $L_s^{2\text{sp}}$ a factor of $1/3$ and for $L_d^{2\text{sp}}$ a factor of $1/2$ applies.

For the constant part ϵ_0 , there are several ways to calculate it. Firstly, one can embed the linked-clusters similarly to the thermodynamic limit on the lattice. Secondly, one can consider the diagonal matrix element in the effective Hamiltonian of a state with only one single colour. Here, all permutations of the effective Hamiltonian contribute and need to be subtracted to get the constant part. Thirdly, one can also consider another diagonal matrix element of the effective model and subtract all couplings of exchanges contributing to this element. Following the first method, several versions of the 4-site plaquette constants have to be taken into account, as described for the nearest-neighbour exchange above. We find

$$\begin{aligned}
\epsilon_0 &= 3\tilde{A}_1 + 15\tilde{A}_2 + 2\tilde{A}_3 + 2\tilde{A}_4^{\Phi\neq 0} + \tilde{A}_4^{\Phi=0} \\
&\quad + \frac{5}{2}\tilde{A}_4^{\text{pbc},\Phi=0} + 2\tilde{A}_4^{\text{pbc},\Phi\neq 0} \\
&= -6 \left(\frac{t}{U}\right)^2 - 12 \cos(\Phi) \left(\frac{t}{U}\right)^3 + (-54 - 32 \cos(2\Phi)) \left(\frac{t}{U}\right)^4.
\end{aligned} \tag{4.2.13}$$

Apart from performing the linked-cluster expansion we also verified all exchanges by applying perturbation theory on the 12-site cluster directly, where the chosen gauge was used. However, one could also derive an effective model for the 12-site cluster in which neither phases around the torus nor distinct exchange constants for topologically equivalent interactions (like for J_{hor} and J_{dia}) occur. This can be achieved by fulfilling the Φ -flux condition on every triangle without assigning specific phases to specific bonds. The eigenenergies do of course not depend on the gauge.

4.3. Verification and metal-insulator transition

In order to verify the derived effective models, a direct comparison with the Hubbard model is ideal. Clearly, this is only feasible on small cluster sizes with ED. In Ref. [66], it was done for a triangle and a four-site plaquette. Also, the effective model on the square lattice was compared with previously derived models for $SU(2)$. Here, we show a direct

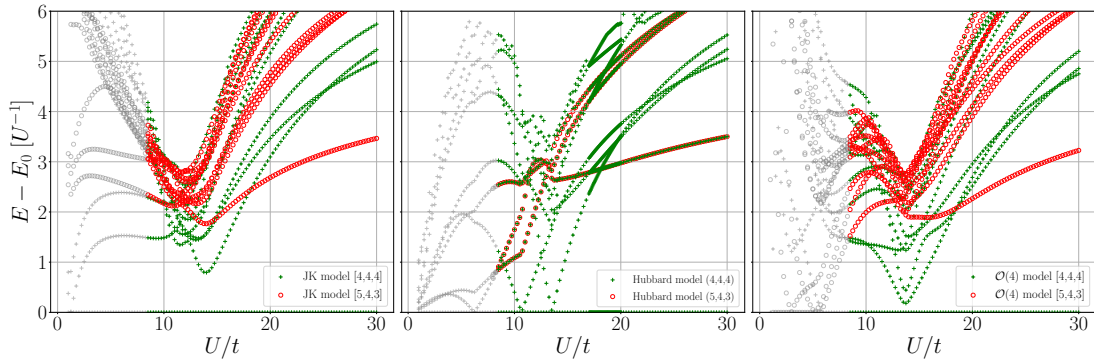


Fig. 4.10.: Comparison of the excitation spectra between the J - K model (left), the Hubbard model (middle), and the $\mathcal{O}(4)$ (order four) effective model (right) on the 12-site cluster from ED for $SU(3)$. Since the couplings in the effective descriptions are polynomials in t/U , the energies from the spin models are multiplied by U to be comparable to the energies of the Hubbard model. For $U \approx 30t$ the spectra agree very well, but differences become noticeable as U decreases. The grey regions of the spectra are not in the Mott-insulating phase of the Hubbard model and the effective models are not valid. This figure is published in Ref. [100].

comparison for $SU(3)$ between the energies of the Hubbard model on the 12-site cluster with PBCs and the effective model for this finite system, derived in Subection 4.2.3. The ED for the effective models was done preliminary by the present author, and then by Clemens Ganahl and Andreas Läuchli, who also performed the ED of the Hubbard model. For details on the employed symmetries, see Ref. [100], where the parts of this subsection are published.

The energy spectra of the $SU(3)$ Hubbard model (3.3.1), the J - K model (3.3.3), and the order four $[\mathcal{O}(4)]$ effective spin model (4.2.7) on the 12-site cluster are shown in Fig. 4.10. For the spin models the numbers in the square brackets label a certain irrep of the $SU(3)$ group. The numbers in the round brackets for the Hubbard model give the number of particles of a certain colour. For $U \approx 30t$ the spectra of both effective models are in reasonable agreement with the spectrum of the Hubbard model. The first excitation in the spin models is in the adjoint representation $[N_s/3 + 1, N_s/3, N_s/3 - 1]$ followed by three singlet levels. For decreasing couplings U , the energetically higher singlets start to cross each other in the spin models, just like the corresponding excited states in the Hubbard model. In the effective models at $U \approx 15 - 20t$, the first excited singlet crosses the low-energy state of the adjoint representation, which for even smaller values of U is also crossed by two more singlets. A similar behaviour exists in the spectrum of the Hubbard model, even though the order in which the crossings occur is not exactly the same. As expected, the level crossings of the $\mathcal{O}(4)$ model seem to match those of the Hubbard model slightly better than those of the J - K model.

To check the effective description more quantitatively, we compare the differences between the ground-state energies of the spin models with those of the Hubbard model in Fig. 4.11. The errors of the ground-state energies decay with one order higher than the corresponding order of the effective model, signalling a valid perturbative description. Overall, there is a qualitative agreement between the effective description and the Hubbard model in the strong-coupling Mott regime.

An important aspect of the problem is that the effective description breaks down

at the metal-insulator transition. This is due to the perturbative approach based on an adiabatic connection. The metallic state is not reflected within \mathcal{H}_0 . Therefore, the physics captured in the effective spin model is only valid in the Mott phase and it is important to estimate the metal-insulator transition point. The first theoretical estimate for the metal-insulator transition in the SU(3) Hubbard model on the triangular lattice at 1/3-filling for vanishing flux was found to be $(U/t)_c \simeq 10.7$ by SU(N) real-space dynamical mean-field theory in 2018 [168]. However, we are most interested in the π -flux SU(3) Hubbard model, for which we compute the particle-hole charge gap on the 12-site cluster. The calculations were performed by Clemens Ganahl and Andreas Läuchli. The charge gap in ED can be determined by the lowest energies from three different Hilbert space sectors, the one with the same number of particles per colour at 1/3-filling, $E_0(0)$, the one with an additional fermion, $E_0(+1)$, and the one with one fermion less, $E_0(-1)$. With this notation the particle-hole charge gap is

$$\Delta_{\text{charge}} = E_0(+1) - 2 \cdot E_0(0) + E_0(-1) . \quad (4.3.1)$$

The metal-insulator transition point, $(U/t)_c^{\text{mi}}$, is then estimated by extrapolating the linear part at large values of U . The Mott-insulating phase breaks down, where this extrapolated charge gap closes. For SU(3) on the 12-site cluster the results are shown in Fig. 4.12. They indicate that the metal-insulator transition is located at $(U/t)_c^{\text{mi}} \approx 8.5$.

From ED on the 12-site cluster for the spin-1/2 Hubbard model without fluxes (1.0.1) the transition point was determined to be $(U/t)_c^{\text{mi},1/2} \approx 12$ [169]. Another route for spin-1/2 Hubbard models with a filling of one fermion per site to estimate the metal-insulator phase transition point can be gained from the tight-binding model, $U = 0$ in Eq. (1.0.1). The idea is that the energy a state can gain is related to the bandwidth of the spectrum in momentum space. If this energy is as large as the coupling constant U the charge gap closes. This can also be understood with perturbation theory, where the hopping of a doublon and a holon gives the first-order contribution, which gets subtracted from

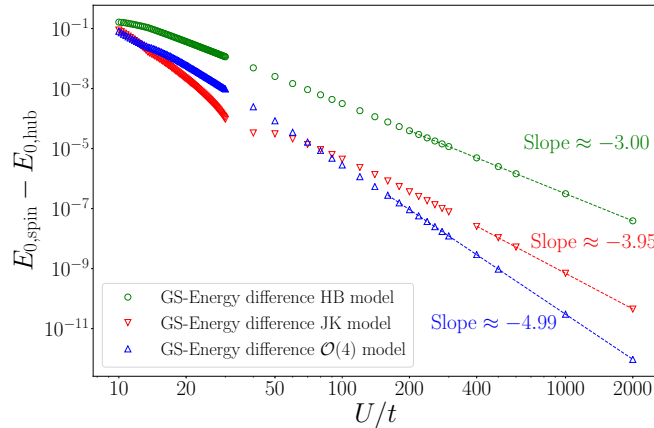


Fig. 4.11.: Scaling of the differences in the ground-state energies between various spin models and the Hubbard model on the 12-site cluster from ED for SU(3). The effective second-order Heisenberg model is abbreviated by HB model. A line is fitted for each spin model to estimate the scaling behaviour. The slopes are in good agreement with the expectations. This figure is published in Ref. [100].

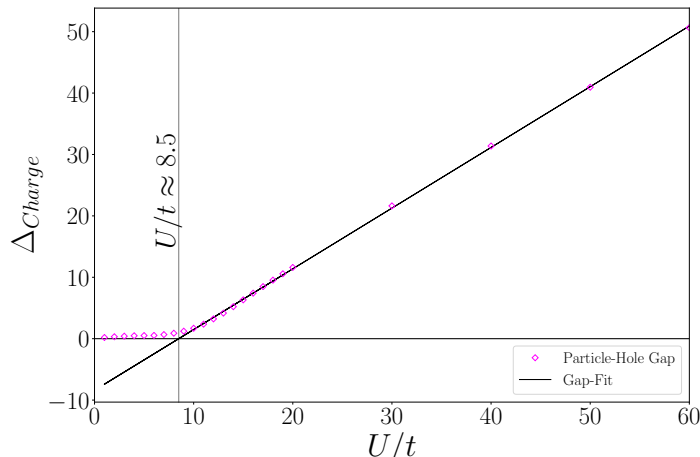


Fig. 4.12.: Particle-hole gap for the SU(3) Hubbard model with $\Phi = \pi$ from ED on the 12-site cluster indicating the estimation of the metal-insulator transition. This figure is published in Ref. [100].

the unperturbed energy difference U . If the energy difference vanishes, the charge gap closes and the Mott-insulating phase breaks down. For spin-1/2 the energies of the holon and the doublon are identical. The calculation for π -flux yields $(U/t)_c^{\text{mi},1/2} \approx 6$, and for vanishing flux $(U/t)_c^{\text{mi},1/2} \approx 12$. This does not hold for SU(3), which was first pointed out by Karlo Penc.

In the ED calculations on 12 sites, the charge gap (given in Fig. 4.12) shows a linear behaviour above $U \approx 10|t|$, and we interpret this result in first-order perturbation theory around the limit of strong coupling at filling 1/3. Assuming linear behaviour for the charge gap, the transition point yields $\Delta_{\text{charge}} \approx U - 8.5t$, and the first order term must arise from the kinetics of charge excitations, the doublon-hole pairs. In the case of the SU(2) model, both the hole and the doubly occupied site are featureless objects, in fact SU(2) singlets, and they behave similarly. In contrast, in the case of the SU(3) Hubbard model, the doubly occupied site forms the three-dimensional anti-symmetrical irrep, and the motion of the doubly occupied site is more complicated than the motion of the hole. The energy $-8.5t$ originates from the hoppings of the hole and the doubly occupied sites, the contribution from the hole is $E_0(-1) - E_0(0) \approx -0.02U - 3.30t$, and the contribution of the doubly occupied site is $E_0(+1) - E_0(0) \approx 1.01U - 5.10t$ [compare Eq. (4.3.1)]. We can see, that the kinetic energy of the doubly occupied site is larger than that of the hole. A similar calculation for SU(7)-symmetric fermions in the Hubbard model is not feasible, due to the large Hilbert space.

In this chapter, we derived effective low-energy descriptions for the SU(N) Hubbard model in the strong-coupling regime. The validity range was studied in three ways. First, the convergence behaviour of the series was analysed. Second, the effective model in third- and fourth-order was compared directly with the SU(3) Hubbard model on the 12-site cluster with ED. Third, the break down of the Mott-insulating phase was estimated from this 12-site calculation for SU(3). In the next two chapters, the effective models are investigated for SU(7)- and SU(3)-symmetric fermions, respectively.

5. SU(7) symmetric fermions on the triangular lattice

The strong-coupling regime of the Mott-insulating phase in third order of t/U is captured by the J - K model, introduced in Section 3.3. For SU(7)-symmetric fermions at $\Phi = \pi/2$ a $\pi/7$ -flux CSL was found [62]. It was identified by ED and VMC states, as well as by chiral edge modes on systems with open boundary conditions in ED. The signature for SU(7) in comparison to other values of N was particularly strong, which is why we choose $N = 7$ as a promising value, and investigate the presence of this CSL phase in the same model for all fluxes Φ including the case $\Phi = \pi$.

5.1. J - K model

5.1.1. Chiral phase on systems with periodic boundary conditions

The $\pi/7$ -flux CSL on a torus has a topological ground-state degeneracy of seven if time-reversal symmetry is explicitly broken, and fourteen if not [52,53]. The low-energy spectrum from ED on the 21-site cluster is illustrated for varying fluxes $0.2\pi \leq \Phi \leq \pi$ at $|K|/J = 0.45$ in Fig. 5.1. At $\Phi = \pi/2$, so for purely imaginary ring exchange, the ground state and the first excited state are very close in energy in comparison to the difference

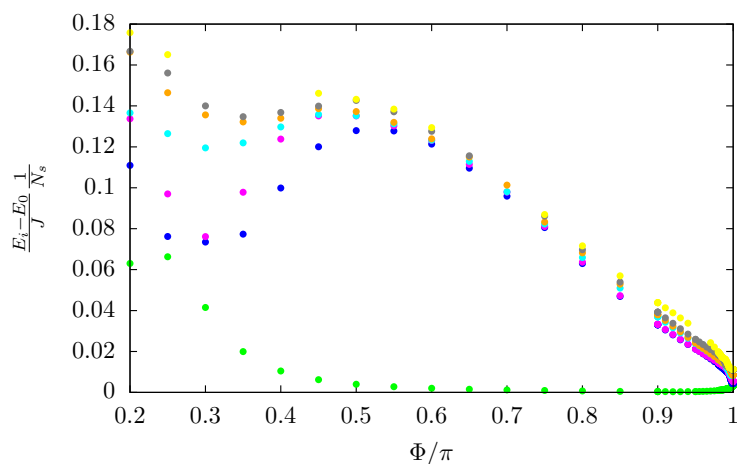


Fig. 5.1.: Energy difference between excited states and the ground state for the SU(7) J - K model at $|K|/J = 0.45$ on the 21-site cluster with PBCs from ED. All states are from the singlet sector $[3, 3, 3, 3, 3, 3, 3]$. The ground state is non-degenerate, the first excited state (green) is six-fold degenerate at $0.25 \lesssim \Phi < \pi$. At $\Phi = \pi$ the four lowest levels have the degeneracies one-six-one-six from bottom to top. A zoom on the area close to $\Phi = \pi$ is shown in Fig. 5.2.

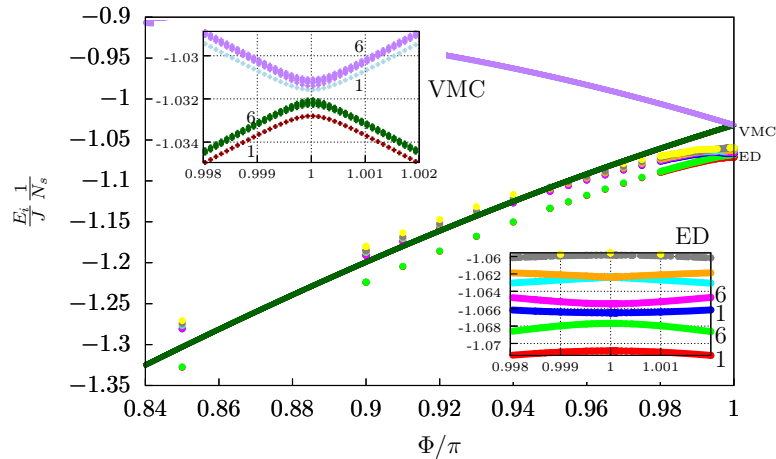


Fig. 5.2.: Energy spectrum for the $SU(7)$ J - K model at $|K|/J = 0.45$ close to $\Phi = \pi$ on the 21-site cluster with PBCs from ED, where all shown energies are singlets, and VMC .

towards the next higher levels. The ground state is non-degenerate and the first-excited state is six-fold degenerate. These one-plus-six states are expected to form the seven-fold degenerate ground-state manifold of the $\pi/7$ -flux CSL in the thermodynamic limit [62]. For smaller fluxes Φ , the splitting of states within the manifold increases and eventually the six-fold degenerate state crosses with other excited states. Here, the CSL breaks down. To our knowledge, the nature of the small- K phase is not yet understood. For fluxes larger than $\pi/2$, the seven low-energy states remain energetically close. However, the difference to the higher energies decreases and the separation between the states of the ground-state manifold and the excited states becomes less pronounced. Still, the signature of the CSL remains present for the whole range of fluxes up to $\Phi = \pi$.

For this special case, where time-reversal symmetry is not explicitly broken, the low-energy spectrum is different. It is shown for fluxes around $\Phi = \pi$ at $|K|/J = 0.45$ in Fig. 5.2. The seven low-lying states at $0.25 \lesssim \Phi < \pi$ remain below all other states also at $\Phi = \pi$. The energy differences towards the higher excited states decrease significantly though while approaching $\Phi = \pi$, such that at $\Phi = \pi$ the first excited level is actually closer to the two levels above than to the ground state. The degeneracies of these four low-energy states are one-six-one-six, and therefore add up to fourteen. This is exactly the ground-state degeneracy expected for a spontaneous time-reversal symmetry breaking $\pi/7$ -flux CSL phase. The energies within this supposed ground-state manifold are not significantly separated from the levels above, which might be related to the relatively small cluster size of 21 sites. The reasoning in favour of this phase is supported by the CSL states from VMC. The according energies are also included in Fig. 5.2. They have the same degeneracies, and the behaviour looks very similar, in particular also close to the π -flux case. This good agreement supports the presence of a spontaneous time-reversal symmetry breaking CSL. The VMC was done by Miklós Lajkó and the method is motivated in Subsection 6.1.1.

In Fig. 5.3 the energy differences between excited states and the ground state from ED on the 21-site cluster are shown for the most interesting case $\Phi = \pi$ and varying coupling

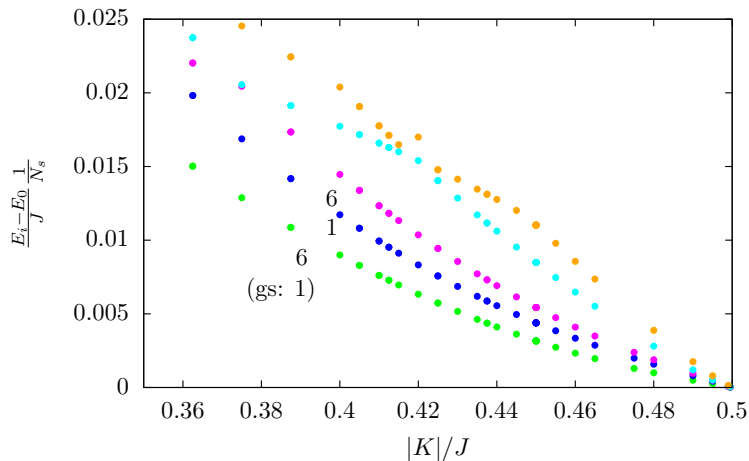


Fig. 5.3.: Energy difference between excited states and the ground state for the $SU(7)$ J - K model at $\Phi = \pi$ on the 21-site cluster with PBCs from ED.

ratios $|K|/J$. The set of states forming the potential fourteen-fold degenerate ground-state manifold in the thermodynamic limit occurs at $(|K|/J)_c \approx 0.37$ and remains present over the whole range up to $K/J = 0.5$, where a large ground-state degeneracy occurs. This might be linked to an effective reduction of the number of colours present in the ground state similar to the $SU(3)$ -symmetric J - K model at $\Phi = \pi$ and $K/J = -0.5$, compare Section 6.1.1. In order to clarify this issue, one could study the TOS. The separation between the ground-state manifold and the next excited levels varies with $|K|/J$. It is not very pronounced at any point, which could be linked to the small cluster size, and it is plausible that the CSL is present in the thermodynamic limit. ED on larger clusters or other methods could validate (or falsify) this. Another option is to determine chiral edge states with ED on systems with open boundary conditions, which was already shown for $\Phi = \pi/2$ [62]. In the next subsection, we present similar investigations for an extended parameter regime of the CSL including fluxes $\pi/2 \leq \Phi \leq \pi$.

5.1.2. Chiral edge states

Topological phases on systems with open boundary conditions possess chiral edge states. These are characterised by a linear behaviour between energy and momentum quantum number, which looks like a branch. The edge state velocity is defined by the slope of the branch. Chiral edge states are gapless excitations, hence there is no topological ground-state degeneracy on such geometries. For systems where time-reversal symmetry is explicitly broken, $[H, \mathcal{T}] \neq 0$, chiral edge states propagate in a single direction. In contrast, if time-reversal symmetry is spontaneously broken, $[H, \mathcal{T}] = 0$, states propagate in both directions, i.e. two branches of states with opposite velocity occur.

For $SU(7)$ -symmetric fermions in the J - K model with purely imaginary ring exchange, $\Phi = \pi/2$, chiral edge states were numerically found at $|K|/J = 1$ [62]. This was done by ED on a 19-site cluster with open boundary conditions. The specific cluster is illustrated in Fig. 5.4. It is invariant under rotations around angles $l\pi/3$, thus the angular momentum yields good quantum numbers $l \in \{0, \dots, 5\}$. The eigenvalues are $e^{il\pi/3}$. Po-

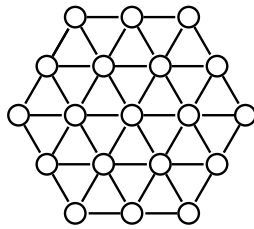


Fig. 5.4.: 19-site cluster with open boundary conditions used for the study of chiral edge states with ED.

tential branches of chiral edge states are energetically split due to the finite system size. For explicitly broken time-reversal symmetry, analytic predictions for the 19-site cluster from the $SU(7)_1$ WZNW conformal field theory (CFT) in the case of a $\pi/7$ -flux CSL are known [62]. A specific set of states from different irreps at certain momenta is expected and summarised in Tab. 5.2. For spontaneous time-reversal symmetry breaking no CFT predictions are available in the literature. They should be similar to an $SU(7)_1$ theory, which numerically relates to the behaviour of an antiferromagnetic $SU(7)$ -Heisenberg chain with PBCs.

For $\Phi = \pi/2$, the branch of chiral edge states can be seen in the energy spectrum in Fig. 5.5 for $|K|/J = 0.45$, where the energies are plotted in respect to the ground-state energy against the angular momentum quantum numbers. The ground state has angular momentum $l = 2$. With increasing angular momentum, the energies rise and constitute the branch of chiral excitations propagating with a positive edge state velocity. The according states with $l = \{2, 3, 4\}$ fit to the irreps predicted by CFT for a CSL phase given in Tab. 5.2.

In the following, we present similar numerical results for larger fluxes including $\Phi = \pi$, where time-reversal symmetry is not explicitly broken. The eigenenergies in respect to the ground-state energy are plotted against fluxes $\pi/2 \leq \Phi \leq \pi$ in Fig. 5.6, where the point shape indicates the irrep of the state. No level crossings occur up to $\Phi \approx 0.77\pi$ and the structure of the angular momentum spectrum remains similar to the one for $\Phi = \pi/2$ in Fig. 5.5. Therefore, the correspondence between irreps and angular momentum quantum numbers in the branch fits the CFT prediction in this whole flux-range. For fluxes $\Phi \gtrsim 0.77\pi$ the structure of the low-lying energies changes. Six states from the irrep **21** and two states from the irrep **28** are separated energetically from all other irreps, which are higher in energy. The set of states at low energies rearranges internally. The angular momentum spectrum for $\Phi = 0.9\pi$ is shown in the left panel of Fig. 5.7.

| label | Young tableau | dimension | multiplicity | Casimir |
|-------|-----------------------|------------|--------------|---------|
| 0 | [3, 3, 3, 3, 3, 2, 2] | 21 | 831042 | 25 |
| 1 | [3, 3, 3, 3, 3, 3, 1] | 28 | 554268 | 29 |
| 2 | [4, 3, 3, 3, 3, 2, 1] | 735 | 5819814 | 41 |
| 3 | [4, 3, 3, 3, 2, 2, 2] | 224 | 4434144 | 35 |
| 4 | [4, 3, 3, 3, 3, 3] | 560 | 1108536 | 47 |
| 5 | [4, 4, 3, 2, 2, 2, 2] | 490 | 6466460 | 41 |

Tab. 5.1.: Relevant $SU(7)$ symmetry sectors for 19 particles.

| angular momentum | sectors of chiral edge states |
|------------------|--|
| $l - l_0 = 0$ | 21 |
| $l - l_0 = 1$ | 21 \oplus 28 \oplus 224 |
| $l - l_0 = 2$ | $3 \times$ 21 \oplus 28 \oplus $2 \times$ 224 \oplus 735 \oplus 490 |

Tab. 5.2.: Expectations of states from certain irreps on finite systems for explicitly broken time-reversal symmetry from the $SU(7)_1$ WZNW conformal field theory. The irreps are given by their dimensions, which can be found in Tab. 5.2.

At fluxes just below $\Phi = \pi$, the separation of the six-plus-two low-energy states from the irreps **21** and **28** and the other irreps decreases again. This is due to several states from the irreps **21** and **28**, which evolve with a large negative slope.

The ground state does not change in the whole range of fluxes $\pi/2 \leq \Phi \leq \pi$. At $\Phi = \pi$, it becomes degenerate, because another level crosses, such that for $\Phi > \pi$ a different ground state is present. The angular momentum spectrum at $|K|/J = 0.45$ and $\Phi = \pi$ is given in the right panel of Fig. 5.7. It is significantly different compared to the ones at other fluxes. On top of the degenerate ground states at angular momenta $l_i - 2 = 0$ and $l_i - 2 = 2$, the number of low-energy states is larger than for smaller fluxes. We note, that the energies at the ground-state momenta as well as at $l_i - 2 = 3$ and $l_i - 2 = 5$ are the same, hinting towards the existence of two counter propagating branches. However, without predictions for the expected irreps in the case of a spontaneous time-reversal symmetry breaking CSL this can not be confirmed. The according $SU(7)_1$ CFT has not been studied analytically yet, so we do not have the exact predictions for the π -flux case. They should resemble though the energy spectra of the antiferromagnetic $SU(7)$ -Heisenberg model on periodic chains. We therefore study this model on a ring of 19 sites with ED. The angular momentum operator is defined by rotations along the ring. The possible angles are $l \cdot \frac{2\pi}{19}$ with the quantum numbers

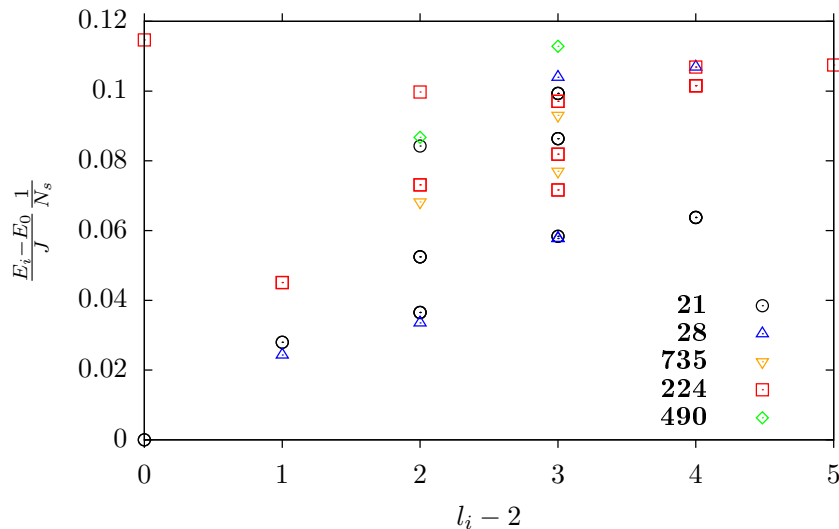


Fig. 5.5.: Angular momentum energy spectrum in respect to the ground-state energy for the $SU(7)$ J - K model at $\Phi = 0.5\pi$ and $|K|/J = 0.45$.

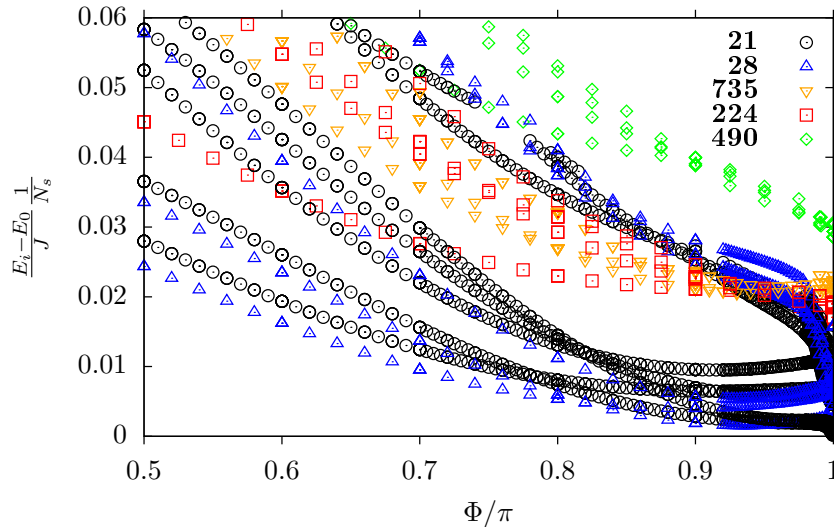


Fig. 5.6.: Energy spectrum in respect to the ground-state energy for the $SU(7)$ J - K model at $|K/J| = 0.45$ against flux Φ on the 19-site cluster with open boundary conditions .

$l \in \{0, \dots, 18\}$. The energy spectrum plotted against the angular momentum is shown in Fig. 5.8. There are some similarities with the energies of the J - K model at $\Phi = \pi$ in the right panel of Fig. 5.7, but the overall picture is quite different. In both models, the ground states are two-fold degenerate and from the irrep **21**. Also the low-energy states are from the same irreps, but the Heisenberg model has fewer states close to the ground state. The energies from the Heisenberg model do not simply resemble the ones of the J - K model at $\Phi = \pi$. Surprisingly, the spectrum of the J - K model at $\Phi = 0.9\pi$ in the left panel of Fig. 5.7 resembles the one of the antiferromagnetic $SU(7)$ -Heisenberg model in Fig. 5.8.

In regard of the energy spectra from ED and VMC with PBCs, compare Fig. 5.3, it seems rather unlikely that no CSL is realised. In this case, one possible explanation

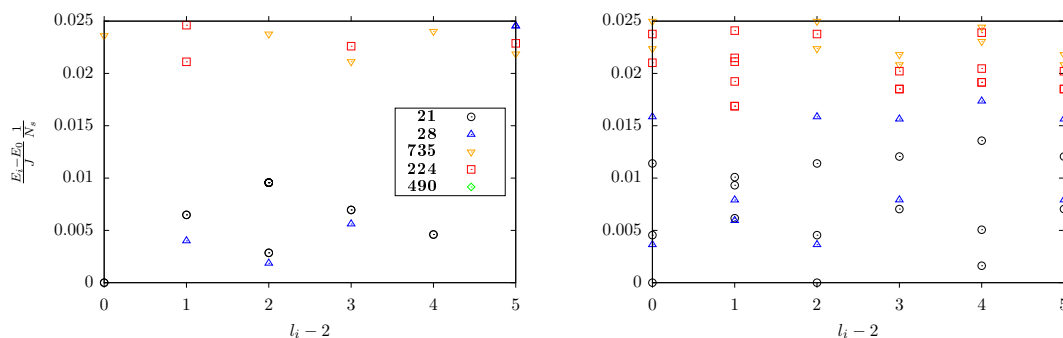


Fig. 5.7.: Energy differences to the ground-state energy in respect to the angular momentum quantum number on 19-site clusters for the $SU(7)$ J - K model. On the left for $\Phi = 0.9\pi$ and in the middle for $\Phi = \pi$ for the $SU(7)$ J - K model at $|K/J| = 0.45$. The angular momentum quantum numbers are shifted for a better comparison with the energies of the antiferromagnetic $SU(7)$ -Heisenberg 19-site ring in Fig. 5.8.

of the spectrum at $\Phi = \pi$ with open boundary conditions is that the gap between the chiral edge branches and the continuum on top is not resolved because of finite-size effects. This separation is already quite small for the CSL at $\Phi = \pi/2$, where time-reversal symmetry is explicitly broken, even for $|K|/J = 1$ deep inside the CSL phase [62]. Another difficulty is linked to the expectation that if the CSLs are realised, while crossing $\Phi = \pi$ a left moving branch is exchanged by a right moving branch and at $\Phi = \pi$ both branches are present. On the one hand, if two branches come into place at $\Phi = \pi$, their energies are already low for fluxes close to π , due to the finite system size. Then, these energies intersect with the single branch present for explicitly time-reversal symmetry breaking fluxes. On the other hand, the spontaneous time-reversal symmetry breaking is only realised at a single flux value, where again the distinct levels of the surrounding phases interfere. These drastic modifications could be related to the large changes in the spectrum around $\Phi = \pi$ as shown in Fig. 5.6.

How these findings can be understood exactly remains open. In order to get a better understanding of the chiral edge states, ED on the 26-site cluster for the J - K model might be insightful. Furthermore, either predictions from CFT or a systematic evaluation of the Heisenberg model on different clusters would be required to potentially allow putting the presented findings into context.

Another route for the clarification could be experiments with ultra cold atoms in optical lattices, see Section 3.2. In order to invert the sign of the hopping amplitude t either a gauge field, or a filling of $6/7$ would be required for $SU(7)$ -symmetric fermions. For $SU(3)$ this inversion can be realised by a filling of $2/3$. Further, for $SU(3)$ we already estimated the metal-insulator transition point from ED of the Hubbard model on the 12-site cluster. Such a calculation would be not feasible for $SU(7)$ with the current techniques. Therefore, we turn to the question if similar CSL phases as for $SU(7)$ are realised in the $SU(3)$ -symmetric J - K model in particular at $\Phi = \pi$, and then continue analysing higher-order terms.

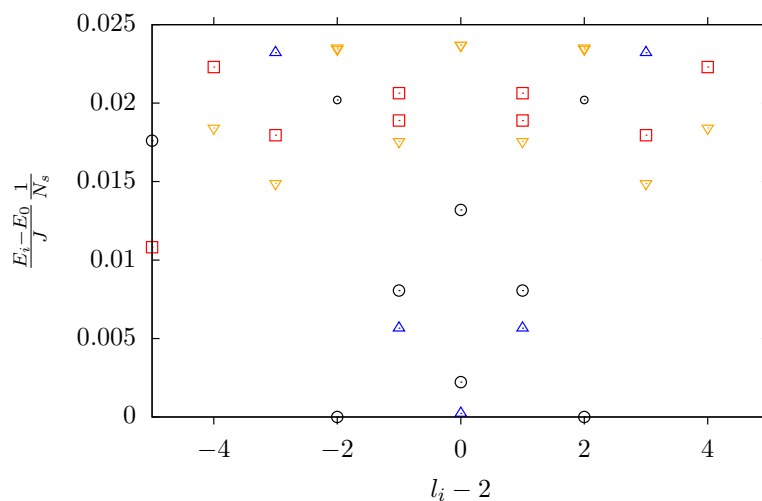


Fig. 5.8.: Energy differences to the ground-state energy in respect to the angular momentum quantum number of the antiferromagnetic $SU(7)$ -Heisenberg ring with 19 sites.

6. SU(3) symmetric fermions on the triangular lattice

6.1. J - K model

First, we review former theoretical findings for SU(3)-symmetric spins in the J - K model. For only nearest-neighbour interactions, $K = 0$, the model is identical to the symmetric spin-1 bilinear-biquadratic Heisenberg model with equal bilinear and biquadratic term

$$H_{\text{bb}} = \sum_{\langle i,j \rangle} \left[\vec{S}_i \cdot \vec{S}_j + \left(\vec{S}_i \cdot \vec{S}_j \right)^2 \right] \quad (6.1.1)$$

with the spin-1 operator \vec{S}_i on site i [81]. The bilinear-biquadratic model was introduced to study the interplay between magnetic dipole and quadrupolar order. The interaction between the quadrupoles is included in the Hamiltonian as

$$\vec{Q}_i \cdot \vec{Q}_j = 2 \left(\vec{S}_i \cdot \vec{S}_j \right)^2 + \vec{S}_i \cdot \vec{S}_j - \frac{8}{3}. \quad (6.1.2)$$

In the symmetric case, the SU(2) symmetry of the spin-1 model is increased to SU(3). This can be seen in the relation

$$\vec{Q}_i \cdot \vec{Q}_j + \vec{S}_i \cdot \vec{S}_j = 2P_{ij} - \frac{2}{3}, \quad (6.1.3)$$

where only an effective permutation of the spins remains, completely independent of the colour. At the SU(3)-symmetric point with antiferromagnetic couplings, a second order phase transition between a three-sublattice 120°-antiferromagnetic phase (AFM) and a three-sublattice antiferroquadrupolar (AFQ) phase occurs [143].

In terms of a site-factorised Ansatz, three-sublattice ordered states can be written as

$$|\Psi\rangle = \prod_{j=1}^3 \prod_i |d_j\rangle_i, \quad (6.1.4)$$

where the first product runs over the sublattices j and the second one over all sites i in each sublattice. The on-site states are defined by

$$|d\rangle = \sum_{\alpha \in \{x,y,z\}} d_\alpha |\alpha\rangle \quad (6.1.5)$$

with normalised vectors $\mathbf{d} = (d_x, d_y, d_z)$ using the fundamental time-reversal invariant SU(3) representation in Eq. (3.1.4) for $|\alpha\rangle$. In this notation, a quadrupolar phase is given if the components of the vector \mathbf{d} , which is called the director in this case, are real

$d_\nu \in \mathbb{R}$. In the AFQ phase of the bilinear-biquadratic model, directors on neighbouring sites are mutually perpendicular. Quadrupolar phases do not break time-reversal symmetry and the spin fluctuations are the strongest in the direction orthogonal to the director. Therefore, the $SU(2)$ symmetry is broken by anisotropic quantum fluctuations, but the states do not show a magnetic moment, i.e. magnetic long-range order [143]. In contrast, the AFM shows non-vanishing quadrupolar-quadrupolar and spin-spin correlations. It has distinct magnetic moments on every sublattice described by an orientational difference between moments on different sublattices of $2\pi/3$ (compare the right panel of Fig. 3.3). Both phases are connected by a global $SU(3)$ symmetry at the symmetric point. The ordering vector of 3-SL ordered phases is at the K point [$\vec{k} = (4\pi/3, 0)$] in the first Brillouin zone [143], and the $SU(3)$ symmetry is spontaneously broken. Therefore, the phase has gapless Goldstone modes.

The presence of this 3-SL LRO phase in the $SU(3)$ Heisenberg model was confirmed by linear flavour-wave theory, ED, density-matrix renormalization group calculations, and iPEPS [170]. It was also found by Bieri et al. using VMC [63]. In this study, a first phase diagram for the J - K model for real ring exchange K was determined. For small values of K , a 3-SL LRO 120° AFM remains present. This phase is part of the ground-state manifold of the model at $K = 0$, where the AFQ and AFM phase are degenerate. For finite values of K the system exhibits the 3-SL LRO 120° AFM [170].

In the opposite limit with $J = 0$, a three-sublattice 120° - or \mathcal{J} -nematic phase was found [63]. This phase was thought to be characterised by a vanishing spin order parameter and only a non-vanishing quadrupolar order parameter, just like the AFQ phase in the bilinear-biquadratic spin-1 model [143]. However, due to the $SU(3)$ symmetry, this does not hold, and we refer to it as a 120° LRO phase. Further details are given in Subsection 6.1.1. The same order of magnetic states was confirmed by a numerical site-factorised state study in 2013 [64].

At intermediate parameters, a $d_x + id_y$ CSL for real ring exchange $0.6 \leq K/J \leq 1.5$ was proposed by Bieri et al. [63]. This topological spin liquid has a Fermi surface of deconfined spinons. The lattice rotation symmetry is unbroken, but ferro-quadrupolar order occurs, and the phase has Chern number two.

The uniform $\pi/3$ -flux and $2\pi/3$ -flux CSL states were not considered in this VMC study and therefore not observed. These CSLs also break time-reversal symmetry and parity but not their product, and exhibit chiral edge states on systems with open boundary conditions. In contrast to the $d_x + id_y$ CSL, the ground state on a system with PBCs is gapped [62]. The ground-state degeneracy is non-trivial and depends on the topology of the system. Further, these CSLs exhibit anyonic excitations [52]. In 2013, these states were first considered to occur in the J - K model [64]. However, in this work, the magnetically ordered states and the CSL states were approached with different methods such that the derived energies were not comparable [64]. Namely, a numerical site-factorised state study for the magnetically ordered phases, and a slave-fermion mean-field calculation for the triangular plaquette phase, the uniform $\pi/3$ -flux CSL phase, and the uniform $2\pi/3$ -flux CSL phase was performed. For the magnetically ordered states the same sequence of three-sublattice ordered phases as in Ref. [63] was determined. The energies of the CSL states were found to be lower than the one of the previously suggested $d_x + id_y$ CSL phase [63], such that in the intermediate area between $0.6 \lesssim K/J \lesssim 1.5$ the $\pi/3$ -flux CSL phase is predicted. It was also shown that

the $\pi/3$ -CSL phase has a Chern number one and two anyonic excitations with self- and mutual statistics of $2\pi/3$.

The ambiguity in these previous findings suggesting different types of unconventional CSLs calls for further studies with more elaborate methods. In the case of purely imaginary ring exchange a $\pi/3$ -flux CSL was already found by ED on top of VMC [62]. In the following subsections, we investigate the full phase diagram of the J - K model with these two techniques.

6.1.1. Full phase diagram without fluxes

In this subsection, we study the $SU(3)$ -symmetric J - K model in Eq. (3.3.3) for real ring exchange, $\text{Im } K = 0$, corresponding to fluxes $\Phi = 0$ and $\Phi = \pi$. Parts of this subsection are published in Ref. [100]. The phase diagrams, shown in Fig. 6.1, are determined by ED on the 12-, 21-, and 27-site clusters and by VMC on the 144-site cluster with PBCs. The first ED calculations were done by the author of the present thesis on 12 and 21 sites, determining eigenenergies, eigenstates, symmetries and degeneracies. Then, this was taken over by Clemens Ganahl and Andreas Läuchli, who were able to determine the structure factors, chiralities, and TOS, as well as to study the 27-site cluster. The ED was performed in the basis of standard Young tableaux under the exploitation of the $SU(N)$ symmetry as briefly described in Section 3.1. The idea behind VMC is to design a nearest-neighbour tight-binding Hamiltonian depending on variational parameters, which allows the investigation of several variational states with distinct properties. To this end, various symmetries can be broken explicitly in the Hamiltonian. In order to achieve states with only one particle per site, a Gutzwiller projection is performed. The state of lowest energy in a certain physical parameter regime is determined by a Monte Carlo simulation. VMC also allows the calculation of

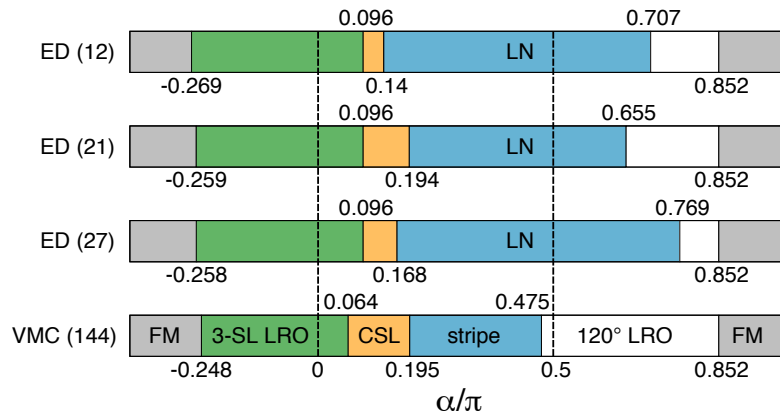


Fig. 6.1.: Comparison of the predicted phase diagram for the triangular lattice $SU(3)$ J - K model on the 12-, 21-, and 27-site clusters from ED (top three rows) and the 144-site cluster from VMC (bottom row). Around the Heisenberg point ($\alpha = 0$), the 3-SL LRO phase (green) is present. For increasing values of α up to $\alpha = \pi$, a $\pi/3$ -flux CSL (orange), a LN phase (blue), a 120° LRO phase (white), and a ferromagnetically ordered phase (grey) occur. The stripe state from VMC is expected to be closely related to the LN phase from ED. This figure is published in Ref. [100].

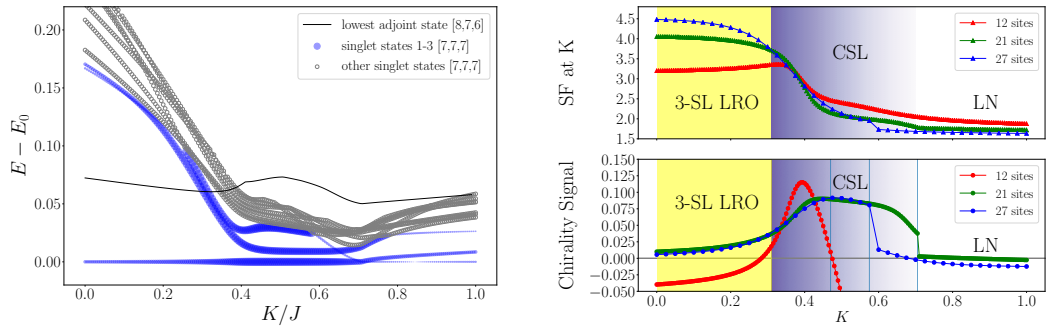


Fig. 6.2.: On the left: Spectrum of the $SU(3)$ J - K model on the 21-site cluster from ED. The marker size corresponds to the overall chirality signal and is plotted for the lowest three states. Three low-lying singlets with strong chiral signal indicate the presence of a CSL phase in an extended parameter space at intermediate values of K/J . On the right: Structure factor at the K point (top) and chirality signal per lattice site (bottom) for the J - K model from ED on the 12-, 21-, and 27-site clusters. Coming from the 3-SL LRO phase at small ratios K/J , the structure factors at the ordering momentum K decrease as the chirality signals increase, indicating the CSL. In the regime, where the chirality signal decreases, a LN phase occurs. Both figures are published in Ref. [100].

observables and degeneracies. The VMC was performed by Miklós Lajkó and details on the method and all considered states, namely CSLs, plaquette order, stripe order, and colour order, are given in Ref. [100].

For small ring exchanges K (around $\alpha = 0$), the 3-SL LRO phase is present. This is clear from the low-energy spectrum of the 21-site cluster from ED in the left panel of Fig. 6.2. For small values of K/J , the first excited state above the singlet ground state is in the adjoint irrep, [8, 7, 6], which corresponds to the TOS expected for the 3-SL LRO phase [171]. This fits to the large extensive structure factor at the K point in this regime, determined from different cluster sizes and shown in the right top panel of Fig. 6.2. In VMC, the 3-SL LRO phase is modelled by different chemical potentials on distinct sites with 0-flux per plaquette, breaking the $SU(3)$ symmetry explicitly. The energies of this 3-SL LRO phase and of the 120° AFM order proposed by Bieri et al. [63] are almost exactly matched for the coupling regime $-0.248\pi < \alpha < 0.064\pi$ ($J > 0$, $-0.99 < K/J < 0.20$). In fact, for special values of the parameters used by Bieri et al. their variational states are equivalent to our 3-SL LRO variational states. Namely, for $\sin \eta = \sqrt{2/3}$ in Eq. (15) of their paper, the three \mathbf{d} vectors [compare Eq. (6.1.4)] become mutually orthogonal to each other, and their mean-field Ansatz can be transformed to ours with an $SU(3)$ rotation. We find that the 3-SL LRO phase is the more appropriate identification of this phase, as the 120° order is just a special case, and in fact not all members of the ground-state manifold have dipole ordering due to the $SU(3)$ symmetry of the model, which can mix the dipolar and quadrupolar moments of the spins. The 3-SL LRO phase is expected in a slightly smaller area for $K > 0$ in VMC than in ED. This is most likely linked to the neighbouring state at larger ring exchanges $K > 0$, which is particularly well described as a variational state, the $\pi/3$ -flux CSL.

In ED, the occurrence of the CSL is signalled by the crossing of two singlets with the

adjoint irrep around $(K/J)_c \approx 0.31$ ($\alpha_c \approx 0.096\pi$). These two new lowest excitations together with the ground state have the degeneracies one-four-one corresponding to a total of six states, which may form a six-fold degenerate ground state in the thermodynamic limit. Such a degeneracy, $2 \cdot 3$, is associated with spontaneous chiral symmetry breaking in the $SU(3)$ -symmetric $\pi/3$ -CSL on a torus, in contrast to a 3-fold degeneracy in the explicitly time-reversal symmetry broken case [53]. However, these six states are not very well separated from higher excited states on the 21-site cluster. The signature is more pronounced than on the 12-site cluster though. On the 27-site cluster the splitting between the six low-energy states and the states above is comparable to that on the 21-site cluster. In the parameter range of the level crossings, the magnetic structure factor at the ordering momentum of the 3-SL LRO phase, the K point, decreases, as can be seen in the right top panel of Fig. 6.2. In the right bottom panel of Fig. 6.2, the total chirality signals of the ground state on the 12-, 21-, and 27-site clusters are shown, which increase in the range where the structure factor decreases. On the 21-site cluster not only the total chirality of the ground state, but also of the two levels from the singlet sector above, increase. This is illustrated by the point size in Fig. 6.2. We find an almost uniform distribution in the connected chirality correlator for the first three singlets, whereas the third excited state exhibits no pronounced chiral order anymore (compare Fig. 8 in Ref. [100]). These properties strongly support the decay of magnetic ordering and the occurrence of a $\pi/3$ -flux CSL phase. The phase boundary in the right panels of Fig. 6.2 is determined by the crossing of the two lowest singlet excitations with the adjoint irrep on the 21-site cluster. The signature of the CSL phase varies in its extension in parameter space for different cluster sizes. It is larger for the 21-site cluster than for the 12- and 27-site clusters. This is due to the nature of the adjacent phase at larger values of K/J (α), which seems to have its ordering momentum (although not very strong in magnitude) close to the X point. While the 12 sites cluster has this particular point, the 21 and 27 sites cluster do not, which may lead to an increased parameter space for the CSL phase on those clusters. With VMC, we find the $\pi/3$ -flux CSL phase for $0.064\pi < \alpha < 0.195\pi$ ($K > 0$, $0.20 < K/J < 0.70$). This is reached by a tight-binding Hamiltonian without chemical potentials (on-site terms) and homogeneous nearest-neighbour hopping amplitudes for all colours. The phase accumulated by a fermion hopping around a triangle is set to $\pi/3$, i.e. a $\pi/3$ -flux. This state was not considered by Bieri et al. [63], but was predicted by the mean-field study of Lai [65].

| | | | | | | |
|-------------|------------------|--------------------|--------------------|------------------|--------------------|--------------------|
| | $ \Psi_1\rangle$ | $ \Psi_2\rangle$ | $ \Psi_3\rangle$ | $ \Psi_4\rangle$ | $ \Psi_5\rangle$ | $ \Psi_6\rangle$ |
| t_1 | 1 | $e^{-i2\pi/3}$ | $e^{i2\pi/3}$ | 1 | $e^{-i2\pi/3}$ | $e^{i2\pi/3}$ |
| t_2 | 1 | $e^{i2\pi/3}$ | $e^{-i2\pi/3}$ | 1 | $e^{i2\pi/3}$ | $e^{-i2\pi/3}$ |
| | $ \Psi_1\rangle$ | $ \Psi_2^*\rangle$ | $ \Psi_3^*\rangle$ | $ \Psi_4\rangle$ | $ \Psi_5^*\rangle$ | $ \Psi_6^*\rangle$ |
| $r_{\pi/3}$ | 1 | $e^{-i2\pi/3}$ | $e^{i\pi/3}$ | 1 | $e^{i2\pi/3}$ | $e^{-i\pi/3}$ |

Tab. 6.1.: Eigenvalues of symmetry operators for the six chiral states $|\Psi_i\rangle$ or $|\Psi_i^*\rangle$ ($|\Psi_1\rangle$ is the ground state, $|\Psi_2\rangle$ and $|\Psi_3\rangle$ are the first-excited states, etc.) on the 12-site cluster. The states $|\Psi_2\rangle$ and $|\Psi_3\rangle$ as well as $|\Psi_5\rangle$ and $|\Psi_6\rangle$ are degenerate. The eigenvalues $t_1(t_2)$ correspond to a translation along \vec{r}_1 (\vec{r}_2). The eigenstates denoted without (with) a star are diagonalised in the joint eigenbasis of the Hamiltonian and the translation (rotation) operator. The results from ED and VMC are identical.

| | | | | | | |
|-------------|------------------|--------------------|--------------------|------------------|--------------------|--------------------|
| | $ \Psi_1\rangle$ | $ \Psi_2\rangle$ | $ \Psi_3\rangle$ | $ \Psi_4\rangle$ | $ \Psi_5\rangle$ | $ \Psi_6\rangle$ |
| t_1 | 1 | $e^{-i2\pi/3}$ | $e^{i2\pi/3}$ | 1 | $e^{-i2\pi/3}$ | $e^{i2\pi/3}$ |
| t_2 | 1 | $e^{i2\pi/3}$ | $e^{-i2\pi/3}$ | 1 | $e^{i2\pi/3}$ | $e^{-i2\pi/3}$ |
| | $ \Psi_1\rangle$ | $ \Psi_2^*\rangle$ | $ \Psi_3^*\rangle$ | $ \Psi_4\rangle$ | $ \Psi_5^*\rangle$ | $ \Psi_6^*\rangle$ |
| $r_{\pi/3}$ | -1 | $e^{-i2\pi/3}$ | $e^{i\pi/3}$ | -1 | $e^{i2\pi/3}$ | $e^{-i\pi/3}$ |

Tab. 6.2.: Eigenvalues of symmetry operators for the six chiral states on the 21-site cluster. The notation is as in Tab. 6.1. The degeneracies on 12 and 21 sites are identical, as are the results from ED and VMC.

The direct correspondence of the CSL states in VMC and ED can be seen by their symmetry properties. Let the lattice constant be a and the lattice vectors

$$\vec{r}_1 = (a, 0)^T \quad \text{and} \quad \vec{r}_2 = a(\cos(\pi/3), \sin(\pi/3))^T, \quad (6.1.6)$$

and let us denote by T_1 and T_2 the corresponding translation operators. Furthermore, let us define the rotation operator $R_{\pi/3}$ that rotates counterclockwise by an angle $\pi/3$. These translations and the rotation do not have a joint eigenbasis. To distinguish them, we mark the eigenstates of H and $R_{\pi/3}$ with a star. The eigenvalues for the six chiral states on the 12- and 21-site clusters are given in Tab. 6.1 and 6.2, respectively. The results from the $\pm\pi/3$ CSL variational states from VMC and from the low-lying energy eigenstates at $K/J = 0.35$ ($\alpha \approx 0.11\pi$) from ED show a perfect match.

The spectrum of the 12-site cluster is discussed in Subsection 6.1.2. On this particular system, the ground-state manifold of six states is intertwined with another state. However, if the states are analysed with respect to their symmetry values, the apparent six low-lying CSL states can be identified. The symmetry properties of the chiral states for clusters larger than 21 sites were only studied by VMC. For systems where the vectors defining the torus lie in the \vec{r}_1 and \vec{r}_2 directions all six chiral states have a wave vector zero. The smallest example is the 36-site cluster for which we provide the symmetry properties in Tab. 6.3. For this specific finite size, only one pair of states is degenerate, the other states are not.

The phase next to the CSL is a previously unreported spatial symmetry breaking phase, which is characterised by strong bonds along one lattice direction and weak bonds along the other lattice directions. It therefore breaks the rotational symmetry of the lattice, leaving a strong signature in the dimer-dimer correlations (compare with Fig. 9 in Ref. [100]). Given the limitations in reachable cluster sizes using ED, it remains an open question whether there is any sort of magnetic ordering in this lattice nematic (LN) phase or not. In the VMC beyond the $\pi/3$ -flux CSL phase between

| | | | | | | |
|----------------|------------------|------------------|------------------|------------------|------------------|------------------|
| | $ \Psi_1\rangle$ | $ \Psi_2\rangle$ | $ \Psi_3\rangle$ | $ \Psi_4\rangle$ | $ \Psi_5\rangle$ | $ \Psi_6\rangle$ |
| t_1, t_2 | 1 | 1 | 1 | 1 | 1 | 1 |
| $r_{\pi/3}$ | 1 | 1 | $e^{-i2\pi/3}$ | $e^{i2\pi/3}$ | -1 | -1 |
| irrep of D_6 | A_1 | A_2 | E_2 | | B_2 | B_1 |

Tab. 6.3.: Eigenvalues of symmetry operators for the six chiral states on the 36-site cluster from VMC only. The notation is similar to Tab. 6.1. On 36 sites the states $|\Psi_3\rangle$ and $|\Psi_4\rangle$ are degenerate, the others are not.

$0.195\pi < \alpha < 0.475\pi$, a striped state with stronger bonds along straight chains with $t_{\text{inter-chain}}/t_{\text{intra-chain}} \approx 0.2$ and a uniform π flux has the lowest energy, superseding both the $d_x + id_y$ phase proposed by Bieri et al. and the $2\pi/3$ -flux CSL proposed by Lai [65]. This striped state is linked to the LN phase in ED, since both break rotational symmetry. We therefore assume that these phases correspond to the same ground state in the thermodynamic limit, and stick with the term LN in the following.

Increasing K/J (α) further leads to an $SU(2)$ -like behaviour with one colour less. With ED this is observed as an $SU(2)$ TOS at large K/J where the ground state is in the irrep $[N_s/2, N_s/2]$ (or $[(N_s - 1)/2 + 1, (N_s - 1)/2]$ if the number of lattice sites N_s is odd) of $SU(3)$ (compare with Fig. 10 in Ref. [100]). According to Eq. (6.1.7), the ground-state energies in this region can be compared to ED results on the nearest-neighbour spin-1/2 triangular lattice [128], and we find a perfect match. In VMC for $0.475\pi < \alpha < 0.85\pi$ ($K > 0$, $K/J > 12.7$, and $K/J < -0.51$), the 120° -nematic or \mathcal{J} -nematic phase proposed by Bieri et al. is clearly dominant. Its energy is not matched by any of the states we considered. In the construction by Bieri et al., the on-site terms before the projection select states with directors in an "umbrella" configuration (see Eq. (16) in Ref. [63]), interpolating between a ferroquadrupolar and a 120° quadrupolar order. However, due to the $SU(3)$ symmetry of the model there are many other degenerate states, containing not only nematic states, but other states obtained by global $SU(3)$ rotations. Therefore, we find that a 120° LRO state is more suitable in this context. In

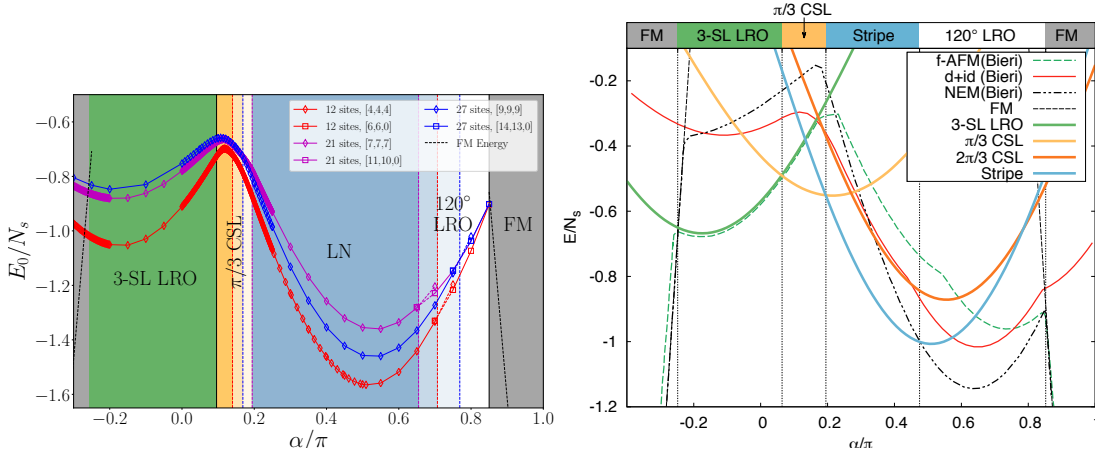


Fig. 6.3.: On the left: Ground-state energies from ED on clusters with $N_s = \{12, 21, 27\}$ sites for the $SU(3)$ J - K model. Different point shapes indicate different symmetry sectors. The singlet sector $[N_s/3, N_s/3, N_s/3]$ yields the ground states of the 3-SL LRO phase, CSL, and LN phase below $\alpha/\pi \approx 0.7$. For $0.7 \lesssim \alpha/\pi \lesssim 0.85$, the 120° colour order state, which contains only two colours from the sector $[N_s/2, N_s/2, 0]$, or $[(N_s + 1)/2, (N_s - 1)/2, 0]$, is present. In the FM phase for $\alpha/\pi \gtrsim 0.85$, where the energy per site is identical for all clusters, only a single colour occurs and the ground states lie in the symmetry sectors $[N_s, 0, 0]$. Wherever the phase boundaries are not the same for different lattice sites N_s , the colour of the boundary indicates the corresponding cluster size. On the right: Variational energies for the J - K model with real K of the most competitive states for the 144-site system compared to the results by Bieri et al. [63] (based on Fig. 3 of their paper). Both figures are published in Ref. [100].

the $SU(3)$ language, a 120° fully colour-ordered state is only built out of two colours, while the third colour is missing in the system. Interestingly, in this subspace the Hamiltonian of the J - K model is simplified since the nearest-neighbour exchange and the ring exchange terms are not independent. Namely, for three sites i , j , and k on a triangle, it is

$$\mathcal{P}_{ij} + \mathcal{P}_{jk} + \mathcal{P}_{ki} = \mathcal{P}_{ijk} + \mathcal{P}_{ijk}^{-1} + 1 \quad (6.1.7)$$

in the two-colour subspace, just as in the spin-1/2 case. As a result, at the special point $K = -J/2$, the Hamiltonian for the two-colour states is a constant, giving the same energy for any state in this subspace. This macroscopic degeneracy can also be seen in ED results, and the transition between the 120° LRO and the following ferromagnetic $SU(3)$ phases is found quite accurately at $\alpha_c = \arctan(-1/2) = 0.852\pi$ [$K > 0$, $(K/J)_c > -0.50$] in both ED and VMC. Note, that this value of α corresponds to ferromagnetic nearest-neighbour coupling, $J < 0$, therefore only considering antiferromagnetic J , the 120° LRO persists for $K \rightarrow \infty$. On the opposite end of the phase, the transition to the LN phase is strongly dependent on method and system size. This is probably linked to a not very accurate VMC Ansatz for the striped phase, as well as to the symmetries of different clusters.

The ferromagnetic phase is given as a simple product state and the exact energy is $E_{\text{FM}}/N_s = 3 \cos \alpha + 4 \sin \alpha$, as shown in Fig. 6.3. In VMC, the phase transition between the FM phase and the 3-SL LRO phase occurs at $\alpha_c = -0.248\pi$ [$K < 0$, $(K/J)_c = -0.988$]. The extension of the FM phase is similar in ED.

The phase diagram of the J - K model for purely real ring exchange, K , is surprisingly versatile. Besides magnetically ordered phases it hosts the $\pi/3$ -flux CSL phase, for which the modular matrices were used to determine the anyonic properties of the excitations with VMC in Ref. [100]. Next, we turn towards the question, if this spontaneously time-reversal symmetry breaking CSL is connected to the CSL at $\Phi = \pi/2$ [62].

6.1.2. Chiral phases at moderate values of K

We determine the phase diagram of the J - K model at small to moderate values of K/J for all fluxes, Φ . This allows the connection of the CSL discovered at $\Phi = \pi/2$ in Ref. [62] with the spontaneously time-reversal symmetry breaking CSL at $\Phi = \pi$ discussed in the last subsection. The phase diagram of this model is shown in Fig. 6.4 for $|K|/J \leq 0.5$ and complex phases of the three-site ring exchange $\Phi \in [0, \pi]$. It was determined by ED on the 21-site cluster, and from VMC on the 36-site cluster under the consideration of the same states mentioned before except for the striped state. The VMC was performed by Miklós Lajkó.

At small values $|K|/J$, the 3-SL LRO phase [170, 172] is present for all values of Φ depicted as a white area in Fig. 6.4. It dominates the phase diagram for ferromagnetic ring exchange with $\text{Re } K/J < 0$ as long as $|K|/J$ is not too strong. For the purely imaginary case, the phase transition to the $\pi/3$ -flux CSL phase (yellow area) emerges [62]. We find that this CSL remains stable for a wide range of phases, Φ , and extends to the purely real case at $\Phi = \pi$, for which the CSL was determined in the last subsection, and where time-reversal symmetry is spontaneously broken.

The logic we use to map out the phase diagram is best explained by following a

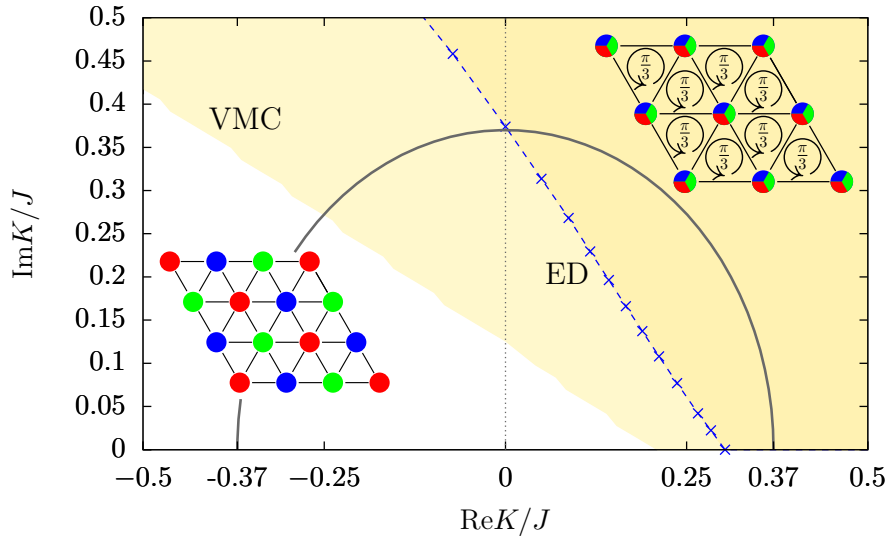


Fig. 6.4.: Phase diagram of the SU(3) J - K model including complex ring exchange, K . White phase: 3-SL LRO phase according to VMC on 36 sites. Yellow phase: CSL according to VMC (light and dark) and ED (dark). The blue crosses show the phase transition induced from the level crossing of the excited states in the 21-site cluster from ED. The grey semi-circle indicates the path of the energy spectrum shown in Fig. 6.5.

characteristic energy spectrum with constant $|K|/J = 0.37$ (grey semi-circle in Fig. 6.4). The evolution of the spectrum as a function of Φ is shown in Fig. 6.5 for ED (left) and VMC (right). In ED, for small fluxes a TOS is present signalling a long-range ordered phase [127, 143]. The TOS contains the ground state from the singlet sector (blue circles), and the first excited state (black circles) from the irrep $\mathbf{8}$. Since this signature is adiabatically connected to the Heisenberg point, $K = 0$, we identify this part of the phase diagram with the 3-SL LRO phase as in the previous subsection [143, 170, 172]. This ordered phase extends up to $\Phi \approx \pi/2$, where the spectrum exhibits a level crossing of the first excited state, such that the first excitation (red circles) lies in the singlet sector and is two-fold degenerate for larger values of $\pi/2 \lesssim \Phi < \pi$. As a consequence, a manifold of three low-lying states emerges consisting of the non-degenerate ground state (blue circles) and this two-fold degenerate first-excited state (red circles). On a torus, this is characteristic for a topologically ordered CSL when time-reversal symmetry is explicitly broken [52]. We therefore use the presence of these three low-energy states as the indicator for such a CSL in ED, as done amongst other signatures for $\Phi = \pi/2$ in Ref. [62]. Again, the fidelity of this identification depends on the energy splitting within the manifold compared to the energy gap to the other excited states, which is a consequence of the finite cluster size. On the 21-site cluster, the splitting of the manifold becomes smaller and the energy gap to higher excited states becomes larger with increasing values of $\Phi > \pi/2$ deeper in the CSL phase. A quantitative finite-size scaling cannot be performed since larger clusters were not studied with ED for general fluxes. Nevertheless, the comparison with the 12-site cluster, for which the spectrum is shown in Fig. 6.6, confirms our identification of the CSL: the splitting is larger and the gap smaller. Finally, close to the particularly important case $\Phi = \pi$, another set of three states drops down. This results into the six low-energy states at $\Phi = \pi$, the

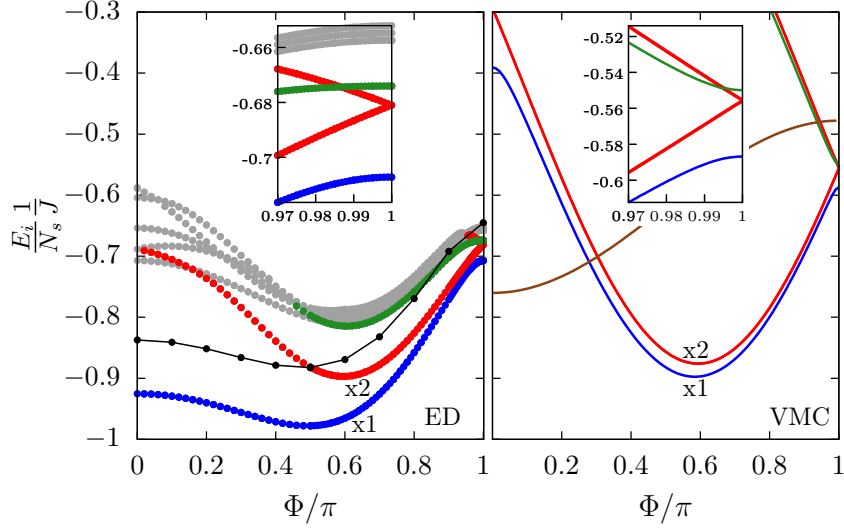


Fig. 6.5.: Energy spectrum of the $SU(3)$ J - K model as a function of Φ for fixed $|K|/J = 0.37$ on a 21-site cluster. Left panel: ED. The energies from the eight-dimensional irrep, $\mathbf{8}$, are shown in black. All other colours belong to the singlet sector, $\mathbf{1}$. Right panel: VMC. The 3-SL LRO state is shown in brown, all other states represent chiral states. The colours of the chiral states keep track of the degeneracies and symmetries. They are given explicitly in Tab. 6.2.

non-degenerate ground state (blue circles), a four-fold degenerate first-excited state (red circles), and a non-degenerate second-excited state (green circles).

These findings are fully confirmed by VMC, for which the energies along $|K|/J = 0.37$

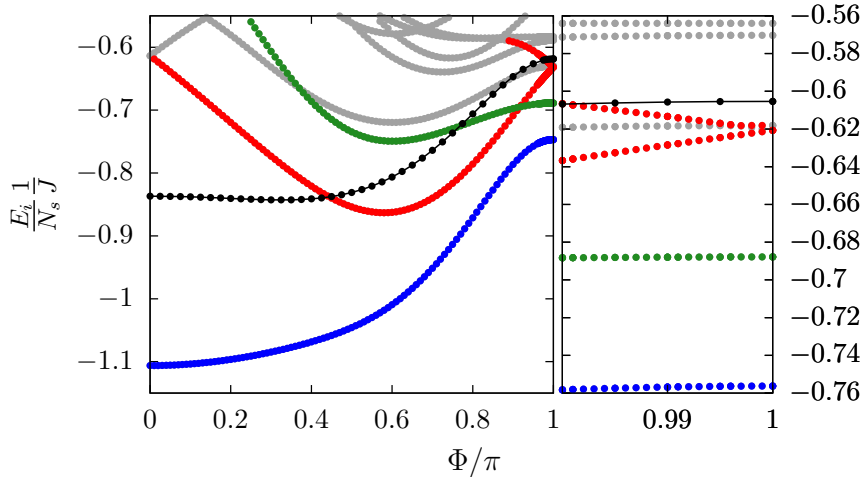


Fig. 6.6.: Energy spectrum of the $SU(3)$ J - K model as a function of Φ for fixed $\text{Re } K/J = 0.37$ from ED on a cluster with 12 sites and PBCs. The right panel shows a zoom on the area close to $\Phi = \pi$. The energies from the eight-dimensional irrep, $\mathbf{8}$, are illustrated in black, whereas all other colours belong to the singlet sector. The colours of the chiral states signify the same degeneracies and symmetries and are given explicitly in Tab. 6.1.

are shown in the right panel of Fig. 6.5. The same sequence of ground states, i.e. 3-SL LRO (brown line) for $0 \leq \Phi \lesssim 0.28\pi$ and a CSL (blue, red, and green lines) for larger values of the flux is found. We note that the critical phase $\Phi_c \approx 0.28\pi$ is smaller than in ED which is due to the fact that the 3-SL LRO state is captured less accurately within VMC. However, the low-energy states show the same degeneracies and symmetries in VMC and ED. The ground-state phase diagrams of ED and VMC therefore agree in all qualitative aspects for the J - K model.

6.2. Chiral phases in the Hubbard model

Next, we analyse the effective spin model on the triangular lattice in Eq. (4.2.5) for the specific case $N = 3$ with a flux $\Phi = \pi$. We comment on our results on the $\Phi = \pi/2$ case briefly at the end of the section. The presented content is published in Ref. [100] and the corresponding Appendix. Again, the VMC was done by Miklós Lajkó. The ED was performed by Clemens Ganahl and Andreas Läuchli, after preliminary work by the present author.

The phase diagram for $\Phi = \pi$ is given in Fig. 6.7. Within the Mott-insulating phase for strong couplings the same order of phases as in the J - K model occurs: the 3-SL LRO and the CSL with spontaneously broken time-reversal symmetry. Eventually for weakening coupling U/t , the insulating phase breaks down.

For small values of t/U , the couplings up to third order are dominant, hence the J - K model is well converged. The phase transition between the 3-SL LRO and the CSL occurs at $(K/J)_c \approx 0.31$, which translates to $(t/U)_c \approx 0.09$ [$(U/t)_c \approx 11$] in bare fifth-order. Interestingly, this critical value changes only slightly to $(t/U)_c \approx 0.1$ [$(U/t)_c \approx 10$] when applying Padé extrapolations to the couplings J and K . For both couplings several Padé extrapolants give essentially the same result in this t/U -regime so that the extrapolations work well for the most important interactions of the effective model (see inset in Fig. 4.4). The small difference between the critical ratios from bare series and extrapolation within the J - K model indicates that even the bare series is almost converged up to these t/U values for the couplings J and K . Note, that the complex phase of the ring exchange in the J - K model equals the flux through an elementary plaquette in the Hubbard model only in order three.

Since the impact of all the other smaller terms is not obvious a priori, we explicitly

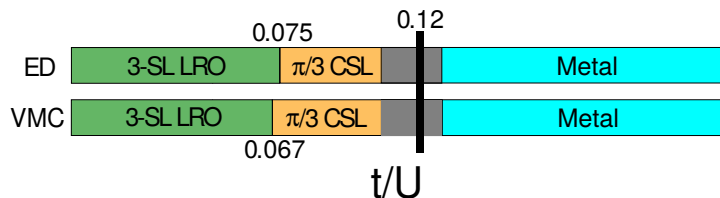


Fig. 6.7.: Phase diagram of the $SU(3)$ Hubbard model with $\Phi = \pi$ on the triangular lattice. In the Mott-insulating phase for small t/U the 3-SL LRO and $\pi/3$ -CSL are found by ED and VMC. The metal-insulator transition is estimated in Section 4.3 as $(t/U)_c^{\text{mi}} \approx 1/8.5 \approx 0.12$ (ED on 12 sites for the Hubbard model). The large uncertainty on this value and the nature of the Mott phase in that area is indicated by the grey area. This figure is published in Ref. [100].

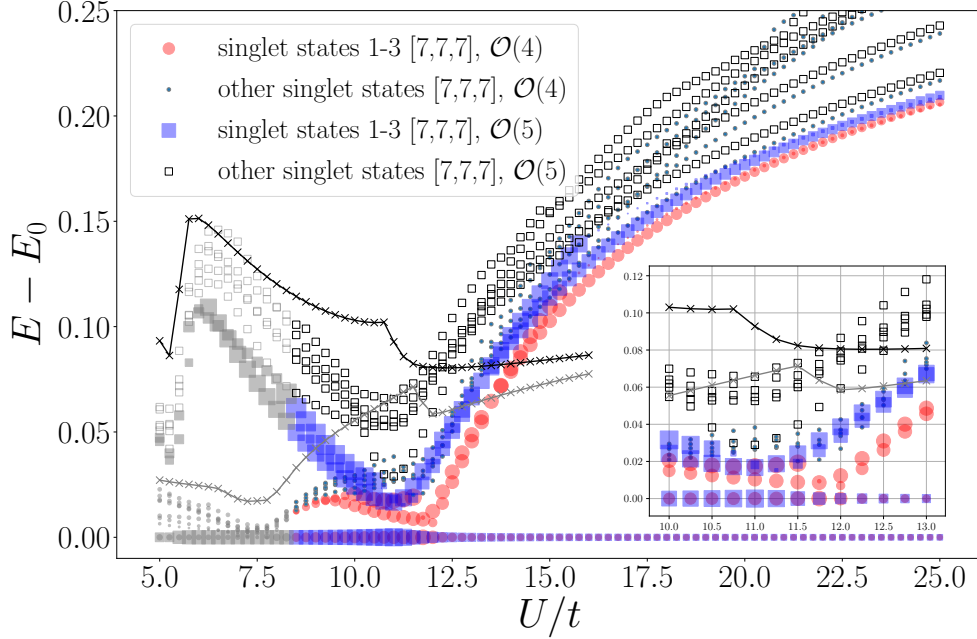


Fig. 6.8.: Spectrum of the fourth- and fifth-order effective model for $\Phi = \pi$ from ED on the 21-site cluster. The marker size corresponds to the overall chirality signal and is plotted for the lowest three states. Three low lying singlets with strong chirality signal indicate the presence of a CSL phase around $U/t \approx 12$. The grey regions of the spectra are not in the Mott-insulating phase of the Hubbard model and the effective models are not valid. The grey (black) solid line indicates the lowest energy eigenstate in the adjoint irrep $[8, 7, 6]$ of the fourth- (fifth-)order effective model. The inset is a zoom into the CSL region. This figure is published in Ref. [100].

study them with the set of Padé extrapolants discussed in Subsection 4.2.2 using ED and VMC. The low-energy spectra of the fourth- and fifth-order effective model for flux $\Phi = \pi$ on the 21-site cluster from ED are given in Fig. 6.8, where the point size for the lowest three singlets illustrates the chirality signal. For large values of U/t , the signature of a TOS is present, as expected for the 3-SL LRO phase. This is in agreement with the large structure factor and its extensive scaling at the K point, given in the upper panel of Fig. 6.9. In the fifth-order model, the TOS disappears at $(U/t)_c^{\text{ED}, \mathcal{O}(5)} \lesssim 13$ [$(t/U)_c^{\text{ED}, \mathcal{O}(5)} \gtrsim 0.075$], where three low-lying singlet levels occur with the same degeneracies one-four-one as in the CSL of the J - K model (compare left panel of Fig. 6.2). The direct correspondence between the states in the effective models is also clear from the symmetries discussed in Subsection 6.1.1. Therefore, the CSL is most plausibly present here as well. In the same parameter range $U/t \approx 13$, the chirality signal of the ground state increases, as can be seen in the bottom panel of Fig. 6.9, whereas the structure factor at the K point decreases. This behaviour agrees perfectly with the phase transition from the 3-SL LRO phase to the CSL. For values $(U/t)_c^{\text{ED}, \mathcal{O}(5)} \lesssim 11$ [or $(t/U)_c^{\text{ED}, \mathcal{O}(5)} \gtrsim 0.09$] another state drops down, and the signature of six low-lying states is lost. However, the chirality signal in the lowest states remains large.

Within the area of the potential CSL the manifold of six low-lying states is not very well separated from the excited states, but the indications are stronger on the 21-site

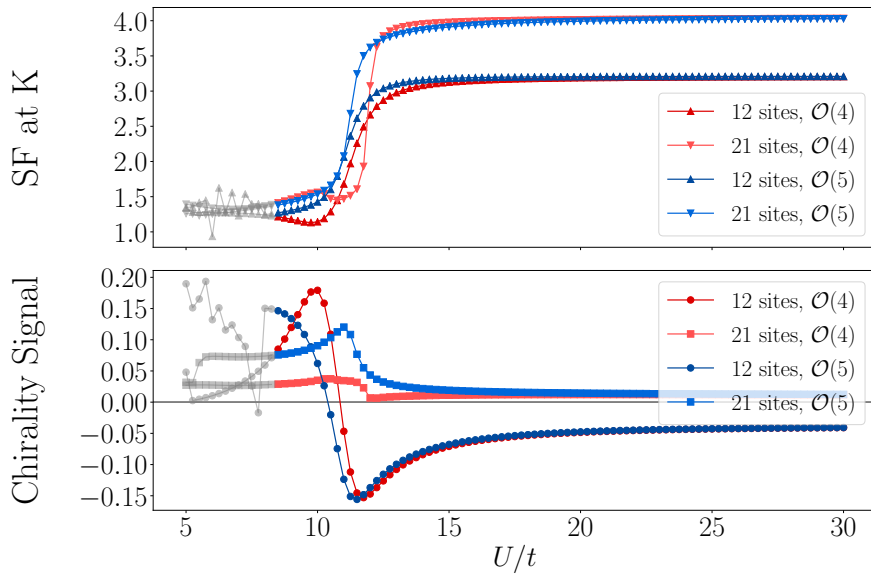


Fig. 6.9.: Structure factor at the K point (top) and chirality signal per lattice site (bottom) for the fourth- and fifth-order effective model for $\Phi = \pi$ from ED on the 21-site cluster. Coming from the 3-SL LRO phase at large ratios U/t , the structure factors at the ordering momentum K decrease as the chirality signals increase around $U/t \approx 12$. The grey regions of the structure factors and the chirality signals are not in the Mott-insulating phase of the Hubbard model and the effective models are not valid. This figure is published in Ref. [100].

cluster than on the 12-site one (not shown). Since ED including all exchanges is a lot more costly than for the J - K model, we did not study the 27-site cluster. However, with VMC on the 21-site cluster, we find the same phase transition from the 3-SL LRO to the $\pi/3$ -flux CSL at $(U/t)_c^{\text{VMC}, \mathcal{O}(5)} \approx 14.9$ [$(t/U)_c^{\text{VMC}, \mathcal{O}(5)} \approx 0.067$]. The CSL states behave very similar to the lowest eigenstates from ED regarding energy spectra and symmetries. All these findings strongly point to the realisation of a $\pi/3$ -flux CSL phase with spontaneous breaking of time-reversal symmetry.

The energy spectra of the fourth- and fifth-order model from ED in Fig. 6.8 behave fairly similar for $U/t \gtrsim 10$. For large ratios U/t the eigenenergies approach each other, as expected. With increasing perturbation (decreasing U/t) the differences increase. Nevertheless, the same manifolds of six low-lying states emerge. Also on the level of observables, the signature of the CSL is present in both models as shown in Fig. 6.9. So, even though the effective model is not quantitatively converged in the relevant area $11 \lesssim U/t \lesssim 13$, the signature of the CSL occurs in the third-, fourth-, and fifth-order model, which implies that it is a definite feature of the effective description of the $\text{SU}(3)$ Hubbard model in this U/t regime. For coupling ratios $U/t \lesssim 10$ the behaviour of the eigenstates is rather different in the fourth- and fifth-order model, so no statements about this parameter range can be made, apart from the fact that the Mott phase breaks down eventually.

The question is whether the potential CSL phase is within the Mott phase of the $\text{SU}(3)$ Hubbard model with flux $\Phi = \pi$. The metal-insulator transition from ED on the 12-site cluster at $(U/t)_c^{\text{mi}} \approx 8.5$ [$(t/U)_c^{\text{mi}} \approx 0.12$] occurs for weaker coupling strengths U than the phase transition towards the CSL. For the J - K model the estimated transition

point between 3-SL LRO and CSL is located at slightly larger values $(U/t)_c \approx 10$, and therefore lies within the crudely estimated extension of the Mott phase. The fifth-order effective model with the CSL below $(U/t) \lesssim 13$ includes a larger variety of quantum fluctuations and is therefore more reliable. We thus expect that the Mott phase of the $SU(3)$ π -flux Hubbard model on the triangular lattice realises, besides the 3-SL LRO phase, a spontaneous time-reversal symmetry broken CSL phase before the Mott insulating phase breaks down. The full phase diagram for the purely real Hubbard model is illustrated in Fig. 6.7.

The $\pi/3$ -flux CSL in the $SU(3)$ J - K model was first predicted for $\Phi = \pi/2$, hence for purely imaginary ring exchange [62]. In order to theoretically answer, whether this CSL is reachable in experiments with artificial gauge fields, one needs to determine if it is a feature of the Hubbard model. In Subsection 4.2.2, we studied the fifth-order effective model in Eq. (4.2.5) for $\Phi = \pi/2$ and found that the same set of Padé extrapolations as described for $\Phi = \pi$ works best. The numerical study of the full fifth-order effective model yields the signature of the CSL phase by three low-lying chiral states. Using ED on the 21-site cluster, we find $(t/U)_c^{\mathcal{O}(3),\text{ED}} \approx (t/U)_c^{\mathcal{O}(5),\text{ED}} \approx 0.09$ for the third- and fifth-order effective model. In VMC, the values are smaller, which is plausible since the VMC captures CSL phases more naturally than long-range ordered phases. The VMC method finds $(t/U)_c^{\mathcal{O}(3),\text{VMC}} \approx (t/U)_c^{\mathcal{O}(5),\text{VMC}} \approx 0.04$. The apparent areas in Fig. 4.7 and Fig. 4.8 are shaded in yellow. The metal-insulator transition was not determined for this case, and it remains open if the CSL occurs within the validity range of the effective model, and therefore in experiments.

Part II.

Plaquette phases in extended
Shastry-Sutherland models and
 $\text{SrCu}_2(\text{BO}_3)_2$

7. Introduction: The Shastry-Sutherland model and $\text{SrCu}_2(\text{BO}_3)_2$

The Shastry-Sutherland model was introduced by Shastry and Sutherland in 1981 as a highly frustrated quantum system. At that point, it was particularly outstanding because it is a two-dimensional model hosting an analytically exact product ground state [38]. Later, it also became famous for the realisation of a number of magnetisation plateaux under the application of magnetic fields [44–47]. An overview and further references in particular on these plateaux are given in Ref. [173]. The model describes spins-1/2 aligned on orthogonal dimers as depicted in Fig. 7.1. These dimers are connected by an effective square lattice, where the dimers give frustrating diagonal couplings on every second square-plaquette. The spins are coupled via Heisenberg interactions scaling with the coupling constant J on the dimers and J' between the dimers, both chosen antiferromagnetically ($J, J' \geq 0$). The Hamiltonian reads

$$H = J \sum_{\langle\langle i,j \rangle\rangle} \vec{S}_i \cdot \vec{S}_j + J' \sum_{\langle i,j \rangle} \vec{S}_i \cdot \vec{S}_j, \quad (7.0.1)$$

where the first sum runs over all diagonal dimer bonds and the second sum over inter-dimer bonds aligned on the square lattice. Since the Hamiltonian consists of Heisenberg interactions, it is symmetric under $\text{SU}(2)$ spin-rotations, so the total spin, s , is conserved. Further, the magnetisation is conserved and we choose the z -direction, s_z , as the good quantum number. The lattice symmetries are given by translations \mathcal{T} along the lattice vectors shown in Fig. 7.1, as well as by rotations \mathcal{C} and reflections \mathcal{R} . The rotational symmetry of the lattice is four-fold \mathcal{C}_4 for all turns around center points of plaquettes without internal diagonal bonds. The reflection symmetries \mathcal{R}_1 and \mathcal{R}_2 give reflections over the perpendicular diagonals.

This model can also be seen as the effective low-energy theory of the Mott-insulating phase of the Hubbard model given in Eq. (1.0.1) [67]. On the Shastry-Sutherland lattice, hopping between different dimers scaling with the amplitude $-t_1$ and on dimers scaling with the amplitude $-t_2$ is included. The model is exactly solvable in the tight-binding limit and the band structure consists of four-bands of which the extrema of two are touching with a quadratic behaviour. At half filling, this leads to a semi-metallic behaviour, so without Hubbard interaction the system is not an insulator. However, under the inclusion of the repulsive interaction U eventually the metal-insulator transition occurs and a Mott-insulating phase is present. From the strong-coupling limit, the couplings in the Shastry-Sutherland model (7.0.1) are dominant and behave like $J'/J = (t_1/t_2)^2$ [67, 174].

The underlying property of the Shastry-Sutherland model (7.0.1) is that the product state of singlets on all dimers is an exact eigenstate also for non-vanishing inter-dimer interactions [38]. This can be understood if one rewrites the inter-dimer parts of the

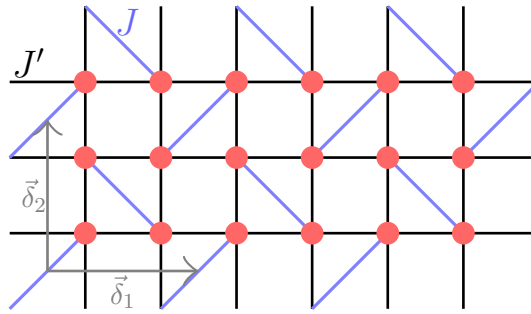


Fig. 7.1.: The Shastry-Sutherland lattice is given by a square lattice of nearest-neighbour bonds, J' , which are illustrated in black. Every second plaquette contains an orthogonal diagonal coupling, J , shown in blue. The spins are located on the vertices, given as red circles. The lattice vectors are $\vec{\delta}_1$ and $\vec{\delta}_2$.

Hamiltonian such that spin operators of one dimer only appear in sums. Let the operators \vec{S}_2 and \vec{S}_3 act on the two spins of a single dimer, then the inter-dimer exchange with some spin operator \vec{S}_1 of a neighbouring dimer can be written as $\vec{S}_1 \cdot (\vec{S}_2 + \vec{S}_3)$. If the dimer is in a singlet state the sum vanishes, and therefore the inter-dimer interactions do not contribute. The model effectively reduces to decoupled dimers and the product state of dimer singlets has the exact eigenenergy per spin $\epsilon = -3J/8$. Clearly, for vanishing inter-dimer couplings $J' = 0$ this is the ground-state energy. Shastry and Sutherland proved by variational arguments and a reformulation of the Hamiltonian in terms of triangles, that the dimer singlet product state remains the exact ground state for inter-dimer coupling values of at least $J'/J < 1/2$. More detailed explanations of the proof are given in Refs. [67, 175]. We use very similar arguments in Chapter 11. The dimer singlet product state is unique and can be interpreted as a vacuum. The excitations in the limit of decoupled dimer singlets are triplets, and are transformed into triplons under the inclusion of inter-dimer contributions, which do not vanish in this case and remain degenerate.

In the limit of vanishing dimer couplings $J = 0$, the model reduces to antiferromagnetically coupled spins on a square lattice yielding a quantum analogon of the classical Néel state, which is gapless and magnetically ordered [4]. The intermediate parameter regime has been a subject to discussions for nearly four decades and many proposals on the existence and the potential nature of intermediate phases have been made. The first prediction in favour of an intermediate phase suggested a helical state [69]. Next, evidence supporting a plaquette singlet phase, with dressed singlets located on one set of plaquettes without internal diagonal dimer bonds, which we call the EPP, was given [70, 71]. Further, a columnar-dimer ordered phase was suggested [72]. Another candidate phase is characterised by dressed singlets on filled four-site plaquettes, i.e. plaquettes including an internal diagonal dimer bond. This phase is referred to as FPP and was found in Ref. [73], where no distinction between both plaquette phases was made. Unlike the exact dimer singlet phase, both plaquette phases are generally not exact product states, but are entangled via quantum fluctuations, which is why the local states on the plaquettes are dressed singlets. These states, are mainly set up by singlets, but also have other contributions. Both plaquette phases are adiabatically

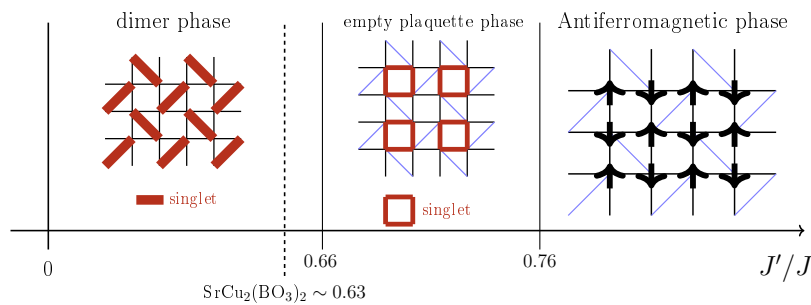


Fig. 7.2.: Phase diagram of the Shastry-Sutherland model. The phase transition points are taken from Ref. [74].

connected to pure product states in the limits of decoupled plaquettes.

In 2013, the application of iPEPS was able to clarify this issue convincingly. The comparison of the energies of differently biased states led to the conclusion, that there is a single intermediate phase for coupling ratios $0.675(2) < J'/J < 0.765(15)$, which is given by the EPP [74]. It is invariant under translations, \mathcal{C}_4 rotations, and the $\text{SU}(2)$ spin rotation. The reflection symmetries \mathcal{R}_1 and \mathcal{R}_2 along the diagonals are spontaneously broken [74, 176]. The low-energy excitation is given by a plaquette triplon, very similar to the dimer singlet phase and the energy gap was studied by perturbation theory in Ref. [70]. The full phase diagram of the Shastry-Sutherland model is given in Fig. 7.2.

Certain aspects of this phase diagram are still under debate, like the nature of the phase transition between the EPP and the Néel phase. It is either of weak first order, which it should be following Landau, since the Néel phase breaks the continuous $\text{SU}(2)$ symmetry, while the EPP breaks translational symmetry, or potentially a deconfined quantum critical point [177]. Also, the existence of an additional phase transition within the intermediate phase between two types of plaquette phases was suggested from ED [178]. Another topic relevant for the present thesis is the spin-lattice coupling for the plaquette phases. This was studied in Ref. [177], where distinct lattice distortions for the EPP and FPP were found. In both phases, these are given by strengthened couplings on the plaquettes hosting dressed singlets. So, the understanding of the Shastry-Sutherland model remains a very active field of theoretical physics on strongly-correlated systems [179–181].

When Shastry and Sutherland first invented the model, it was not at all expected to yield an accurate description for a solid state material. It was a great surprise in 1999, when the compound Strontium-Copper-Borat, $\text{SrCu}_2(\text{BO}_3)_2$, which was first synthesised in 1991 [183], was discovered to be very well described by the Shastry-Sutherland model in the low-temperature regime [44, 68]. A review on the description of $\text{SrCu}_2(\text{BO}_3)_2$ by the Shastry-Sutherland model is given in Ref. [184]. A first point of agreement was found by measurements of the magnetic susceptibility indicating a finite energy gap of $\Delta \approx 30$ K [68]. Following experiments extracted slightly larger values, like $\Delta \approx 34$ K [185], or $\Delta \approx 34.4$ K [186]. Nuclear quadrupole resonance allowed to identify a dimer singlet ground state [68]. These findings fit the Shastry-Sutherland model at strong dimer couplings J/J' . Furthermore, under the application of a magnetic field several magnetisation plateaux were found and match theoretical prediction for the

Shastry-Sutherland model [44,47,68,187–190]. The first excitation in $\text{SrCu}_2(\text{BO}_3)_2$ was measured to be nearly dispersionless by INS, which was explained using series expansions for the Shastry-Sutherland model in the dimer singlet phase, where the frustration leads to a suppressed hopping of the triplons [191,192].

In the following, the main structural properties of $\text{SrCu}_2(\text{BO}_3)_2$ are stated. The compound consists of quasi two-dimensional magnetic layers of CuBO_3 , which are nearly completely decoupled by intermediate non-magnetic Strontium layers [183]. The layers are slightly buckled [193] and the axis normal to the layers is given by the crystallographic direction [001] [183]. In the magnetic layers, the Cu^{2+} -ions possess spins $s = 1/2$. These yield the only magnetic moments in the material and are aligned on orthogonal dimers in the crystallographic directions [110] and $[-110]$. A projection onto one magnetic layer is depicted in Fig. 7.3. In alternating magnetic layers, the dimers are turned by $\pi/2$ and lie on top of each other [39]. At room temperature, the lattice constant within the planes is $a = b = 8.995\text{\AA}$ and $c = 6.649\text{\AA}$ between the planes [183], the distance between two Cu-ions on the same dimer is 2.905\AA and on neighbouring dimers 5.132\AA [68]. There is no structural phase transition for temperatures below room temperature, however some structural changes appear, which are most likely due to spin-lattice coupling [194]. Structural distortions under pressure are discussed in the following Section 7.1 and Chapter 10.

The intra-dimer nearest-neighbour exchange J occurs via two oxygen atoms as a super exchange. In contrast, the Cu^{2+} -ions from different dimers interact via BO_3 groups determining the inter-dimer exchange J' . Apart from these two large couplings, a range of weaker exchanges of the order of a few percent of J was found by ab initio calculations [195]. Some of these are symmetric, like a small inter-layer exchange J'' , which leaves the dimer singlet state exact [39], whereas some are antisymmetric and therefore disturb the exact ground state in the sense that some triplet contributions are included. These antisymmetric couplings are mainly given by intra-dimer Dzyaloshinski-Moriya interactions of the form $\vec{S}_i \times \vec{S}_j$, where the components scale with exchange amplitudes

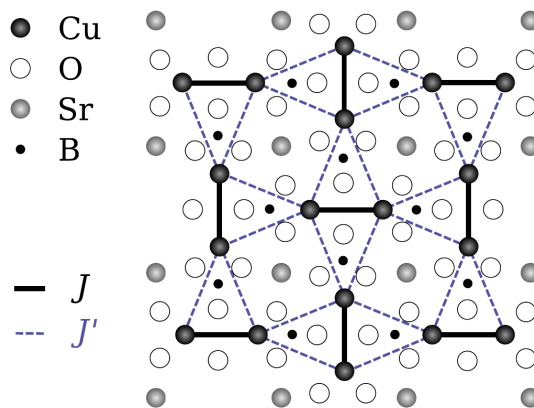


Fig. 7.3.: Projection of $\text{SrCu}_2(\text{BO}_3)_2$ into the $[\bar{1}10]$, $[110]$ plane from Ref. [182]. The CuBO_3 and Sr atoms lie in different planes in the material. The Cu sites provide the spin-1/2 degrees of freedom and are arranged as in the Shastry-Sutherland model. In contrast to Fig. 7.1, the nearest-neighbour interactions are coloured blue here.

of $\approx 3\%J$ [195]. Various coupling constants were extracted. For instance, Miyahara and Ueda suggested $J = 84$ K, $J' = 54$ K, and $J'' = 8$ K [184], corresponding to the relevant ratio $J'/J = 0.635$. They did not take any Dzyaloshinski-Moriya interactions into account. At the same time, Knetter et al. found $J \approx 71$ K, $J' \approx 43$ K, and $J'' \approx 15$ K for the Shastry-Sutherland model, so $J'/J = 0.603(3)$ [196]. More recent estimates are comparable [76, 77, 188], as discussed in the next section, where we also consider the behaviour under the application of pressure.

7.1. $\text{SrCu}_2(\text{BO}_3)_2$ under hydrostatic pressure

In the last two decades, a range of experiments on $\text{SrCu}_2(\text{BO}_3)_2$ under high pressure was performed. The hydrostatic pressure changes the location of the atoms by an overall decreasing lattice constant [197], and therefore the intermediate exchange integrals. The Cu-ions on the dimers are connected via oxygen atoms about an angle of $\approx 0.98^\circ$ [183]. If the lattice constant is decreased only slightly, the relative reduction of the angle is large, which triggers a large decrease of the exchange integrals, J [77]. The nearest-neighbour couplings, J' , on the other hand arise from a more standard geometry and decrease much less. Therefore, the inter-dimer interactions become stronger in respect to the intra-dimer couplings, also confirmed by density functional theory [198]. In terms of the Shastry-Sutherland model this means an increase of the ratio J'/J , which eventually leads to a phase transition from the dimer singlet to the EPP. A structural phase transition was found by X-ray measurements depending on the temperature between pressures 4 – 5 GPa [197, 199]. This is well above the magnetic phase transition discovered by nuclear magnetic resonance (NMR) [75], inelastic neutron scattering (INS) [76], electron spin resonance (ESR) [77], specific heat measurements [78], and most recently, Raman spectroscopy of the pantograph mode [80]. In this section, we sketch the experimental techniques and give an overview about the apparent findings.

In NMR, a material is exposed to a strong static magnetic field in which the nuclei magnetic spins align. In the second step, a weak oscillating magnetic field is applied that triggers a response of the nuclei spins. These electromagnetic waves can be measured and allow to determine the magnetic field at the nucleus. A fundamental request for such experiments is the occurrence of a nucleus with an odd number of protons and/or neutrons, which provides a non-zero nuclear spin. Reviews are given in Refs. [200, 201].

In 2007, Waki et al. performed NMR on $\text{SrCu}_2(\text{BO}_3)_2$ under pressure [75]. At that time the question on the intermediate phase of the Shastry-Sutherland model was not yet resolved theoretically. The Bor ^{11}B nuclei within $\text{SrCu}_2(\text{BO}_3)_2$ were studied at a magnetic field of 7.006 T and pressures up to 2.4 GPa (24 kBar). Under the application of these conditions, a magnetic phase transition was found at a temperature of 3.6 K [75]. The data suggests that the low-temperature phase has a unit cell, which is twice as large as for the dimer singlet phase. Differently orientated dimers have different magnetisations. One set of these dimers is nearly in a singlet state, whereas the other one has a finite magnetisation, which means that it is rather triplet-like. The magnetic hyperfine shift data also indicates that this remain true in the limit $T \rightarrow 0$ K. Furthermore, if a weak structural deformation around the phase transition occurs, it is weak. Still the four-fold rotational symmetry \mathcal{C}_4 gets lost, caused by the magnetic structure of the new phase, whereas the reflection symmetries \mathcal{R}_1 and \mathcal{R}_2 are preserved. The overall

ground state of the new phase is estimated to have no finite magnetic moment at zero magnetic field, such that it is expected to be a singlet. From these findings Waki et al. do not draw any further conclusions on the precise nature of the low-temperature phase. However, they specify the following features: a singlet ground state, a unit cell of two dimers, one dimer is a singlet and one dimer is a triplet, and a loss of the \mathcal{C}_4 . Nearly all of these findings are directly relevant for the case of a vanishing magnetic field.

A review on INS in the field of frustrated magnetism is given in Ref. [202]. As the name suggests, in INS experiments neutrons are scattered by a material sample. In contrast to many other experimental setups, INS allows to examine the microscopic properties. Neutrons do not carry any charge and therefore propagate well inside the probed structure, the mean free path is in the order of millimetres, which is why such neutrons enter the bulk before they scatter. The technique is very well suited to study the magnetic properties of the sample, since neutrons carry a spin-1/2. If a neutron and a spin in the material interact and flip, the neutron changes by $\Delta s_z = 1$. Therefore, if the interacting spin is in a singlet ground state with total spin zero and $s_z = 0$ only triplet excitations with total spin one and $s_z = \pm 1$ can occur. Singlet excitations are not observed. In order to probe magnetic excitations in solid state materials, thermal neutrons with an energy of a few meV are used, which is comparable to the energy of the excitations. Then, the neutron-material interactions lead to a transfer of energy and momentum, which gets extracted from the scattered neutrons by the dynamic structure factor, $S(Q, E = \hbar\omega)$, where Q gives the momentum and $E = \hbar\omega$ the energy transfer. At temperatures close to $T = 0$ K, it reflects the excitation energies from the ground state at specific momenta. The intensities of these excitations are directly linked to the number of neutrons with specific energy and momentum per time. A downside of INS measurements are the high requirements. The neutrons are mainly taken from research reactors, which are expensive to run and maintain, and therefore, beam time is rare.

Nevertheless, INS on a single crystal of $\text{SrCu}_2(\text{BO}_3)_2$ under high-pressure was performed by Zayed et al. and published in 2017 [76]. For further details see the thesis of the first author from 2010 [203]. The experiments were done at various facilities for different pressures. The most interesting pressure values, where the results indicate a new phase, were applied in Grenoble during summer time, and unfortunately a black-out led to the termination of the experiment and the dispersion could only be measured for a few momentum values. Still, the observations provide important information on the new phase of $\text{SrCu}_2(\text{BO}_3)_2$ and are summarised in the following.

At low-temperatures of 0.5 K and pressures between 0 kBar and 16 kBar, the excitations behave as expected for the dimer singlet phase. The lowest band is nearly dispersionless and relates to the triplon [191, 192]. The energetically higher two-triplon bound state is also present in the whole range, and both excitation energies decrease with increasing pressure, due to weakening exchange amplitudes [76, 196, 204]. Between 16 kBar and 21.5 kBar a new low-energy excitation arises, such that the excitations exhibit a discontinuity, which corresponds to a first-order phase transition. For the new high-pressure phase the dispersion was measured at 21.5 kBar for a few points along the direction $(H, 0, 1)$ in terms of reciprocal lattice vectors, or $(k_x, k_y = 0, k_z = 2\pi)$ in momentum space, which is defined for the crystal vectors illustrated in Fig. 7.1. We note that the determination of the exact high-pressure values in INS experiments is

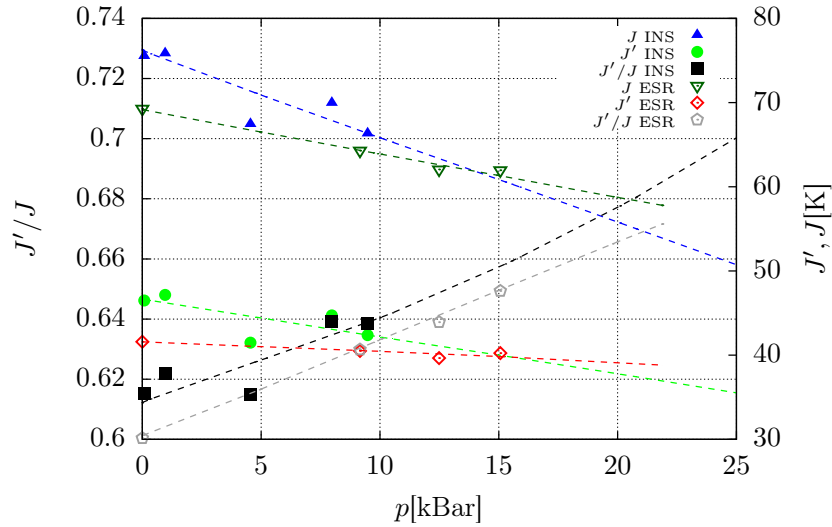


Fig. 7.4.: Estimated coupling constants for the description of $\text{SrCu}_2(\text{BO}_3)_2$ under pressure by the Shastry-Sutherland model from INS and ED [76] and from ESR and ED [77]. In the latter study Dzyaloshinski-Moriya interactions were taken into account. The dashed lines correspond to fits.

extremely difficult. The new low-energy excitation has a minimum at $H = 1$, $k_x = 2\pi$, with a large intensity. The mode shows a dispersion of ≈ 0.4 meV, wherein all measured points at other momenta have comparable values and smaller intensities, in particular close to $k_x = 4\pi$ the intensities are very small. For the intensities a non-periodic behaviour is plausible. The excitation energies however should follow a period of 2π , which is not the case if one compares the values of the low-energy excitation at $H = 1$ and $H = 2$. This is an indication for the poor quality of the data. Overall, for the low-lying excitation only the point at $H = 1$ with a high intensity is fully reliable. The mode above is nearly flat, similar to the triplet mode of the dimer singlet phase, at energies between 1.8 and 2 meV, peaking around $H = 1.5$. The intensities show intermediate values compared to the other mode.

In the same study, also the magnetic susceptibility was measured up to moderate pressures of $p \approx 10$ kBar and then fitted to ED calculations for the Shastry-Sutherland model on a 20-site cluster with PBCs. From this the coupling constants are estimated to be $0.66 < (J'/J)_c < 0.68$ at the phase transition. The couplings over the whole range have been replotted in Fig. 7.4.

The high-pressure data is interpreted by a calculation of the dynamic structure factor on a single four-spin plaquette with and without an internal diagonal bond, in the sense that this is the simplest approximation for the EPP and FPP. In both cases, one of the excitations has a large intensity somewhere close to $(H = 1, 0)$ similar to the measurement. The structure factors for the second excitation of both plaquettes differ. For the filled plaquette the same pattern as for a dimer triplet is recovered. It gets associated with the higher excitation, since it energetically continues the triplet of the dimer singlet phase and is similarly dispersionless. Furthermore, a comparison with the excitations of the FPP from series expansions by Koga et al. is done [73].

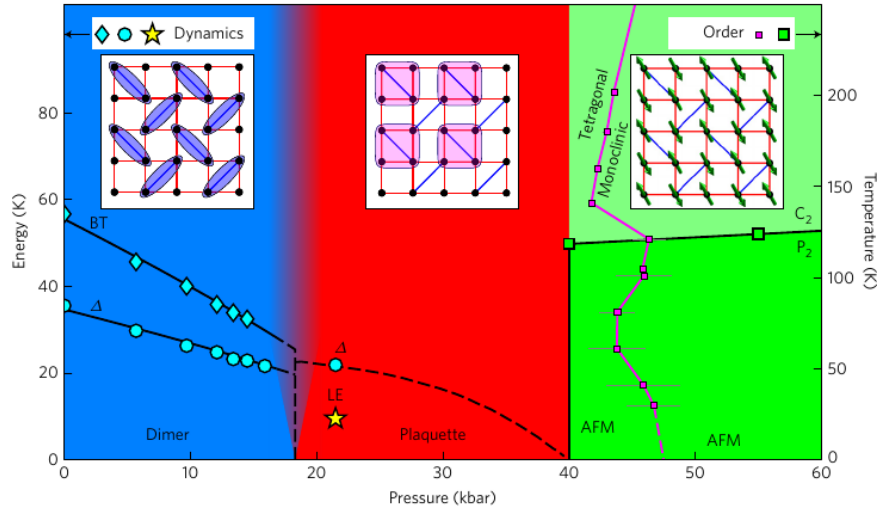


Fig. 7.5.: Phase diagram of $\text{SrCu}_2(\text{BO}_3)_2$ under pressure with excitation energies. These are given by points for triplets, diamonds for the according two-triplet bound state, a star for the new low-energy excitation, and squares for magnetic Bragg-peaks from Ref. [76]. The background colour indicates the extracted phases: dimer singlet, FPP, and AFM, which we refer to as Néel phase.

However, in this article only the gap energies are stated without noting the momentum, and the excitations were calculated for the symmetric Shastry-Sutherland model, where the FPP does not yield the ground state.

The full phase diagram from Ref. [76] including the measured low excitation energies is given in Fig. 7.5. It also includes the phase transition from the FPP to the Néel phase at $\approx 40\text{kBar}$. The connection to the NMR results gets drawn such, that the magnetic field would be sufficient to close the gap and therefore lead to condensed triplets within the magnetic ground state. As we see in the following section, only one of two low-energy triplets on the filled plaquette has a triplet on the diagonal dimer and fits this explanation.

The ESR experiments are in principle similar to NMR. A sample in a constant magnetic field is hit by microwaves, and the resonating signal is measured and interpreted. The main difference is that instead of exciting the nuclei spins the electronic spins are studied, and a requirement for the application is that the material possesses unpaired electrons. Some details on the application of ESR on $\text{SrCu}_2(\text{BO}_3)_2$ are given in Ref. [184].

The first ESR measurements on $\text{SrCu}_2(\text{BO}_3)_2$ for pressures up to 12 kBar were done in Ref. [205], where the decreasing triplet excitation energy of the dimer singlet phase was observed. In 2015, this was increased up to pressure values of 1.51 GPa [206]. Recently, new data from high-pressure ESR on a single crystal of $\text{SrCu}_2(\text{BO}_3)_2$ was published [77]. For pressure values up to 2.1 GPa, a low-lying triplet was observed with a clear first-order phase transition at 1.85 ± 0.05 GPa indicated again by a discontinuity in the excitation energy. Additionally, a two-triplon bound state and another excitation were observed. The excitation energies plotted against pressure were used together with ED of the Shastry-Sutherland model including Dzyaloshinski-Moriya in-

interactions on a 20-site cluster with PBCs to determine the pressure dependence of the coupling constants. These are plotted together with the values from magnetic susceptibility [76] in Fig. 7.4. Profiting from this relation, the phase transition point relates to $(J'/J)_c = 0.660 \pm 0.003$ in the Shastry-Sutherland model. In contrast to the INS measurements at 21.5 kBar [76], the ESR did not observe the second low-energy excitation above 1.85 GPa. This might be linked to some selection rules or to too high temperatures. The lowest excitation was proven to be a triplet by Zeeman splitting [77]. Again, the series expansions by Takushima et al. are used to draw the conclusion of a plaquette phase at pressures above 1.85 ± 0.05 GPa. In order to explain the different phase transition points found for $\text{SrCu}_2(\text{BO}_3)_2$ under pressure and the Shastry-Sutherland model, it is suggested, that the dimer bonds might be not identical in the material under pressure. A first qualitative phase diagram for this scenario was calculated in Ref. [176]. We improve these findings in Section 10.1.1.

Recently, experimental investigations were done by heat capacity measurements [78]. The heat capacities for several single crystals of $\text{SrCu}_2(\text{BO}_3)_2$ for temperature ranges $0.4 \text{ K} \leq T \leq 294 \text{ K}$ and pressures $0 \leq 4.9 \text{ GPa}$ were measured. For all pressures, where the Shastry-Sutherland model is relevant, the heat capacity with decreasing temperatures shows a broad maximum, called a hump. It occurs due to newly arising correlations leading to a decreasing entropy, and was previously found to signal the dimer singlet phase [207]. For pressures between $p \approx 1.7 \text{ GPa}$ and $p = 2.4 \text{ GPa}$ and at temperatures $T \lesssim 2 \text{ K}$, a second smaller peak emerges and is interpreted as the phase transition towards a plaquette singlet phase. If it corresponds to the EPP or FPP, can not be clarified directly from these measurements. Also, the parameter region at larger pressures $2.4 \text{ GPa} < p < 3.1 \text{ GPa}$ and smaller temperatures $T \lesssim 1 \text{ K}$ could not be resolved. The data was used to map out an extended phase diagram of $\text{SrCu}_2(\text{BO}_3)_2$ in pressure and temperature. Furthermore, the energies of the excitation gap were de-

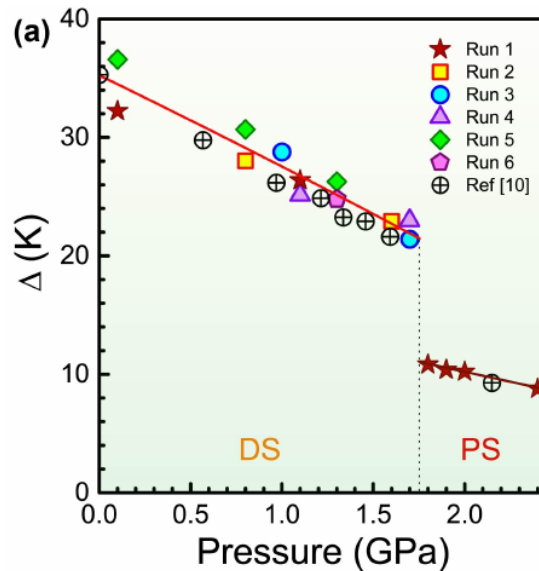


Fig. 7.6.: Excitation energies from fits of the low-temperature specific heat measurements from Ref. [78]. The points marked by [10] in the key are from INS in Ref. [76].

rived by fitting the heat capacity. This is shown in Fig. 7.6, where also the data point from INS [76] is included and matches well. We investigate the gap in Section 10.4, theoretically. Modeling the heat capacity of $\text{SrCu}_2(\text{BO}_3)_2$ by the Shastry-Sutherland model using ED yields phase transition points $J'/J \approx 0.665$ for the dimer to plaquette transition and $J'/J \approx 0.69 - 0.71$ for the transition to the Néel phase [78]. The first value is similar to other estimates, compare Fig. 7.4 [76, 77], and also close to the phase transition in the Shastry-Sutherland model, see Fig. 7.2 [74]. The second value however is smaller than the transition point in the Shastry-Sutherland model.

New results on the phase transition towards the high-pressure phase were detected by Raman scattering and an analysis of the pantograph mode [80]. This mode is directly linked to the dimer spin correlations. With increasing pressure at $p \approx 22$ kBar the correlations switch from antiferromagnetic to ferromagnetic, which fits a phase transition from the dimer singlet to a plaquette singlet phase. There are no indications for structural transitions in this data.

Most of the experiments point towards the existence of the FPP at intermediate to high pressure in $\text{SrCu}_2(\text{BO}_3)_2$. This phase however does not occur in the Shastry-Sutherland model and the question arises, whether the new phase is indeed not the FPP but the EPP, or if the Shastry-Sutherland model is distorted in some way, or if some additional interactions become relevant. Therefore, we introduce extended Shastry-Sutherland models and discuss according former theoretical findings in Section 7.3. Before, some details on the fundamental building blocks of relevant singlet phases, dimers and plaquettes, are given in the next section.

7.2. 4-spin-1/2 plaquettes

The EPP and FPP are adiabatically connected to product states of singlets on individual 4-site plaquettes, yielding the fundamental units of these phases. Therefore, we study various decoupled plaquettes in this section.

We start the discussion with the simplest case of a single empty plaquette (ep) depicted in Fig. 7.7(a). This plaquette p consists of four spins-1/2 interacting via four

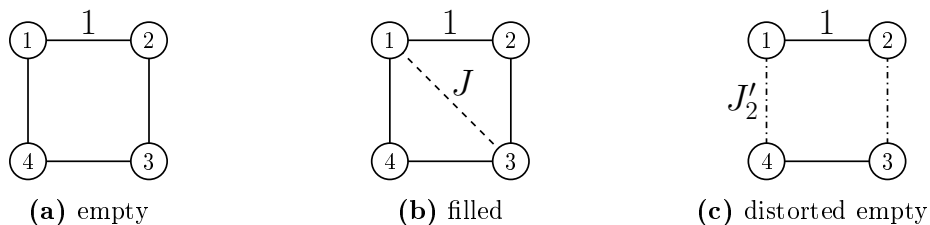


Fig. 7.7.: Single decoupled plaquettes normalised on nearest-neighbour couplings (solid). In (a) a symmetric empty plaquette without an intra-plaquette diagonal bond is shown. The filled plaquette including a diagonal interaction with coupling strength J (dashed) is illustrated in (b). In (c) a distorted version of an empty plaquette is shown, where neighbouring bonds have distinct coupling constants, and opposing bonds have identical coupling constants set to one (solid) and J_2 (dashed-dotted).

nearest-neighbour Heisenberg interactions

$$\begin{aligned} H^{\text{ep}} &= \vec{S}_{p,1} \cdot \vec{S}_{p,2} + \vec{S}_{p,2} \cdot \vec{S}_{p,3} + \vec{S}_{p,3} \cdot \vec{S}_{p,4} + \vec{S}_{p,4} \cdot \vec{S}_{p,1} \\ &= (\vec{S}_{p,1} + \vec{S}_{p,3}) \cdot (\vec{S}_{p,2} + \vec{S}_{p,4}) . \end{aligned} \quad (7.2.1)$$

For simplicity, here, all couplings are set to one. The straightforward basis is given by the product states of the spins on all sites, which can either be up $|s_z = \frac{1}{2}\rangle = |\uparrow\rangle$ or down $|s_z = -\frac{1}{2}\rangle = |\downarrow\rangle$. It contains $2^4 = 16$ states.

The total spin $(\vec{S}_{p,1} + \vec{S}_{p,2} + \vec{S}_{p,3} + \vec{S}_{p,4})^2$ together with the z -component of the spin $(S_{p,1}^z + S_{p,2}^z + S_{p,3}^z + S_{p,4}^z)$ give a full set of good quantum numbers $s^p \in \{0, 1, 2\}$ and $s_z \in \{-2, -1, \dots, 2\}$ for a plaquette p , respectively. Additionally, the operator $(\vec{S}_{p,1} + \vec{S}_{p,3})^2$ gives a good quantum number of the form $s_v^p(s_v^p + 1)$, which take the values $s_v^p \in \{0, 1\}$. Analogously, $(\vec{S}_{p,2} + \vec{S}_{p,4})^2$ gives $s_h^p \in \{0, 1\}$. These quantities can be insightful for understanding the nature of the eigenstates. The spatial symmetries of the problem yield good quantum numbers as well. The rotation \mathcal{R}_π around the center point by π gives the eigenvalues r_π . For the rotation around $\pi/2$ one needs to add up the rotations around both directions, $\pi/2$ and $-\pi/2$, in order to get a Hermitian operator $\mathcal{R}_{\pm\pi/2} = (\mathcal{R}_{\pi/2} + \mathcal{R}_{-\pi/2})/2$. The associated eigenvalues are $r_{\pm\pi/2}$. Also, the reflections over both diagonals ($1 \leftrightarrow 3, 2 \leftrightarrow 4$) and the centres between both sides ($1 \leftrightarrow 3, 2 \leftrightarrow 4$) give conserved quantities. The energy spectrum is summarised in Tab. 7.1 with $J = 0$. It consists of a singlet ground state with eigenenergy $E_0^{s^p=0, s_v^p=1} = -2$, a triplet with energy $E_1^{s^p=1, s_h^p=1} = -1$, a singlet $E_2^{s^p=0, s_v^p=0}$ and two triplets at $E_2^{s^p=1, s_h^p=1, s_v^p=0} = E_2^{s^p=1, s_h^p=0, s_v^p=1} = 0$, and a quintuplet with energy

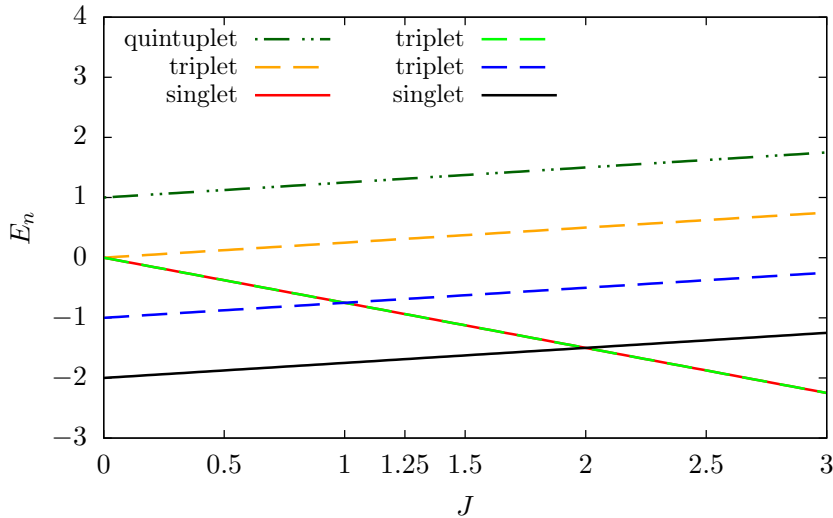


Fig. 7.8.: Energy spectrum of a single filled plaquette, p , [Fig. 7.7(b)]. For $J = 0$, the system reduces to an empty plaquette [Fig. 7.7(a)] and the ground state has a triplet on both diagonals $s_h^p = s_v^p = 1$. At infinite diagonal coupling $J \rightarrow \infty$ the ground state has a singlet on the J -bond, $s_v^p = 0$, and the spins on sites 2 and 4 are free.

| states | E_n | s_z^p | s^p | s_h^p | s_v^p |
|--|------------|----------|-------|---------|---------|
| $ s_0\rangle \{ 0\rangle\}$ | $-2 + J/4$ | 0 | 0 | 1 | 1 |
| $ t_0^{s_z}\rangle \{ 1\rangle, 2\rangle, 3\rangle\}$ | $-1 + J/4$ | -1,0,1 | 1 | 1 | 1 |
| $ s_1\rangle \{ 4\rangle\}$ | $-3J/4$ | 0 | 0 | 0 | 0 |
| $ t_1^{s_z}\rangle \{ 5\rangle, 6\rangle, 7\rangle\}$ | $-3J/4$ | -1,0,1 | 1 | 1 | 0 |
| $ t_2^{s_z}\rangle \{ 8\rangle, 9\rangle, 10\rangle\}$ | $J/4$ | -1,0,1 | 1 | 0 | 1 |
| $ q^{s_z}\rangle \{ 11\rangle, 12\rangle, 13\rangle, 14\rangle, 15\rangle\}$ | $1 + J/4$ | -2,...,2 | 2 | 1 | 1 |

Tab. 7.1.: Eigenstates on a single plaquette of an empty plaquette for $J = 0$ and a filled plaquette for $J > 0$ with eigenenergies and quantum numbers s_z^p , s^p , s_h^p , and s_v^p . The explicit states given in the first column can be found in Eq. (7.2.2).

$E_3^{s^p=2, s_v^p=1} = 1$. The explicit energy eigenstates can be written as

$$\begin{aligned}
|0\rangle &= \frac{1}{\sqrt{12}} (-2 |\uparrow\downarrow\uparrow\downarrow\rangle - 2 |\downarrow\uparrow\downarrow\uparrow\rangle + |\uparrow\downarrow\downarrow\uparrow\rangle + |\downarrow\uparrow\uparrow\uparrow\rangle + |\downarrow\uparrow\uparrow\downarrow\rangle + |\uparrow\uparrow\downarrow\downarrow\rangle) , \\
|1\rangle &= \frac{1}{2} (-|\uparrow\downarrow\downarrow\downarrow\rangle + |\downarrow\uparrow\downarrow\downarrow\rangle - |\downarrow\downarrow\uparrow\downarrow\rangle + |\downarrow\downarrow\uparrow\uparrow\rangle) , \\
|2\rangle &= \frac{1}{\sqrt{2}} (|\downarrow\uparrow\downarrow\uparrow\rangle - |\uparrow\downarrow\uparrow\downarrow\rangle) , \\
|3\rangle &= \frac{1}{2} (-|\downarrow\uparrow\uparrow\uparrow\rangle + |\uparrow\downarrow\uparrow\uparrow\rangle - |\uparrow\uparrow\downarrow\uparrow\rangle + |\uparrow\uparrow\uparrow\downarrow\rangle) , \\
|4\rangle &= \frac{1}{2} (-|\uparrow\downarrow\downarrow\uparrow\rangle + |\downarrow\downarrow\uparrow\uparrow\rangle - |\downarrow\uparrow\uparrow\downarrow\rangle + |\uparrow\uparrow\downarrow\downarrow\rangle) , \\
|5\rangle &= \frac{1}{\sqrt{2}} (-|\downarrow\uparrow\downarrow\downarrow\rangle + |\downarrow\downarrow\uparrow\uparrow\rangle) , \\
|6\rangle &= \frac{1}{2} (-|\uparrow\downarrow\downarrow\uparrow\rangle - |\downarrow\downarrow\uparrow\uparrow\rangle + |\downarrow\uparrow\uparrow\downarrow\rangle + |\uparrow\uparrow\downarrow\downarrow\rangle) , \\
|7\rangle &= \frac{1}{\sqrt{2}} (-|\uparrow\downarrow\uparrow\uparrow\rangle + |\uparrow\uparrow\uparrow\downarrow\rangle) , \\
|8\rangle &= \frac{1}{\sqrt{2}} (-|\uparrow\downarrow\downarrow\downarrow\rangle + |\downarrow\downarrow\uparrow\downarrow\rangle) , \\
|9\rangle &= \frac{1}{2} (|\uparrow\downarrow\downarrow\uparrow\rangle - |\downarrow\downarrow\uparrow\uparrow\rangle - |\downarrow\uparrow\uparrow\downarrow\rangle + |\uparrow\uparrow\downarrow\downarrow\rangle) , \\
|10\rangle &= \frac{1}{\sqrt{2}} (-|\downarrow\uparrow\uparrow\uparrow\rangle + |\uparrow\uparrow\downarrow\uparrow\rangle) , \\
|11\rangle &= |\downarrow\downarrow\downarrow\downarrow\rangle , \\
|12\rangle &= \frac{1}{2} (|\uparrow\downarrow\downarrow\downarrow\rangle + |\downarrow\uparrow\downarrow\downarrow\rangle + |\downarrow\downarrow\uparrow\downarrow\rangle + |\downarrow\downarrow\uparrow\uparrow\rangle) , \\
|13\rangle &= \frac{1}{\sqrt{6}} (|\uparrow\downarrow\uparrow\downarrow\rangle + |\downarrow\uparrow\downarrow\uparrow\rangle + |\uparrow\downarrow\downarrow\uparrow\rangle + |\downarrow\downarrow\uparrow\uparrow\rangle + |\downarrow\uparrow\uparrow\downarrow\rangle + |\uparrow\uparrow\downarrow\downarrow\rangle) , \\
|14\rangle &= \frac{1}{2} (|\downarrow\uparrow\uparrow\uparrow\rangle + |\uparrow\downarrow\uparrow\uparrow\rangle + |\uparrow\uparrow\downarrow\uparrow\rangle + |\uparrow\uparrow\uparrow\downarrow\rangle) , \quad \text{and} \\
|15\rangle &= |\uparrow\uparrow\uparrow\uparrow\rangle ,
\end{aligned} \tag{7.2.2}$$

where the order of spins in the product states signals the site on the plaquette.

The empty plaquette enriched by an additional diagonal interaction between two spins scaling with the coupling constant J is called filled plaquette. It is sketched in Fig. 7.7(b). The Hamiltonian is given by

$$\begin{aligned} H^{\text{fp}} &= H^{\text{ep}} + J \left(\vec{S}_{p,1} \cdot \vec{S}_{p,3} \right) \\ &= (\vec{S}_{p,1} + \vec{S}_{p,3}) \cdot (\vec{S}_{p,2} + \vec{S}_{p,4}) + J \left(\vec{S}_{p,1} \cdot \vec{S}_{p,3} \right) . \end{aligned} \quad (7.2.3)$$

The total spins on the diagonals still yield good quantum numbers s_{h}^p and s_{v}^p . The energy eigenstates do not depend on the value of J and are equal to the ones of the empty plaquette. For $J = 0$, the empty plaquette is recovered and the plaquette singlet state $|0\rangle$ is the ground state. This remains true up to $J = 2$. At this point, the ground state changes towards the degenerate states $\{|4\rangle, |5\rangle, |6\rangle, |7\rangle\}$. These states have a total diagonal spin $s_{\text{v}}^p = 0$, so the diagonal dimer is a singlet. In this state, the two additional spins on the other diagonal are free, which is the reason for the four-fold degeneracy. The expressions for the eigenenergies of the filled plaquette are given in Tab. 7.1 and plotted as functions of J in Fig. 7.8.

Regarding the excited states the most interesting feature of the energy spectrum is the level crossing within the first excitation on the singlet background at $J = 1$. For $1 < J < 2$, the first excitation of the filled plaquette singlet does not have the same characteristics as the one of the empty plaquette. Furthermore, the filled plaquette phase with diagonal coupling strengths comparable to nearest-neighbour interactions $J \approx 1$ possesses two low-energy excitations, which are of comparable energy close to the level crossing.

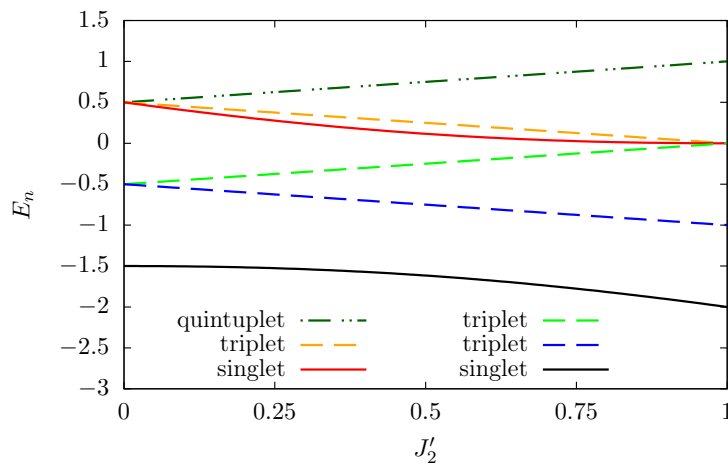


Fig. 7.9.: Energy spectrum for an empty plaquette as shown in Fig. 7.2.3(c). For $J'_2 = 1$, the empty plaquette given in Fig. 7.2.3(a) is recovered. For $J'_2 = 0$, two decoupled dimers are realised.

We also consider an empty plaquette with distinct exchange strengths on vertical and horizontal bonds with couplings J'_2 and one. This is sketched in Fig. 7.7(c). The

Hamiltonian reads

$$H = \left(\vec{S}_{p,1} \cdot \vec{S}_{p,2} + \vec{S}_{p,3} \cdot \vec{S}_{p,4} \right) + J'_2 \left(\vec{S}_{p,1} \cdot \vec{S}_{p,4} + \vec{S}_{p,2} \cdot \vec{S}_{p,3} \right). \quad (7.2.4)$$

The eigenenergies in respect to J'_2 are plotted in Fig. 7.9. In the limit $J'_2 = 0$, the situation reduces to two decoupled dimers. In this case, the product states of singlets and triplets on both dimers yield a proper eigenbasis. The ground state is given by two singlets with an energy $E_0^{s^p=0} = -3/2$. At $E_0^{s^p=1} = -1/2$, a manifold of two degenerate states with one singlet and one triplet exists. The highest eigenenergy is $E_2^{s^p=0} = E_2^{s^p=1} = E_2^{s^p=2} = 1/2$, where the eigenstates consist of two triplets. More details on these states are given in Ref. [114]. If one increases the inter-dimer interactions J'_2 , the eigenstates of the dimers get mixed via quantum fluctuations and are no longer the energy eigenstates of the plaquette, since the Hamiltonian does not commute with the operators $(S_{p,1} + S_{p,3})^2$ and $(S_{p,2} + S_{p,4})^2$ for $J'_2 \neq 0$. Then, the energy eigenstates represented in an eigenbasis of the quantum numbers s_z^p and s^p depend on J'_2 . The nature of the eigenstates of the empty plaquette at $J'_2 = 1$ are fundamentally different from the eigenstates on the decoupled dimers at $J'_2 = 0$.

7.3. Extended Shastry-Sutherland models

The experimental findings on $\text{SrCu}_2(\text{BO}_3)_2$ under pressure do not simply fit to the EPP predicted for the Shastry-Sutherland model. This, together with pure theoretical interest, led to the introduction and study of various extended Shastry-Sutherland models, which are reviewed in this section. The presented former findings lay the basis for our results in Chapters 9 and 10. We focus on models, which distinguish several exchange constants within the Shastry-Sutherland model and do not consider additional couplings like Dzyaloshinski-Moriya interactions.

In $\text{SrCu}_2(\text{BO}_3)_2$, the underlying structure of the atoms imposes symmetries on the lattice and without doping a loss of translation symmetry is not expected. Instead, a reduction of the rotational symmetry is more likely. As discussed in the beginning of this section, the Shastry-Sutherland model offers a \mathcal{C}_4 rotational symmetry, which in the extended models gets reduced to a \mathcal{C}_2 rotational symmetry. In terms of plaquettes on the lattice, this means that there are two distinguishable sets with perpendicular diagonal couplings. Still obeying the \mathcal{C}_2 rotational symmetry, four nearest-neighbour couplings, two on every type of plaquette can be chosen independently, as well as two dimer couplings. If all of these are taken into account, a five dimensional phase diagram arises. In former works, three of these couplings were investigated.

In 2001, Takushima, Koga, and Kawakami used series expansions to investigate an extended Shastry-Sutherland model in the spirit of an adiabatic connection to decoupled orthogonal-dimer chains [73]. This limit is included in an extension of the Shastry-Sutherland model, where nearest-neighbour couplings J'_1 and J'_2 on the two sets of filled plaquettes with differently orientated internal diagonal bonds are distinguished. The

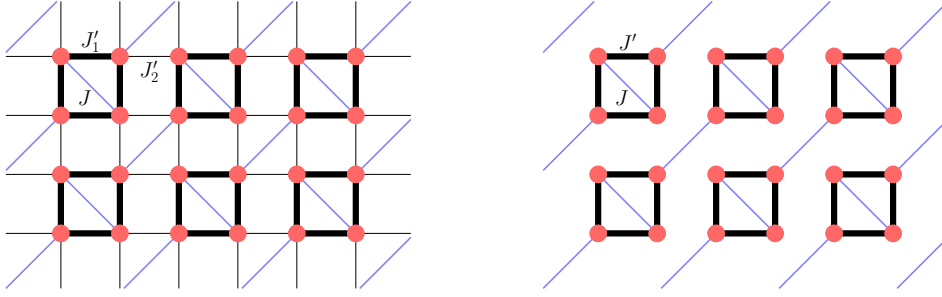


Fig. 7.10.: In the left panel, the asymmetrical Shastry-Sutherland model is shown, which is biased towards the FPP by a strong difference in the nearest-neighbour couplings J'_1 and J'_2 . In the right panel, the limit of vanishing J'_2 leading to a set of decoupled orthogonal-dimer spin chains is illustrated, where J'_1 is set to J' .

diagonal couplings J remain identical. The Hamiltonian reads

$$H = J'_1 \sum_{\langle i,j \rangle} \vec{S}_i \cdot \vec{S}_j + J'_2 \sum_{\langle\langle i,j \rangle\rangle} \vec{S}_i \cdot \vec{S}_j + J \sum_{\langle i,j \rangle} \vec{S}_i \cdot \vec{S}_j \quad (7.3.1)$$

and the model is illustrated in the left panel of Fig. 7.10.

If either $J'_1 = 0$ or $J'_2 = 0$, the two-dimensional model reduces to an infinite number of decoupled one-dimensional orthogonal-dimer chains, as can be seen in the right panel of Fig. 7.10, where $J'_2 = 0$ and $J'_1 = J'$. Such a chain consists of a single type of filled plaquettes linked by bonds orthogonal to the intra-plaquette diagonal bonds. The orthogonal-dimer chain was studied also by Kawakami's group in a previous article [208]. They performed series expansions up to order eleven for the ground-state energy of the FPP as well as ED. A very important property of the orthogonal-dimer chain is that the total spin on the diagonal, s_v^p , is a good quantum number for every plaquette individually. In the following, s_v denotes that all diagonals are in the same state $s_v^p \forall p$ with the value $s_v \equiv s_v^p$. The symmetry sectors with $s_v = 0$ and $s_v = 1$ are completely decoupled. The commutation of the Hamiltonian and the total diagonal spin operator $[(\vec{S}_1 + \vec{S}_3)^2$ in Section 7.2] can be seen from the geometry of the orthogonal dimer-chain, where spins on inter-plaquette bonds do not interact with the spins on the diagonal intra-



Fig. 7.11.: The blue bonds indicate, where the total spins s_v^p are located. On the left, this leads to a protected quantum number. On the right, it does not.

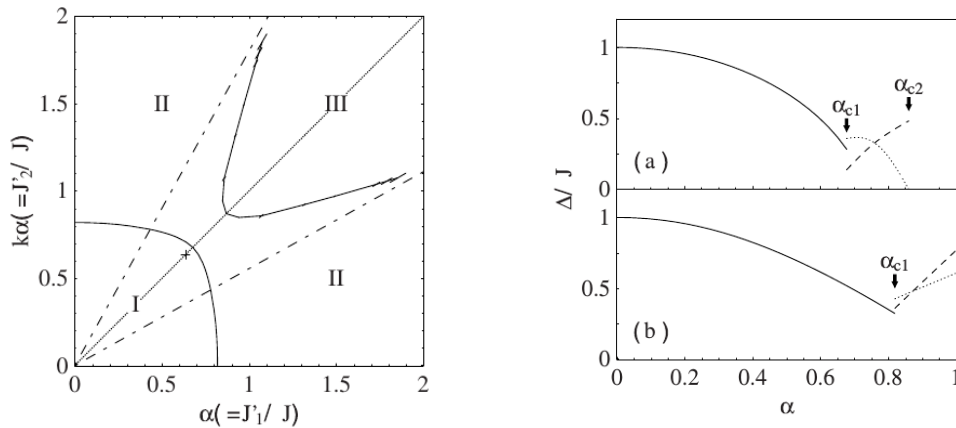


Fig. 7.12.: On the left, the phase diagram of the extended Shastry-Sutherland model with different nearest-neighbour couplings on filled plaquettes defined in Eq. (7.3.1) with dimer singlet (I), FPP (II), and Néel (III) phase is shown. On the right, the energy gaps for (a) the Shastry-Sutherland model ($J'_2 = J'_1$) and (b) the orthogonal-dimer chain is given. The parameter denotes $\alpha = J'_1/J$. All results were derived by Takushima et al. in Ref. [73].

plaquette interactions. The situation is depicted in Fig. 7.11(a). The phase diagram exhibits the dimer singlet phase for values $J'/J < 0.81900$ and the FPP otherwise [208]. The phase transition is of first order and is accompanied by a discontinuity in the lowest energy excitation, which jumps from the triplet excitation of the dimer singlet phase to a four-fold degenerate localised state in the FPP as shown in the right panel of Fig. 7.12(b). Interestingly, within the FPP the first excitation changes towards a triplet state at $J'/J = 0.872$. The excitation energy of the latter was studied perturbatively in order seven and is also included in Fig. 7.12(b). The position of the energy gap in k -space is not given in Ref. [208]. For further details see Section 9.2.

If we go back to the full extended model with no vanishing couplings, a large variety of phases is plausible, similar to the symmetric Shastry-Sutherland model at $J'_2 = J'_1$. Back in 2001, it was not known that the EPP yields the intermediate phase of the Shastry-Sutherland model and it was not considered in the phase diagram by Takushima et al. shown in the left panel of Fig. 7.12, where only the dimer singlet (I), the FPP (II), and the Néel (III) phase are included [73]. Actually, their article reads as if they did not realise that the EPP and the FPP are different phases, since they used series expansions for the ground-state energy of the EPP as if it was the FPP to confirm their results. This is stated in a single sentence of the paper. Anyways, the work by Koga and his group remains important, since the adiabatic connection between the orthogonal-dimer chains and the extended Shastry-Sutherland model for the FPP is valid up to the phase transition towards the EPP at some value $J'_1 < J'_2$ or $J'_2 < J'_1$. Concerning the transition towards the Néel phase, they expected it to be of second order, but it has been shown that it is weakly first order [74] or deconfined quantum critical [177]. In this sense, the extension of the FPP towards the Néel phase got overestimated. The phase transition between the FPP and the dimer singlet phase is of first order for the whole parameter range [70].

The excitations of the FPP in the two-dimensional model behave very similar to the ones on the orthogonal-dimer chain and the excitation energies are depicted in the right panel of Fig. 7.12 at the top (a) [73] for the symmetric Shastry-Sutherland model, so actually for a regime where the FPP does not yield the ground state. They were calculated by series expansions in order five. At the believed first-order phase transition from the dimer phase to the FPP, the gap shows a discontinuity and within the FPP a level crossing between two excitations occurs at $J'_1/J \simeq 0.76$. In contrast to the orthogonal-dimer chain, these excitations are both triplons, since the inter-chain couplings lift the four-fold degeneracy. The two-dimensional nature of the model also breaks the conservation of the total spin on diagonals of plaquettes. More details on these issues are discussed in Section 10.2.2. Again, the position of the energy gap in k -space is not given in Ref. [73], and it is not completely clear to us if the proper energy gap was studied over the whole parameter range, which we discuss in Subsection 10.2.2. The work by Takushima et al. is slightly misleading and leaves the open issue of clarifying the phase diagram under the inclusion of the EPP as well as the study of the excitations of the EPP and the FPP in the proper parameter regimes. We investigate these issues in Subsection 10.1.2 and Section 10.2.

Less than one year later, another study was published [72], where series expansions were applied to all kinds of possible intermediate phases of the Shastry-Sutherland model, under the application of deformed perturbative models. The expansion for the FPP is done by a distorted Hamiltonian, but not described precisely. Details are given in Chapter 8. For the FPP, a triplet excitation energy was calculated upto order six, which has its minimum at an intermediate momentum value with $k_x = k_y$ [72]. By recalculating the results, we find that instead of the lowest triplet of H_0 with $s_v^p = 1$ the second excitation with $s_v^p = 0$ is studied in Ref. [72].

The second extension to the Shastry-Sutherland model, which reflects a plausible distortion for $\text{SrCu}_2(\text{BO}_3)_2$ under pressure is given by different coupling strengths for differently orientated diagonal bonds J_1 and J_2 illustrated in the left panel of Fig. 7.13.

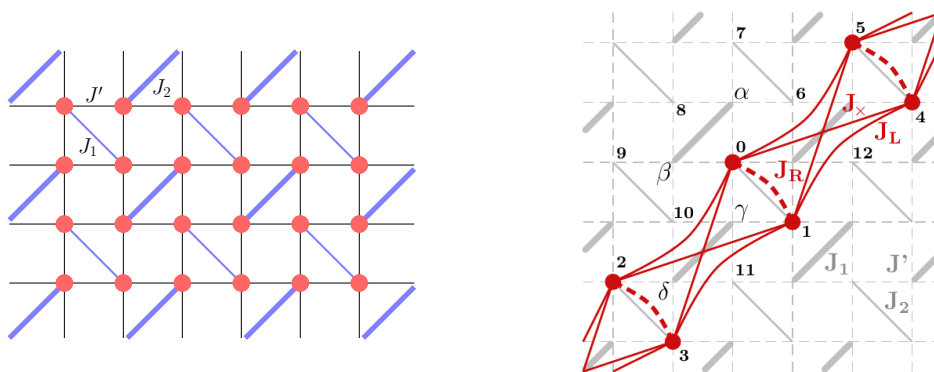


Fig. 7.13.: Sketches of the asymmetrical Shastry-Sutherland model with different couplings J_1 and J_2 on the diagonal dimer bonds. On the left, the notation used in this work is shown. On the right, the notation used by Moliner et al. is indicated together with the reduced one-dimensional second-order ladder [176].

The Hamiltonian can be written as

$$H = J_1 \sum_{\langle\langle i,j \rangle\rangle} \vec{S}_i \cdot \vec{S}_j + J_2 \sum_{\langle i,j \rangle} \vec{S}_i \cdot \vec{S}_j + J' \sum_{\langle i,j \rangle} \vec{S}_i \cdot \vec{S}_j. \quad (7.3.2)$$

This model was previously studied by Moliner et al. [176]. They used ED, a mean field approach based on quadrumer boson operators and perturbation theory to derive the phase diagram shown on the left of Fig. 7.14. Perturbatively, they started from the limit where one dimer coupling is dominant in respect to the other one $J_1 \gg J_2$ and where the intra-dimer coupling is large in comparison to the inter-dimer coupling $J_1 \gg J'$. In second order in J' , the extended Shastry-Sutherland model reduces to an effective model of decoupled completely frustrated two-leg spin ladders with effective leg J_L , rung J_R , and frustrated J_x couplings illustrated in the right panel of Fig. 7.13. A single ladder exhibits the exact dimer singlet phase and a Haldane gapped phase, which is characterised by spin-1 triplets on the J_2 -bonds. The first-order phase transition from the dimer singlet to the Haldane phase is at $J_R/J_L \approx 1.4$, which in terms of the extended Shastry-Sutherland model is $J_2 = 1.7J'^2/J_1$ indicated as the dashed line L1 in the left plot of Fig. 7.14. The line L1' corresponds to the third-order result. This phase transition was confirmed by ED, where it was identified by the spin-spin correlations between nearest-neighbour sites in the ground state, which exhibit a clear change from strong singlets on diagonals to a triplet on the J_2 -bonds as is shown in the right plots of Fig. 7.14. The ED also served as the indicator for the phase transition in the area, where the perturbation theory is not well converged. The transition points are indicated by symbols with lines in the phase diagram in the left plot of Fig. 7.14.

The energy spectrum of the Haldane phase is characterised by the first excitation,

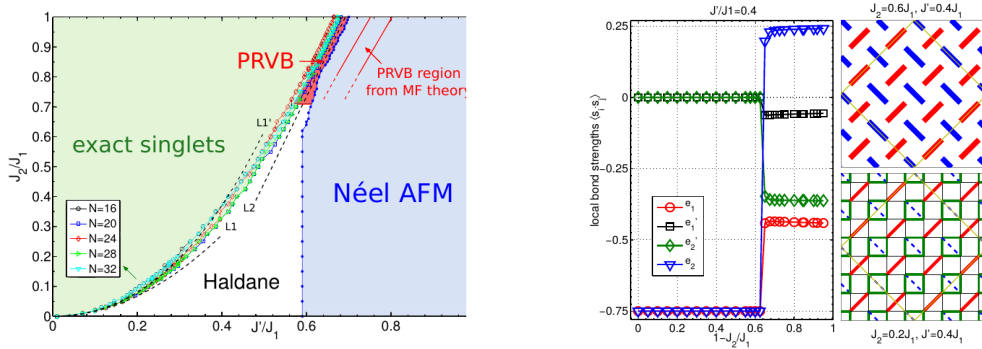


Fig. 7.14.: In the left plot, the phase diagram of the extended Shastry-Sutherland model with different coupling strengths on the diagonal couplings is shown. In the right plots, the expectation values of local bond strengths for the ground state of the extended Shastry-Sutherland model with different coupling strengths on the diagonal couplings at a coupling ratio of $J'/J_1 = 0.4$ is given in the left panel. The labels e_1, e_2 indicate the diagonal dimers with J_1, J_2 and the e_1', e_2' the according surrounding nearest-neighbour bonds. On the right, the corresponding local energy profiles at $J_2 = 0.6J_1, J' = 0.4J_1$ in the upper and $J_2 = 0.2J_1, J' = 0.4J_1$ in the lower panel are given. Solid lines indicate negative, dashed lines positive values. All plots are from ED on a 32-site cluster by Moliner et al. in Ref. [176].

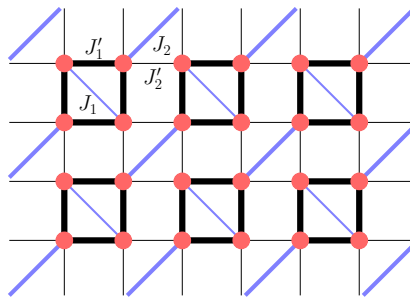


Fig. 7.15.: Sketch of the asymmetrical Shastry-Sutherland model with different couplings J'_1 and J'_2 on different set of filled plaquettes including J_1 and J_2 diagonal dimer bonds, respectively.

which is dispersive with a maximum at $k \approx \pi/2$, the Haldane gap at $k = \pi$ and decay into the continuum for $k \lesssim \pi/4$ [209–212]. The Haldane gap in the extended Shastry-Sutherland model was studied by Moliner et al. using ED. It is independent of J_2 , which can be understood, since all diagonal bonds J_2 are already occupied by triplets. In contrast in the dimer singlet phase, the gap decreases and scales linearly with J_2 relating to the energy difference between a singlet and a triplet state on the apparent diagonal couplings.

Another extended Shastry-Sutherland model is given if both of the previously described asymmetries occur, such that the parameters on the different sets of filled plaquettes are J'_1 and J'_2 and on corresponding intra-plaquette dimers J_1 and J_2 , respectively. This model is illustrated in Fig. 7.15 and the Hamiltonian reads

$$H = J'_1 \sum_{\langle i,j \rangle} \vec{S}_i \cdot \vec{S}_j + J'_2 \sum_{\langle i,j \rangle} \vec{S}_i \cdot \vec{S}_j + J_1 \sum_{\langle\langle i,j \rangle\rangle} \vec{S}_i \cdot \vec{S}_j + J_2 \sum_{\langle\langle i,j \rangle\rangle} \vec{S}_i \cdot \vec{S}_j. \quad (7.3.3)$$

It was studied for the special one-dimensional case with $J'_1 = 0$ or $J'_2 = 0$ resulting in an asymmetric orthogonal-dimer chain by Richter et al. in Ref. [213]. They employed series expansions as well as ED and variational techniques. For the non-frustrated case with $J_1 = 0$ and from the limit $J_2/J' \gg 1$, the system is effectively described by a fully frustrated ladder in second order. Therefore, an effective Haldane phase with triplets on the plaquette diagonals and singlets on the J_1 dimers forms, as in the distorted Shastry-Sutherland model with $J_2 \gg J_1$. In the opposite limit, the FPP arises, and a crossover between the two phases is conjectured. However, in their ED spectra no crossings are observed. As we motivate in Chapter 9 and numerically prove in Subsection 10.1.3 the FPP and Haldane phase are identical. Under the inclusion of frustration $J_1 > 0$, a phase transition towards the exact dimer singlet phase occurs, as already discussed for the symmetric orthogonal-dimer chain. The upper bound derived for the extension of the ground state of the unfrustrated model is plotted in our phase diagram in Fig. 9.2. The excitations of the dimer singlet phase are triplets, which are fully localised in the one-dimensional model. The excitation energy for the Haldane phase/FPP from both limits was derived in order two. We investigate this model in detail in Chapter 9. The fully distorted Shastry-Sutherland model in Eq. (7.3.1) was not studied prior to this

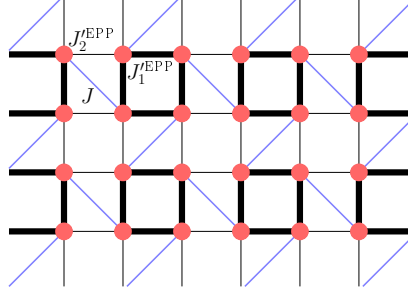


Fig. 7.16.: Illustration of the asymmetrical Shastry-Sutherland model, which is biased towards the EPP by different nearest-neighbour couplings J_1^{EPP} and J_2^{EPP} around distinct sets of empty plaquettes.

thesis. Results on the model are given in Chapter 10.

One can also study different nearest-neighbour exchanges J_1^{EPP} and J_2^{EPP} on both sets of empty plaquettes. This yields a bias towards the EPP, and is the relevant lattice distortion arising through a spin-lattice coupling if the EPP occurs [177]. The Hamiltonian is

$$H = J_1^{\text{EPP}} \sum_{\langle i,j \rangle} \vec{S}_i \cdot \vec{S}_j + J_2^{\text{EPP}} \sum_{\langle i,j \rangle} \vec{S}_i \cdot \vec{S}_j + J \sum_{\langle\langle i,j \rangle\rangle} \vec{S}_i \cdot \vec{S}_j, \quad (7.3.4)$$

as depicted in Fig. 7.16.

There are many further options to extend the Shastry-Sutherland model even without adding interactions. For instance, if the Shastry-Sutherland model is distorted parallel to the square lattice, all vertical nearest-neighbour bonds get shortened and one has different vertical and horizontal nearest-neighbour couplings on all plaquettes. In this work, we focus on the first three extended Shastry-Sutherland models defined above in Eqs. (7.3.1), (7.3.2), and (7.3.3). The model in Eq. (7.3.4) is briefly discussed in Subsection 10.2.1 and Section 10.4. The models are mainly investigated by series expansions, and the details on the approaches, quantities, series, and convergence are given next.

8. Series expansion approaches for plaquette singlet phases

In this chapter, specific series expansions for plaquette singlet phases in extended Shastry-Sutherland models are explained. This is done for the most general extension given in Eq. (7.3.3), which can be simplified afterwards. The first step is the definition of perturbative Hamiltonians of the form (2.1.1) in Section 8.1. These can then be investigated following the methodological setting given in Section 2.1, so various perturbative approaches are used on finite linked clusters and results in the thermodynamic limit are reached by linked-cluster expansions. Details on the quantities of interest are explained in Section 8.2, before studying and comparing the convergence behaviour of distinct series expansions in Section 8.3. Parts of this chapter are published in Ref. [79] and the associated Supplemental Material in a condensed form. The additional results presented here, yield further underlying work and insights regarding the series expansions of that publication.

8.1. Models

The idea behind the perturbative study of the extended Shastry-Sutherland model is to connect it with exactly solvable models where the ground state is known to be either the filled or empty plaquette singlet product state via a perturbative parameter λ ranging from zero to one. At vanishing perturbation, the models consist of completely decoupled potentially distorted filled or empty plaquettes, which form the super-sites of the expansion and are investigated in Subsection 7.2. The perturbative processes between the super-sites cause transitions within a basis of 256 nearest-neighbour plaquette states.

We apply different perturbative approaches: i) perturbation theory after Löwdin and Takahashi and ii) pCUTs. They are grouped together in this way, because the requirements on the unperturbed Hamiltonians H_0 differ as explained in Section 2.1. Most significantly, for pCUTs an equidistant spectrum of the unperturbed system is needed, in contrast to the Löwdin and Takahashi expansions where this is not necessary. The pCUTs are motivated by the general capability to calculate intensive properties, like excitation energies, in linked-cluster expansions. Actually, we find that Takahashi's approach works for all studied spin-one excitations of plaquette phases as well. Below, specifically adapted Hamiltonians carrying out the adiabatic connection between the model with an exact empty or full singlet plaquette ground state and the extended Shastry-Sutherland model for every pair of method i) or ii) and phase are introduced. Note, that the parameter spaces in the perturbation λ of the various Hamiltonians are not identical, and we distinguish the perturbative parameters as λ_E and λ_F for expansions in the EPP and FPP, respectively, even though further differences will occur. For all expansions, the nearest-neighbour interactions between the spins forming plaquette

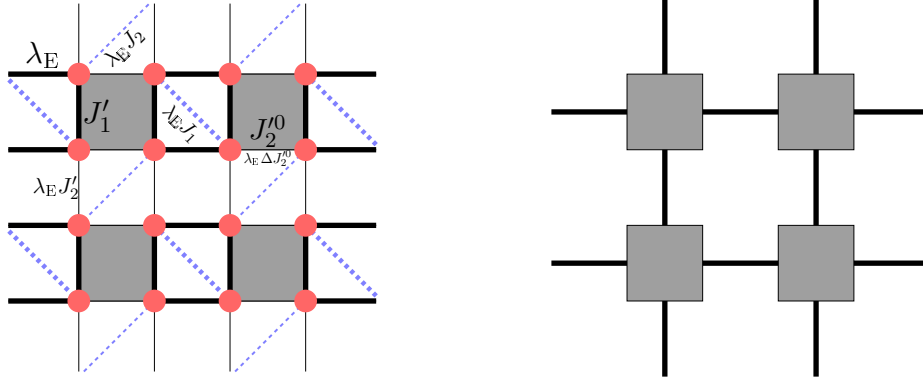


Fig. 8.1.: Illustration of the perturbative models adiabatically connecting the exact empty plaquette ground state with the extended Shastry-Sutherland model on the left. The unperturbed plaquettes at $\lambda_E = 0$ are shaded in grey and form the super-sites. The square lattice of super-sites relevant for the linked-cluster expansion is given on the right, where horizontal exchanges include several interactions. The figure on the left is modified from the Supplemental Material of Ref. [79].

singlets are included in the unperturbed model H_0 as $J'_1 = 1$ in the following. All inter-plaquette interactions vanish.

The series expansions about the EPP are carried out by perturbative Hamiltonians of the form

$$\begin{aligned}
 H_0^{\text{EPP}} &= \sum_{\substack{\langle i,j \rangle \\ \text{vertical} \\ \text{bold}}} \vec{S}_i \cdot \vec{S}_j + J_2^0 \sum_{\substack{\langle i,j \rangle \\ \text{horizontal} \\ \text{thin}}} \vec{S}_i \cdot \vec{S}_j, \\
 V^{\text{EPP}} &= \Delta J'_2 \sum_{\substack{\langle i,j \rangle \\ \text{horizontal} \\ \text{thin}}} \vec{S}_i \cdot \vec{S}_j + \sum_{\substack{\langle i,j \rangle \\ \text{horizontal} \\ \text{bold}}} \vec{S}_i \cdot \vec{S}_j + J'_2 \sum_{\substack{\langle i,j \rangle \\ \text{vertical} \\ \text{thin}}} \vec{S}_i \cdot \vec{S}_j \\
 &\quad + J_1 \sum_{\substack{\langle\langle i,j \rangle\rangle \\ \text{bold}}} \vec{S}_i \cdot \vec{S}_j + J_2 \sum_{\substack{\langle\langle i,j \rangle\rangle \\ \text{thin}}} \vec{S}_i \cdot \vec{S}_j.
 \end{aligned} \tag{8.1.1}$$

The sums can be understood with the lattice shown in the left panel of Fig. 8.1, where the plaquettes interacting in H_0^{EPP} are shaded grey. They form the super-sites of the expansion. The relevant lattice of super-sites for the linked-cluster expansion is depicted in the right panel of Fig. 8.1. An individual super-site is sketched in Fig. 7.7(c) and was studied at the end of Section 7.2. In the unperturbed model H_0^{EPP} , the plaquettes potentially have different strengths on neighbouring bonds $J'_1 = 1 \neq J_2^0$ and no intra-plaquette diagonal coupling. The unperturbed coupling strength J_2^0 can be adjusted by an additional interaction on the same bonds introduced as an on-super-site perturbation scaling with $\Delta J'_2 = J'_2 - J_2^0$. It may be disregarded, if the physical value J'_2 on the disconnected plaquettes is chosen at $\lambda = 0$. However, this requires an individual expansion for every ratio J'_1/J'_2 of interest. Therefore, the on-super-site perturbation can be employed to scan a larger parameter space efficiently, in particular since it can be chosen small $\Delta J'_2 \lesssim 0.3$. All inter-plaquette interactions arise perturbatively. In the next step, the Hamiltonian in Eq. (8.1.1) is studied perturbatively. If $J_2^0 \neq J'_1$ the

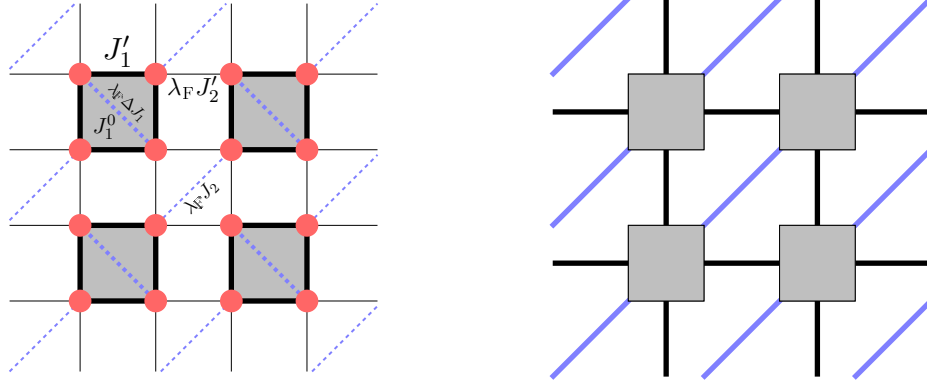


Fig. 8.2.: Illustration of the perturbative models adiabatically connecting the exact filled plaquette ground state with the extended Shastry-Sutherland model on the left. The unperturbed plaquettes at $\lambda_F = 0$ are shaded in grey and form the super-sites. The triangular lattice of super-sites relevant for the linked-cluster expansion is given on the right, where horizontal and vertical exchanges include two interactions. The figure on the left is modified from the Supplemental Material of Ref. [79].

spectrum of H_0^{EPP} is not equidistant and the Takahashi or Löwdin algorithms are applicable. The symmetric choice $J_2^0 = J_1^0 = 1$ allows to perform pCUTs. Then, the asymmetry between the nearest-neighbour couplings is included perturbatively with ΔJ_2^0 . The perturbation V^{EPP} scales with λ_E , but the parameter spaces performing the adiabatic connection for different choices of J_2^0 are not identical, so the same values of λ_E relate to different models.

The general form of the expansion about the filled plaquette state is given by

$$\begin{aligned}
 H_0^{\text{FPP}} &= \sum_{\langle i,j \rangle_{\text{bold}}} \vec{S}_i \cdot \vec{S}_j + J_1^0 \sum_{\langle\langle i,j \rangle\rangle_{\text{bold}}} \vec{S}_i \cdot \vec{S}_j, \\
 V^{\text{FPP}} &= J_2^0 \sum_{\langle i,j \rangle_{\text{thin}}} \vec{S}_i \cdot \vec{S}_j + \Delta J_1 \sum_{\langle\langle i,j \rangle\rangle_{\text{bold}}} \vec{S}_i \cdot \vec{S}_j + J_2 \sum_{\langle\langle i,j \rangle\rangle_{\text{thin}}} \vec{S}_i \cdot \vec{S}_j,
 \end{aligned} \tag{8.1.2}$$

which can be understood together with the left panel of Fig. 8.2. The perturbation V^{FPP} scales with λ_F , and the parameter spaces in λ_F differ for different choices of J_1^0 . The diagonal coupling on the singlet plaquettes J_1 can be included in two ways. Firstly, in H_0^{FPP} with J_1^0 and secondly in V^{FPP} with $\Delta J_1 = J_1 - J_1^0$. A simple setting is given if the on-super-site dimer coupling is completely included at $\lambda = 0$, so $J_1 = J_1^0$ and $\Delta J_1 = 0$. However, in this form an individual calculation for every diagonal coupling J_1 is necessary. This can be overcome by the inclusion of the additional diagonal coupling ΔJ_1 , which allows to adapt the coupling strength within the final series. The quality of convergence is expected to decrease for increasing differences ΔJ_1 , and a reasonable route is to choose J_1^0 at an intermediate value in the area of interest. The Hamiltonian (8.1.2) can be studied perturbatively with the Takahashi or Löwdin formalism for all values of J_1^0 . In contrast, the application of pCUTs requires an unperturbed Hamiltonian, H_0 , with an equidistant spectrum bounded from below. A single filled plaquette offers three coupling ratios of diagonal to nearest-neighbour strengths with

an equidistant spectrum $J/J' = 0$, $J/J' = 1$, and $J/J' = 3$, as discussed in Section 7.2.

The first case with $J_1^0 = 0$ is counter-intuitive to start with, given that the FPP is attempted to be accessed from a limit of decoupled empty plaquettes. However, if the model is in the EPP or in the FPP does not depend on the coupling value of J_1^0 as long as the ground state on the plaquette is the singlet at $J_1^0 < 2$. The distinction between both phases arises from the location of the singlets on the lattice. So, as long as the empty plaquettes with $J_1^0 = 0$ at $\lambda_F = 0$ evolve into filled plaquettes at $\lambda_F = 1$ the FPP is the phase under study.

A filled plaquette with identical couplings on all bonds $J_1^0 = 1$ possesses a much better starting point in the sense of convergence behaviour for coupling ratios of interest $J_1 > J_1^0$. The Hamiltonian is given by Eq. (8.1.2) with $J_1^0 = 1$ and $\Delta J_1 = J_1 - 1$. The physical value J_1 is reached again perturbatively, but in this setting the perturbation is much smaller for the parameter space of interest. This unperturbed Hamiltonian is in particular useful to approach the excitations of the FPP, since the one-quasi-particle sector of the unperturbed plaquettes consists of two triplets and a singlet state.

At $J_1^0 = 3$, the energy spectrum of H_0 is also equidistant, where the ground state is given by a four-fold degenerate level of a singlet on the diagonal and two free spins. Approaching this other phase from the decoupled plaquette limit with $J_1^0 = 3$ therefore yields an effective Hamiltonian in the basis of sets containing a singlet and two spins, which would require further approximation or an extensive numerical study. Still, this large- J ground state is important for the understanding of plaquette singlet phases as discussed in Chapter 9.

The pCUT is based on a perturbation, V , written as a sum over creation and annihilation operators of quasi-particles on super-sites T_n introduced in Eq. (2.1.18). For all expansions defined above accessible by pCUT, such operators exist with $n \in \{-4, 4\}$. The linked-cluster expansions are valid for ground-state energies independent of the perturbative approach. They also work for excitation energies and dynamic structure factors with the pCUT. For the Löwdin and Takahashi approaches, this only holds if the ground- and the excited state or excited states have differing conserved quantum numbers. In the present case, this clearly holds for triplon excitations, since the ground state is a singlet. This criterion can be understood, if one considers two disconnected linked clusters, where one is in the vacuum state, whereas the other one hosts a triplon. As long as the total spin is a good quantum number, the total spin on each cluster can not be changed and therefore the triplon and the vacuum can not exchange between the clusters, which is the requirement for cluster additivity. We derive the ground-state energies with the Löwdin algorithm, since its computational performance is better than the one of pCUTs and Takahashi. The dispersions and dynamic structure factors are determined using pCUTs, since there is no doubt for them to be applicable. We verified that Takahashi yields the same physical results. For expansions with two distinct triplons in the one-quasi-particle sector, the effective Hamiltonians differ from the pCUT calculation, the resulting energies however are identical.

We perform full graph decompositions in the linked-cluster expansions. For all expansions, the graphs are directed, for instance, a trimer of three super-sites has differing contributions for the direction $(2, 0)^T$ and $(1, 1)^T$ and hence needs to be calculated several times. This increases the number of graphs. Due to the directed graphs, the large number of perturbative processes between singlet plaquettes and the increased

number of various interaction couplings in the extended Shastry-Sutherland model the expansions can not be pushed to as high orders as known for other models [25, 72, 214].

8.2. Quantities

We calculate ground-state and excitation energies as well as dynamic structure factors. The general steps for the linked-cluster expansion are explained in Subsection 2.1.1. Here, they are applied more specifically to plaquette phases for the extended Shastry-Sutherland model.

The ground-state energies of both phases follow directly from the linked-cluster expansion, since the plaquette singlet states are non-degenerate in the perturbative approaches and the according block of the effective Hamiltonian consists of a single element. Note, that we call the lowest energy determined for the subsector belonging to a certain phase the ground-state energy even though it might be considered at parameters, where another state yields the true ground state. In the linked-cluster expansion, a linked cluster contributes after subtraction if the number of links contained in a loop plus twice the number of links not contained in a loop is smaller or equal to the calculated order. For the extended Shastry-Sutherland model (7.3.3) we derived the ground-state energies $\epsilon_0^{(E)}$ in the EPP and $\epsilon_0^{(F)}$ in the FPP up to order eight in λ_E and λ_F , which required series expansions on 212 graphs on a directed square lattice, and on 2849 graphs on a directed triangular lattice, as seen in the right panels of Fig. 8.1 and Fig. 8.2, respectively. In the special cases $J_1 = J_2$ and $J'_1 = J'_2$ order nine for $\epsilon_0^{(E)}$ was reached from separate calculations on 244 graphs. In the extended Shastry-Sutherland model there are two distinct FPPs. One has plaquette singlets located on plaquettes including diagonal J_1 -bonds and one has singlets on plaquettes with J_2 -bonds. The energies of both these phases are accessible from a single expansion. Naively, we consider the FPP on the J_1 -plaquettes with parameters J'_1, J_1, J'_2 , and J_2 normalised on the nearest-neighbour exchanges present in H_0 , i.e. $J'_1 = 1$. In order to study the FPP on J_2 -plaquettes, the parameters in the final series have to be chosen as $\tilde{J}'_2 = 1/J'_2, \tilde{J}_1 = J_2/J'_2$, and $\tilde{J}_2 = J_1/J'_2$. This yields the FPP J_2 energies in units of J'_2 , and can be compared with the ones of the FPP on J_1 -plaquettes after multiplying by J'_2 . The energies of both phases are shown along some set of parameters in Fig. 10.8.

All expansions of the first excitation energy around plaquettes with diagonal couplings $J_1^0 \neq 1$ at $\lambda = 0$ reach a single quasi-particle. If $J_1^0 < 1$, it is the triplon connected to the triplet with $s_v^p = 1$, for $1 < J_1^0 < 2$ it is the one with $s_v^p = 0$. It is sufficient to consider only one state of each triplet, since the extended Shastry-Sutherland model is symmetric under $SU(2)$. Higher excited states are accessible by the same scheme, for instance the $s_v^p = 0$ triplet as the second excitation at values $1 < J_1^0 < 2$. The one-quasi-particle block in the effective Hamiltonian consists of a static part as well as of hoppings of the triplon, and a Fourier-transformation directly yields the dispersion

$$\omega_i(\vec{k}) = \epsilon_i^{(0)} - \epsilon_0^{(0)} + \sum_{\vec{r}} a_{\vec{r}} e^{i\vec{r}\cdot\vec{k}} , \quad (8.2.1)$$

where the unperturbed energies of the ground $\epsilon_0^{(0)}$ and excited state $\epsilon_i^{(0)}$ are considered.

The sum includes local hopping processes $a_{\vec{0}}$ from which the vacuum energy needs to be subtracted. This is done for every cluster individually. For the hopping amplitudes $a_{\vec{r}}$ the index \vec{r} indicates the spatial separation of the initial and final position of the quasi-particle. Note, that the hopping amplitudes and the resulting dispersions for the EPP are not completely symmetric in real space under $x \leftrightarrow y$, and in momentum space with $\vec{k} \equiv (k_x, k_y)$ under $k_x \leftrightarrow k_y$ starting from order three. This is due to some minus signs in the local structure. Without long-range interactions, the extension of processes in real space, and therefore the upper limit of the sum, depends on the order in λ . Generally, for the linked-cluster expansion all linked clusters, which have a number of links smaller or equal to the calculated order, contribute after subtraction. The one-triplon dispersions are determined up to order six for the extended Shastry-Sutherland model. For a single triplon in the FPP this requires 25439, and in the EPP 2223 calculations.

For expansions around filled plaquettes with $J_1^0 = 1$ two different relevant triplets are present in the one-quasi-particle sector, which we label as a and b . The one-quasi-particle block in the effective Hamiltonian in Fourier-space is a 2×2 matrix. In a basis of a and b particles in momentum space, it reads

$$\omega_{ab}(\vec{k}) = \begin{pmatrix} 1 + \sum_{\vec{r}} a_{\vec{r}} e^{i\vec{r} \cdot \vec{k}} & \sum_{\vec{r}} c_{\vec{r}}^* e^{-i\vec{r} \cdot \vec{k}} \\ \sum_{\vec{r}} c_{\vec{r}} e^{i\vec{r} \cdot \vec{k}} & 1 + \sum_{\vec{r}} b_{\vec{r}} e^{i\vec{r} \cdot \vec{k}} \end{pmatrix} \quad (8.2.2)$$

with the hopping amplitudes $a_{\vec{r}}$ and $b_{\vec{r}}$ for particles a and b in real space, and the processes transforming a to b scaling with $c_{\vec{r}}$. The diagonal elements include local hopping processes $a_{\vec{0}}$ and $b_{\vec{0}}$ from which the vacuum energy needs to be subtracted. The eigenvalues of this matrix as a Taylor expansion up to the calculated order give the dispersion relations of the triplons $\omega_a(\vec{k})$ and $\omega_b(\vec{k})$, as already explained in Subsection 2.1.1. Such an expansion is able to yield results for the EPP, as long as the internal diagonal bonds vanishes at $\lambda = 1$ and appropriate inter-plaquette diagonal couplings are in place. In the linked-cluster expansion in order six for the FPP with two-quasi-particles in the one-quasi-particle sector for the three relevant matrix elements $2 \cdot 25439 + 49685$ calculations on linked-clusters are performed. The FPP dispersions in the asymmetric orthogonal-dimer chain $J_2' = 0$ are calculated in order eight. This requires expansions of the local hopping, eight non-local hopping amplitudes, and the vacuum contributions.

From the one-quasi-particle dispersion the lower band edge (lbe) of the apparent two-quasi-particle continuum can be determined by

$$\omega_{\text{lbe}}^i(\vec{k}) = \min_{\vec{q}} \left(\omega_i \left(\frac{\vec{k}}{2} + \vec{q} \right) + \omega_i \left(\frac{\vec{k}}{2} - \vec{q} \right) \right). \quad (8.2.3)$$

In the case of multiple one-quasi-particles, several continua exist, set up from different combinations of quasi-particles. The lower bound of a two-quasi-particle continuum of different particles a and b at momentum \vec{k} is determined by

$$\omega_{\text{lbe}}^{ab}(\vec{k}) = \min_{\vec{q}} \left(\omega_a \left(\frac{\vec{k}}{2} + \vec{q} \right) + \omega_b \left(\frac{\vec{k}}{2} - \vec{q} \right) \right). \quad (8.2.4)$$

Unless a mode is protected by symmetry, the lowest band edge is relevant for decay.

In Subsection 10.2.1, we briefly study a single-triplon excitation in the two-quasi-particle sector for the EPP. For an unperturbed Hamiltonian of decoupled empty plaquettes this sector consists of two triplets with $s_v^p = 0$ and $s_v^p = 1$, and a singlet. In the regime where the triplons are protected by s_v^p on the full lattice, the derivation of the dispersion for the triplon connected to the triplet with $s_v^p = 0$ is identical to the one in the one-quasi-particle sector apart from the considered state. Therefore, we determine it for momenta $\vec{k} = \{(0, 0)^T, (0, \pi)^T, (\pi, 0)^T, (k, k)^T\}$. Here, the asymmetry between k_x and k_y for the dispersion becomes very clear, since it arises in first order of the J_1 and J_2 couplings.

The dynamic structure factor gives the intensities measured in INS in the approximation of linear response theory, which usually works very well. We determine the magnetic dynamic structure factor for the EPP and FPP. A detailed description of the approach for the dimer singlet phase in the Shastry-Sutherland model is given in Ref. [113]. The dynamic structure factor $S(\vec{k}, \omega)$ reads

$$S(\vec{k}, \omega) = -\frac{1}{\pi} \text{Im} \left\langle 0 \left| \mathcal{O}^\dagger(\vec{k}) \frac{1}{\omega - (H - \epsilon_0)} \mathcal{O}(\vec{k}) \right| 0 \right\rangle, \quad (8.2.5)$$

where the ground state is denoted with $|0\rangle$. The relevant operator for the comparison with INS is given by

$$\mathcal{O}(\vec{k}) = \sum_i \sum_\alpha S^\alpha(\vec{r}_i) e^{i\vec{k} \cdot \vec{r}_i}. \quad (8.2.6)$$

It is the Fourier-transform of the sum of all spin operators $S^\alpha(\vec{r}_i)$ with $\alpha \in \{x, y, z\}$ at positions \vec{r}_i . Since the problem is SU(2) invariant, it is sufficient to study only $\alpha = z$ and multiply the result by three. For the investigations of plaquette phases of extended Shastry-Sutherland models, it is most appropriate to label the position of a spin by the position of the plaquette \vec{p} it belongs to and the position of the spin within the plaquette \vec{v}_j with $j \in \{1, 2, 3, 4\}$ instead of \vec{r}_i . In the following, the vector \vec{v} suggests that all sites of the plaquette are addressed. We apply pCUTs to calculate the dynamic structure factors order by order [106] using the model in Eq. (8.1.1) with $J_2^0 = J_1'$ for the EPP and in Eq. (8.1.2) with $J_1^0 = 1$ for the FPP. For the EPP in the unperturbed case, the application of the observable leads to the creation or annihilation of a single type of triplet on the very same plaquette at \vec{p} in the one-quasi-particle sector. One can therefore express the observable as

$$\mathcal{O}_{\vec{p}, \vec{v}} = a_{\text{EPP}}^{\vec{v}} \left(t_{\vec{p}}^\dagger + t_{\vec{p}} \right) + \dots \quad (8.2.7)$$

using the creation and annihilation operators $t_{\vec{p}}^\dagger$ and $t_{\vec{p}}$. Here, $a_{\text{EPP}}^{\vec{v}}$ are the one-triplon amplitudes at $\lambda = 0$ and \dots represents all other multi-quasi-particle processes. After the pCUT in the effective description, this process is less confined in space and the area which gets affected by the application of the operator grows with the order o . The effective observable between the one-triplon and the vacuum sector, $\mathcal{O}_{1\text{QP}, 0}$ in

Eq. (2.1.22) reads

$$\mathcal{O}_{\vec{p},\vec{v}}^{\text{eff},1\text{QP},0} = U^\dagger \mathcal{O}_{\vec{p},\vec{v}} U \Big|_{1\text{QP},0} = \sum_{\vec{\delta}} a_{\vec{\delta},\text{EPP}}^{\vec{v}} \left(t_{\vec{p}+\vec{\delta}}^\dagger + t_{\vec{p}-\vec{\delta}} \right), \quad (8.2.8)$$

where the index $\vec{\delta}$ runs over all plaquettes in infinite order. In the present case and in finite orders, only a finite number of plaquettes is involved. For the calculation of the dynamic structure factor

$$S(\vec{k}, \omega) = -\frac{1}{\pi} \text{Im} \left(\frac{\langle 0 | \mathcal{O}_{\text{eff}}^{1\text{QP}\dagger}(\vec{k}) \mathcal{O}_{\text{eff}}^{1\text{QP}}(\vec{k}) | 0 \rangle}{H_{\text{eff}}^{1\text{QP}}(\vec{k}) - \omega + i\delta} \right), \quad (8.2.9)$$

the effective operator is taken in momentum space

$$\mathcal{O}_{\text{eff}}^{1\text{QP}}(\vec{k}) = a(\vec{k}) \left(t_{\vec{k}}^\dagger + t_{-\vec{k}} \right) \quad \text{with} \quad a(\vec{k}) = \sum_j \sum_{\vec{\delta}} e^{i\vec{k}(\vec{v}_j - \vec{\delta})} a_{\vec{\delta}}^{\vec{v}_j}. \quad (8.2.10)$$

The operators $t_{\vec{k}}^\dagger$ and $t_{-\vec{k}}$ create and annihilate a triplon with momentum \vec{k} , respectively. Then, the one-triplon part of the dynamic structure factor reduces to

$$S^{1\text{QP}}(\vec{k}, \omega) = |a(\vec{k})|^2 \delta(\omega(\vec{k}) - \omega). \quad (8.2.11)$$

The full information on the intensity is therefore given by $3 \cdot |a(\vec{k})|^2$, where the factor 3 accounts for the three spin components S^α with $\alpha \in \{x, y, z\}$ in Eq. (8.2.6).

If the one-quasi-particle sector exists of two excitations $|a\rangle$ and $|b\rangle$ as for the FPP, the apparent effective Hamiltonian is given by a 2×2 matrix (8.2.2), which needs to be diagonalised to get the proper excitations $|\tilde{a}\rangle$ and $|\tilde{b}\rangle$. The eigenvectors are denoted by

$$\begin{aligned} |\tilde{a}\rangle &= \tilde{a}_1 |a\rangle + \tilde{a}_2 |b\rangle \quad \text{and} \\ |\tilde{b}\rangle &= \tilde{b}_1 |a\rangle + \tilde{b}_2 |b\rangle. \end{aligned} \quad (8.2.12)$$

For the dynamic structure factor of these excitations, it is therefore necessary to study the linear combination of contributions

$$\begin{aligned} S^{\tilde{a}}(\vec{k}, \omega) &= \left(\tilde{a}_1 |a(\vec{k})|^2 + \tilde{a}_2 |b(\vec{k})|^2 \right) \delta(\omega_{\tilde{a}}(\vec{k}) - \omega) \quad \text{and} \\ S^{\tilde{b}}(\vec{k}, \omega) &= \left(\tilde{b}_1 |a(\vec{k})|^2 + \tilde{b}_2 |b(\vec{k})|^2 \right) \delta(\omega_{\tilde{b}}(\vec{k}) - \omega). \end{aligned} \quad (8.2.13)$$

The static and dynamic structure factors are calculated up to order five for the extended Shastry-Sutherland model. The selection rules for relevant graphs in the linked-cluster expansion are the same as for the excitation energies.

The derived orders for energies and dispersions are similar to other plaquette expansions [72, 73, 215, 216]. For the extended Shastry-Sutherland model, we increased the maximal perturbative order of the ground-state energies by two compared to Ref. [73]. To our knowledge the dynamic structure factor was not calculated before.

8.3. Convergence

Achieving reliable results from high-order series expansions requires the study of convergence. For small perturbations, the bare series in different orders are effectively identical, here the series are converged. At larger perturbations, the bare series diverge and Padé extrapolants are useful. They are taken as valid results, if no spurious poles occur and if they show comparable behaviour. In our approach of adiabatic connection, the convergence is expected to work best for unperturbed Hamiltonians H_0 chosen close to the parameter space of the physical model at $\lambda = 1$, so the results from the Löwdin and Takahashi approaches should be superior to the pCUT in this sense. In this section, bare series and Padé extrapolants are compared for increasing perturbations. We study the ground-state and excitation energies in the EPP and FPP. For the ground-state energies, various perturbative Hamiltonians are employed, in order to compare models accessible to pCUTs with those beyond, and to illustrate the characteristic convergence behaviour. All ground-state energies are derived by the Löwdin algorithm. In principle, all excitation energies could have been calculated by the Takahashi algorithm, whereas only for asymmetric plaquettes in H_0 this was required. However, we employed pCUT wherever possible. The limiting factor for the derived orders of the excitations was the data for the linked-cluster expansions.

The ground-state energies of the models in Eq. (8.1.1) with $J_2^0 = 1$ for the EPP and in Eq. (8.1.2) with $J_1^0 = 0$ for the FPP are shown in the left and right panels of Fig. 8.3, respectively, yielding the extended Shastry-Sutherland model with equal dimer bonds $J_1 = J_2$ and distinct nearest-neighbour bonds $J_1'/J = 0.72$, $J_2'/J = 0.7$,

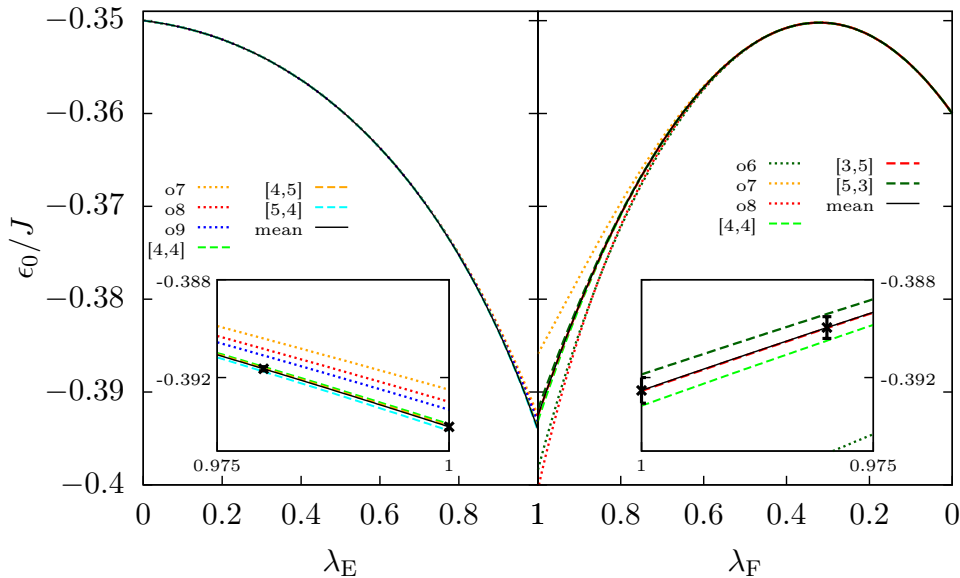


Fig. 8.3.: Ground-state energies as bare series, Padé extrapolants and mean values of the expansions for the EPP on the left and for the FPP on the right. The perturbative Hamiltonian for the EPP is given in Eq. (8.1.1) with $J_2^0 = 1$, and for the FPP in Eq. (8.1.2) with $J_1^0 = 0$. The physically relevant extended Shastry-Sutherland model with $J_1'/J = 0.72$ and $J_2'/J = 0.7$ is reached at $\lambda = 1$.

so $J'_2/J'_1 \approx 0.97$, at $\lambda = 1$. Given are the bare series in orders seven, eight, and nine, and Padé extrapolants with the exponents $[4, 4]$, $[4, 5]$, and $[5, 4]$ for the EPP and bare series in orders six, seven and eight as well as extrapolants $[4, 4]$, $[3, 5]$, and $[5, 3]$ for the FPP together with the resultant mean values with corresponding standard deviations. The calculations for the FPP are more demanding, which is why we only reach order eight. The extrapolants of the FPP energies show a relatively large splitting of $\Delta \approx 0.001J$ at $\lambda = 1$ and are not very well converged. This behaviour can be understood if one considers the actual dependence of the FPP energies on λ in Fig. 8.3. At small perturbations, the energy increases up to $\lambda_F \approx 0.4$ due to the inclusion of the locally frustrating diagonal bond, which gives a positive first-order contribution of $0.0625/J'_1$ and is energetically expensive. For larger values of λ_F , this effect is suppressed by inter-plaquette interactions and the energy decreases again. The precise description of such a non-monotonous behaviour in a series expansion requires very high orders. In principle for the expansion about the EPP, this is similar, due to the difference in the nearest-neighbour couplings. However, this non-monotonous behaviour can be circumvented.

The associated first-order coefficient is $(1 - J'_2/J'_1)/4$. From the perturbative approach itself one naively expects the expansion to work best for $J'_1 \geq J'_2$, since this keeps the perturbatively included couplings the smallest. However, the specific first-order contribution makes an expansion with $\tilde{J}'_2 > \tilde{J}'_1$ favourable, which yields the identical model if $J'_1 = \tilde{J}'_2$, $J'_2 = \tilde{J}'_1$, and $\tilde{J} = J'_1/J'_2 \cdot J$ up to a scaling constant. The energies from this expansion are shown in the left panel of Fig. 8.3. They decrease already at small perturbations, in contrast to the FPP in the right panel and the EPP expansion

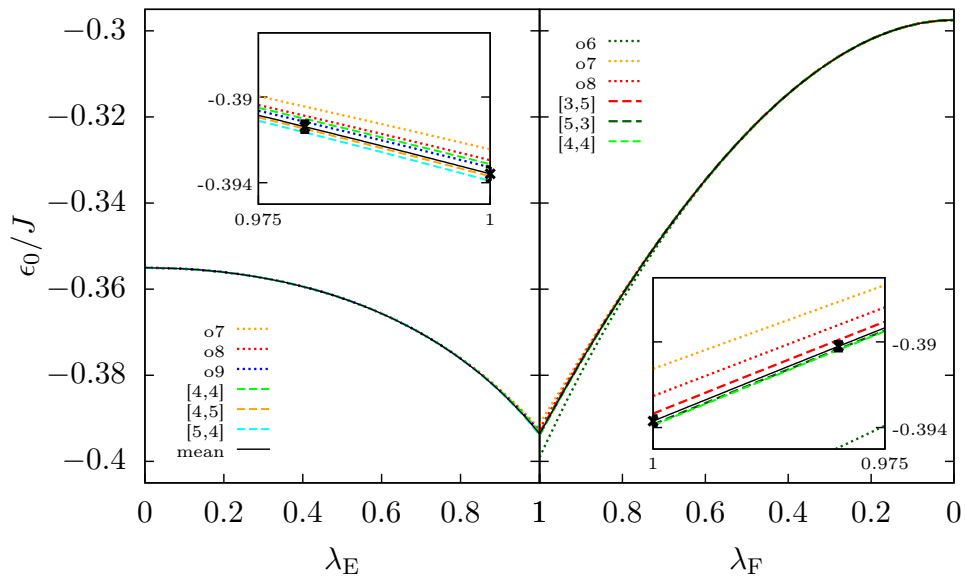


Fig. 8.4.: Ground-state energies as bare series, Padé extrapolants and mean values at $J/J'_1 = 1/0.72$ and $J/J'_2 = 1/0.7$ for the EPP on the left and for the FPP on the right. The Löwdin approach is employed on the perturbative Hamiltonian in Eq. (8.1.1) with $J_2^0 = 0.7/0.72$ for the EPP, and in Eq. (8.1.2) with $J_1^0 = 1/0.72$ for the FPP. The physically relevant extended Shastry-Sutherland model with $J'_1/J = 0.72$ and $J'_2/J = 0.7$ is reached at $\lambda = 1$.

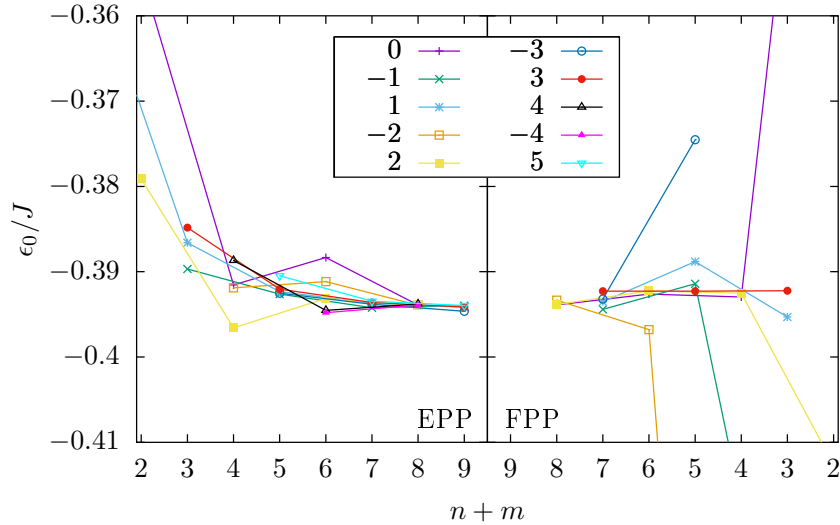


Fig. 8.5.: Ground-state energies from EPP on the left and FPP on the right for $J/J'_1 = 1/0.72$ and $J/J'_2 = 1/0.7$ from the unperturbed models with $J_2^0 = J'_2$ and $J_1^0 = J_1$, respectively. They are plotted as bare series and Padé extrapolants against the order. Members of the same families have the same colour and are labelled by the same difference between the exponents $n - m$.

with $J'_1 \geq J'_2$ (not shown). The difference between the energies of the EPP and FPP at $\lambda = 0$ is related to the scaling of the EPP approach with $\tilde{J}'_2 > \tilde{J}'_1$. The standard deviation for the energy of the EPP is noticeably smaller than of the FPP.

The Löwdin algorithm allows to start from initial models H_0 , which include the local asymmetry of the plaquettes and therefore the perturbations required to reach the extended Shastry-Sutherland model are weaker than with the pCUT. That is why, we expect these expansions to yield more accurate results in particular for the FPP. Here, we discuss the case where the asymmetries are completely included in the unperturbed models already. The energies at the same physical parameters ($J/J'_1 = 0.72$, $J/J'_2 = 0.7$) as before derived from unperturbed models with $J_2^0 = J'_2$ in Eq. (8.1.1) for the EPP and with $J_1^0 = J_1$ in Eq. (8.1.2) for the FPP depending on the perturbation parameters λ_E and λ_F are shown on the left and right in Fig. 8.4, respectively. Plotted are the highest bare orders eight and nine for the EPP and six, seven, and eight for the FPP as well as Padé extrapolants. For the EPP the series are very well converged, similar to the symmetric starting point, and we take the mean value of the Padé extrapolations $[4, 4]$, $[4, 5]$, and $[5, 4]$. For the FPP the mean value is taken from the Padé extrapolants $[4, 4]$, $[3, 5]$, and $[5, 3]$. In contrast to the unperturbed model with $J_1^0 = 0$, the series is monotonous here. The challenge is rather given by the relatively large difference between the energies at $\lambda = 0$ and $\lambda = 1$, which is more than twice as large for the FPP than for the EPP, due to the increased ground-state energy of a single plaquette with a diagonal bond. However, this difference is more accessible to series expansions and the splitting between various extrapolants at $\lambda = 1$ is smaller in the latter expansion. The energies of the FPP in the physical model at $\lambda = 1$ from the expansions with $J_1^0 = 0$ and $J_1^0 = 1/0.72$ differ noticeably by $\Delta\epsilon^{(F)} \approx 0.002J$, whereas for the EPP the energies from both expansions with and without asymmetry give rather similar energies. The

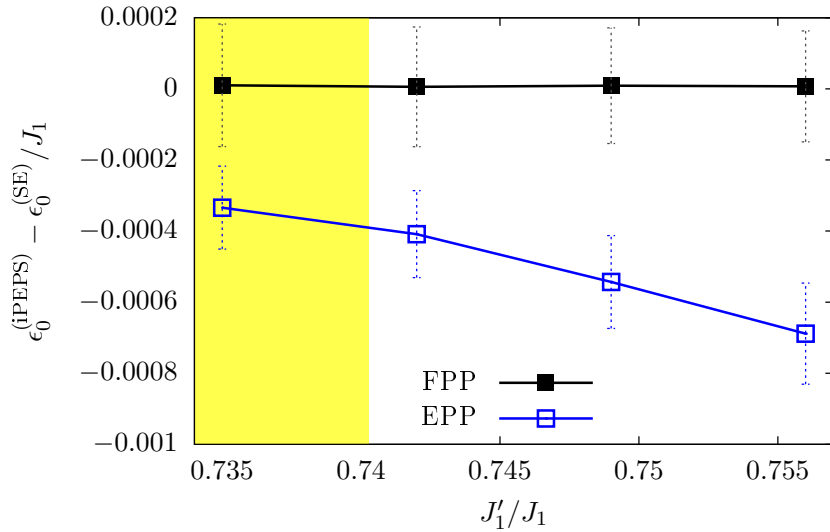


Fig. 8.6.: Energy differences between ground-state energies from iPEPS and series expansions along the line $J'_2/J_2 = 0.7$ with $J_1/J_2 = 1$. The yellow background colour indicates where the EPP is the ground state and no background colour signals the FPP as found by iPEPS. This figure is contained in the Supplemental Material of Ref. [79].

standard deviations of both expansions are comparable with these approaches.

An elaborate way to investigate the convergence behaviour employs Padé extrapolants grouped into families, so characterised by the difference between the exponents of nominator and denominator $n - m$. Then, the convergence within every family can be studied individually. For the same physical parameters as before, this is shown in Fig. 8.5, where the energies of the EPP and FPP from the unperturbed models with $J_2^0 = J_2$ and $J_1^0 = J_1$ are plotted against the order and characterised by the family. For the EPP, the different families are all converged in orders eight and nine. For the FPP, the large ground-state energy at $\lambda = 0$ leads to stronger deviations between the extrapolants than for the EPP. All values approach the same range of energies. The families 1 and -1 show an alternating behaviour with increasing orders. The family of extrapolants with identical exponents seems to be very well converged, so does the one with 2. Additionally, and for reasons of symmetry we employ the one with -2 , which leads to the average of $[3, 5]$, $[5, 3]$, and $[4, 4]$.

As another check, the energies from series expansions are compared with results from iPEPS by Schelto Crone, Ido Niesen, and Philippe Corboz. The energy differences between both methods can be seen in Fig. 8.6 along the line $J'_2/J_2 = 0.7$ for $J_1/J_2 = 1$. The error bars reflect the standard deviations from the Padé extrapolants of the series expansions and not the errors from iPEPS, which are $\approx 0.0002J_1$ for $J'_1/J_1 = 0.735$ and $\approx 0.0001J_1$ for $J'_1/J_1 = 0.75$. For these particular ratios $J'_2/J_2 = 0.7$, $J_1/J_2 = 1$, the iPEPS energies are extrapolated to the limit of infinite bond dimension. Details are given in the Supplemental Material of Ref. [79]. The FPP energies of both approaches agree extremely well, whereas for the EPP the difference between iPEPS and series expansions energies is larger with a value of $\approx 0.0005J_1$. This difference increases with

the ratio J'_1/J_1 , as does the standard deviation, because the asymmetry on the EPP super-sites becomes stronger, which corresponds to a larger perturbation. The point in parameter space at $\lambda = 0$ is noticeably closer to the distorted Shastry-Sutherland model of interest for the FPP than for the EPP, since one of the strong intra-dimer couplings is mainly included in the unperturbed part of the FPP expansion. In this sense, the perturbation for the EPP is larger, which might lead to an error on the EPP energies that is not reflected in the standard deviation of the Padé extrapolants, but would rather require higher-order calculations to become evident. Nevertheless, both methods yield only deviations in the order of $< 0.0007J_1$ and therefore agree very well. Note, that the standard deviations are smaller in the regime where the energy corresponds to the ground state of the system, compared to the area where it is not.

We also study Shastry-Sutherland models with distinct nearest-neighbour coupling and distinct dimer couplings J_1 and J_2 , where we only reach order eight for both plaquette phases. In order to efficiently probe a whole range of parameters, we choose a perturbative Hamiltonian in Eq. (8.1.2) with $J_1^0 = 1/0.74$ for the expansion about the FPP and include the local perturbation ΔJ_1 . For the EPP expansion we saw, that the difference between including or not including an initial asymmetry is very small, which is why $J_2^0 = 1$ is taken and then modified perturbatively with $\Delta J_2'$ in Eq. (8.1.1). The convergence behaves very similar to the case with $J_1 = J_2$ and we take a set of Padé extrapolants $[3, 5]$, $[5, 3]$, and $[4, 4]$. In the special case where only J_1 and J_2 are not identical for the EPP order nine was reached, and the extrapolants $[4, 5]$, $[5, 4]$, and $[4, 4]$ are used.

Next, we discuss the convergence behaviour of the excitation energies of the FPP. The EPP was studied similarly, which is not shown in detail. For the distorted orthogonal-dimer chain with $J_2' = 0$, $J_1 = 0.5$, and $J_2 = 1.2$, the convergence behaviour is illustrated at $\vec{k} = (\pi/2, \pi/2)$ in Fig. 8.7 for a perturbative model with $J_1^0 = 1$. At this set of parameters, the series are well converged and a mean value of the Padé extrapolants $[3, 4]$, $[4, 3]$, and $[4, 4]$ is plausible. If one considers smaller values of k though, where the two-triplon continuum crosses with the dispersive one-triplon mode, the Padé approximants of this one-triplon excitation yield physical divergencies corresponding to a finite decay of the mode into the two-triplon continuum. For the one-triplon dispersion and the two-triplon continuum shown in Fig. 9.4, we therefore take the mean value of the bare

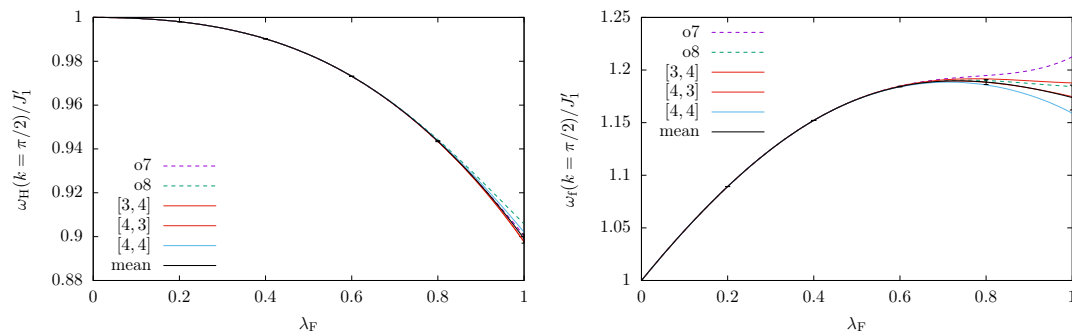


Fig. 8.7.: Convergence of both one-triplon branches ω_H (left) and ω_f (right) at $J_2' = 0$, $J_1 = 0.5$, and $J_2 = 1.2$ at $k = \pi/2$. Shown are the bare series in order seven and eight, several Padé extrapolants and their mean value with standard deviation as error bars.

series in order seven and eight. The flat one-triplon mode is protected by symmetry and the mean value of the Padé extrapolants [3, 4], [4, 3], and [4, 4] gives the most reliable result. For the two-dimensional distorted Shastry-Sutherland model, the convergence behaviour is generally worse than for the orthogonal-dimer chain. This has several reasons. Firstly, we only reach the series up to order six. Secondly, more perturbative exchange interactions have to be tuned to get from the unperturbed model to the two-dimensional model at $\lambda = 1$. To be precise, we investigate two perturbative models. The first model with $J_1^0 = J_1'^0$ is also accessible to pCUTs and has two triplons in the one-quasi-particle sector. At specific momenta with $\vec{k} = (k, k)$ as well as $\vec{k} = (\pm\pi, 0)$ and $\vec{k} = (0, \pm\pi)$, the two triplon modes are protected. For the second model with $J_1^0 = 1/0.74$, the degeneracy in H_0 is lifted and we consider the two lowest energy excitations, which are adiabatically connected to the two triplon modes studied with the first model $J_1^0 = J_1'^0$. The convergence in λ for $\vec{k} = (0, 0)$ is depicted for the physical parameters $J_2/J_2' = 1/0.74$, $J_1' = J_2'$, and $J_1 = 0.9J_2$ in Fig. 8.8. The Padé extrapolant [3, 3] of ω_H and [3, 2] for ω_f show nonphysical divergencies. The different starting points at $\lambda = 0$ lead to differing energies for the excitation ω_f at small perturbations. In the second expansion, the energy is closer to the value at physical parameters and the standard deviation is smaller than in the first approach as expected. The improved quality of convergence also stems from the fact, that both triplon modes in the first expansion typically mix and therefore more quantum fluctuations contribute. The energy values at $\lambda = 1$ from both perturbative models are similar.

The convergence behaviour is strongly dependent on the momentum value. For certain momenta, like $\vec{k} = (0, 0)$, the series converge and yield reliable results. In large areas of \vec{k} -space in the relevant parameter space of the extended Shastry-Sutherland model, however, the majority of extrapolants is affected by divergencies. This indicates decay, which is indeed the case, as explained in Section 10.2.2. The convergence of the dynamic structure factors determined in Section 10.3 is studied analogously.

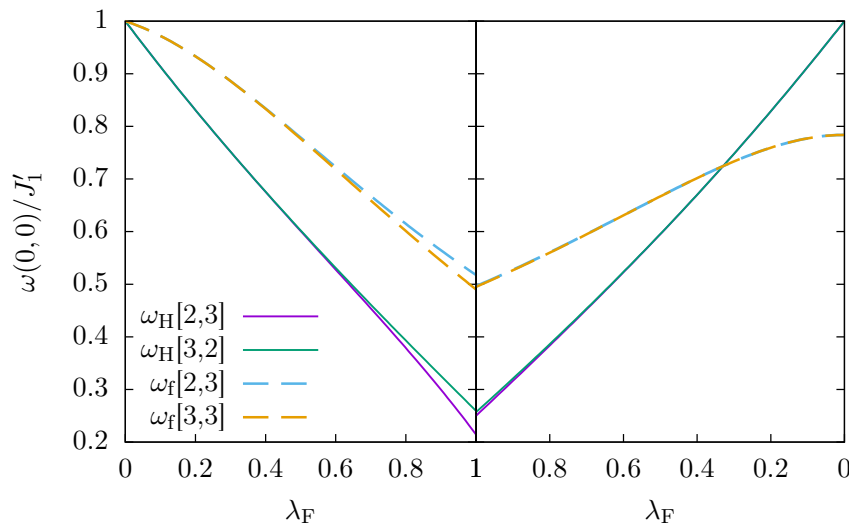


Fig. 8.8.: Excitation energies for the FPP at $\vec{k} = (0, 0)$, $J_1/J_1' = 1/0.74$, $J_1' = J_2'$, and $J_1 = 0.9J_2$ expanded around the limit with $J_1^0 = J_1'$ on the left and $J_1^0 = J_1$ on the right.

In this Chapter, we introduced a number of models, which are well suited to investigate plaquette phases in extended Shastry-Sutherland models. The lowest energy of these states, as well as excitation energies and dynamic structure factors can be determined in this way. Finally, we discussed the convergence behaviour for some of the derived series. These insights are applied in the following chapters on the asymmetrical orthogonal-dimer chain and two-dimensional extended Shastry-Sutherland models.

9. Asymmetric orthogonal-dimer spin chains

In the limit $J'_2 = 0$, the distorted Shastry-Sutherland model (7.3.3) reduces to decoupled orthogonal-dimer spin chains. They consist of filled plaquettes coupled by inter-plaquette interactions as depicted on the left in Fig. 9.1. This quasi one-dimensional model is very well suited to understand some of the main features also present in the distorted Shastry-Sutherland model. One of the first studies on this model is given in Ref. [217]. In the following, we study the phase diagram and excitations from two distinct perturbative approaches in H_0 : One with decoupled filled plaquettes, and one with decoupled inter-plaquette dimers and pairs of free spins. As we will see the phases present in both limits, the FPP and the Haldane phase, are actually identical. Some parts of this chapter are contained in the Supplemental Material of Ref. [79]. Here, we present additional detailed results in particular concerning the excitations of the FPP/Haldane phase.

9.1. Phase diagram

We start with series expansions about the limit $J'_1 \gg J_2$, which adiabatically connects to the FPP, where the plaquette singlets are located on the J_1 plaquettes (FPP J_1), and have protected quantum numbers $s_v = 1$. The ground-state energy is derived up to order eight in J_2/J'_1 for an unperturbed Hamiltonian with vanishing diagonal bonds $J_1^0 = 0$. The intra-plaquette diagonal interactions commute with the rest of the Hamiltonian and can be included by the energy per spin $\epsilon^0 = \epsilon_{J_1=0}^0 + J_1/16$, since the ground state has triplets on the diagonal $s_v = 1$. We take the average value of the Padé extrapolations with the exponents [3, 4], [4, 3], and [4, 4] and compare with the exact dimer singlet energies simply given by

$$\epsilon_0^d = \frac{1}{4} \left(-\frac{3}{4}J_1 - \frac{3}{4}J_2 \right) = -\frac{3}{8}(J_1 + J_2) . \quad (9.1.1)$$

The phase diagram is illustrated as the background colour with red for the dimer singlet phase and white for the FPP in Fig. 9.2. Clearly, for $J_2 = 0$, the phase transition point is at $J_1/J'_1 = 2$. With increasing inter-plaquette interactions J_2 the phase boundary shifts to smaller ratios J_1/J'_1 , somehow related to the average strength of the dimer couplings. For large inter-plaquette couplings $J_2 > 2.5$ the convergence behaviour of these series decreases significantly.

Another limit that can be investigated with series expansions is $J_2 \gg J_1, J'_1$ and $J_1 \gg J'_1$ [176, 213]. Here, we derive the model for the chain in order four. The ground state of the unperturbed system is degenerate and consists of the manifold of states with a singlet on the J_2 -bonds and isolated intermediate spins on the intra-plaquette

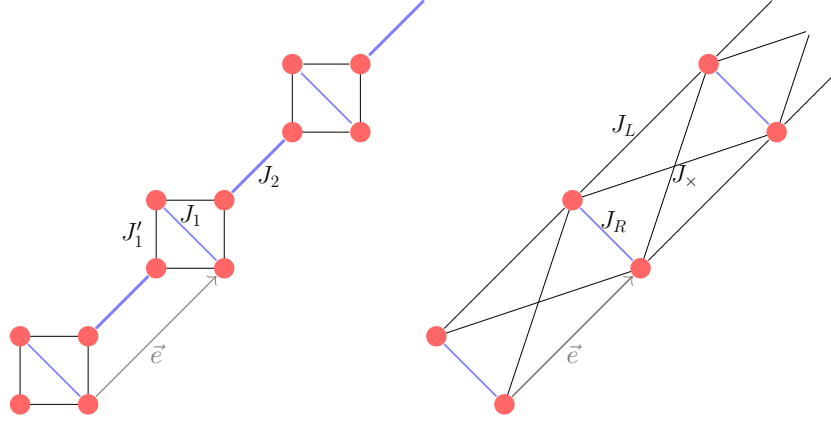


Fig. 9.1.: On the left, the orthogonal-dimer spin chain including the spatial unit cell vector in grey is sketched. On the right, the frustrated spin ladder giving the effective description in the limit $J_2 \gg J_1, J'_1$ is depicted.

diagonal bonds. In third order in J'_1/J_2 , the effective model is given by an effective frustrated Heisenberg ladder with rung couplings J_R , leg couplings J_L , and diagonal couplings between opposite sites of neighbouring rungs J_\times , with $J_L = J_\times$ as shown on the right of Fig. 9.1 (compare with the right panel of Fig. 7.13). In fourth-order perturbation theory, additional effective four-spin interactions arise. Also, the distorted Shastry-Sutherland model is no longer described by a one-dimensional effective model. For the asymmetric orthogonal-dimer chain, the effective Hamiltonian in order four is given by

$$\begin{aligned}
 H_{\text{eff}}^{\mathcal{O}(4)} = & N_s \cdot \epsilon_0 + J_R \sum_{\substack{i \\ j}} \vec{S}_i \cdot \vec{S}_j + J_L \sum_{i-j} \vec{S}_i \cdot \vec{S}_j + J_\times \sum_{\substack{i \times j \\ l \times k}} \vec{S}_i \cdot \vec{S}_k + \vec{S}_j \cdot \vec{S}_l \\
 & + J_K^R \sum_{\substack{i \quad j \\ l \quad k}} (\vec{S}_i \cdot \vec{S}_l)(\vec{S}_j \cdot \vec{S}_k) + J_K^L \sum_{i-j, l-k} (\vec{S}_i \cdot \vec{S}_j)(\vec{S}_l \cdot \vec{S}_k) + J_K^\times \sum_{\substack{i \times j \\ l \times k}} (\vec{S}_i \cdot \vec{S}_k)(\vec{S}_l \cdot \vec{S}_j) ,
 \end{aligned} \tag{9.1.2}$$

with the effective coupling parameters

$$\begin{aligned}
 J_R = J_1 - \frac{J_1'^2}{J_2} - \frac{1}{2} \frac{J_1'^3}{J_2^2} + \frac{5}{8} \frac{J_1'^4}{J_2^3}, \quad J_L = \frac{1}{2} \frac{J_1'^2}{J_2} + \frac{3}{4} \frac{J_1'^3}{J_2^2} - \frac{5}{8} \frac{J_1'^4}{J_2^3}, \\
 J_\times = J_L, \quad J_K^R = -\frac{1}{2} \frac{J_1'^4}{J_2^3}, \quad J_K^L = \frac{J_1'^4}{J_2^3}, \quad J_K^\times = J_K^L,
 \end{aligned} \tag{9.1.3}$$

and the constant

$$\epsilon_0 = -\frac{1}{4} \frac{J_1'^2}{J_2} - \frac{7}{8} \frac{J_1'^3}{J_2^2} + \frac{11}{8} \frac{J_1'^4}{J_2^3}. \tag{9.1.4}$$

For the analysis the third-order model is particularly useful, since it has been studied before [218]. The total spin quantum number on every rung is conserved and in the limit $J_R \gg J_L$, or $J_2 \gg J_1'^2/J_1$, the system exhibits a ground state with singlets on every

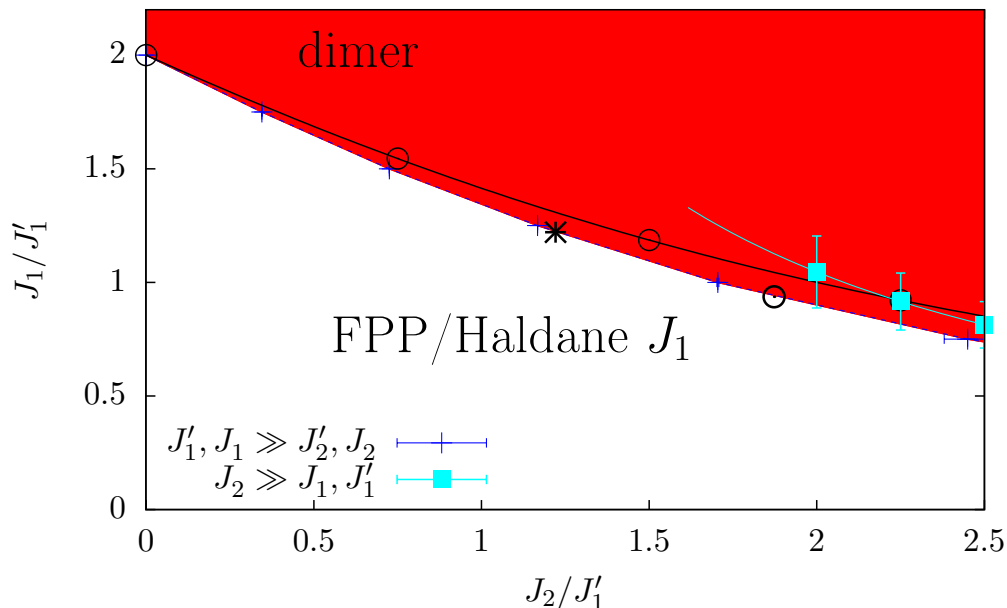


Fig. 9.2.: The phase diagram of the orthogonal-dimer chain with distinct dimer couplings J_1 and J_2 . The background colour shows results derived by series expansions around the limit $J_1' \gg J_2$. The red(white) area represents where the dimer singlet(FPP/Haldane J_1) phase is present. The phase boundary found from the limit $J_2 \gg J_1, J_1'$ and $J_1 \gg J_1'$ is illustrated in cyan. For comparison, a numerical phase transition point and an upper bound for the extension of the FPP/Haldane phase are shown as black circles from Ref. [213] and as a black star from Ref. [208]. This figure is contained in the Supplemental Material of Ref. [79].

rung. At $J_R/J_L \approx 1.4$, a first-order phase transition takes place to a state where all rungs are occupied by triplets. This state corresponds to a spin-1 chain and therefore is associated with the Haldane phase. In terms of the coupling constants of the asymmetric orthogonal-dimer chain, the phase transition is at $J_1|_{\text{cr}} \simeq 1.7 \frac{J_1^2}{J_2} + 1.55 \frac{J_1^3}{J_2^2} + 1.5 \frac{J_1^4}{J_2^3}$, where the fourth-order term is not exact due to the additional four-spin interactions. This phase transition by the average of the bare second-, third-, and fourth-order series is included as a cyan line in the phase diagram in Fig. 9.2. In the specific limit $J_2/J_1' \rightarrow \infty$, $J_1/J_1' = 0$, the Haldane phase is present, however an infinitesimal intra-plaquette diagonal coupling $J_1 > 0$ triggers the transition towards the dimer singlet phase [219]. Around $J_2/J_1' \approx 2$, the phase transition lines from both limits $J_2 \gg J_1, J_1'$ and $J_1' \gg J_2$ yield similar results, which hints towards the equality of the FPP and the Haldane phase. This is also implied by the ED results from Richter et al. along the line $J_1 = 0$, where no level crossings for the ground state occur [213]. We also included some results from the literature in our phase diagram in Fig. 9.2. In the symmetric case $J_1 = J_2$, our series expansions results agree very well with the value $J/J_1'|_{\text{cr}} = 1.22100$ by Koga et al. [208]. Along the line $J_2 = 2J_1$, the ED by Richter et al. revealed another transition point [213], which also matches our findings. In the latter work, a lower and an upper bound for the extension of the ground states of the non-frustrated model, i.e. the same ground states as for $J_1 = 0$, were derived. The lower bound is given by $J_1/J_1' = 0$, whilst the upper one is included as a black line with black circles in our

phase diagram. This upper limit lies just above the phase transition we discovered by series expansions and is therefore consistent.

An instructive picture for the equality of the FPP and Haldane phase has singlets on the inter-plaquette dimers and triplets on the intra-plaquette dimers. This setting is exactly what arises from the Haldane limit $J_2 \gg J_1, J'_1$. In the FPP, the plaquette singlets also have triplets as total diagonal spins $s_v = 1$. In this way, the features known for both phases are identical. This is of course not a proof, but the statement is strongly supported numerically as shown in Subsection 10.1.3. We therefore refer to it as the FPP/Haldane phase in the following. It is the FPP/Haldane J_1 phase if the dressed plaquette singlets are located on plaquettes including a diagonal J_1 -bond. The equality is also discussed for the distorted Shastry-Sutherland model with distinct dimer couplings in Subsection 10.1.1.

9.2. Excitations

The excitations of the FPP/Haldane phase on the orthogonal-dimer chain are very closely related to the ones in extended two-dimensional Shastry-Sutherland models. The momentum vector of the Shastry-Sutherland lattice, $\vec{k} = (k_x, k_y)^T$, and the orthogonal-dimer chain, k , are connected by $k = k_x + k_y$ as illustrated in Fig. 9.1. In order to understand the excitations, we employ the same limits as for the ground-state energies. From the unperturbed model of decoupled filled plaquettes $J'_1 \gg J_2$, it is expected that there are two low-lying triplet excitations in the FPP/Haldane J_1 phase if the coupling values are comparable $J_1 \approx J'_1$ as becomes clear from the energy spectrum of a single filled plaquette in Fig. 7.8. The total diagonal spins s_v^p are conserved on every plaquette individually on the chain, so states with distinct quantum numbers are protected and therefore show actual level crossings and not anti-crossings in the energy spectrum. For small inter-plaquette couplings J_2/J'_1 and small diagonal couplings $J_1 \lesssim J'_1$, the first excitation is the triplet with $s_v^p = 1$, for which hopping between super-sites occurs in first-order perturbation theory. Its dispersion is labelled with $\omega_H(k)$. At $J_1 \approx J'_1$, the first and second excitation are expected to cross. The first excitation $\omega_f(k)$ at $J_1 \gtrsim J'_1$ is four-fold degenerate and has $s_v^p = 0$, which is why it does not hop on top of the ground-state background where all plaquettes have $s_v^p = 1$. The dispersion is completely flat.

In the following, we start the investigation with the symmetric orthogonal-dimer spin chain $J_1 = J_2 \equiv J$ before studying the asymmetric case with $J_1 \neq J_2$, where also series expansions from the limit $J_2 \gg J_1, J'_1$ are employed. The magnetic excitations for two choices of diagonal couplings $J = 1.2J'_1$ and $J = J'_1$ are shown in Fig. 9.3(a) and (b), respectively. These include the two low-lying triplon modes $\omega_H(k)$ and $\omega_f(k) \equiv \omega_f$ as well as the two-triplon continuum from two modes $\omega_H(k)$. The flat mode is protected from this continuum by distinct values of s_v^p . The two-quasi particle continuum of two flat modes is at an energy $2 \cdot \omega_f$, so at least under the inclusion of these low-energy excitations the flat mode does not decay. However, the other mode $\omega_H(k)$ decays and the extrapolations show divergencies in this area. That is why, the average of the bare series in order seven and eight in λ is used. The continuum is extrapolated with the Padé extrapolants with exponents $[3, 4]$ and $[4, 3]$, which is possible since only the energies around the gap are relevant. For the flat mode ω_f , the extrapolants $[4, 3]$ and $[4, 4]$ are used. The standard deviations are shown as error bars and we note that the

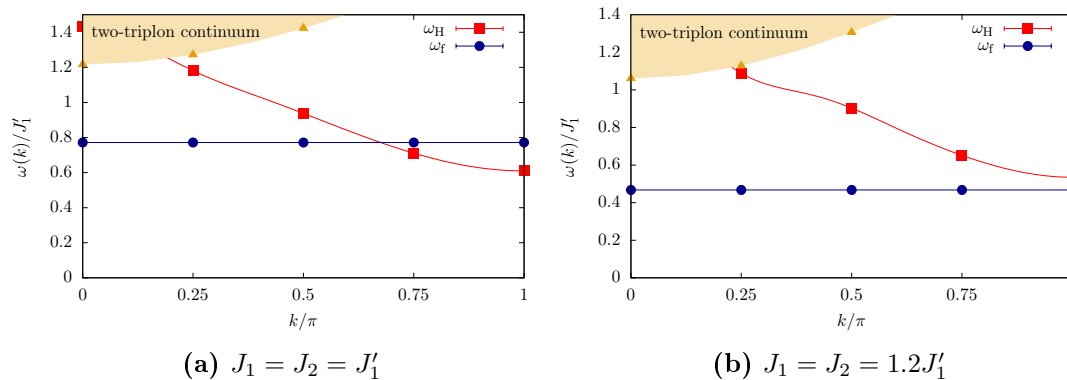


Fig. 9.3.: Magnetic low-energy excitations for the symmetric orthogonal-dimer spin chain. The excitations are protected by symmetry and the lower dispersionless excitation is given by the triplet with $s_v^p = 0$. The yellow area indicates the two quasi-particle continuum. For details on the extrapolations see the text.

series are well converged. The dispersive mode $\omega_H(k)$ evolves a minimum at $k = \pi$ and decays into the continuum for small momenta around $k = 0$. The relative position of the flat mode ω_f depends on the value of the diagonal coupling J/J_1' . An increasing diagonal coupling J triggers a lowering of the flat mode, exemplified by the difference between the left and the right panel of Fig. 9.3. It can be understood from an increasing intra-plaquette diagonal coupling J_1 , which lowers the energy of the $s_v^p = 0$ excitation and increases the energy of the $s_v = 1$ ground state. The dispersive mode $\omega_H(k)$ is not effected. This is plausible, since it has the same total diagonal quantum numbers $s_v = 1$ as the ground state. For couplings close to the phase transition towards the dimer singlet phase at $J_c = 1.221J_1'$, the energy gap stems from the flat mode, which was discovered in Refs. [208, 217].

In the asymmetric orthogonal-dimer chain, the phase transition from the FPP/Haldane J_1 phase to the dimer singlet phase is shifted to larger values of J_2 for $J_1 < J_2$ in respect to $J_1 = J_2$ as seen in Section 9.1. A magnetic excitation spectrum for the asymmetric orthogonal-dimer chain with $J_1 = 0.5J_1'$ and $J_2 = 1.2J_1'$ is shown in Fig. 9.4. Again, the bare series in orders seven and eight are used for the dispersive mode $\omega_H(k)$. The flat mode ω_f is shown as the average of the extrapolants with the exponents [4, 3] and [4, 4], whereas for the continuum also [3, 4] yields valid results. The spectrum does not look fundamentally different to the symmetric case. The energy gap is located at $k = \pi$ and is given by the dispersive mode $\omega_H(k)$. It decays into the two quasi-particle continuum at small momenta. The flat excitation at these parameters lies above the Haldane mode and also overlaps with the continuum, still it does not decay. The general tendency is such that an increasing inter-plaquette coupling J_2 shifts the flat band higher, whereas the dispersion of the other band becomes more pronounced and eventually yields a local maximum at intermediate momenta $k \approx 0.45\pi$. All these three features, the gap at $k = \pi$, a local maximum, and decay at $k = 0$, are also known from the spin-1 Heisenberg chain [209] and this set of parameters is already somehow close to the Haldane limit with $J_2 \gg J_1', J_1$ and $J_1 \gg J_1'$, discussed below. The same tendency for increasing J_2 is also present in the symmetric case comparing $J = J_1'$ and $J = 1.2J_1'$ in Fig. 9.3(a) and (b), where the dispersive band gets a hump at intermediate momenta with increasing

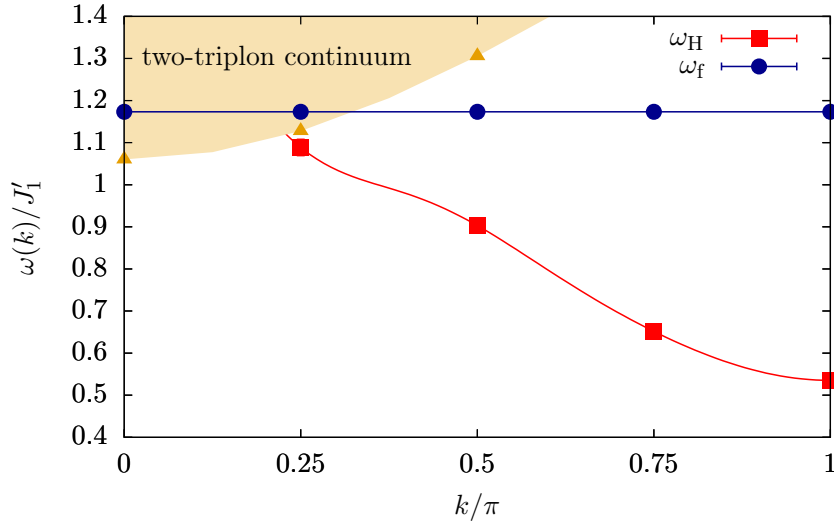


Fig. 9.4.: One quasi-particle excitations for the asymmetric orthogonal-dimer spin chain. The diagonal couplings are chosen as $J_1/J'_1 = 0.5$ and $J_2/J'_1 = 1.2$. The shaded area indicates the two quasi-particle continuum. This figure is contained in the Supplemental Material of Ref. [79].

diagonal coupling J . For $J = J'_1$, it is nearly linear in k , whereas for $J = 1.2J'_1$ an almost saddle-point is present.

Starting from the other limit $J_2 \gg J_1, J'_1$ and $J_1 \gg J'_1$, it is known that the Haldane phase of the spin-1 chain exhibits a low-lying dispersive excitation. The minimum gives the Haldane gap $\Delta_H = 0.41$ at $k = \pi$ [209, 220] and the mode decays at small momenta into a continuum [209]. In terms of the frustrated ladder shown in the right panel of Fig. 9.1, the energy gap is $\Delta_H = 0.41J_L$. Another excitation is given by a rung singlet and is therefore completely localised, on top of the background of rung triplets. The excitation energy of this state is linked to the energy difference between a spin-1 chain with periodic and with open boundary conditions. It has been determined to be $1.21J_L$ [218]. In terms of the frustrated ladder with an interaction on the bond of the flipped triplet, the energy gained by the local singlet needs to be subtracted $\Delta_f = 1.21J_L - J_R$. The excitation energies from this second approach are not included in Fig. 9.3, because the series are too erratic. Similarly, the energy gap extrapolated from both distinct limits is not accurate enough to give comparable results.

At last, we make contact between the asymmetrical orthogonal-dimer chain and $\text{SrCu}_2(\text{BO}_3)_2$ under pressure in the intermediate phase, despite the fact that this is a very rudimentary description of the quantum material. The INS data shows, that the ratio between the two lowest excitations at $\vec{k} = \vec{0}$ is roughly two [76]. The energy gap must be located somewhere close to $\vec{k} = \vec{0}$ as becomes clear from the comparison of specific heat and INS data [76, 77]. Therefore, we study the ratio Δ_f/Δ_H at $k = \pi$, where the gap occurs in the asymmetric orthogonal-dimer chain. Also, the dispersive mode in the orthogonal-dimer chain decays at zero momentum. A detailed comparison between theoretical findings and measurements on $\text{SrCu}_2(\text{BO}_3)_2$ under pressure is given in Section 10.4.

In Fig. 9.5, the background colour illustrates the ratio between the excitations Δ_f/Δ_H

from the series expansions around $J'_1 \gg J_2$ with averages or single values of the Padé extrapolants with the exponents [3, 4] and [4, 3] depending on the parameters. The convergence breaks down in the white area. The most relevant ratios $\Delta_f/\Delta_H = 2$ and $\Delta_f/\Delta_H = 1/2$ are indicated by dashed lines as well. From the large- J_2 limit the excitation energies together with the apparent interaction constants of the effective model in Eq. (9.1.3) yield the parameters at which the ratio Δ_f/Δ_H between both excitation energies is equal to two

$$\left. \frac{J_1}{J'_1} \right|_{\Delta_f/\Delta_H=2} = 1.19 \frac{J'_1}{J_2} + 0.79 \left(\frac{J'_1}{J_2} \right)^2 - 0.87 \left(\frac{J'_1}{J_2} \right)^3. \quad (9.2.1)$$

The average of this result in orders two, three, and four is plotted as a dashed magenta line in Fig. 9.5. The ratios between the excitation energies from both series expansions give somewhat similar values for $1.5J'_1 \lesssim J_2 \lesssim 2J'_1$. Both cases $\Delta_f/\Delta_H = 1/2$ and $\Delta_f/\Delta_H = 2$ are present in the studied parameter regime. The latter is realised from both limits, along a line nearly parallel to the phase transition line to the dimer phase.

In this chapter, we resolved the full phase diagram of the asymmetric orthogonal-dimer chain by series expansions from two distinct limits, and found evidence for the equality of the FPP and the Haldane phase. The Haldane phase is connected to the limit with singlets on inter-plaquette J_2 -bonds and triplets forming on the intra-plaquette

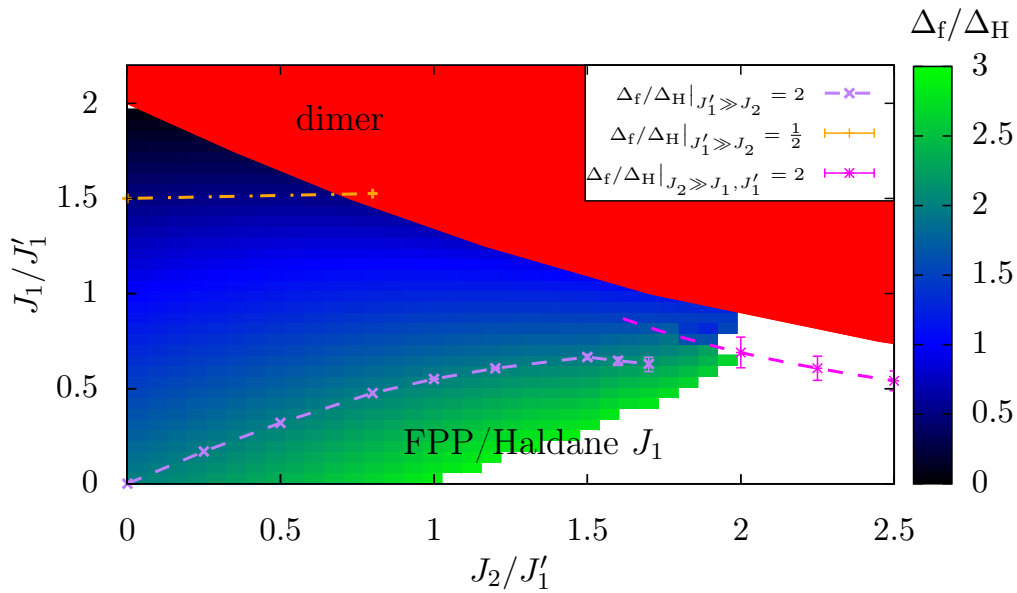


Fig. 9.5.: Same parameter space as for the phase diagram in Fig. 9.3. Here, for the FPP/Haldane J_1 phase the ratios between excitation energies Δ_f/Δ_H at $k = \pi$ are included. The plain red background colour at the top right shows the extension of the dimer singlet phase. In the other area, the background colour indicates the excitation ratios from series expansions about the limit $J'_1 \gg J_1$. Important ratios are marked additionally. For the choice of extrapolants see the text. From the second limit $J_2 \gg J_1, J'_1$, only the ratio $\Delta_f/\Delta_H = 2$ is marked. The convergence of the excitations breaks down in the white area.

diagonal J_1 -bonds, which fits with the triplets on these bonds present in the FPP. We therefore extended the previous knowledge on the asymmetric orthogonal dimer-chain by an extensive study of the phase diagram, which is now known not only for particular parameters, but over the whole parameter range. We then studied the magnetic low-energy excitations in momentum space. The FPP evolves a dispersionless triplon mode, which yields the energy gap close to the dimer phase, whereas otherwise it is given by a dispersive triplon mode at $k = \pi$. In the limit of large J_2 -couplings, the excitation spectrum resembles the one of the Haldane phase. At last, the ratio between both excitation energies at $k = \pi$ was investigated in an extended area, in order to make a first contact to experiments on $\text{SrCu}_2(\text{BO}_3)_2$. Such a study of the two triplon excitations in momentum space for several parameters showing tendencies for varying couplings was not performed before. In the following chapter, similar studies are done for two-dimensional extended Shastry-Sutherland models.

10. Extended Shastry-Sutherland models

In this chapter, the extended Shastry-Sutherland model with nearest-neighbour couplings, J'_1 and J'_2 , and diagonal dimer couplings, J_1 and J_2 , from Eq. (7.3.3) depicted in Fig. 7.15 is investigated. We determine the ground-state phase diagrams, as well as excitations and dynamic structure factors of plaquette singlet phases. For the two-dimensional Shastry-Sutherland model, the sectors with distinct total diagonal dimer spins s_V^p are not decoupled. The main findings given in this chapter are published in Ref. [79]. Here, the results are described in more detail, and additional results, in particular for phase diagrams of the completely distorted Shastry-Sutherland model, the dispersions, and the comparison with experiments, are presented. All iPEPS calculations were performed by Schelto Crone, Ido Niesen, and Philippe Corboz.

10.1. Phase diagrams

At first, the phase diagrams for an asymmetric choice of differently oriented diagonal coupling strengths, J_1 and J_2 , and symmetric nearest-neighbour couplings, $J'_1 = J'_2$, [Eq. (7.3.2)] is considered. At second, the case with $J_1 = J_2$ and distinct nearest-neighbour couplings is studied [Eq. (7.3.1)], and we give some details on the determination of the phase diagrams. In the end, both cases are connected in the completely asymmetric model with four distinct coupling strengths. Here, we demonstrate the equality of the FPP and the Haldane phase, ergo the FPP/Haldane phase. We perform series expansions of the ground-state energies over the limit $J'_1 \gg J_2$ for the EPP and FPP/Haldane phase, where the Hamiltonians in Eq. (8.1.1) with $J_1^0 = J_2^0$ and Eq. (8.1.2) with $J_1^0 = 1/0.74$ are employed, respectively. The energy of the dimer singlet phase is known exactly, compare Eq. (9.1.1). Further details are given in Chapter 8 and are discussed in Subsection 10.1.2. The phase diagrams were also determined with iPEPS by Schelto Crone, Ido Niesen, and Philippe Corboz, who additionally to the series expansions resolved the transition towards the Néel phase and calculated magnetic correlations. A precise knowledge on the phase diagrams is required for the study of the excitation spectra in the next section.

10.1.1. Distinct dimer couplings

In this subsection, we revisit the former findings on the extended Shastry-Sutherland model with different dimer couplings J_1 and J_2 (Fig. 7.13) discussed in Section 7.3. Our ground-state phase diagram is given in Fig. 10.1. The energies from series expansions are averaged over the Padé extrapolants [4, 4], [4, 5], and [5, 4] for the EPP and over [3, 5], [5, 3], and [4, 4] for the FPP/Haldane phase. The phase diagram in Fig. 10.1 also contains the iPEPS results, which yield the phase transition line towards the Néel phase. Qualitatively, our findings are the same as in the left panel of Fig. 7.14 [176].

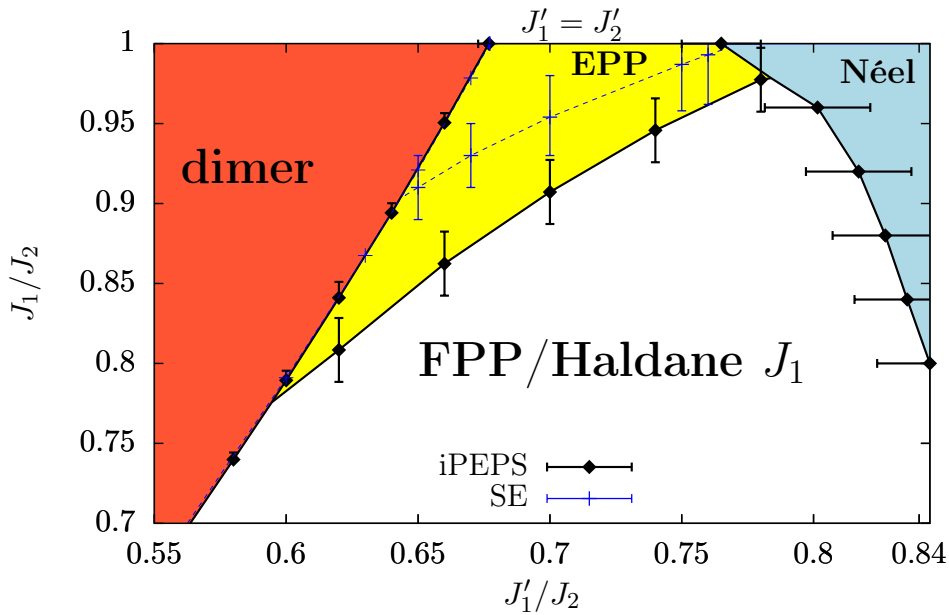


Fig. 10.1.: Phase diagram of the extended Shastry-Sutherland model with varying coupling strengths on the diagonal couplings and identical nearest-neighbour couplings $J'_1 = J'_2$, based on series expansions of the ground-state energies in order nine for the EPP and order eight for the FPP/Haldane phase and iPEPS. This figure is published in Ref. [79].

For the symmetric Shastry-Sutherland model ($J_1/J_2 = 1$) with increasing ratio J'_1/J_2 the dimer singlet, EPP, and Néel phase occur. The EPP present in the symmetric Shastry-Sutherland model, is ruled out by the FPP/Haldane phase under the inclusion of asymmetric dimer couplings. We find that the extension of the EPP is considerably reduced in comparison to previous results [176], and accordingly the FPP/Haldane J_1 phase is stabilised in a much larger parameter range that extends up to $J_1/J_2 \simeq 0.98$, very close to the isotropic point. The empty plaquette singlet state in this extended model remains two-fold degenerate as in the symmetric Shastry-Sutherland model, since both sets of empty plaquettes hosting singlets are identical. In contrast, both sets of filled plaquettes differ by $J_1 \neq J_2$ and the filled plaquette singlet states are non-degenerate. So, if one exchanges the ratio $J_1/J_2 < 1$ by $J_2/J_1 < 1$ the location of the filled plaquette singlets changes from the plaquettes including a J_1 -bond to the ones with a J_2 -bond. Therefore, the phases at both distinct ratios are not identical, and are labelled by FPP/Haldane J_1 and J_2 phase. The phase boundaries are symmetric under $J_1 \leftrightarrow J_2$ as long as $J'_1 = J'_2$.

The results from series expansions and iPEPS agree quite well for the transition between the dimer and the plaquette phases, in contrast to a larger difference for the transition between the FPP/Haldane phase and the EPP, where the series expansions finds the latter to be less extended. This issue is discussed in the next subsection along the energies shown in Fig. 10.5.

In the limit of strong dimer couplings $J_2 \gg J'_1, J'_2, J_1$, the effective model up to order three is identical to the one for the one-dimensional asymmetric-orthogonal dimer chain [176]. For $J_2 \gg J_1^2/J_1, J_2 \gg J_2^2/J_1$ the Haldane J_1 phase is realised, which is

singlet-like on the inter-plaquette singlet J_2 -bonds and triplet-like on the intra-plaquette singlet J_1 -bonds, therefore $J_1 < J_2$ yields a lower energy than $J_2 = J_1$. That is why, the Néel phase is pushed to larger inter-dimer couplings with an increasing asymmetry between the dimers. Unsurprisingly, we can not resolve the phase boundary between the FPP/Haldane and the dimer singlet phase close to the large- J_2 limit by series expansions from $J'_1 \gg J_2, J_1, J'_2$, due to an insufficient quality of convergence.

The same situation with $J'_1 = J'_2$ is depicted in the phase diagram in Fig. 10.2, which we refer to in Subsection 10.1.3, where it is connected to asymmetric orthogonal-dimer chains. Here, the symmetric Shastry-Sutherland model is located on the diagonal with $J_1 = J_2$. The area of the Néel phase is not precise, but only determined from two known points for the symmetric Shastry-Sutherland model $J_1/J' = J_2/J' = 1/0.765 \approx 1.31$ [74] and for a vanishing diagonal coupling $J_2 = 0$ and $J_1/J' \approx 1/0.59 \approx 1.7$, $J_1 = 0$ and $J_2/J' \approx 1.7$ [176]. In this phase diagram, both distinct FPP/Haldane J_1 and J_2 phases with singlets on differing filled plaquettes are present. For $J_1 < J_2$, the plaquette singlets with triplet-like diagonals are located on the J_1 -plaquettes (FPP/Haldane J_1), whereas for $J_1 > J_2$ they are on the J_2 -plaquettes (FPP/Haldane J_2). These two phases in this parameter space are separated by the EPP.

The spin-spin correlations of the EPP for the symmetric Shastry-Sutherland model with $J'/J = 0.7$ from iPEPS are shown in Fig. 10.3(a). As expected, the bonds around one set of empty plaquettes are strongly negative, indicating the singlet structure. The symmetry between both sets of plaquettes is spontaneously broken, which is possible with iPEPS in contrast to ED. The correlations for the FPP/Haldane J_1 phase at $J'_1 = J'_2$, $J_1/J_2 = 0.9$, and $J'_2/J_2 = 0.74$ are given in Fig. 10.3(b), where strong bonds exist around one set of full plaquettes. All dimer bonds are positive. However, the intra-plaquette singlet J_1 -dimers are more so. Clearly, the specific correlation values depend

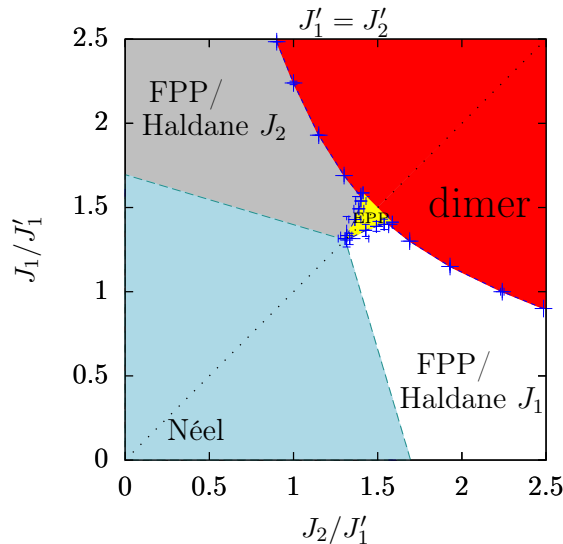


Fig. 10.2.: Phase diagram of the extended Shastry-Sutherland model with distinct diagonal couplings J_1 and J_2 from series expansions around the limit of decoupled plaquettes. The area of the Néel phase is only an estimate apart from the limiting cases $J_1/J'_1 = 0$, $J_2/J'_1 = 0$, and $J_1/J'_1 = J_2/J'_1$.

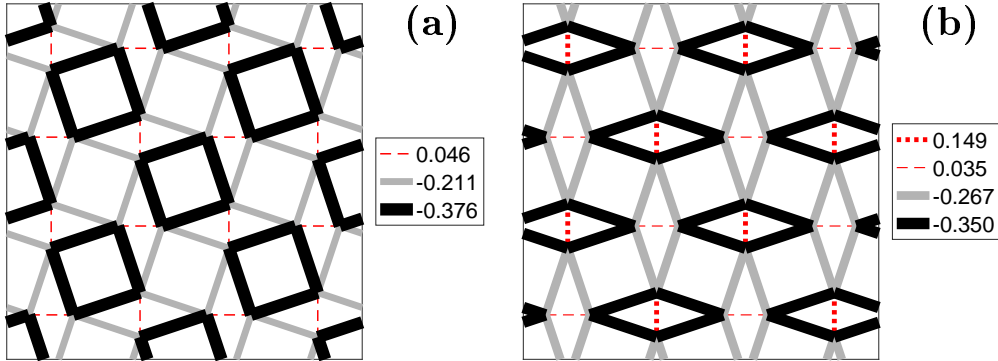


Fig. 10.3.: Spin-spin correlations (a) in the EPP at $J'_1 = J'_2$, $J'_1/J_1 = J'_2/J_2 = 0.7$ and (b) in the FPP/Haldane J_1 phase at $J'_1 = J'_2$, $J_1 = 0.9J_2$, and $J'_2/J_2 = 0.74$ obtained with iPEPS. This figure is published in Ref. [79].

on the set of parameters. In Fig. 10.3(b) at $J'_1 = J'_2$, $J_1/J_2 = 0.9$, and $J'_2/J_2 = 0.74$, the FPP/Haldane J_1 phase is relatively close to the isotropic point and the signature of strong plaquettes dominates over the formation of inter-plaquette singlet-like dimers. Similar correlations from ED at $J_2/J_1 = 0.2$, $J'/J_1 = 0.4$ are shown in the right panel on the bottom right of Fig. 7.14 [176]. At these parameters, the one-dimensional nature of the Haldane phase is more pronounced and the inter-plaquette singlet diagonals are strongly negative, whereas the intra-plaquette singlet diagonals remain positive.

The perturbative understanding of the FPP/Haldane J_1 and J_2 phases depends on the choice of plaquette on the lattice in the unperturbed model H_0 . In the limit $J'_1 \gg J_1, J_2$, plaquette singlets with $s_v^p = 1$ are located on the plaquettes with diagonal J_1 -couplings. This corresponds directly to the limiting case of the Haldane phase $J_2 \gg J'_1, J'_2, J_1$ with $J_2 \gg J_1^2/J_1$, $J_2 \gg J_2^2/J_1$, where singlets form on the J_2 -bonds, and triplets on the J_1 -bonds. In this description, the Haldane and FPP are the same phases and the transition present for an isolated plaquette at $J/J' = 2$ relates to an exchange of the Haldane dimer singlets and filled plaquette singlets from one set of plaquettes to another.

10.1.2. Distinct nearest-neighbour couplings

The extended Shastry-Sutherland model with nearest-neighbour couplings $J'_1 \neq J'_2$ around plaquettes including differently oriented diagonal bonds $J_1 = J_2$ is defined in Eq. (7.3.1) and depicted in the left panel of Fig. 7.10. It was first studied by Takushima et al. in Ref. [73], however they did not distinguish between the FPP and the EPP. This is exactly the issue we tackle in the following. Our phase diagram from series expansions, with extrapolants [4, 4], [4, 5], and [5, 4] for the EPP and [3, 5], [5, 3], and [4, 4] for the FPP/Haldane phase, and iPEPS is shown in Fig. 10.4.

The symmetric Shastry-Sutherland model ($J'_1 = J'_2$) is included on the diagonal. In this case, again, the exact dimer singlet phase (red) at strong dimer couplings, the EPP (yellow) in the intermediate regime, and the Néel phase (blue) at small dimer couplings occur. For weakly distorted nearest-neighbour couplings $J'_1 \neq J'_2$, the EPP remains stable. At a critical distortion, the strengths on one set of filled plaquettes is

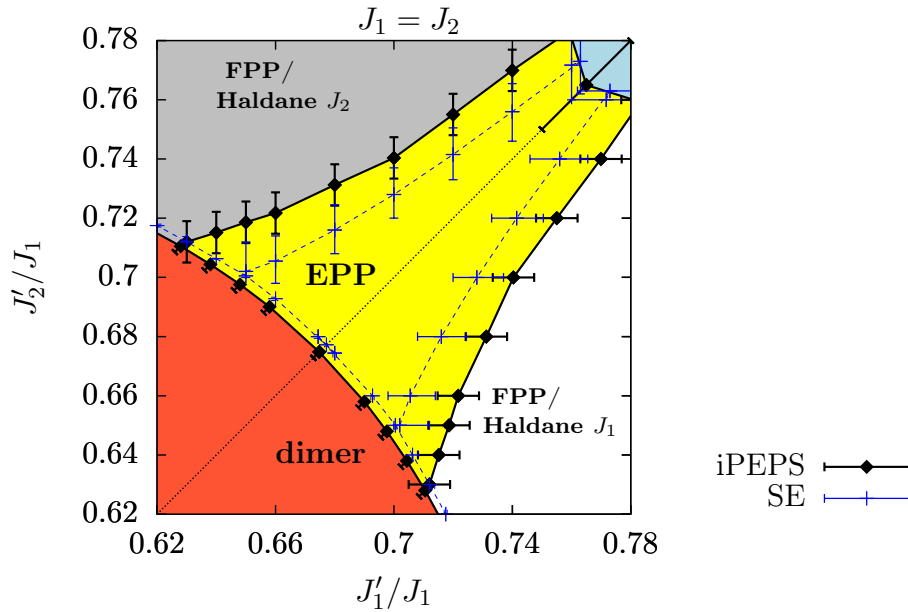


Fig. 10.4.: Phase diagram of the extended Shastry-Sutherland model for identical diagonals $J_1 = J_2$ and varying nearest-neighbour couplings based on series expansions and iPEPS. This figure is published, up to small modifications, in Ref. [79].

large enough to trigger the formation of plaquette singlets on these plaquettes, and the FPP/Haldane phase (white) arises. As for the model with distinct diagonal couplings, there are the same two choices of filled plaquettes. The distortion $J'_1 > J'_2$ leads to the FPP/Haldane J_1 phase, whereas $J'_2 > J'_1$ yields the FPP/Haldane J_2 phase. The phase transition between the dimer and the plaquette singlet phases mainly relates to the average of the nearest-neighbour couplings J'_1 and J'_2 . The Néel phase occurs at larger ratios of J'_1/J_1 , J'_2/J_1 with increasing asymmetry $J'_1 \neq J'_2$ as can be seen in the left panel of Fig. 7.12 [73]. This is plausible, since the increased nearest-neighbour couplings around one set of plaquettes favour the FPP/Haldane phase. The phase boundary between the EPP and the Néel phase again relates to the average of the nearest-neighbour couplings.

All phase diagrams are derived by comparing the lowest energies in relevant phases. In Fig. 10.5, this is exemplified for varying J'_1/J_1 at $J'_2/J_1 = 0.7$. The same values are given as differences between iPEPS and series expansions results in Fig. 8.6, where also the errors of the iPEPS energies, of the order $\approx 0.0002J_1$, are discussed. The energy of the dimer singlet phase $\epsilon_0/J_1 = -3/8 = -0.375$ lies well above the ones of the plaquette phases. The challenge in determining the phase boundary accurately stems from the very similar slopes of both energies. Already small uncertainties lead to relatively large uncertainties for the phase transition. This can be seen by the error bars in Fig. 10.4, which are much larger for the transitions between the EPP and FPPs/Haldane phases for both methods, in contrast to the plaquette singlet to dimer singlet transition, since the dimer singlet energy is constant and exact. The EPP energies from series expansions are not quite as low as from iPEPS, as discussed in Section 8.3, which is the reason for the decreased extension of the EPP in the phase diagrams. For all phased diagrams,

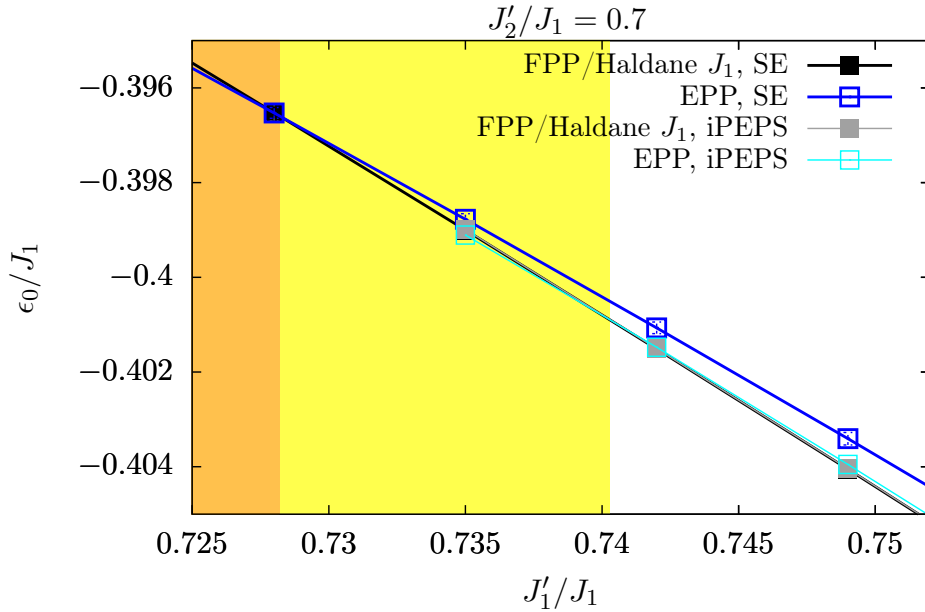


Fig. 10.5.: Ground-state energies per site of the empty and full plaquette states along the line $J'_2/J_1 = 0.7$ calculated with iPEPS and series expansions (SE) about the perturbative limit with $J_2^0 = J_1$ for the EPP and with $J_1^0 = 1/0.74$ for the FPP/Haldane J_1 phase. The choice of Padé extrapolants is given in the text. Note, that the FPP energies from series expansions basically coincides with the one from iPEPS and lie behind. The yellow background indicates, where the EPP is found by iPEPS, and the orange background where the EPP is found by iPEPS and series expansions.

where we do not show data from iPEPS, it is therefore plausible to assume, that the area of the EPP is larger than shown.

At $J'_2 = 0$, the model reduces to orthogonal-dimer chains containing only plaquettes with diagonal J_1 -bonds, and therefore solely the FPP/Haldane J_1 phase occurs. From this one-dimensional limit increasing inter-chain couplings $J'_2 > 0$ favour the FPP/Haldane J_1 phase over the dimer singlet phase and the phase transition shifts to smaller ratios J'_1/J_1 , as was already observed by Koga et al. [208] shown in the left panel of Fig. 7.12. The model with distinct nearest-neighbour couplings does not contain the Haldane limit, since $J_1 = J_2$. Both limits exist in the fully distorted Shastry-Sutherland model.

10.1.3. Completely distorted

The model in the completely distorted case is shown in Fig. 7.10. In the following, we start from previously discussed special cases and include further distortions in order to see when the phase transition to the FPP/Haldane phase is triggered, and to show that the FPP and the Haldane phase are identical. We start by connecting the asymmetric orthogonal-dimer chain $J'_2 = 0$, $J_1 \neq J_2$ to the extended Shastry-Sutherland model with identical nearest-neighbour couplings $J'_1 = J'_2$. Next, we deform the extended Shastry-Sutherland model with distinct diagonal couplings $J_1 \neq J_2$ to slightly different nearest-neighbour couplings $J'_1 \neq J'_2$, which is in particularly interesting for the case, where $J_1 > J_2$ and $J'_2 < J'_1$. At last, we connect the FPP and Haldane phase in a phase

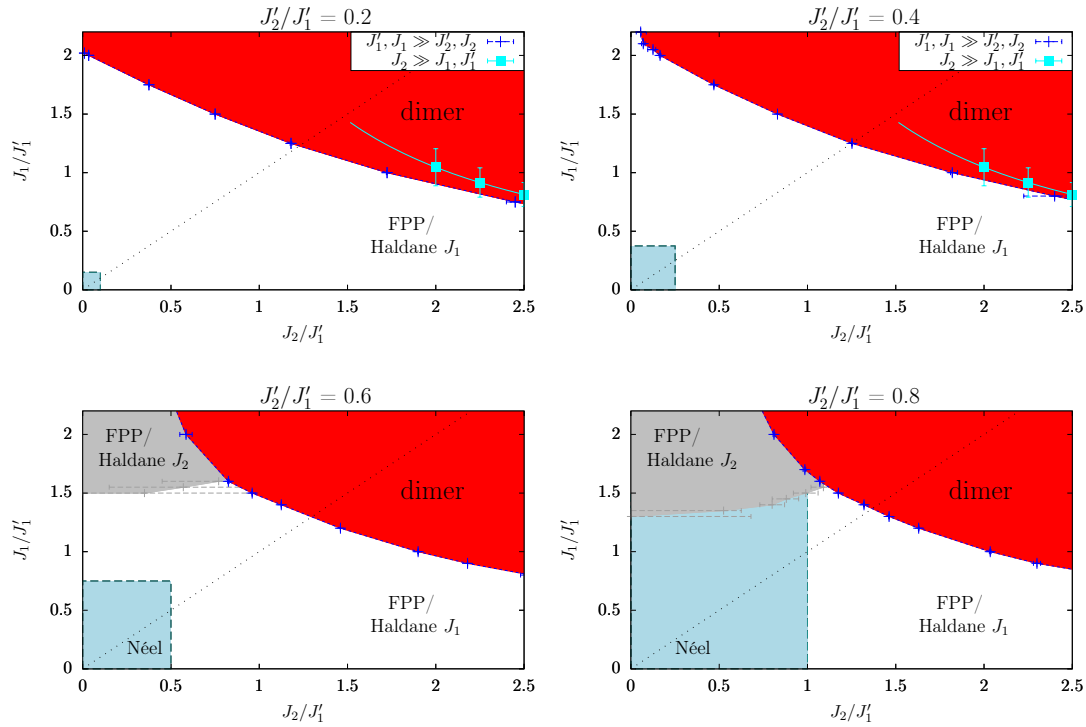


Fig. 10.6.: Phase diagram of the extended Shastry-Sutherland model with varying coupling strengths on the diagonals for fixed ratios J'_2/J'_1 ranging between the nearly one-dimensional case at $J'_2/J'_1 = 0.2$ and the almost two-dimensional case at $J'_2/J'_1 = 0.8$ from left to right and top to bottom by series expansions. For $J'_2/J'_1 = \{0.2, 0.4\}$ the same phase transition line as in Fig. 9.2 is included. The Néel phase is expected and sketched as a guide to the eye.

diagram at constant $J'_2/J_2 = 0.68$ and prove numerically that both phases are identical by correlations from iPEPS.

The phase diagrams connecting the asymmetric orthogonal-dimer chain with the distorted Shastry-Sutherland model with identical nearest-neighbour and distinct diagonal couplings are given in Fig. 9.2 ($J'_2/J'_1 = 0$), Fig. 10.6 ($J'_2/J'_1 = \{0.2, 0.4, 0.6, 0.8\}$), and Fig. 10.2 ($J'_2/J'_1 = 1$). The averages of ground-state energies are taken from Padé extrapolants [3, 4], [4, 3], and [4, 4], chosen such that no divergencies occur. Both FPP/Haldane J_1 and J_2 phases are present. Note, that we expect the FPP/Haldane J_2 phase to occur as well at $J'_2/J'_1 = 0.4$ already within the plotted parameter range. However, we can not resolve it, since the series are not well converged in this regime of large perturbations $\tilde{J}'_2/\tilde{J}'_1 = 2.5$. The Néel phase must occur for finite J'_2 couplings and vanishing diagonals $J_1 = J_2 = 0$ [4]. The precise borders are not known. We plot them biased in a way, that the Néel phase is less extended for $J_1 < J_2$ than for $J_2 < J_1$, since the energy of the FPP/Haldane J_1 phase is lower in this area for $J'_2 < J'_1$. This stems from the triplet-like J_1 -bond, which is energetically less costly if J_1 decreases. In contrast, the energy of the dimer singlet state increases in this case. The nearest-neighbour couplings do not effect the dimer singlet state, however, the energies of the

FPPs/Haldane phases are reduced with increasing J'_1 and J'_2 due to quantum fluctuations, which is why the extension of the dimer singlet phase decreases whilst connecting the asymmetric orthogonal-dimer chain with the extended Shastry-Sutherland model with distinct diagonal couplings.

Next, we consider the case where on top of the distortion of the dimer couplings J_1 and J_2 , for which the phase diagram is shown in Fig. 10.1, also the nearest-neighbour couplings J'_1 and J'_2 are distorted. A couple of phase diagrams for $J'_2/J'_1 = 0.95$ and $J'_2/J'_1 = 0.9$ are illustrated in Fig. 10.7, where the extrapolants [4, 4], [3, 5], and [5, 3] are taken for the energy averages of all plaquette phases. This asymmetry of the nearest-neighbour couplings $J'_2 < J'_1$ favours the FPP/Haldane J_1 phase, and for $J_1 < J_2$ the extension of the EPP is reduced. However, for $J_1 > J_2$ the energy of the FPP/Haldane J_1 phase increases, whereas the energy of the FPP/Haldane J_2 phase decreases, and it is not at all obvious which phase emerges. For the ratios J'_2/J'_1 shown in Fig. 10.7 a direct phase transition from the FPP/Haldane J_1 phase to the EPP occurs. So, in contrast to solely distorted diagonal bonds $J_1 \neq J_2$ (Fig. 10.1), the additional difference in the nearest-neighbour bonds $J'_2 < J'_1$ yields the EPP instead of the FPP/Haldane J_2 phase. For this case, the energies are shown explicitly along the line $J'_2/J'_1 = 0.9$, $J_1/J_2 = 1.15$ in Fig. 10.8. For these couplings, the FPP/Haldane J_2 phase is not very competitive. However, for weaker distortions of the nearest-neighbour couplings J'_2/J'_1 it is relevant at $J_1 > J_2$.

Finally, in Fig. 10.9, we show a phase diagram in which both ratios J_1/J_2 and J'_2/J'_1 vary for a fixed value of $J'_2/J_2 = 0.68$. The energies from series expansions are averaged over the Padé extrapolants [3, 5], [5, 3], and [4, 4]. On the one hand, at the bottom left corner ($J'_1/J'_2 = 1$, $J_1/J_2 = 0.88$) the Haldane J_1 phase has to be stabilised, as we know

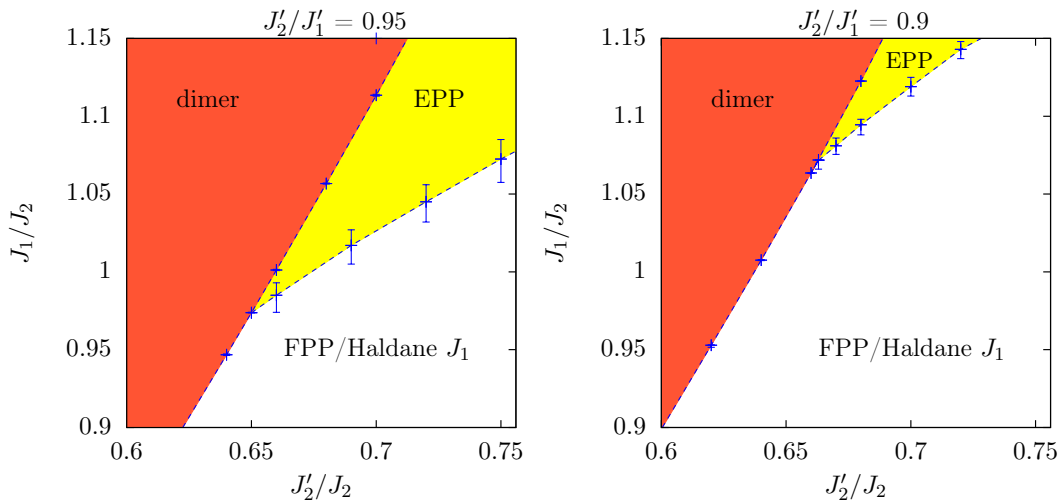


Fig. 10.7.: Phase diagram of the extended Shastry-Sutherland model at constant ratios between nearest-neighbour couplings $J'_2/J'_1 = 0.95$ (left) and $J'_2/J'_1 = 0.9$ (right) for varying strengths on the diagonal bonds J_1 and J_2 from series expansions. Note, that the y -axis is extended in comparison to Fig. 10.1.

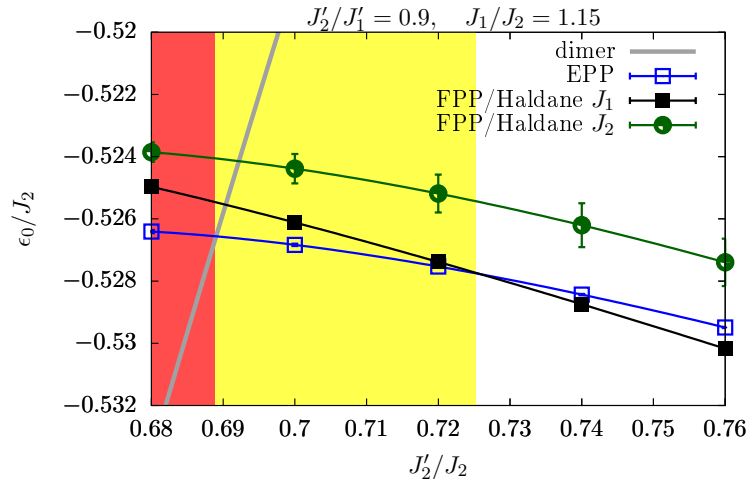


Fig. 10.8.: Ground-state energies of the dimer singlet, EPP, FPP/Haldane J_1 and J_2 phases for a cut through parameter space with $J_2'/J_1' = 0.9$ and $J_1/J_2 = 1.15$. The background colours represent the ground state with the same colour code as in the phase diagrams.

from Fig. 10.1, where this point is connected to the Haldane limit $J_2 \gg J_1', J_2', J_1$ with $J_2 \gg J_1'^2/J_1, J_2 \gg J_2'^2/J_1$. On the other hand, at the top right corner ($J_1/J_2 = 1, J_1'/J_2' = 1.12$) the FPP J_1 is stabilised. This is clear from Fig. 10.4, which connects to the orthogonal-dimer chain limit, and therefore contains the FPP J_1 for sufficiently small diagonal couplings. We saw several other indications for the identity of the FPP, adiabatically connected to the limit $J_1' \gg J_2', J_2$, and the Haldane phase, from the limit $J_2 \gg J_1', J_2', J_1$ with $J_2 \gg J_1'^2/J_1, J_2 \gg J_2'^2/J_1$, in this section and in Chapter 9. In order to verify this, the spin-spin correlations along a path through parameter space connecting both phases were studied with iPEPS by Schelto Crone, Ido Niesen, and

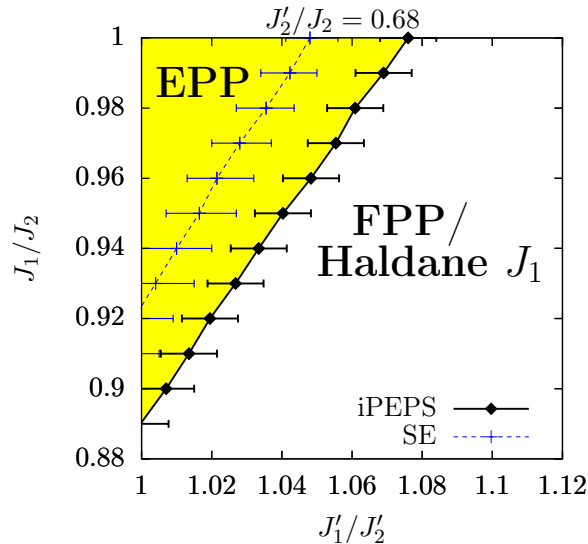


Fig. 10.9.: Phase diagram of the extended Shastry-Sutherland model at $J_2'/J_2 = 0.68$ from iPEPS and series expansions. This figure is published in Ref. [79].

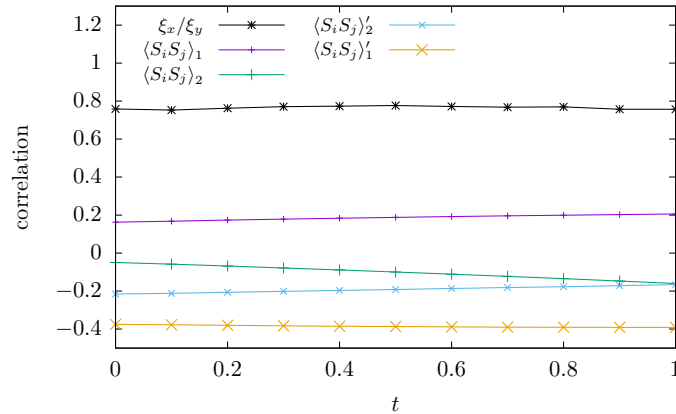


Fig. 10.10.: Various correlations along a path connecting the model with only asymmetric intra-dimer couplings to the model with only asymmetric inter-dimer couplings from iPEPS. The path is parametrised by $(J'_2/J_2, J'_1/J'_2, J_1/J_2) = (0.66 - 0.1t, 1.10 - 0.1t, 1 - 0.5t)$ with $t \in [0, 1]$. The correlations with a prime $\langle \bullet \rangle'$ refer to inter-dimer bonds, the ones without a prime $\langle \bullet \rangle$ to the intra-dimer bonds. Additionally, the anisotropy in the correlation length ξ_x/ξ_y is shown. This figure is contained in the Supplemental Material of Ref. [79].

Philippe Corboz. The correlations between spins on dimers and intra-dimer bonds for the path described by $(J'_2/J_2, J'_1/J'_2, J_1/J_2) = (0.66 - 0.1t, 1.10 - 0.1t, 1 - 0.5t)$ with $t \in [0, 1]$ are given in Fig. 10.10. All correlations behave smoothly and no drastic changes, as expected for a phase transition, are present. Therefore, there is no indication for a phase transition, and the FPP and Haldane phase are identical. They constitute a single quasi-one dimensional phase in which strong correlations are concentrated around full plaquettes (see Fig. 10.10(a) and right panel on the bottom right of Fig. 7.14 [176]).

In this section, we showed, that the EPP present in the symmetric Shastry-Sutherland model is ruled out by the FPP, which was numerically proven to be identical to the Haldane phase. There are two distinct spatial locations for this type of phase, and therefore two phases, the FPP/Haldane J_1 and J_2 phases. A number of phase diagrams was derived by series expansions and iPEPS, which are used in the next section to determine the ground state at some set of parameters in order to investigate the excitation spectra of the EPP and FPP/Haldane phase, which can then also be compared to experiments.

10.2. Excitations of plaquette phases

In this section, we discuss the excitations of the EPP and FPP in various extended Shastry-Sutherland models by series expansions. This is mainly motivated by the comparison with INS [76], ESR [77], and specific heat measurements [78] on $\text{SrCu}_2(\text{BO}_3)_2$ in the Section 10.4. Since the excitations only occur, if the system is in the proper ground state, the parameters of the model have to be chosen accordingly. This can be done along the lines of the phase diagrams determined in the previous section. We derive the dispersions with perturbation theory from Chapter 2 and the explicit perturbative Hamiltonians discussed in Chapter 8. The dispersions are calculated up to order six in the according parameters λ . Since the energy gap is not expected to vanish

in the studied parameter range we employ Padé rather than DlogPadé extrapolations, which was done previously [72].

10.2.1. Empty plaquette singlet phase

We study the excitations of the EPP by series expansions about the limit of decoupled symmetric empty plaquettes, i.e. $J_2^0 = J_1$ in Eq. (8.1.1). In the one-quasi-particle sector, a single triplon is present, which is connected to a triplet with $s_v^p = 1$ on a single plaquette ($|t_0^{sz}\rangle$). We also derived the series for the excitation energies of the triplon from the two-quasi-particle block in H_0 , linked to the $s_v^p = 0$ triplet ($|t_1^{sz}\rangle$). However, these series do not yield relevant converged results, i.e. either the extrapolants are erratic, or the resulting energy values are quite large. Therefore, we focus on the mode from the one-quasi-particle sector connected to $|t_0^{sz}\rangle$. We start with the symmetric Shastry-Sutherland model from Eq. (7.0.1), before investigating the EPP in two extended Shastry-Sutherland models. One with a small bias towards the FPP in Eq. (7.3.2), and one biased towards the EPP, depicted in Fig. 7.16.

The dispersion for the symmetric Shastry-Sutherland model at $J'/J = 0.72$ is shown in the left panel of Fig. 10.11, where also data from ED on the 32-site cluster with PBCs performed by Hong-Yu Yang is included [221]. The excitation energy is averaged over various sets of extrapolants out of [2, 3], [3, 2], and [3, 3], depending on the specific momenta, which is the reason for the small jumps in the plotted lines. The continuum is simply determined from the extrapolant [2, 3] and no error bars are given. The energy gap is located at intermediate values of $\vec{k} \approx (0.3\pi, 0.3\pi)^T$, which only becomes clear in higher orders of perturbation theory as already discussed in Ref. [72]. The precise momentum of the energy gap depends on the value of the coupling ratio J'/J . The mode is dispersive and has a maximum at $\vec{k} = (\pi, \pi)^T$. In the vicinity of this area, it also decays into the two-triplon continuum. At $\vec{k} = (\pi, \pi)^T$, the energies from ED lie below the ones from series expansions. Actually, the ED discovers four low-energy

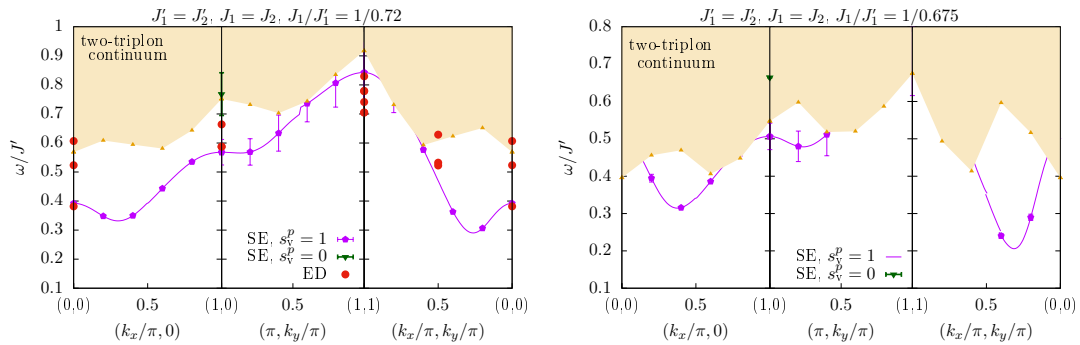


Fig. 10.11.: Dispersion of the EPP in the symmetric Shastry-Sutherland model. On the left for $J'/J = 0.72$, also energies from ED by Hong-Yu Yang are included as red points [221]. On the right, the dispersion at the phase transition towards the dimer phase $J'/J = 0.675$ is shown. The quantum number s_v^p is valid only in the unperturbed limit $\lambda = 0$ of the series expansions. The shaded area indicates the two-triplon continuum. For details on the extrapolants see the text.

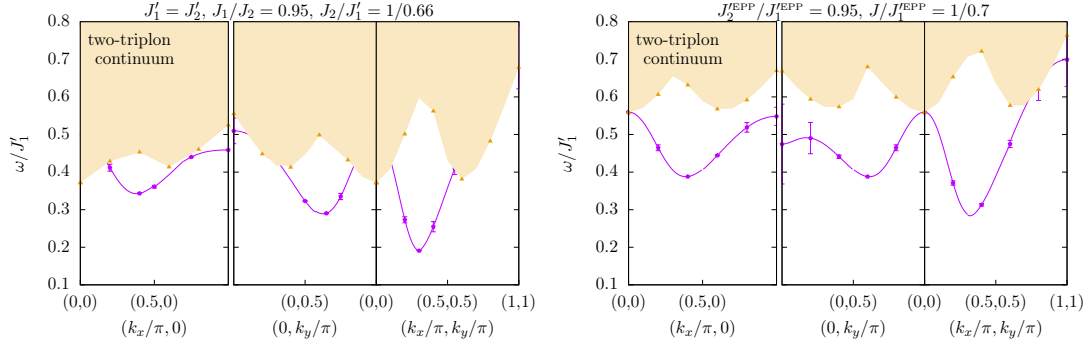


Fig. 10.12.: Dispersion of the EPP in asymmetric Shastry-Sutherland models. On the left, for the Hamiltonian in Eq. (7.3.3) with $J_2/J'_1 = 1/0.66$, $J_1/J_2 = 0.95$, and $J'_1 = J'_2$. On the right, the nearest-neighbour couplings on the singlet plaquettes are stronger than the others (7.3.4) with $J_2^{EPP}/J_1^{EPP} = 0.95$ for $J'_1/J = 0.7$. The shaded area indicates the two-triplon continuum. For details on the extrapolants see the text.

states at this point, which might be the signature of the continuum on the finite cluster, and the convergence of the series might be undermined by decay. For all other momenta available on the 32-site cluster, the lowest energy from ED and the one-triplon mode from the series expansions agree rather well. In particular at $\vec{k} = (0, 0)^T$, which is the lowest energy found in ED. There are several eigenstates on the finite cluster between the one-triplon mode and the two-triplon continuum from series expansions. These could be due to finite size effects. They could also have physical reasons though, and correspond to states from the two-quasi-particle sector, like a bound state with two one-quasi-particle triplons. The excitation energies we derived for the triplon connected to a triplet with $s_v^p = 0$ are not well converged at $\vec{k} = (0, 0)^T$. For $\vec{k} = (\pi, 0)^T$, the convergence works rather well and we find an energy $(0.77 \pm 0.02)J'$, which is higher than the energies from ED. At $\vec{k} = (0, \pi)^T$ and $\vec{k} = (\pi, \pi)^T$ all Padé extrapolants diverge and we expect the mode to decay.

The dispersion at the phase transition point to the dimer singlet phase $(J/J')_c = 0.675$ is shown in the right panel of Fig. 10.11. In comparison to $J/J' = 0.72$, the energy gap is lower, and the triplon mode decays into the two-triplon continuum in larger areas of momentum space. The energy gap does not close, which is in accordance with the first-order phase transition towards the dimer singlet phase [74]. We note, that the difference between the gap and the excitation energy at $\vec{k} = \vec{0}$ increases for decreasing coupling ratios. Next, we investigate the effects, which arise from distortions of the Shastry-Sutherland models.

As we saw in the last section, the extended Shastry-Sutherland model in Eq. (7.3.2) stays in the EPP for small deviations $J'_2 < J'_1$ and $J_2 > J_1$. This can be seen in the phase diagrams in Fig. 10.1 and Fig. 10.4. So, the question arises if the dispersion for these parameters changes significantly compared to the symmetric model. It is given for the couplings $J_2/J'_1 = 1/0.66$, $J_1/J_2 = 0.95$, and $J'_1 = J'_2$, which are the values suggested for $\text{SrCu}_2(\text{BO}_3)_2$ under pressure in Ref. [77], in Fig. 7.16. Overall, the excitation spectrum is comparable to the one in the symmetric Shastry-Sutherland

model at $J'/J = 0.675$ shown in the right panel of Fig. 10.11. Note, that the path through momentum space is not identical in the center panels and is inverted in the right panels, since the asymmetry between k_x and k_y becomes more pronounced in the asymmetric case.

Another relevant setting is the EPP in an extended Shastry-Sutherland model with strong nearest-neighbour couplings on the empty plaquettes hosting singlets as depicted in Fig. 7.16. This model is biased towards the EPP and yields the natural lattice distortion of this phase [177]. The excitation spectrum for couplings $J_2^{\text{EPP}}/J_1^{\text{EPP}} = 0.95$, $J_1^{\text{EPP}}/J = 0.7$ is given in the right panel of Fig. 10.12. This is again a larger ratio between the nearest-neighbour and diagonal interactions, so the energy gap as well as the continuum are located at higher energies. The spectrum does not change significantly to before.

Previously, the excitation energy of the triplon of the EPP in the symmetric Shastry-Sutherland model at $\vec{k} = \vec{0}$ was determined up to fifth-order perturbation theory in Ref. [70]. These findings agree qualitatively with ours. A direct comparison is difficult, since no precise values and series are given. The dispersion was also derived up to order seven in Ref. [72], where the dependence of the location of the gap in momentum space on the coupling ratio was described similarly to our findings. In this work, the series were analysed by DlogPadé extrapolations, which is misleading, since no second-order phase transition is expected [74]. The series at $\vec{k} = \vec{0}$ for two coupling ratios, as well as for the energy gap for one coupling ratio, are explicitly given and we verified these results.

10.2.2. Filled plaquette singlet phase

10.2.2.1. Dispersions

We study the low-energy dispersions of the FPP/Haldane phase in extended Shastry-Sutherland models by series expansions of the Hamiltonian in Eq. (8.1.2) with $J_1^0 = J_1'$, if not stated differently. Results from other values J_1^0 potentially yield smaller standard deviations, however individual calculations are quite costly. All shown excitation energies from the one-quasi-particle sector are averages over the Padé extrapolants [2, 3], [3, 2], and [3, 3], chosen such that nonphysical divergencies are excluded. At $\lambda = 0$, the Hamiltonian in Eq. (8.1.2) consists of decoupled filled plaquettes. These filled plaquettes host two low-lying triplet excitations for parameters $J_1 \approx J_1'$. The one-quasi-particle singlet is not studied here. In the two-dimensional system, the total spin on the diagonal of the filled plaquettes s_v^p is not a good quantum number for all momenta. This is due to the fact that the spins on the intra-plaquette diagonal interact with spins from other plaquettes, which do not address both spins of the diagonal. However, for momenta in the direction of the orthogonal-dimer chain $\vec{k} = (k, k)^T$, the total spin on the diagonal s_v^p still yields a good quantum number on every plaquette and both excitations are protected from each other. This is also the case for $\vec{k} = \{(\pi, 0)^T, (0, \pi)^T\}$. As shown in Subsection 10.1.3 the FPP and the Haldane phase from two distinct limits constitute the same phase. Therefore, the dispersive mode of this phase is referred to as the Haldane mode (compare Chapter 9).

We start by interconnecting orthogonal-dimer chains, which were discussed in Section 9.2. In first-order perturbation theory, the dispersions for momenta where the

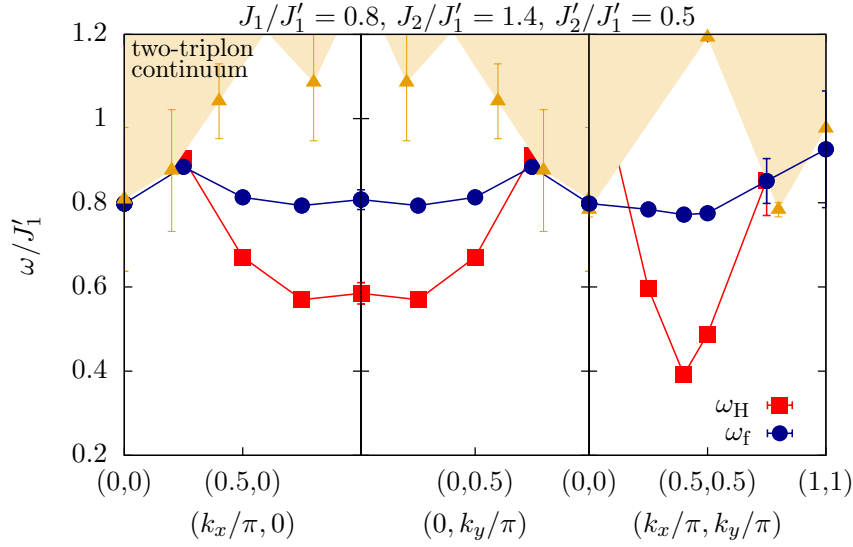


Fig. 10.13.: Low-energy dispersions of the FPP/Haldane phase in the extended Shastry-Sutherland model with $J_1/J'_1 = 0.8$, $J_2/J'_1 = 1.4$, and $J'_2/J'_1 = 0.5$. The excitations are exactly ω_H and ω_f only along $\vec{k} = (k, k)^T$ and at $\vec{k} = \{(\pi, 0)^T, (0, \pi)^T\}$. The shaded area indicates the two-triplon continuum. For details on the extrapolants see the text.

modes do not mix, are given by

$$\begin{aligned}\omega_H(\vec{k})/J'_1 &= 1 - \frac{2}{3}J'_2\lambda(\cos k_x + \cos k_y) + \frac{1}{3}J_2\lambda\cos(k_x + k_y), \\ \omega_f(\vec{k})/J'_1 &= 1 + \lambda(1 - J_1).\end{aligned}\tag{10.2.1}$$

Therefore, at small perturbations and for these momenta the minimal energy for $\omega_H(\vec{k})$ is located at $k_x = k_y \approx \arccos(J'_2/J_2)$ [72]. For $J'_2 \neq 0$, the mode ω_H becomes dispersive in the direction $\vec{k} = (k, -k)^T$, so perpendicular to the direction of the orthogonal-dimer chains. We investigate this behaviour including higher-order effects up to order six for the extended Shastry-Sutherland model with the coupling ratios $J_1/J'_1 = 0.5$, $J_2/J'_1 = 1.2$, and $J'_2/J'_1 = 0.5$. The excitation spectrum is shown in Fig. 10.13. In comparison to the asymmetric orthogonal-dimer chain, the flat excitation becomes slightly dispersive with an energy difference between maximum and minimum $\approx 0.15J'_1$. The energy gap still stems from the more dispersive mode $\omega_H(\vec{k})$, however the position of the gap is moved to an intermediate value k along $\vec{k} = (k, k)^T$. In general, we observe that the flat mode becomes more dispersive with increasing inter-chain couplings, J'_2 , as well as with increasing values of J_1 , which additionally reduces the overall energy of this mode. This is plausible, since the plaquette triplon is singlet-like on the diagonal J_1 -bond. The two-triplon continuum interferes with the one-triplon mode connected to $\omega_H(\vec{k})$ in the areas around $\vec{k} = (0, 0)^T$ and $\vec{k} = (\pi, \pi)^T$, where it decays. This finite lifetime can lead to diverging Padé extrapolants, which turns the calculation of the continua into a non-trivial problem, since the whole momentum space is relevant in Eq. (8.2.4). For momenta where the lower band edge of the two-triplon continuum is determined by the energy gap, so $\vec{k} = \vec{0}$ and $\vec{k} = 2\vec{k}_\Delta$, this is not a problem. However, in order to study all momenta, a feasible way is to use the bare series, which yields rather

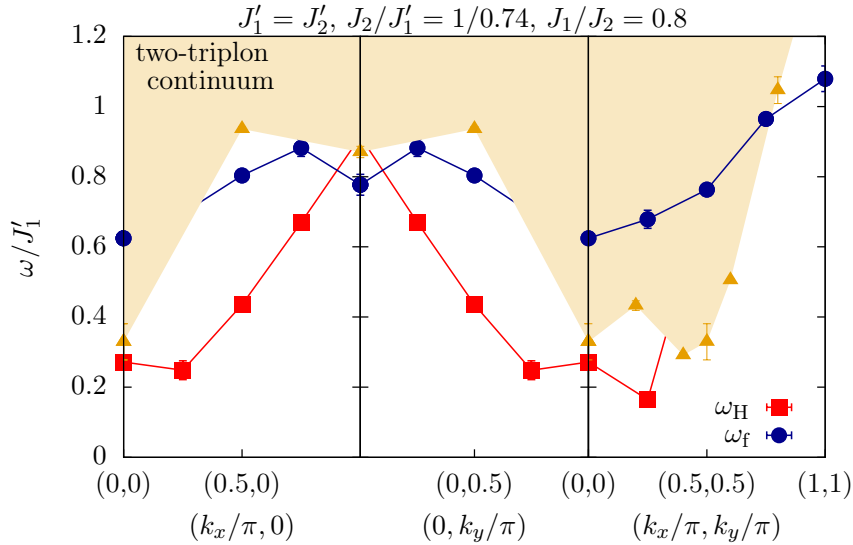


Fig. 10.14.: Low-energy dispersions of the FPP/Haldane phase in the extended Shastry-Sutherland model with $J_2/J'_1 = 1/0.74$, $J_1/J_2 = 0.8$, and $J'_2 = J'_1$. The excitations are exactly ω_H and ω_f only along $\vec{k} = (k, k)^T$ and at $\vec{k} = \{(\pi, 0)^T, (0, \pi)^T\}$. The shaded area indicates the two-triplon continuum. For details on the extrapolants see the text.

approximate results. This is shown in Fig. 10.13 for $\vec{k} = (k_x, 0)^T$ and $\vec{k} = (0, k_y)^T$, where the series expansions are done with $J_1^0 = 0$ in Eq. (8.1.2). This ensures that the mode is certainly connected to $\omega_H(\vec{k})$. For $\vec{k} = (k, k)^T$, averages over Padé extrapolants ($J_1^0 = J'_1$) from the same direction are used. Along this line, the mode ω_f is protected from the low-lying continuum and does not decay. The large standard deviation at $\vec{k} = (\pi, \pi)^T$ is not linked to the continuum.

The excitation spectrum for the Shastry-Sutherland model distorted in the diagonal dimer bonds with $J_1/J_2 = 0.8$, $J_2 = J'_1/0.74$, and $J'_2 = J'_1$ is given in Fig. 10.14. The lower-band edge of the two-triplon continuum is determined from the Padé extrapolants employed for the triplon modes, depicted in the same figure. However, these do not converge in the whole momentum space and the continuum might be below the given values, except for the momenta where two triplons located at the energy gap \vec{k}_Δ form the continuum, so $\vec{k} = \vec{0}$ and $\vec{k} = 2 \cdot \vec{k}_\Delta$. For momenta around $\vec{k} = (\pi, \pi)^T$, the given two-triplon continuum is actually determined by modes with a finite lifetime at $\vec{k} = (\pi/2, \pi/2)^T$, so the excitations of this continuum also decay, and instead an even lower multi-particle continuum occurs (not shown). Overall the excitation energies at these parameters are lower in energy than for the Shastry-Sutherland model closer to the orthogonal-dimer chains. This relates to the fact that stronger perturbations lower the energies. The position of the energy gap is slightly shifted, compared to Fig. 10.13, but remains at an intermediate value along $\vec{k} = (k, k)^T$. It stems from the Haldane mode ω_H , which is very dispersive and decays in a large area around the center of the Brillouin zone $\vec{k} = (\pi, \pi)^T$. Similarly, the second excitation has a finite lifetime in a larger momentum range along the directions $\vec{k} = (k, 0)^T$ and $\vec{k} = (0, k)^T$.

Prior to this thesis, the excitation spectrum of the FPP in the symmetric Shastry-Sutherland model was studied by Koga et al. at $\vec{k} = \vec{0}$, where they extracted the energy gap [73]. They discovered the presence of the two low-energy excitations and a crossing

with increasing coupling ratio J'/J . At that time, it was not known that the FPP does not yield the ground state in the Shastry-Sutherland model. Another study resolved the excitation, which is connected to the triplet ω_H on a single plaquette [72]. They did not investigate the other excitation. In both works, a second-order phase transition to the Néel phase is assumed, and the extrapolations of the series are performed with this bias. We revised these articles and for the first time show the excitation energies and the continuum resolved over a range of momenta in plausible *distorted* Shastry-Sutherland models, where the FPP/Haldane phase actually occurs.

10.2.2.2. Ratios of excitation energies

One aspect that is relevant for the experimental signature of the intermediate high-pressure phase of $\text{SrCu}_2(\text{BO}_3)_2$ is the ratio between the two lowest excitation energies at $\vec{k} = \vec{0}$, since this is the most reliable available experimental data point [76–78]. Therefore, we study this ratio between the energies from both triplon modes in the FPP/Haldane phase for the extended Shastry-Sutherland model, as already for the asymmetric orthogonal-dimer chain in Section 9.2.

In Fig. 10.15, the ratio ω_f/ω_H at $\vec{k} = \vec{0}$ obtained from series expansions as a heat map together with the ground-state phase diagram given in Fig. 10.9 is shown. We employ the perturbative Hamiltonian in Eq. (8.1.2). With $J_1^0 = 1/0.72$, the flat mode in the unperturbed model H_0 is lower in energy than the Haldane mode ω_H . With increasing perturbation both modes cross, and the Padé extrapolants of the flat mode break down. Therefore, we use only the excitation energies of the Haldane mode from this unperturbed starting point, where the Padé extrapolants [2, 3] and [3, 3] yield valid results. For the excitation energies of the flat mode Eq. (8.1.2) with $J_1^0 = 1$ is suited better, since there are no level crossings. The average is taken over the Padé extrapolants

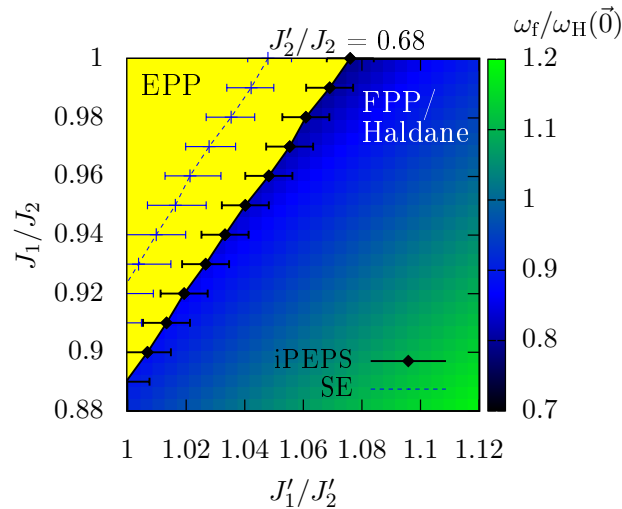


Fig. 10.15.: The ratio $\omega_f/\omega_H(\vec{0})$ of the low-lying excitations in the FPP/Haldane phase at $J'_2/J_2 = 0.68$, obtained from series expansions, is displayed as a heat map together with the ground-state phase diagram from iPEPS and series expansions as in Fig. 10.9. For details on the extrapolants see the text.

[2, 3] and [3, 3]. The Padé extrapolants of the Haldane mode excitation energy mostly break down at these parameters though, so we compare excitation energies of the same phase from different unperturbed starting points in the same physical model at $\lambda = 1$. Interestingly, ω_f/ω_H is the closest to a ratio of 1/2 next to the border to the EPP, the experimentally most realistic regime where the anisotropy of the exchange couplings is not too large. At these parameters, the series expansions further predict that the true gap is located along the diagonal close to $\vec{k} = (0.25\pi, 0.25\pi)^T$ (consistent with Ref. [72] for the symmetric Shastry-Sutherland model), and that it is given by the triplon branch associated with the Haldane mode. As a consequence, both triplon branches have to cross in the Brillouin zone.

However, as we see in Section 10.3, this scenario explaining the experimental findings does not fit with the dynamic structure factors. We therefore consider a larger ratio $J'_2/J_2 = 0.74$ for which a similar plot is shown in Fig. 10.16. Note, that for this value no iPEPS data for the phase transition line was calculated. From the other phase diagrams in Section 10.1 we know, that the EPP is likely to be more extended than what follows from series expansions. Here, both excitation energies are derived with the perturbative model in Eq. (8.1.2) with $J_1^0 = 1$ and the Padé extrapolants [2, 3] and [3, 3] for the flat mode, and [2, 3] and [3, 2] for the Haldane mode are averaged. In contrast to the behaviour at $J'_2/J_2 = 0.68$, the excitation energy of the flat mode is higher in energy than the one of the Haldane mode. The ratio approaches 2/1 at a distortion of $J_1 \approx 0.9J_2$, which therefore yields a realistic scenario for the explanation of the experimental findings.

In this section, we investigated the excitations of both plaquette phases in the Shastry-Sutherland model and in extended Shastry-Sutherland models. For the EPP a single low-energy triplon and for the FPP/Haldane phase two low-energy triplons were

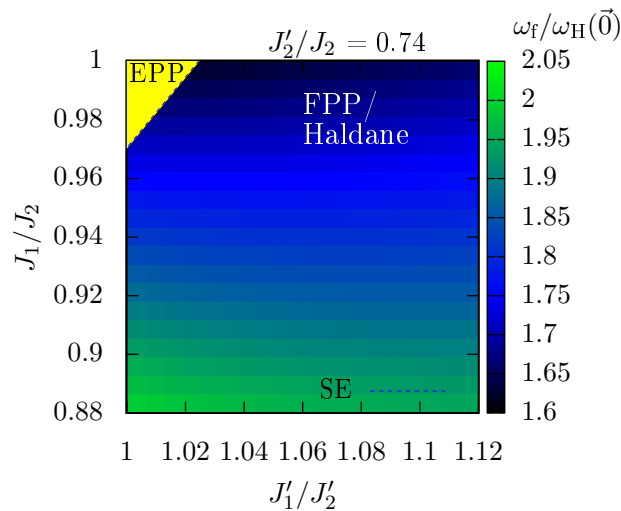


Fig. 10.16.: The ratio $\omega_f/\omega_H(\vec{0})$ of the low-lying excitations in the FPP/Haldane phase at fixed ratio $J'_2/J_2 = 0.74$, obtained from series expansions, is displayed as a heat map together with the ground-state phase diagram from series expansions. For details on the extrapolants see the text.

found. In both cases for relevant couplings not too far from the the symmetric Shastry-Sutherland model, the energy gap is located at intermediate values along $\vec{k} = (k, k)^T$. We already made the first contact to experiments for the FPP/Haldane phase in an extended Shastry-Sutherland model by studying the ratio between both excitation energies, where relevant sets of parameters for further investigations in the following sections were found.

10.3. Dynamic structure factor

In this section, we study the dynamic structure factor for the EPP and FPP/Haldane phase, which was introduced in Section 8.2. The frequency integration gives the static structure factor, and can be investigated without the knowledge of excitation energies. We determine the structure factor in direct correspondence to specific excitations of which the energies were already studied in Section 10.2.

For the comparison with experiments on $\text{SrCu}_2(\text{BO}_3)_2$ not only the lattice topology has to be taken into account, but also the the proper real space distances. They have been measured to be

$$a = 8.99 \text{ \AA}, \quad h = 5.120 \text{ \AA}, \quad \text{and} \quad d = 2.905 \text{ \AA} \quad [183] \quad (10.3.1)$$

with the parameters in Fig. 10.17. For convenience we define

$$\tilde{h} = \sqrt{\left(h^2 - \left(\frac{d}{2}\right)^2\right)} / 2. \quad (10.3.2)$$

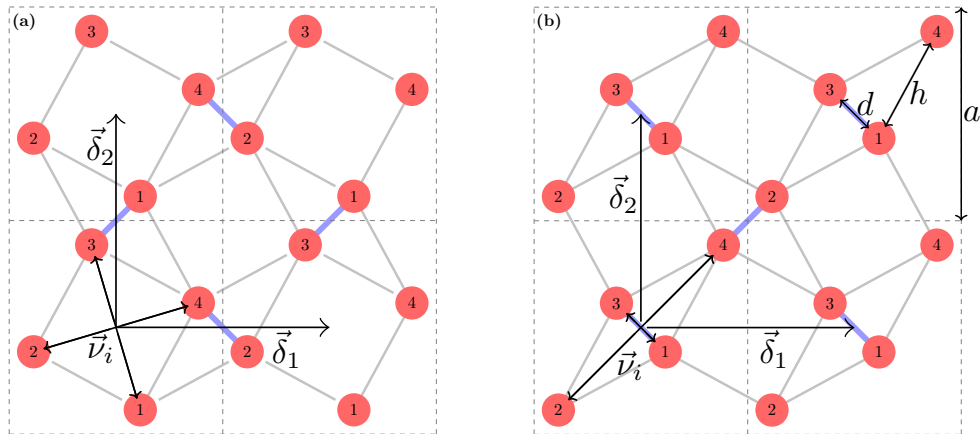


Fig. 10.17.: Illustrations of the Shastry-Sutherland lattice. The distances a , d , and h are given in the text. The spins are labelled by the position within their plaquette $\nu \in \{1, 2, 3, 4\}$. The vectors from the plaquette center to the spins are plotted and indicated as \vec{v}_i . The lattice vectors are illustrated as $\vec{\delta}_1$ and $\vec{\delta}_2$. On the left, the unit cell of one of the choices for the empty plaquettes is given. On the right, the unit cell is chosen to be centred around a filled plaquette with a diagonal coupling between the top left spin and the bottom right spin. This figure is contained in the Supplemental Material of Ref. [79].

The crystal vectors are $\vec{\delta}_1 = a(1,0)^T$ and $\vec{\delta}_2 = a(0,1)^T$. The lattice offers two distinct orientations for both empty and filled plaquettes. Here we choose a single one, under the expectation that the symmetry is broken by the realisation of either of the plaquette phases, leading to one distinct choice. The other orientation leads to the same structure factors rotated in momentum space ($k_x \rightarrow k_x, k_y \rightarrow -k_y$). The inclusion of both orientations is only necessary if the material exhibits several domains, which is not expected for a single crystal.

We perform pCUTs for both phases using a linked-cluster expansion similar to the one for the energy excitations and derive the series up to order five in λ . The unperturbed Hamiltonians are given in Eq. (8.1.1) with $J_1^0 = J_2^0$ for the EPP and in Eq. 8.1.2 with $J_1^0 = J_1'$ for the FPP/Haldane phase. The shown results are then obtained by averages over the Padé extrapolants with the exponents [2, 3] and [3, 2].

10.3.1. Empty plaquette singlet phase

For the empty plaquettes chosen in the left panel of Fig. 10.17, the position vectors of the spins can be written as

$$\begin{aligned} \vec{v}_1 &= \frac{a}{2} \begin{pmatrix} 1 \\ 0 \end{pmatrix} + \tilde{h} \begin{pmatrix} -1 \\ -1 \end{pmatrix}, & \vec{v}_2 &= -\frac{a}{2} \begin{pmatrix} 1 \\ 0 \end{pmatrix} + \frac{d}{2\sqrt{2}} \begin{pmatrix} 1 \\ -1 \end{pmatrix}, \\ \vec{v}_3 &= -\frac{a}{2} \begin{pmatrix} 1 \\ 0 \end{pmatrix} + \tilde{h} \begin{pmatrix} 1 \\ 1 \end{pmatrix}, & \text{and } \vec{v}_4 &= \frac{a}{2} \begin{pmatrix} 1 \\ 0 \end{pmatrix} + \frac{d}{2\sqrt{2}} \begin{pmatrix} -1 \\ 1 \end{pmatrix}. \end{aligned} \quad (10.3.3)$$

For a single empty plaquette in order zero perturbation theory, one finds

$$a_{\text{EPP}}(\vec{k}) = 3 \cdot (0.816497(\cos(0.113833k_x - 0.386167k_y) - \cos(0.385754k_x + 0.114246k_y))), \quad (10.3.4)$$

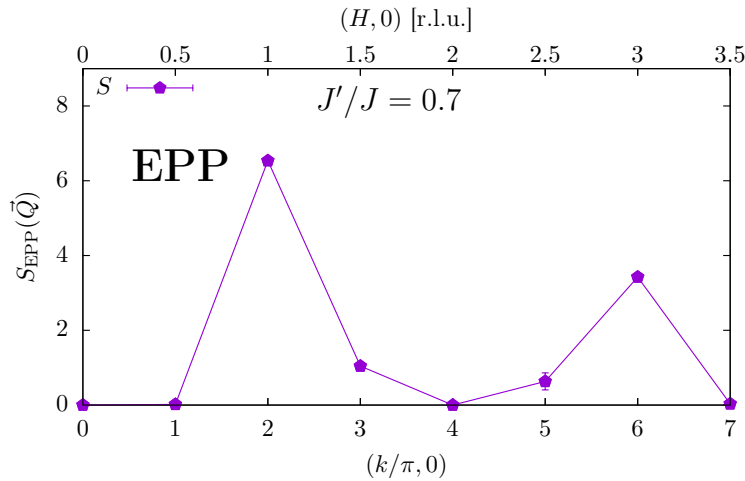


Fig. 10.18.: Static structure factor for the one-quasi-particle triplon excitation of the EPP in the symmetric Shastry-Sutherland model with $J'/J = 0.7$. This figure is published in Ref. [79].

which is identical to the calculation on a single plaquette [76]. The momentum vectors are defined in units of $1/a$. Note, that in the INS data the number of reciprocal lattice units is used [76]. The resulting dynamic structure factor for the low-energy triplon excitation of the EPP in the Shastry-Sutherland model at $J'/J = 0.7$ along the direction $\vec{k} = (k, 0)^T$ in fifth-order is shown in Fig. 10.18. It has a maximum at $\vec{k} = (2\pi, 0)^T$ and decreases for increasing momenta at $\vec{k} = (4\pi, 0)^T$. Then, a second smaller maximum occurs at $\vec{k} = (6\pi, 0)^T$. These findings are used for the comparison with the experimental data in Section 10.4.

10.3.2. Filled plaquette singlet phase

For the FPP/Haldane phase, the unit cell is chosen to be centred around a filled plaquette as illustrated in the right panel of Fig. 10.17. The positions of the spins within the unit cells are given by

$$\begin{aligned} \vec{v}_1 &= \frac{d}{2\sqrt{2}} \begin{pmatrix} 1 \\ -1 \end{pmatrix}, & \vec{v}_2 &= \tilde{h} \begin{pmatrix} -1 \\ -1 \end{pmatrix}, \\ \vec{v}_3 &= \frac{d}{2\sqrt{2}} \begin{pmatrix} -1 \\ 1 \end{pmatrix}, & \text{and } \vec{v}_4 &= \tilde{h} \begin{pmatrix} 1 \\ 1 \end{pmatrix}. \end{aligned} \quad (10.3.5)$$

In order zero perturbation theory, one finds

$$\begin{aligned} a_{\text{FPP}}(\vec{k}) &= 3 \cdot (0.816497 \cos(0.114246(k_x - k_y)) \\ &\quad - 0.386167 \cos(1.21318(k_x + k_y))), \\ b_{\text{FPP}}(\vec{k}) &= 3 \cdot 0.57735i \cdot \sin(0.114246 \cdot (k_x - k_y)), \end{aligned} \quad (10.3.6)$$

which is the same as for a single filled plaquette. The momentum vector is again considered in units of the inverse lattice constant $1/a$. Here, $a_{\text{FPP}}(\vec{k})$ corresponds to

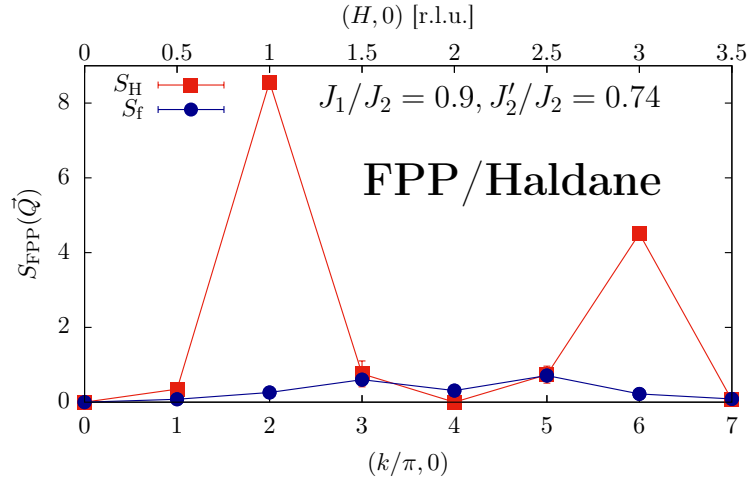


Fig. 10.19.: Static structure factor for the two low-lying triplon excitations of the FPP/Haldane phase in the extended Shastry-Sutherland model in Eq. (7.3.2) with $J_1/J_2 = 0.9$, $J_2'/J_2 = 0.74$, and $J_1' = J_2'$. This figure is published in Ref. [79].

the Haldane and $b_{\text{FPP}}(\vec{k})$ to the flat mode. On a single plaquette, the matrix elements of the observable are identical for the EPP and FPP. Therefore, at $\lambda = 0$, only the Fourier-transformation leads to a difference in the static structure factor.

With respect to the INS experiments, the ratio between the two low-lying excitations indicates that the distortion of the Shastry-Sutherland model describing $\text{SrCu}_2(\text{BO}_3)_2$ could be mainly in the diagonal dimer bonds $J_1/J_2 \approx 0.9$, if the intermediate pressure phase is given by the FPP/Haldane phase, as shown in Subsection 10.2.2. The dynamic structure factor for such a set of parameters $J'_2/J_2 = 0.74$, $J_1 = 0.9J_2$, and $J'_1 = J'_2$ including higher-order effects is given in Fig. 10.19. The dynamic structure factor of the Haldane mode S_{H} shows the same features as the lowest-energy excitation of the EPP (Fig. 10.18) with the same structure of maxima and minima and a slightly larger amplitude for these parameter choices. Overall, the dynamic structure factors are quite robust against changing parameters. In contrast to the EPP, the FPP/Haldane phase has a second low-lying excitation with a much smaller dynamic structure factor. This fact is considered further in the next section.

10.4. Comparison with experiments

In this section, we compare the signature of the intermediate phase in $\text{SrCu}_2(\text{BO}_3)_2$ under pressure with the derived theoretical properties of the EPP and FPP/Haldane phase. We already saw that the FPP/Haldane phase in contrast to the EPP naturally hosts two low-lying excitations similar to the data from INS [76], and found parameters in the extended Shastry-Sutherland model where the ratio between both energies fits the experimental findings in Section 10.3. We also derived the dynamic structure factors in the last section. Here, we compare these results with the INS, ESR, and specific heat measurements, and extend the theoretical considerations for the plaquette phases by the relation between the energy gap and increasing pressure.

The first indication that the EPP cannot be the intermediate phase of $\text{SrCu}_2(\text{BO}_3)_2$ came from NMR [75] that detected two types of Cu sites. Since NMR is (by necessity) performed in a finite magnetic field, it is interesting to look for complementary evidence in zero-field experiments, like ESR, INS, and specific heat [76–78]. All these experiments confirm the presence of two well defined magnetic excitations, one at an energy comparable to that of the gap in the dimer phase just before the transition (ESR, INS), and one at an energy about two times smaller (INS, specific heat). The INS measurements have followed the dispersion along the line $\vec{k} = (k, 0)^T$ in the Brillouin zone, while the specific heat could keep track of the pressure dependence of the gap with clear evidence that it decreases with pressure. The energy gap determined by specific heat measurements seems to fit the lowest excitation energy at $\vec{k} = \vec{0}$ from INS. The accurate setting of the pressure though is extremely difficult to determine for INS and there might as well be some deviations. However, the energy gap should not be too far below the excitation energy at $\vec{k} = \vec{0}$. INS also revealed that the structure factors of the two low-lying excitations have different momentum dependencies.

To make contact with these experiments, we have studied the magnetic excitations in both phases. Characteristic results are summarised in the left panels (a), (c), and (e) for the EPP and in the right panels (b), (d), and (f) for the FPP/Haldane phase of Fig. 10.20. For the series expansions the Hamiltonians in Eq. (8.1.1) with $J_2^0 = J_1^0$ for

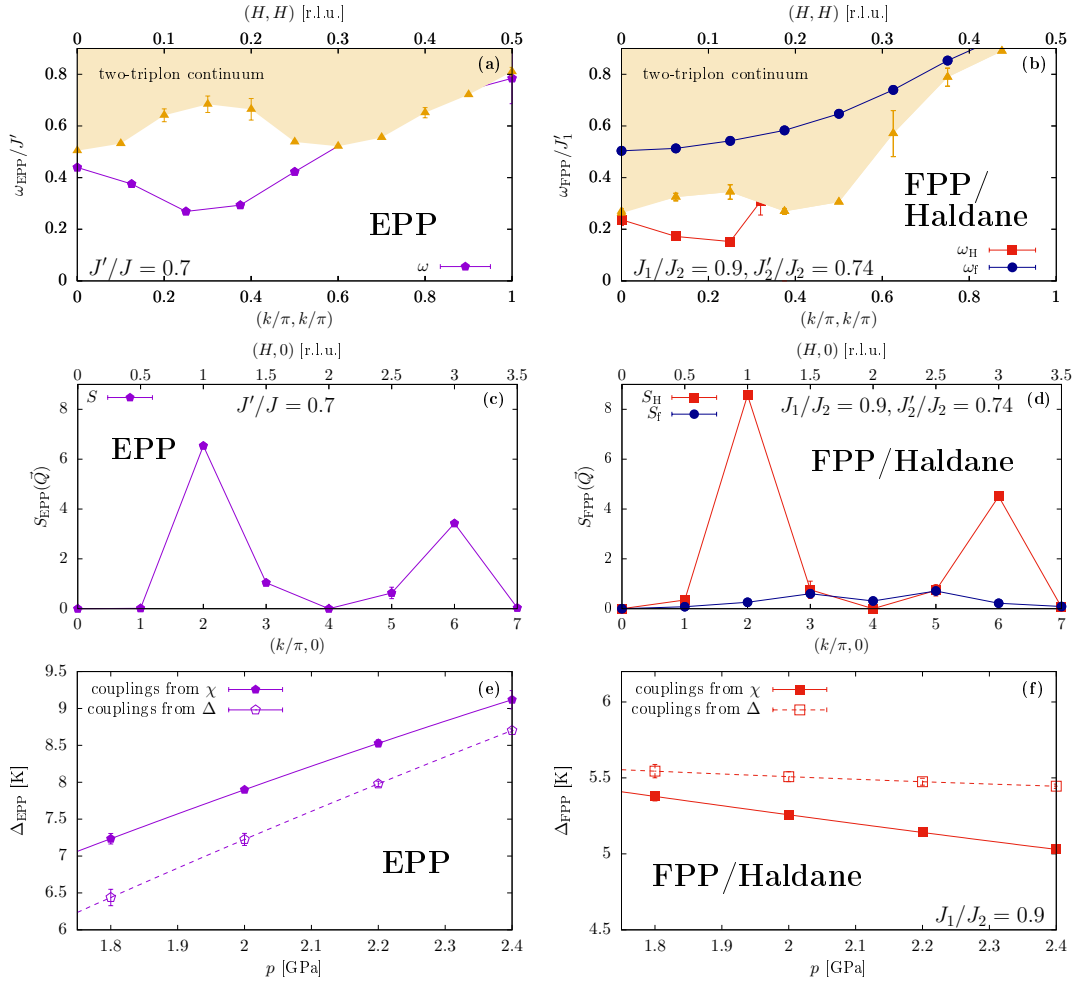


Fig. 10.20.: Magnetic excitations in the EPP (left) and FPP/Haldane phase (right) from series expansions. Details on the extrapolants are given in the text. Panels (a) and (b): magnetic excitation energies along $k_x = k_y$; panels (c) and (d): static structure factors along $k_y = 0$. The parameters are given inside the figures. Panels (e) and (f): pressure dependence of the gap (with couplings from magnetic susceptibility χ [76] and excitation energies Δ measured by ESR [77]). All lines are guides to the eye. These figures are adjusted from Ref. [79].

the EPP, and in Eq. (8.1.2) with $J_1^0 = J_1'$ for the FPP/Haldane phase are employed. For the latter the Padé extrapolants [2, 3] and [3, 2] are used. The Padé extrapolation with exponents [3, 3] shows unphysical divergences in this parameter space. For the EPP combinations of the extrapolants with the exponents [2, 3], [3, 2], and [3, 3] are taken, depending on the convergence behaviour at the specific momentum. The continuum of the EPP is based on the extrapolants [2, 3] and [3, 2].

In the EPP, there is a single low-energy excitation. The dispersion in the symmetric Shastry-Sutherland model for $J'/J = 0.7$ is shown in Fig. 10.20(a). The structure factor matches that of the lowest excitation detected in INS. For small to intermediate ratios J'/J , its dispersion has a minimum along the direction $k_x = k_y$. Since ESR only measures the zero-momentum excitations while the specific heat detects the

gap, this dispersion could be compatible with ESR and specific heat. Both excitation energies of the EPP, the gap Δ at \vec{k}_Δ and $\omega(\vec{0})$, are compared with the ESR data at varying coupling ratios J'_1/J_1 in Fig. 10.21 [77]. The series are averaged over the extrapolants [2, 3] and [3, 2]. In the left panel, the behaviour is illustrated for the symmetric Shastry-Sutherland model, whereas in the right panel it is given for an extended Shastry-Sutherland model with stronger nearest-neighbour couplings J'_1 on the plaquettes forming singlets, depicted in Fig. 7.16, with $J_2^{\text{EPP}}/J_1^{\text{EPP}} = 0.9$. This extension of the Shastry-Sutherland model corresponds to the intrinsic lattice distortion of the EPP [177]. The ESR findings match quite accurately with the excitation energy $\omega(\vec{0})$. Nevertheless, wherever the ratio between both energies is slightly larger than two, the mode at $\vec{k} = \vec{0}$ decays. Therefore, the EPP at these small coupling ratios does not fit to the ESR data. This possibility is also excluded by INS, which observed two well defined excitations at the same momentum. Besides, the energy gap in the EPP increases with pressure as shown in Fig. 10.20(e) where the pressure is introduced by changing the ratio J'/J in the isotropic model following Refs. [76, 77]. This is in clear contradiction with specific heat data. Note, that this also remains true in the extended Shastry-Sutherland model biased towards the EPP (7.3.4).

In the following, we argue that larger coupling ratios could potentially fit the experimental findings better. The behaviour of the energy gap with pressure determined from specific heat in Fig. 7.6 and by series expansions for the EPP in Fig. 10.20(e) evolve with different slopes. These could match, if the dimer coupling J decreases faster than anticipated in Refs. [76, 77], since the EPP energies are multiplied by J in order to convert the units to Kelvin, and hence the slope would change its sign. As seen above, if the value J'/J is slightly larger than experimentally expected (like $J'/J \approx 0.69$), the continuum is above the energy excitation at $\vec{k} = \vec{0}$. Also the ratio between the excitation at $\vec{k} = \vec{0}$ and the gap fits roughly to two. However, this is again ruled out by the INS results, since the energy of the excitation at $\vec{k} = \vec{0}$ fits with the second excitation energy and the lowest excitation is missing. For even larger coupling ratios J'/J , like $J'/J = 0.74$, the energy gap in the EPP shifts towards $\vec{k} = \vec{0}$ and potentially fits the

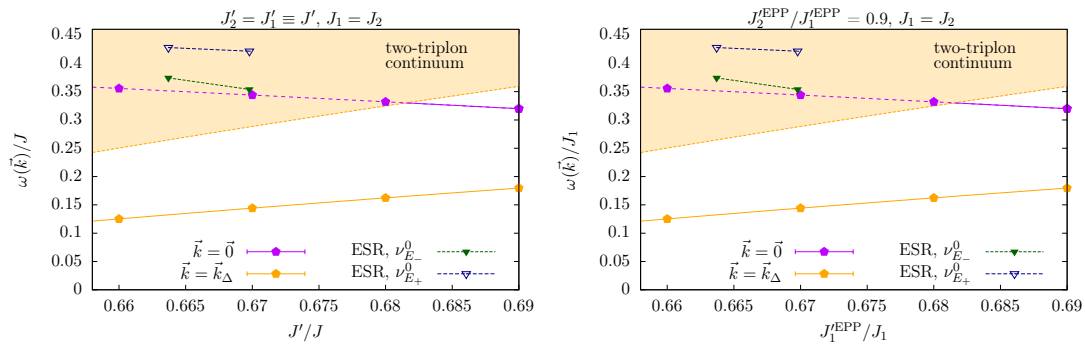


Fig. 10.21.: Lowest energy excitation in the EPP at zero momentum $\vec{k} = \vec{0}$ and at the position of the energy gap $\vec{k} = \vec{k}_\Delta$ for a symmetric Shastry-Sutherland model with $J'/J = 0.7$ on the left and an extended Shastry-Sutherland model (7.3.4) with $J_2^{\text{EPP}}/J_1^{\text{EPP}} = 0.9$ on the right from series expansions. Details on the extrapolants are given in the text. The shaded areas give the two-triplon continuum, where the mode decays (dashed). The excitation energies ν_{\pm}^0 measured by ESR are taken from Ref. [77].

INS results, as becomes clear from Fig. 10.21. In order to resolve a potential second excitation, we determined the series for the single triplon excitation energy from the two-quasi-particle sector, which is adiabatically connected to the triplet with $s_V^p = 0$ in H_0 from Eq. (8.1.1) with $J_2^0 = J_1'$. However, the series are mostly not well converged, and have to be considered only as guiding values. For instance, at $J_1'/J_1 = 1/0.74$, $J_1' = J_2'$, and $J_1 = J_2$ the excitation energy is $\omega_b(0,0) = (0.61 \pm 0.10)J_1'$ (average over the Padé extrapolants [2, 3] and [3, 2]) and $\omega_b(\pi,0) = (0.806 \pm 0.023)J_1'$ ([2, 3] and [3, 3]). The energy of the low-lying excitation is $\omega(0,0) = (0.347 \pm 0.005)J_1'$, so somewhat close to half of the energy of the other excitation $\omega_b(0,0)$. The higher excitation is related to the flat mode in the FPP/Haldane phase (Fig. 10.19) and we take the educated guess that the dynamic structure factors behave similar. The energy gap at these values is still slightly below the lowest excitation at $\vec{k} = (0,0)$ at intermediate momenta $k_x = k_y \approx 0.3\pi$. The second excitation at intermediate momenta $(k_x, 0)$ for $k_x \neq \{0, \pi\}$ and its potential decay was not studied. This scenario could potentially fit, if the coupling ratio J'/J in $\text{SrCu}_2(\text{BO}_3)_2$ increases faster than expected with pressure. The determination of the pressure for INS measurements is very difficult, as already pointed out in Ref. [77].

In the FPP/Haldane phase, the situation is very different. There are two well defined excitations. The dispersions ω_H and ω_f along $k_x = k_y$, which are protected by local symmetries, are shown in Fig. 10.20(b), and, at least not too far from the Néel phase, the lowest one has an energy about half that of the other one at $\vec{k} = 0$. The energy difference between the minimum and the excitation at $\vec{k} = \vec{0}$ seems reasonably small. We determine the lower bound of the two-triplon continuum, which is challenging since the series are only partly converged. Nevertheless, a careful analysis allows to draw conclusions. Up to perturbation strengths where there is no convergence issue, the energy gap is definitely located at some intermediate value \vec{k}_Δ along $k_x = k_y$, and the slopes along this line are smaller than in other directions. In the area around \vec{k}_Δ , the series are well converged. The energy of the gap determines the lower bound of the two-triplon continuum at $\vec{k} = \vec{0}$, as well as at $\vec{k} = 2\vec{k}_\Delta$, and for intermediate values the minima are located on the diagonal $k_x = k_y$. These are the lower bounds of the continuum shown in Fig. 10.20(b). At larger momenta, we continue to use the dispersions along $k_x = k_y$, which may or may not yield the lower bound of the continuum. So, for momenta $k_x = k_y \leq 0.5\pi$ we determine accurately the lower bound of the two-triplon continuum, whereas for larger momenta the true continuum might be below, so in both cases the excitation ω_H decays. The structure factors of these excitations along $k_y = 0$ are shown in Fig. 10.20(d), where we can exclude decay for momenta $k_x/\pi = \{0, 2, 4, 6\}$. They are in good agreement with INS, which resolved a lower excitation with a large intensity at $k_x/\pi = 2$ and a very small intensity at $k_x/\pi = 4$, and an excitation at larger energy with a rather small intensity for all momenta, see Fig. 3(f) of Ref. [76]. In addition, the gap decreases with pressure, which matches with specific heat data. This conclusion has been reached following a path in parameter space assuming $J_1 = 0.9J_2$ and adjusting the average of J_1 and J_2 to the estimates from INS for a symmetric model, but we have checked that the sign of the slope remains negative for similar paths. So the scenario explaining the experimental findings with the FPP/Haldane phase appears to be conclusive.

Within the studied model, there are two plaquette phases possible to be realised in

$\text{SrCu}_2(\text{BO}_3)_2$. The EPP of the Shastry-Sutherland model requires a considerably larger change in the coupling ratio J'/J than expected experimentally. Theoretically, further investigations on the second excitation along the direction $k_y = 0$ are required, whereas experimentally in particular the resolution of the orthogonal direction $k_x = 0$ would be interesting, since the second excitation found in the EPP is highly asymmetric in momentum space for $k_x \leftrightarrow k_y$. The alternative to the EPP is a quasi-one-dimensional phase with strong correlations around full plaquettes, and the properties of this phase appear to be consistent with available data, again if the coupling ratio J'/J is larger than previously expected. If the system was purely two-dimensional, the stabilisation of this phase would induce an orthorhombic distortion since the \mathcal{C}_4 symmetry is lost. This can be expected to remain true for $\text{SrCu}_2(\text{BO}_3)_2$, which is a three-dimensional crystal, if, in all layers, the weak intra-dimer couplings are oriented in the same direction. However, if this direction alternates from one layer to the next, the distortion is not expected any more to be a clear orthorhombic distortion, but to be some local rearrangement inside an essentially unchanged unit cell. The failure so far to detect any clear lattice distortion in the intermediate phase points to the second possibility with alternating directions. There is also an interesting conceptual difference between the two plaquette phases regarding the nature of the phase transition. The EPP is an instability of the Shastry-Sutherland model that spontaneously breaks the symmetry even if all intra- and inter-dimer couplings remain the same. By contrast, the FPP/Haldane phase is not an instability of the Shastry-Sutherland model. It has to be an instability of the coupled spin-lattice system. So, when applying pressure, if there is a direct transition between the dimer phase and the FPP/Haldane phase, it has to take place below the critical ratio at which the transition to the EPP takes place in the Shastry-Sutherland model. Otherwise, there would first be a transition to the EPP. Current estimates of the ratio J'/J at 1.7 GPa from ESR and susceptibility are in the range 0.66-0.665 [76–78], indeed below the critical ratio 0.675 of the EPP.

What could be the next step to confirm or discard the EPP or FPP/Haldane phase as the intermediate phase of $\text{SrCu}_2(\text{BO}_3)_2$? For the FPP a direct identification of the structural distortion would be ideal. A setting to do this is described in Ref. [79]. Alternatively, since in our calculations the details of the excitation spectrum change significantly inside the intermediate phases, additional INS measurements would be most welcome. This would be insightful for both plaquette phases. Finally, a further theoretical investigation of the higher excitations of the EPP, and of the properties of both plaquette phases in a magnetic field to make contact with NMR would be insightful.

11. Orthogonal-plaquette model

After the extensive study of plaquette singlet phases in the Shastry-Sutherland model, the question arises if it is possible to construct a frustrated lattice model in which product states of singlets on plaquettes yield the exact ground states in an extended parameter regime, analogously to the dimer singlet phase in the Shastry-Sutherland model. It turns out that this is indeed the case. Up to small changes this chapter is published in Ref. [222].

The study of exact valence bond crystals in frustrated spin systems dates back to the discovery of the Majumdar-Gosh model [36], which opened a new pathway to exact results. The Shastry-Sutherland model was discovered as the first two-dimensional many-body quantum model with an exact product ground state in an extended parameter regime [38]. Also the three-dimensional version, that is relevant for $\text{SrCu}_2(\text{BO}_3)_2$, was proven to realise this exact dimer singlet ground state [39], as were several other three-dimensional extensions [40]. Overall, the dimer singlet phase is the most commonly studied exact quantum paramagnet in one [36, 37, 81–87], two [38, 88–91] and three dimensions [39, 40, 175]. In these models exhibiting exact valence bond crystals, the specifically designed geometries and interactions often lead to unconventional properties. However, such models are not necessarily realised in materials. One of the few examples, is the Shastry-Sutherland model [38] capturing the physics of $\text{SrCu}_2(\text{BO}_3)_2$ [44, 68]. This match led to a fast development in the field, since the exactness of the phase allowed a very precise theoretical understanding, and features like discretised magnetisation plateaux could be studied [44, 46, 187, 223, 224]. In contrast, general frustrated models rely nearly completely on numerical methods and are therefore more difficult [175]. All models referred to above realise similar exact dimer singlet phases as in the Shastry-Sutherland model, and dimer singlets are by far the most commonly studied units in exact valence bond crystals [175].

In total, the number of known frustrated quantum models with exact ground states is limited, and to our knowledge, so far, no model hosting products of singlets on 4-spin plaquettes as an exact ground state has been proposed. Such a model is desirable from a purely theoretical point of view, since it yields the possibility to gain a fundamental understanding of plaquette phases including excitations, correlations, and magnetisations. The occurring properties are likely to reveal even more fascinating behaviour than dimer singlet phases, due to the 16 states present on a decoupled 4-spin plaquette, in contrast to four states on a dimer. This creates the possibility to tune between two distinct exact plaquette singlet phases via an exact phase transition. Further, both plaquette singlets have different local properties, and allow a variety of triplon excitations [73, 79, 208] as well as bound states. Recently, plaquette phases in the neighbourhood of a long-range ordered Néel phase were discussed in the context of a deconfined quantum critical point [177]. Experimentally, an entangled plaquette phase is realised in $\text{SrCu}_2(\text{BO}_3)_2$ under external pressure [75–78], where further measurements are expected (compare

Section 10.4) for an unambiguous identification of the phase, so a pristine theoretical understanding is in demand.

In the following, we introduce a quasi two-dimensional model hosting exact plaquette singlet ground states. On top of that, the model offers an extensive number of conserved quantities, which enable some exact statements about other phases of the model. This allows the investigation of the phase diagram beyond the analytically determined area of the exact plaquette phases. If the presented model is directly relevant for materials or can be simulated in experiments with artificial crystals remains open at this point. However, this seems not implausible, since the model relies on nearest-neighbour Heisenberg exchanges only. Historically, materials were synthesised, which realise models originally proposed out of purely theoretical motivation, just like $\text{SrCu}_2(\text{BO}_3)_2$ [38, 44, 68].

The quasi two-dimensional model consists of 4-spin plaquettes placed on a Shastry-Sutherland geometry. Every dimer in the Shastry-Sutherland model is replenished by a 45°-tilted plaquette p , which contains a vertical diagonal bond J_v and the horizontal diagonal dimer bond J_h from the Shastry-Sutherland model. This orthogonal-plaquette model is illustrated in Fig. 11.1(a) and from a bird's-eye view in Fig. 11.2. The Hamiltonian reads

$$\begin{aligned}
 H = & J \sum_p \sum_{\langle i,j \rangle} \vec{S}_{p,i} \cdot \vec{S}_{p,j} + J_h \sum_p \vec{S}_{p,2} \cdot \vec{S}_{p,4} \\
 & + J_v \sum_p \vec{S}_{p,1} \cdot \vec{S}_{p,3} + J' \sum_{\substack{\langle p,p' \rangle \\ \langle i,j \rangle}} \vec{S}_{p,i} \cdot \vec{S}_{p',j},
 \end{aligned} \tag{11.0.1}$$

where the spin operator $\vec{S}_{p,i}$ acts on spin i of plaquette p . A plaquette p is illustrated in Fig. 11.1(b). The first sum runs over all spins on intra-plaquette nearest-neighbour bonds (black lines). The second and third sum run over all plaquettes p and the interactions address spins on horizontal diagonals (dashed purple lines) and on vertical diagonals (dashed green lines), respectively. The fourth sum runs over all neighbouring spins on different plaquettes p and p' connected by inter-plaquette bonds (blue lines).

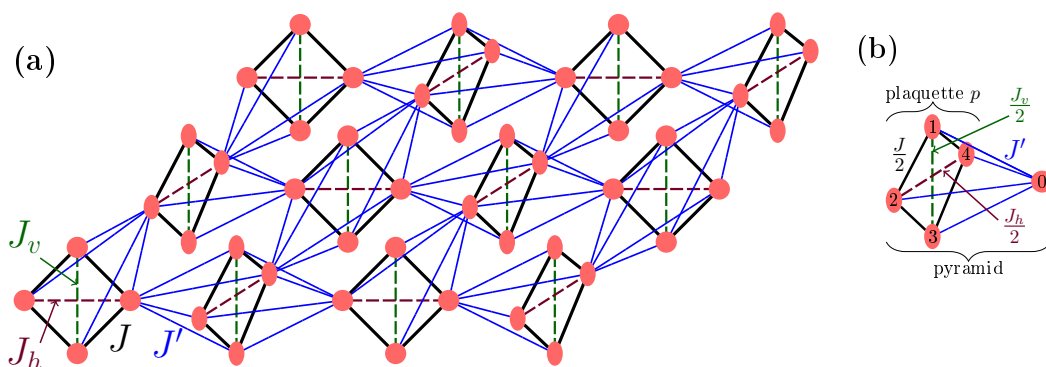


Fig. 11.1.: (a): Orthogonal-plaquette model (11.0.1) realising exact plaquette product ground states with singlets on 4-spin J -plaquettes (solid black lines). The orthogonal J_h -bonds (dashed purple) together with the in-plane J' -bonds (solid blue) yield the Shastry-Sutherland model (compare Fig. 7.1). (b): A 5-spin pyramid with halved intra-plaquette couplings contains a 4-spin plaquette p . The full model (11.0.1) can be decomposed into a sum of such pyramids (11.1.5).

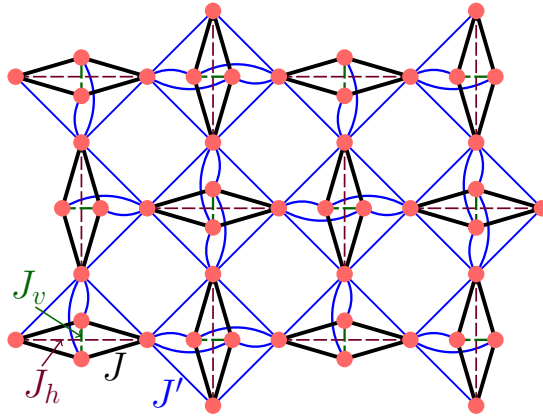


Fig. 11.2.: Bird's eye view of the orthogonal-plaquette model (11.0.1). The J' -couplings present in the Shastry-Sutherland model form a square lattice.

The coupling parameters are chosen in analogy to (not as for) the Shastry-Sutherland model (7.0.1): the exact singlets form on J -bonds and are connected by J' -bonds. The intra-plaquette couplings J_h and J_v introduce further triangles and lead to additional frustration. Without these J_h - and J_v -bonds the model is already frustrated by triangles from an intra-plaquette bond (black lines) and two inter-plaquette bonds (blue lines). The unit cell of the model contains eight spins of two orthogonally oriented plaquettes. Just like the Shastry-Sutherland model (compare Chapter 7), the model is invariant under rotations, \mathcal{C}_4 , around center points between plaquettes, and under reflections \mathcal{R}_1 and \mathcal{R}_2 over the perpendicular J_h -bonds. Further, a full inversion over the J_h -plane holds. The total spin on the vertical intra-plaquette J_v -diagonal, $s_v^p \in \{0, 1\}$ (compare Section 7.2), is a good quantum number for *every* plaquette p individually, similar to the orthogonal-dimer chain [213] (compare Chapter 9). This can be traced back to the lattice structure, which does not have direct interactions between distinct diagonals. As before, s_v denotes that all vertical diagonals are in the same state $s_v^p \forall p$ with the value $s_v \equiv s_v^p$. Interestingly, if $s_v = 0$ the vertical dimer singlets are completely decoupled from all remaining sites, which form a Shastry-Sutherland lattice. This can be seen for the according phases sketched in the phase diagrams in Fig. 11.3 and Fig. 11.5.

11.1. Exact plaquette singlet phases

For $J' = 0$ the orthogonal-plaquette model (11.0.1) decouples into individual 4-spin plaquettes as discussed in Section 7.2. In order to prove the exact singlet plaquette ground states, we argue from two directions. We start by showing that product states of plaquette singlets are eigenstates of the orthogonal-plaquette model (11.0.1) and determine their ground-state energies. Then, the lattice is separated into a sum of small units and a lower bound for the ground-state energy is derived.

i) All product states over plaquette singlets $s^p = 0 \forall p$ are exact eigenstates of the orthogonal-plaquette model (11.0.1) since all inter-plaquette interactions can be written as $\vec{S}_{p',0} \cdot (\vec{S}_{p,1} + \vec{S}_{p,2} + \vec{S}_{p,3} + \vec{S}_{p,4})$ where the spin $\vec{S}_{p',0}$ belongs to one plaquette, and $\vec{S}_{p,1}$ to $\vec{S}_{p,4}$ form the neighbouring plaquette [compare Fig. 11.1(b)]. The situation, where the total spin on all plaquettes is identical $s^p \forall p$ is denoted with $s \equiv s^p$. Gener-

ically, s^p is not a conserved quantity. This only holds if $s = 0$ as for the product states of plaquette singlets. The eigenstate where all plaquettes are in the same singlet $s = 0$ with $s_v = 0$ reads

$$|s = 0, s_v = 0\rangle = \prod_p |s^p = 0, s_v^p = 0\rangle_p, \quad (11.1.1)$$

whereas if $s = 0$ and $s_v = 1$ the eigenstate is given by

$$|s = 0, s_v = 1\rangle = \prod_p |s^p = 0, s_v^p = 1\rangle_p. \quad (11.1.2)$$

The eigenenergies per spin are

$$\epsilon^{s=0, s_v=0} = -3(J_h + J_v)/16 \quad \text{and} \quad (11.1.3)$$

$$\epsilon^{s=0, s_v=1} = -J/2 + (J_h + J_v)/16. \quad (11.1.4)$$

The corresponding eigenenergies of all other product states with combinations of plaquette singlets $s = 0$ with distinct $s_v^p \neq s_v^{p'}$ on different plaquettes p and p' are only as low in energy as $|s = 0, s_v = 0\rangle$ and $|s = 0, s_v = 1\rangle$ where the energies of the latter two states cross.

ii) The Hamiltonian of the orthogonal-plaquette model (11.0.1) can be decomposed into a sum over 5-spin pyramids as shown in Fig. 11.1(b). Let the spins of a pyramid be labeled by $\vec{S}_{p',0}$ and $\vec{S}_{p,1}$ to $\vec{S}_{p,4}$. Spins $\vec{S}_{p,1}$ to $\vec{S}_{p,4}$ are located on the 4-spin plaquette p with nearest-neighbour interactions J , and diagonal J_h - and J_v -bonds between $\vec{S}_{p,2}$ and $\vec{S}_{p,4}$, and $\vec{S}_{p,1}$ and $\vec{S}_{p,3}$, respectively. The additional spin $\vec{S}_{p',0}$ from a neighbouring plaquette p' interacts with all plaquette spins of p with a coupling strength J' . The full Hamiltonian (11.0.1) then reads

$$H = \sum_{\text{pyramids}} \left[\frac{J}{2} (\vec{S}_{p,1} + \vec{S}_{p,3}) \cdot (\vec{S}_{p,2} + \vec{S}_{p,4}) + \frac{J_h}{2} \vec{S}_{p,2} \cdot \vec{S}_{p,4} + \frac{J_v}{2} \vec{S}_{p,1} \cdot \vec{S}_{p,3} + J' \vec{S}_{p',0} \cdot \sum_{i=1}^4 \vec{S}_{p,i} \right]. \quad (11.1.5)$$

A single pyramid containing the plaquette p has two two-fold degenerate eigenstates with singlets on plaquettes, $s^p = 0$, again distinguished by $s_v^p = 0$ and $s_v^p = 1$. The degeneracy is manifested in the free spin $\vec{S}_{p',0}$. It occurs, since the J' -interactions do not contribute if $s^p = 0$. The corresponding eigenenergies of a single pyramid are

$$E_0^{s^p=0, s_v^p=0} = -3(J_h + J_v)/8 \quad \text{and} \quad (11.1.6)$$

$$E_0^{s^p=0, s_v^p=1} = -J + (J_h + J_v)/8.$$

Depending on the parameter regime these plaquette singlets yield the degenerate ground states of the pyramid. For instance, the plaquette singlets with $s_v^p = 1$ yield the ground states for $J_h \leq J$, $J_v \leq J$, and $J' \leq J/2$, as well as for $J_h = 0$, $J_v \leq J$, and $J' \leq J - J_v/2$, whereas the other singlets with $s_v^p = 0$ are lowest in energy for $J_h = J_v$, $J_v \geq J$, and

$J' \leq J_v/2$. Note, that ferromagnetic couplings are excluded, since the proof does not hold in this case.

The lattice can be tiled with the plaquette singlet eigenstates of pyramids without ambiguity and the degeneracy due to $\vec{S}_{p',0}$ is lifted. The sum over all ground-state energies on 5-spin pyramids with plaquette singlets gives a lower bound for the ground-state energy of (11.0.1) for antiferromagnetic couplings. This is based on the argument that joining pyramids cannot decrease the energy of the system: On the one hand, two singlet plaquettes "glued" together do not change the energy per spin. On the other hand, connecting plaquette spins with different pyramids introduces further frustration, which can increase the energy of the system, or leave it unchanged if all contributions of J' -bonds vanish. The lower bounds (lb) for the eigenenergy per spin are

$$\begin{aligned} \epsilon_{0,\text{lb}}^{s=0, s_v=0} &= 2E_0^{s^p=0, s_v^p=0}/4 \quad \text{and} \\ \epsilon_{0,\text{lb}}^{s=0, s_v=1} &= 2E_0^{s^p=0, s_v^p=1}/4. \end{aligned} \tag{11.1.7}$$

These energies are identical to the eigenenergies of the product over plaquette singlets in Eq. (11.1.3) and Eq. (11.1.4). Therefore, wherever a plaquette singlet state is the ground state on a single pyramid, the according product state over the lattice is the ground state of (11.0.1) when the interactions are antiferromagnetic. For example, for $J_h = J_v$, the product state $|s = 0, s_v = 1\rangle$ is the exact ground state of the system for at least $0 \leq J' \leq J/2$ with $0 \leq J_v \leq J$, as illustrated by the light-green area below the dashed black line in the phase diagram in Fig. 11.3. The product state $|s = 0, s_v = 0\rangle$ is the exact ground state for at least $0 \leq J' \leq J/2$ at $J_v \geq J$, which is captured by the light-red area below the dashed black line in the same phase diagram. This case is directly related to the one in the Shastry-Sutherland model [38]. Indeed, the exact state $|s = 0, s_v = 0\rangle$ can be seen as both, an exact plaquette singlet product state and an exact dimer singlet product state, since all dimers are decoupled. At the phase transition between the two exact singlet phases with $s_v = 0$ and $s_v = 1$, all products of plaquette singlets $s = 0$ with arbitrary combinations of $s_v^p = 0$ and $s_v^{p'} = 1$, $p \neq p'$, have the same eigenenergy. Hence, the ground state is extensively degenerate.

11.2. Phase diagrams

Whenever all spins on J_v -diagonals form singlets $s_v = 0$, these singlets are decoupled from the rest of the lattice. This is illustrated from a bird's eye view for the phases with $s_v = 0$ in the phase diagrams in Fig. 11.3 and Fig. 11.5. The vertical J_v -diagonals (dashed green bonds) are located in the center of the plaquettes (black bonds). If $s_v = 0$ (singlets are shaded blue), all bonds between spins, which are connected with both spins of the J_v -bond vanish, i.e. all plaquette J -bonds and half of the inter-plaquette J' -bonds. This leads to the decoupling of the lattice into individual J_v -singlets and a Shastry-Sutherland model of J' - and J_h -bonds, which allows further insights on various phases beyond the exact plaquette singlet product states introduced above (11.1.1), (11.1.2). In the following, we discuss two special sets of parameters, namely $J_h = J_v$ and $J_h = 0$.

11.2.1. $J_h = J_v$

For the symmetric model with $J_h = J_v$, we focus on antiferromagnetic couplings. In this case, both exact phases are realised. For weak inter-plaquette interactions J' the exact plaquette singlet phase $|s = 0, s_v = 1\rangle$ is present, as illustrated by the light-green background colour in the phase diagram in Fig. 11.3. With increasing diagonal couplings an exact first-order phase transition towards the exact dimer singlet phase $|s = 0, s_v = 0\rangle$ (light-red region) occurs. The transition line between the two is located at $J_h = J_v = J$ for at least $J'/J \leq 1/2$ as shown in Fig. 11.3. Along this line the ground state is given by all product states of arbitrary combinations of plaquette singlets, $s_v^p = 0$ and $s_v^{p'} = 1$ for $p \neq p'$, and therefore has an extensive degeneracy.

In the dimer singlet phase, $s = 0$ and $s_v = 0$, the vertical J_v -dimers are decoupled from an independent Shastry-Sutherland model of J' -bonds (solid blue) and J_h -bonds (dashed purple). As long as $s_h = 0 \forall p$, the J' -bonds do not contribute. However, for increasing values of J' beyond the dimer singlet phase, the Shastry-Sutherland model realises the entangled EPP [74]. In the orthogonal-plaquette model (11.0.1), it occurs

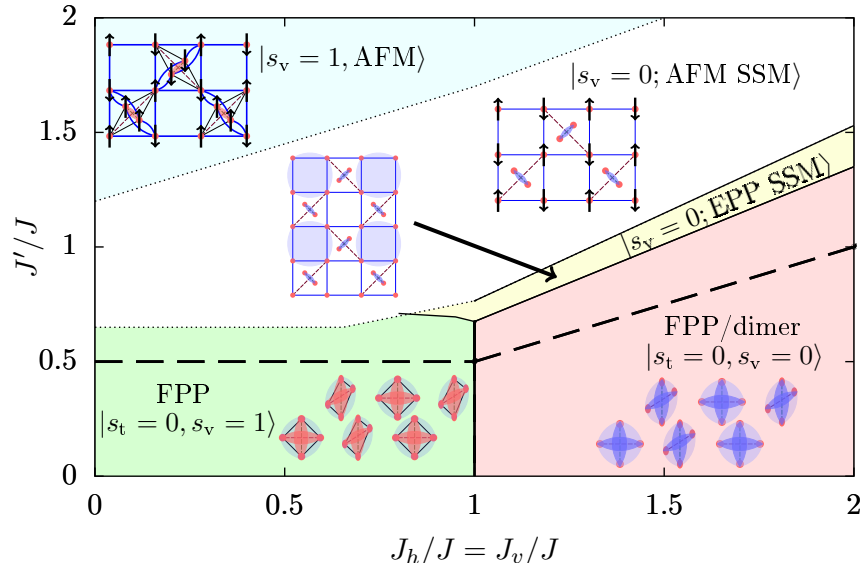


Fig. 11.3.: Phase diagram of the orthogonal-plaquette model (11.0.1) for $J_h = J_v$. The exact plaquette singlet phases $|s = 0, s_v = 1\rangle$ (light-green region) and $|s = 0, s_v = 0\rangle$ (light-red region) are analytically proven to occur in the areas below the dashed black line. The light-yellow and white areas yield the possible extension of an exact dimer singlet state $s_v = 0$ ($s_v^p = 0 \forall p$) in a product with an EPP or AFM on the Shastry-Sutherland lattice, respectively. All dotted lines are only sketched. The AFM with $s_v = 1$ ($s_v^p = 1 \forall p$, light-blue region) is included, but its existence is only clear in the limit $J' \gg J, J_h, J_v$. There might be other phases at intermediate coupling values. The given quantum numbers for all phases are exact. The phases are depicted such that couplings with vanishing contributions are not shown. Entangled local units are shaded blue for singlets and red for triplets. They are all exact apart from the plaquettes in $|s_v = 0; \text{EPP, SSM}\rangle$.

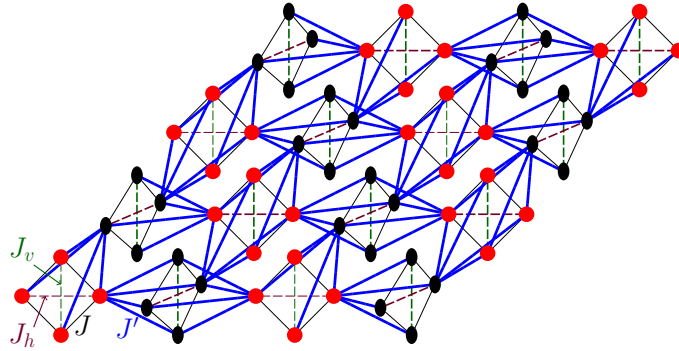


Fig. 11.4.: Orthogonal-plaquette model (11.0.1) for strong J' -bonds (blue). The different colours of the spins indicate the two sublattices of orthogonal plaquettes, which occur for $J = J_h = J_v = 0$.

as a product state with additional dimer singlets

$$|s_v = 0; \text{EPP, SSM}\rangle = \left(\prod_p |s_v^p = 0\rangle_p \right) |\text{EPP}\rangle_{\text{SSM}} . \quad (11.2.1)$$

The phase transition between the dimer singlet phase and the EPP in the Shastry-Sutherland model [74] yields the transition line $J' = 0.675J_v$ for $J_v \geq J$. For $J_v < J$, the dimer singlet phase does not occur, but the exact plaquette singlet phase $|s = 0, s_v = 1\rangle$. In order to determine the phase transition between this phase and the EPP in a product with $s_v = 0$, we employed the energies of the EPP in order 9 in λ derived from the model in Eq. (8.1.1) for $J'_2 = 1$ and $\Delta J'_2 = 0$. The Padé extrapolants [4, 4], [4, 5], and [5, 4] were averaged. The determined extension of the phase $|s_v = 0; \text{EPP, SSM}\rangle$ is shown by the light-yellow background colour in Fig. 11.3.

For larger J' -couplings, the EPP is replaced by the AFM. Therefore, a product of an AFM on the Shastry-Sutherland lattice with singlets on J_v -diagonals

$$|s_v = 0; \text{AFM, SSM}\rangle = \left(\prod_p |s_v = 0\rangle_p \right) |\text{AFM}\rangle_{\text{SSM}} \quad (11.2.2)$$

seems to be a good candidate phase, in particular at relatively weak plaquette couplings J . The transition to the EPP [74] yields, $J' = 0.765J_v$ for $J_v \geq J$, and the extension of the phase is illustrated by the white area in Fig. 11.3. All phase boundaries with dotted lines are only sketched.

In the limit $J = J_h = J_v = 0$, the full model (11.0.1) reduces to 4-spin plaquettes of J' -bonds. The lattice is bipartite and one sublattice consists of all spins on parallel plaquettes, as shown by black and red spins in Fig. 11.4. In this regime also for finite J , J_h , and J_v , the model is expected to host an AFM [4], where all spins on one set of parallel plaquettes are effectively either up or down and inverse on the orthogonal plaquettes. Thus, the total diagonal spin on every plaquette gives an exact triplet $s_v = 1$, and we write the state as $|s_v = 1, \text{AFM}\rangle$. Apart from quantum fluctuations,

all spins point in the same direction on every plaquette and in the limit of decoupled J -plaquettes these states are connected to the quintuplet with $s = 2$. They form a square lattice of macro-spins (4-spin J -plaquettes), which also form an AFM. This phase is indicated by a light-blue background in Fig. 11.3, even though we do not know any quantitative phase boundaries. In principle, other phases with $s_v^p = 1$ for some or all plaquettes p can occur. This seems in particular possible for small diagonal couplings J_h and J_v . For strong diagonal couplings these phases appear to be unlikely, and we expect the product phases with diagonal singlets (11.1.1), (11.2.1), and (11.2.2) to be competitive energetically, since diagonal triplets induce further interactions and frustration.

11.2.2. $J_h = 0$

Next, we discuss the orthogonal-plaquette model (11.0.1) with vanishing horizontal diagonal couplings $J_h = 0$ for ferromagnetic and antiferromagnetic inter-plaquette interactions J' . Again, for small diagonal couplings, the exact plaquette singlet phase $|s = 0, s_v = 1\rangle$ is realised. The smallest possible extension of this phase is illustrated by the dashed black line in the phase diagram in Fig. 11.5. For $J_h = 0$ the exact dimer singlet phase (11.1.1) does not occur, unless $J' = 0$, as explained in the following.

With $s_v = 0$ the system decouples into J_v -singlets and a separate square (sq) lat-

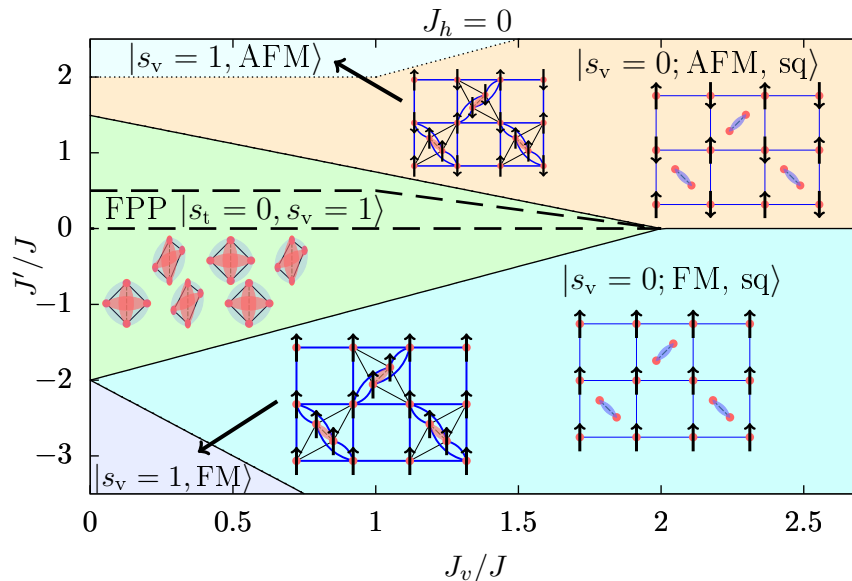


Fig. 11.5.: Phase diagram of the orthogonal-plaquette model (11.0.1) with $J_h = 0$. The exact plaquette singlet phase $|s = 0, s_v = 1\rangle$ (light-green) is analytically proven to occur in the area surrounded by the dashed black line. The light-orange and light-cyan areas yield the extension of products from dimer singlets $s_v = 0$ with an AFM and FM, respectively. A pure FM is shown in light-grey. There might be other phases in these areas. The AFM with $s_v = 1$ ($s_v^p = 1 \forall p$, light-blue) is sketched, and is only clear in the limit $J' \gg J, J_v$. Quantum numbers and correlations can be understood as in Fig. 11.3.

tice of J' -bonds. This is clear, since coming from the Shastry-Sutherland model only the diagonal J_h -couplings are removed. If all plaquettes are in a singlet state $s = 0$ with $s_v = 0$, the J' -couplings do not contribute either. In contrast, if the plaquettes are not in a singlet state, the J' -square lattice is present and leads to a reduction of the energy. Hence, the exact dimer singlet phase $|s = 0, s_v = 0\rangle$ does not occur for $|J'| > 0$. For antiferromagnetic inter-plaquette couplings, $J' > 0$, an AFM occurs on the square lattice [4]. The ground-state energy can be taken from series expansions $\epsilon_0^{\text{AFM, sq}} = (-0.6696 \pm 0.0003)J'$ [225]. The product state from the AFM on the square lattice and J_v -singlets is written as

$$|s_v = 0; \text{AFM, sq}\rangle = \left(\prod_p |s_v = 0\rangle_p \right) |\text{AFM}\rangle_{\text{sq}} . \quad (11.2.3)$$

The eigenenergy per spin is

$$\epsilon^{s_v=0; \text{AFM, sq}} = (-3J_v/16 + \epsilon_0^{\text{AFM, sq}})/2 . \quad (11.2.4)$$

For $J' < 0$ the square lattice exhibits a ferromagnetically ordered phase (FM) with $\epsilon_0^{\text{FM, sq}} = J'/2$. The corresponding product state in the orthogonal-plaquette model reads

$$|s_v = 0; \text{FM, sq}\rangle = \left(\prod_p |s_v = 0\rangle_p \right) |\text{FM}\rangle_{\text{sq}} \quad (11.2.5)$$

and has the eigenenergy per spin

$$\epsilon^{s_v=0; \text{FM, sq}} = -3J_v/16 + J'/4 . \quad (11.2.6)$$

In the limit of decoupled plaquettes, $J' = 0$, both product states of dimer singlets and magnetic order on a square lattice, $|s_v = 0; \text{AFM, sq}\rangle$ and $|s_v = 0; \text{FM, sq}\rangle$, are connected to the same plaquette triplet state with $s_h^p = 1 \forall p$. They are, however, distinguished by the total spin in z -direction $s_z^p \neq s_z^{p'}$ on distinct plaquettes p and p' . In the FM case, all spins on J_h -bonds point in the same direction, and a single plaquette state tiles the lattice. In contrast, in the AFM case the states on perpendicular plaquettes p and p' have to be chosen from different sectors, for instance $s_z^p = 2$ and $s_z^{p'} = -2$.

| state | notation | ϵ |
|--------------------|-----------------------------------|--|
| exact FPP | $ s = 0, s_v = 1\rangle$ | $-J/2 + J_v/16$ |
| exact FPP | $ s = 0, s_v = 0\rangle$ | $-3J_v/16$ |
| dimer singlet, AFM | $ s_v = 0; \text{AFM, sq}\rangle$ | $-3J_v/32 + \epsilon_0^{\text{AFM, square}}/2$ |
| dimer singlet, FM | $ s_v = 0; \text{FM, sq}\rangle$ | $-3J_v/16 + J'/4$ |
| FM | $ s_v = 1, \text{FM}\rangle$ | $J/4 + J_v/16 + 3J'/8$ |

Tab. 11.1.: Eigenstates, quantum numbers, and exactly known eigenenergies for the orthogonal-plaquette model (11.0.1) with only vertical diagonal bonds, $J_h = 0$.

Eventually, for strong ferromagnetic couplings $J' < 0$ with $|J'| \gg J, J_v$ the ferromagnetic phase is expected with the ground-state energy per spin

$$\epsilon_0^{\text{FM}} = J/4 + J_v/16 + 3J'/8. \quad (11.2.7)$$

The comparison of all derived eigenenergies, which are summarised in Tab. 11.1, yields the phase diagram as indicated by the background colours in Fig. 11.5. Again, apart from the regime where the exact plaquette phase was proven, the occurrence of other phases can not be excluded, but seems implausible for strong J_v -couplings. The extension of the antiferromagnetic phase $|s_v = 1, \text{AFM}\rangle$ is sketched and only clear in the limit $J' \gg J_v, J$.

We introduced a quasi two-dimensional orthogonal-plaquette model with four Heisenberg couplings. All products of plaquette singlets were shown to yield exact eigenstates. The product states of a single type of plaquette singlet $|s = 0, s_v = 0\rangle$ and $|s = 0, s_v = 1\rangle$ were proven to be the ground states, wherever the building block of the lattice, a 5-spin pyramid [Fig. 11.1(b)], has such a plaquette singlet ground state. These states are most likely more extended than on a single pyramid, as it was also found for the dimer singlet phase in the Shastry-Sutherland model [38, 74]. All products of plaquette singlets constitute the extensively degenerate ground-state manifold at phase transitions between the two plaquette singlet ground states $|s = 0, s_v = 1\rangle$ and $|s = 0, s_v = 0\rangle$. Further, there is an extensive number of conserved quantities given by the total spin on the J_v -diagonal on every plaquette. We exploited this property and studied the phase diagram beyond the exact plaquette singlet phases. For $J_h = J_v$ and antiferromagnetic couplings, products between J_v -singlets $s_v = 0$ and phases of the Shastry-Sutherland model, i.e. an entangled EPP and an AFM, seem most likely. If $J_h = 0$, the Shastry-Sutherland lattice reduces to a square lattice. In this case, products of J_v -singlets with FM or AFM are realised. In the large intra-plaquette coupling limit, $J' \gg J, J_h, J_v$, an AFM with $s_v = 1$ occurs that is connected to quintuplet states $s = 2$ on individual plaquettes. The search for additional phases is left for future investigations. To this end, apart from ED, series expansions, and iPEPS, for not too large values of J' Quantum Monte-Carlo simulations should be possible, due to the exact ground states. This route was recently taken for the Shastry-Sutherland model in a dimer singlet basis [180].

From the exact properties of the orthogonal-plaquette model, some further statements can be made. In the exact plaquette singlet phase $|s = 0, s_v = 1\rangle$ two triplon modes occur as expected from the limit of disconnected 4-site plaquettes. One of these modes is localised since it has $s_v^{p'} = 0$ on a single plaquette p' , whereas all other plaquettes have $s_v^p = 1 \forall p \neq p'$. The associated one-triplon dispersion is completely flat. The other mode has $s_v^p = 1$ and is expected to be dispersive. For small J_v - and J_h -couplings, the $s_v^p = 1$ excitation should host the gap, whereas for larger couplings J_v and J_h it is the excitation with $s_v^p = 0$. Such a behaviour is known from orthogonal-dimer chains [208]. For $J_h = 0$, it is clear that the exact dimer singlet phase in an AFM background, $|s_v = 0; \text{AFM, sq}\rangle$, has a gapless magnon continuum. The singlets on J_v -dimers yield dispersionless triplon excitations with $s_v^p = 1$. However, for $s_v^p = 1$ the couplings between dimers and the square lattice do not vanish. For a better and quantitative understanding further studies are required.

We note that the construction of models hosting exact product states can be gener-

alised: Instead of 4-spin plaquettes, other units realising a total singlet ground state can be taken. For every pair of interacting spins from two different units on the lattice, at least one of the spins must couple to all spins of this neighbouring unit homogeneously. The lattice must be decomposable into a sum over enlarged units (3-spin triangles for 2-spin dimers, 5-spin pyramids for orthogonal 4-spin plaquettes). Then, if the connection of these enlarged units to the full lattice overall increases the frustration, the product state of singlets on the units yields the ground state of the full model in at least the parameter range, where the singlets determine the ground state of the enlarged unit. For instance, the orthogonal structure of the Shastry-Sutherland model leads to exact valence bond crystals for all plaquettes with local singlets, not only dimers and 4-spin plaquettes, but also hexagons, octagons, or larger shapes. These have an even richer local structure, but seem less likely to be realised in materials. In contrast, the quasi two-dimensional orthogonal plaquette model, especially in the symmetric case with $J_h = J_v$, seems simple enough that an experimental realisation could be possible, either in a material or an artificial system. This would yield a good framework for the combined understanding of plaquette phases in theory and experiments.

12. Conclusion and outlook

This thesis was motivated by the possibility to realise phases of matter, which go beyond the ones known in classical physics or which were discovered in the early days of quantum mechanics, with new fundamental emergent properties. We focused on the magnetic phases in the Mott-insulating regime, and investigated systems from two distinct classes, $SU(N)$ -symmetric fermions with $N > 2$ and strongly-frustrated spin-1/2 quantum magnets.

In the first class, there was already some evidence for the occurrence of unconventional CSL phases within the strong-coupling regime of the Hubbard model with artificial gauge fields, on the honeycomb and on the triangular lattice [62, 166]. We studied the Hubbard model for general fluxes, and determined the effective low-energy description for the honeycomb lattice in order six. This allowed a first estimate of a potential phase transition point to an $SU(6)$ CSL within the parameters of the experimentally relevant coupling ratio U/t . The performance of according experiments with cold atoms in optical lattices would be the logical next step for the clarification of the potential occurrence of this CSL. Theoretically, this issue could be further clarified by an extensive study of all terms in the effective model, as well as the determination of the metal-insulator transition point.

We then turned to the $SU(7)$ -symmetric third-order J - K model on the triangular lattice. It was shown that the previously predicted CSL at $\pi/2$ -flux extends up to the π -flux case, such that this CSL breaks time-reversal symmetry spontaneously. This was done by ED, and VMC performed by Miklós Lajkó. We also followed the chiral edge states in ED, which seem to be robust against changing fluxes within some limits. However, the behaviour close to the π -flux case could not be interpreted conclusively. The analytic CFT predictions would be desirable to clarify this point in the future. Also, the investigation of all further terms and the determination of the metal-insulator transition would be valuable to collect further evidence for this CSL within the Mott-insulating phase of the $SU(7)$ -symmetric Hubbard model. A potential experimental realisation by cold alkaline-rare earth atoms in optical lattices does not require the application of artificial gauge fields at a filling of $6/7$ fermions per site.

For $SU(3)$ -symmetric fermions on the triangular lattice we estimated the metal-insulator transition point and investigated the full effective model in order five, which was derived in Ref. [66]. We extended the value of this effective model by employing Padé extrapolations on the effective coupling parameters in order to improve and assess the convergence behaviour. We then investigated the model for $SU(3)$ numerically with ED. Our collaborators Clemens Ganahl, Andreas Läuchli, and Pierre Nataf performed further ED, and Miklós Lajkó VMC. The previously found $\pi/3$ -flux CSL in the J - K model with purely imaginary ring exchange [62] was shown to be extended, and to occur even for purely real ring exchange. In higher orders of the effective model for explicitly and not explicitly broken time-reversal symmetry, signatures of the same CSL as in the

J - K model were discovered. The spontaneously time-reversal symmetry breaking CSL occurs around $U/t \approx 12$ within the Mott-insulating phase, which is estimated to break down only at $(U/t)_c^{\text{mi}} \approx 8.5$. This CSL could be probed experimentally in an optical lattice with cold alkaline-rare earth atoms at $2/3$ -filling.

The $SU(3)$ and $SU(7)$ CSLs exhibit Abelian anyons that are not suited for the application in topological quantum computers, where non-Abelian anyons are required. However, increasing the most common $SU(2)$ symmetry to $SU(N)$ with $N > 2$ appears to be a successful route to enhance quantum effects and therefore to trigger unconventional phases. It is not obvious whether this path for other values of N or together with additional interactions or particles could potentially lead to phases hosting non-Abelian anyons. Future investigations, both in theoretically and experimentally could help answering this question.

In the second class, we mainly focused on Shastry-Sutherland-like models. The Shastry-Sutherland model does not exhibit phases that would be conventionally called unconventional, but rather well known valence bond crystals. These would not occur in classical systems, and exotic behaviour manifests in quantised magnetisation plateaux, which were measured for $\text{SrCu}_2(\text{BO}_3)_2$ in magnetic fields. Instead of magnetic fields, we focused on the application of pressure on $\text{SrCu}_2(\text{BO}_3)_2$. This is not captured by the Shastry-Sutherland model, since the high-pressure data suggests the occurrence of a FPP [76–78], but the intermediate phase in the Shastry-Sutherland model is the EPP [74]. Therefore, we studied extended Shastry-Sutherland models, where the diagonal dimer and nearest-neighbour couplings are distinct on sets of filled plaquettes with orthogonal diagonals. We showed that an asymmetry in the couplings of only a few percent is sufficient to stabilise the FPP instead of the EPP. This was also supported by iPEPS results from our collaborators Schelto Crone, Ido Niesen, and Philippe Corboz. Further, it led to the clarification of a former phase diagram, Fig. 3 in Ref. [73], where the EPP was not considered. The phase diagram in Fig. 2 of Ref. [176] could be improved significantly. With iPEPS it was proven numerically, that the FPP is identical to the Haldane phase, and is therefore quasi-one-dimensional. This could also be understood in a limiting case of the extended model, the asymmetric orthogonal-dimer chain. We derived a full phase diagram with series expansions for the first time. This was done as for the Shastry-Sutherland model from the limit of decoupled plaquettes, but also from the Haldane limit of strong dimer couplings, where we increased the known order of the effective model by one.

We then determined the triplon dispersion and the dynamic structure factor of the EPP by series expansions for two-dimensional extended Shastry-Sutherland models, and a comparison at the experimentally expected symmetric coupling ratios does not fit the measured data. Only if the coupling ratio would increase much faster with pressure, the EPP could potentially fit the experimental findings. In order to verify this, additional calculations of the dispersion and the dynamic structure factor of the triplon mode that stems from the two-quasi-particle sector, would be required. For the FPP, we also determined the dispersions and the dynamic structure factors, which match the measurements more naturally. Again, the theoretical results only describe the data if the coupling ratios change more than expected.

In the process of determining the intermediate pressure phase of $\text{SrCu}_2(\text{BO}_3)_2$, the most insightful next step would be experimentally, since the measured data under-

lies severe uncertainties. In particular, the dispersion measured by INS [76] does not obey the symmetry of momentum space and only a couple of data points with large intensities at small momenta are reliable. Even though these experiments are very challenging, hopefully more and additional measurements could improve our understanding of $\text{SrCu}_2(\text{BO}_3)_2$. Further, the estimated behaviour of the coupling constants with increasing pressure is exposed to large errors both on the experimental side, where the precise determination of the pressure is difficult and on the theory side, where it is not obvious how the lattice structure behaves precisely at the phase transition, on top of numerical challenges. Solving this very demanding hen-egg problem of the spin-lattice coupling remains open for future investigations.

Our main insight in this respect is that if in $\text{SrCu}_2(\text{BO}_3)_2$ under pressure a plaquette phase is present, then the coupling ratios must change more than previously predicted. It seems more plausible, that a potential plaquette phase is the FPP, and this would go hand in hand with the natural lattice distortion of this phase [177] as studied in this thesis. The intermediate phase of the Shastry-Sutherland model, the EPP, was only resolved recently, which is also related to the fact that many other candidate phases are very close in energy. So, a pristine identification of the intermediate phase in $\text{SrCu}_2(\text{BO}_3)_2$ under pressure by excluding all potential phases will remain very challenging. For the distinction between the plaquette phases themselves this also holds, since they were shown to behave similar in several respects.

Encouraged by the exact dimer phase in the Shastry-Sutherland model, and motivated by open issues on plaquette phases, we then introduced an orthogonal-plaquette model. This model hosts exact plaquette phases and an exact phase transition between them, where an extensively degenerate ground state occurs. To our knowledge, such properties were not discovered before. An extensive number of conserved quantities allowed further insights and a first determination of phase diagrams. Currently, the most interesting open points seem to be potential intermediate phases, which could be resolved numerically, e.g. with ED, and the magnetisation plateaux above the exact phases, which potentially are even richer than for the dimer singlet phase in the Shastry-Sutherland model. Generalisations of the orthogonal-plaquette model to units of an even number of spin-1/2 were briefly introduced.

Both investigated classes of systems rely on basic degrees of freedom and simple interactions. Still, the arising phases cannot be drawn directly from the underlying models, and only occur from the interplay of many constituents as emergent phenomena. These are new fundamental properties of matter. In quantum systems, emergent phenomena can go beyond the scope of our classical understanding, which is due to quantum entanglement. It plays a key role and leads to more complex behaviour than in classical systems. That is why, phases like $\text{SU}(N)$ CSLs are difficult to imagine, but also the reason why they exhibit previously unknown somehow surprising properties. Quantum entanglement can make it notoriously challenging to determine emergent phenomena, as for the intermediate phase in the highly frustrated quantum magnet $\text{SrCu}_2(\text{BO}_3)_2$. On the other hand, it can also lead to a very pristine understanding when exact phases occur. Hopefully, future investigations can answer open questions from this thesis and in this field, both in theory and experiments.

Appendix

A. Effective SU(N) models on small clusters

The results in order five in t/U for the graphs g_1 , g_2 , g_3 , g_4 , and g_5 were derived in Ref. [66]. The exchange parameters are labelled with the graph g_i they belong to and the tilde indicates reduced contributions. The effective models act in a pure spin basis. All contributions for states with multiple occupied sites vanish by projection, P . The flux in complex exchanges is defined for clockwise circulations. The labels of the sites are given in Tab. 4.1.

dimer g_1

$$P\tilde{\mathcal{H}}_{\text{eff}}^{g_1}P = \tilde{A}_1 + \tilde{B}_1P_{12} , \quad (\text{A.0.1})$$

$$\tilde{A}_1 = -2\left(\frac{t}{U}\right)^2 + 8\left(\frac{t}{U}\right)^4 = -\tilde{B}_1 \quad (\text{A.0.2})$$

trimer g_2

$$P\tilde{\mathcal{H}}_{\text{eff}}^{g_2}P = \tilde{A}_2 + \tilde{B}_2(P_{12} + P_{23}) + \tilde{C}_2P_{13} + \tilde{D}_2(P_{123} + \text{h.c.}) , \quad (\text{A.0.3})$$

$$\tilde{A}_2 = -\frac{10}{3}\left(\frac{t}{U}\right)^4 = -\tilde{C}_2 , \quad \tilde{B}_2 = \frac{4}{3}\left(\frac{t}{U}\right)^4 = -\tilde{D}_2 \quad (\text{A.0.4})$$

triangle g_3

$$P\tilde{\mathcal{H}}_{\text{eff}}^{g_3}P = \tilde{A}_3P + \tilde{B}_3(P_{12} + P_{23} + P_{13}) + (\tilde{C}_3P_{123} + \text{h.c.}) , \quad (\text{A.0.5})$$

$$\tilde{A}_3 = \left(-6\left(\frac{t}{U}\right)^3 + 138\left(\frac{t}{U}\right)^5\right)\cos(\Phi_{g_3}) = \tilde{B}_3 , \quad (\text{A.0.6})$$

$$\tilde{C}_3 = -6e^{i\Phi_{g_3}}\left(\frac{t}{U}\right)^3 + (114e^{i\Phi_{g_3}} + 24e^{-i\Phi_{g_3}})\left(\frac{t}{U}\right)^5$$

4-site plaquette g_4

$$P\tilde{\mathcal{H}}_{\text{eff}}^{g_4}P = \tilde{A}_4 + \tilde{B}_4(P_{12} + P_{23} + P_{34} + P_{41}) + \tilde{C}_4(P_{13} + P_{24}) \\ + (\tilde{D}_4(P_{412} + P_{123} + P_{234} + P_{341}) + \text{h.c.}) \quad (\text{A.0.7})$$

$$+ (\tilde{E}_4P_{1234} + \text{h.c.}) ,$$

$$\tilde{A}_4 = -8\left(\frac{t}{U}\right)^4\cos(\Phi_{g_4}) = -\tilde{B}_4 = -\tilde{C}_4 , \quad (\text{A.0.8})$$

$$\tilde{D}_4 = -10e^{i\Phi_{g_4}}\left(\frac{t}{U}\right)^4 , \quad \tilde{E}_4 = 20e^{i\Phi_{g_4}}\left(\frac{t}{U}\right)^4$$

triangle plus one site g_5

$$\begin{aligned}
P\tilde{\mathcal{H}}_{\text{eff}}^{g_5}P &= \tilde{A}_5 + \tilde{B}_5 P_{12} + \tilde{C}_5 (P_{13} + P_{23}) + \tilde{D}_5 P_{34} \\
&\quad + \tilde{E}_5 (P_{24} + P_{14}) + \left(\tilde{F}_5 P_{123} + \text{h.c.} \right) \\
&\quad + \left(\tilde{G}_5 (P_{134} + P_{243}) + \text{h.c.} \right) + \left(\tilde{H}_5 P_{241} + \text{h.c.} \right) \\
&\quad + \left(\tilde{I}_5 (P_{1234} + P_{4312}) + \text{h.c.} \right) + \tilde{J}_5 P_{12} P_{34} ,
\end{aligned} \tag{A.0.9}$$

$$\begin{aligned}
\tilde{A}_5 &= -\frac{46}{3} \cos(\Phi_{g_5}) \left(\frac{t}{U} \right)^5 , & \tilde{B}_5 &= \frac{206}{9} \cos(\Phi_{g_5}) \left(\frac{t}{U} \right)^5 , \\
\tilde{C}_5 &= \frac{20}{3} \cos(\Phi_{g_5}) \left(\frac{t}{U} \right)^5 , & \tilde{D}_5 &= \frac{16}{3} \cos(\Phi_{g_5}) \left(\frac{t}{U} \right)^5 , \\
\tilde{E}_5 &= \frac{26}{3} \cos(\Phi_{g_5}) \left(\frac{t}{U} \right)^5 , & \tilde{F}_5 &= -\frac{94}{9} e^{i\Phi_{g_5}} \left(\frac{t}{U} \right)^5 , \\
\tilde{G}_5 &= \left(\frac{2}{3} e^{-i\Phi_{g_5}} - \frac{10}{3} e^{i\Phi_{g_5}} \right) \left(\frac{t}{U} \right)^5 , \\
\tilde{H}_5 &= -\frac{112}{9} e^{i\Phi_{g_5}} \left(\frac{t}{U} \right)^5 , & \tilde{I}_5 &= \frac{58}{9} e^{i\Phi_{g_5}} \left(\frac{t}{U} \right)^5 , \\
\tilde{J}_5 &= -\frac{116}{9} \cos(\Phi_{g_5}) \left(\frac{t}{U} \right)^5
\end{aligned} \tag{A.0.10}$$

5-site loop g_6

$$\begin{aligned}
P\tilde{\mathcal{H}}_{\text{eff}}^{g_6}P &= \tilde{A}_6 + \tilde{B}_6 \sum_{\langle ij \rangle} P_{ij} + \tilde{C}_6 \sum_{\langle\langle ij \rangle\rangle} P_{ij} \\
&\quad + \sum_{ijk} \left(\tilde{D}_6 (P_{ijk} + P_{ij(k+1)}) + \text{h.c.} \right) \\
&\quad + \sum_{ijkm} \left(\tilde{E}_6 P_{ijkm} + \text{h.c.} \right) + \left(\tilde{F}_6 P_{12345} + \text{h.c.} \right) ,
\end{aligned} \tag{A.0.11}$$

$$\begin{aligned}
\tilde{A}_6 &= -10 \cos(\Phi) \left(\frac{t}{U} \right)^5 = -\tilde{B}_6 = -\tilde{C}_6 , & \tilde{D}_6 &= -15 e^{i\Phi} \left(\frac{t}{U} \right)^5 , \\
\tilde{E}_6 &= 35 e^{i\Phi} \left(\frac{t}{U} \right)^5 , & \tilde{F}_6 &= -70 e^{i\Phi} \left(\frac{t}{U} \right)^5
\end{aligned} \tag{A.0.12}$$

The indices are defined as $i \in \{1, 2, 3, 4, 5\}$, and $j = i + 1$, $k = i + 2$, $m = i + 3$ with periodic boundaries, so for instance for $i = 4$, it is $j = 5$, $k = 1$, and $m = 2$. All distinct possibilities of site locations have to be summed up.

4-site chain g_7

$$\begin{aligned}
P\tilde{\mathcal{H}}_{\text{eff}}^{g_7}P &= \tilde{A}_7 + \tilde{B}_7 (P_{12} + P_{23} + P_{34}) + \tilde{C}_7 (P_{13} + P_{24}) \\
&\quad + \tilde{D}_7 P_{14} + \tilde{E}_7 (P_{123} + P_{234} + \text{h.c.}) \\
&\quad + \tilde{F}_7 (P_{124} + P_{134} + \text{h.c.}) + \tilde{G}_7 (P_{1234} + \text{h.c.}) ,
\end{aligned} \tag{A.0.13}$$

$$\begin{aligned}\tilde{A}_7 &= -\frac{716}{27} \left(\frac{t}{U}\right)^6, & \tilde{B}_7 &= \frac{196}{27} \left(\frac{t}{U}\right)^6 = \tilde{C}_7, & \tilde{D}_7 &= \frac{14}{3} \left(\frac{t}{U}\right)^6, \\ \tilde{E}_7 &= -\frac{160}{27} \left(\frac{t}{U}\right)^6, & \tilde{F}_7 &= -\frac{4}{3} \left(\frac{t}{U}\right)^6, & \tilde{G}_7 &= 2 \left(\frac{t}{U}\right)^6\end{aligned}\quad (\text{A.0.14})$$

4-site \mathbf{T} g_8

$$\begin{aligned}P\tilde{\mathcal{H}}_{\text{eff}}^{g_8}P &= \tilde{A}_8 + \tilde{B}_8 (P_{12} + P_{23} + P_{24}) + \tilde{C}_8 (P_{14} + P_{43} + P_{31}) \\ &\quad + \tilde{D}_8 (P_{143} + P_{341}) + \tilde{E}_8 (P_{124} + P_{423} + P_{321} + \text{h.c.}) \\ &\quad + \tilde{F}_8 (P_{1234} + P_{3241} + P_{4231} + \text{h.c.}) \\ &\quad + \tilde{G}_8 (P_{23}P_{14} + P_{24}P_{13} + P_{12}P_{34}),\end{aligned}\quad (\text{A.0.15})$$

$$\begin{aligned}\tilde{A}_8 &= -\frac{8}{3} \left(\frac{t}{U}\right)^6, & \tilde{B}_8 &= -\frac{79}{9} \left(\frac{t}{U}\right)^6, & \tilde{C}_8 &= \frac{77}{3} \left(\frac{t}{U}\right)^6, \\ \tilde{D}_8 &= -\frac{79}{6} \left(\frac{t}{U}\right)^6, & \tilde{E}_8 &= -\frac{85}{18} \left(\frac{t}{U}\right)^6, \\ \tilde{F}_8 &= \frac{83}{9} \left(\frac{t}{U}\right)^6, & \tilde{G}_8 &= -\frac{146}{9} \left(\frac{t}{U}\right)^6\end{aligned}\quad (\text{A.0.16})$$

6-site loop g_9

$$\begin{aligned}P\tilde{\mathcal{H}}_{\text{eff}}^{g_9}P &= \tilde{A}_9 + \tilde{B}_9 \sum_{\langle ij \rangle} P_{ij} + \tilde{C}_9 \sum_{\langle\langle ij \rangle\rangle} P_{ij} + \tilde{D}_9 \sum_{\langle\langle\langle ij \rangle\rangle\rangle} P_{ij} \\ &\quad + \sum_{\langle ijk \rangle} (\tilde{E}_9 P_{ijk} + \text{h.c.}) + \sum_{ikl} \tilde{F}_9 (P_{ijl} + P_{ikm} + \text{h.c.}) \\ &\quad + \sum_{ijkl} (\tilde{G}_9 P_{ijkl} + \text{h.c.}) + \sum_{ijkm} (\tilde{H}_9 P_{ijkm} + \text{h.c.}) \\ &\quad + \sum_{ijklm} (\tilde{I}_9 P_{ijklm} + \text{h.c.}) + (\tilde{J}_9 P_{123456} + \text{h.c.}),\end{aligned}\quad (\text{A.0.17})$$

$$\begin{aligned}\tilde{A}_9 &= -12 \cos(\Phi_{g_9}) \left(\frac{t}{U}\right)^6 = -\tilde{B}_9 = -\tilde{C}_9 = -\tilde{D}_9, \\ \tilde{E}_9 &= -21e^{i\Phi_{g_9}} \left(\frac{t}{U}\right)^6 = \tilde{F}_9, \\ \tilde{G}_9 &= 56e^{i\Phi_{g_9}} \left(\frac{t}{U}\right)^6 = \tilde{H}_9, \\ \tilde{I}_9 &= -126e^{i\Phi_{g_9}} \left(\frac{t}{U}\right)^6, & \tilde{J}_9 &= 252e^{i\Phi_{g_9}} \left(\frac{t}{U}\right)^6\end{aligned}\quad (\text{A.0.18})$$

The indices i, j, k, l, m, n are defined analogously to the 5-site loop g_6 . Again, all distinct possibilities of site locations have to be summed up.

Bibliography

- [1] L. D. Landau. Theory of phase transformations. I. *Phys. Z. Sowjetunion*, 11(26), 1937.
- [2] L. D. Landau. Theory of phase transformations. II. *Phys. Z. Sowjetunion*, 11(545), 1937.
- [3] T. Brauner. Spontaneous Symmetry Breaking and Nambu–Goldstone Bosons in Quantum Many-Body Systems. *Symmetry*, 2(2):609–657, 2010.
- [4] E. Manousakis. The spin- $\frac{1}{2}$ Heisenberg antiferromagnet on a square lattice and its application to the cuprous oxides. *Rev. Mod. Phys.*, 63:1–62, 1991.
- [5] P. W. Anderson. Resonating valence bonds: A new kind of insulator? *Materials Research Bulletin*, 8(2):153 – 160, 1973.
- [6] C. Lhuillier and G. Misguich. Introduction to Quantum Spin Liquids. In F. Mila C. Lacroix, P. Mendels, editor, *Introduction to Frustrated Magnetism*, volume 164, chapter 2, pages 23–41. Springer Series in Solid-State Sciences, Springer Berlin Heidelberg, 2011.
- [7] L. Savary and L. Balents. Quantum spin liquids: a review. *Reports on Progress in Physics*, 80(1):016502, 2016.
- [8] Y. Zhou, K. Kanoda, and T.-K. Ng. Quantum spin liquid states. *Rev. Mod. Phys.*, 89:025003, 2017.
- [9] X. G. Wen. Vacuum degeneracy of chiral spin states in compactified space. *Phys. Rev. B*, 40:7387–7390, 1989.
- [10] D. C. Tsui, H. L. Stormer, and A. C. Gossard. Two-Dimensional Magnetotransport in the Extreme Quantum Limit. *Phys. Rev. Lett.*, 48:1559–1562, 1982.
- [11] R. B. Laughlin. Anomalous Quantum Hall Effect: An Incompressible Quantum Fluid with Fractionally Charged Excitations. *Phys. Rev. Lett.*, 50:1395–1398, 1983.
- [12] J. E. Moore. The birth of topological insulators. *Nature*, 464(7286):194–198, 2010.
- [13] M. Z. Hasan and C. L. Kane. Colloquium: Topological insulators. *Rev. Mod. Phys.*, 82:3045–3067, 2010.
- [14] B. I. Halperin. Statistics of Quasiparticles and the Hierarchy of Fractional Quantized Hall States. *Phys. Rev. Lett.*, 52:1583–1586, 1984.

-
- [15] G. Moore and N. Read. Nonabelions in the fractional quantum hall effect. *Nuclear Physics B*, 360(2):362 – 396, 1991.
- [16] F. Wilczek. Quantum Mechanics of Fractional-Spin Particles. *Phys. Rev. Lett.*, 49:957–959, 1982.
- [17] A. Kitaev. Fault-tolerant quantum computation by anyons. *Annals of Physics*, 303(1):2–30, 2003.
- [18] A. Kitaev. Anyons in an exactly solved model and beyond. *Annals of Physics*, 321(1):2–111, 2006.
- [19] C. Nayak, S. H. Simon, A. Stern, M. Freedman, and S. Das Sarma. Non-Abelian anyons and topological quantum computation. *Rev. Mod. Phys.*, 80:1083–1159, 2008.
- [20] M. Vojta. Quantum phase transitions. *Reports on Progress in Physics*, 66(12):2069–2110, 2003.
- [21] J. Hubbard. Electron correlations in narrow energy bands. *Proceedings of the Royal Society of London. Series A. Mathematical and Physical Sciences*, 276(1365):238–257, 1963.
- [22] M. Schüler, E. G. C. P. van Loon, M. I. Katsnelson, and T. O. Wehling. First-order metal-insulator transitions in the extended Hubbard model due to self-consistent screening of the effective interaction. *Phys. Rev. B*, 97:165135, 2018.
- [23] O. I. Motrunich. Variational study of triangular lattice spin-1/2 model with ring exchanges and spin liquid state in κ -(ET)₂Cu₂(CN)₃. *Phys. Rev. B*, 72:045105, 2005.
- [24] D. N. Sheng, O. I. Motrunich, and M. P. A. Fisher. Spin Bose-metal phase in a spin- $\frac{1}{2}$ model with ring exchange on a two-leg triangular strip. *Phys. Rev. B*, 79:205112, 2009.
- [25] H.-Y. Yang, A. M. Läuchli, F. Mila, and K. P. Schmidt. Effective Spin Model for the Spin-Liquid Phase of the Hubbard Model on the Triangular Lattice. *Phys. Rev. Lett.*, 105:267204, 2010.
- [26] S. Yan, D. A. Huse, and S. R. White. Spin-Liquid Ground State of the $S = 1/2$ Kagome Heisenberg Antiferromagnet. *Science*, 332(6034):1173–1176, 2011.
- [27] S. Depenbrock, I. P. McCulloch, and U. Schollwöck. Nature of the Spin-Liquid Ground State of the $S = 1/2$ Heisenberg Model on the Kagome Lattice. *Phys. Rev. Lett.*, 109:067201, 2012.
- [28] R. Kaneko, S. Morita, and M. Imada. Gapless Spin-Liquid Phase in an Extended Spin 1/2 Triangular Heisenberg Model. *J. Phys. Soc. Jpn.*, 83(9):093707, 2014.
- [29] W.-J. Hu, S.-S. Gong, W. Zhu, and D. N. Sheng. Competing spin-liquid states in the spin- $\frac{1}{2}$ Heisenberg model on the triangular lattice. *Phys. Rev. B*, 92:140403, 2015.

-
- [30] W.-J. Hu, S.-S. Gong, and D. N. Sheng. Variational Monte Carlo study of chiral spin liquid in quantum antiferromagnet on the triangular lattice. *Phys. Rev. B*, 94:075131, 2016.
- [31] Z. Zhu and S. R. White. Spin liquid phase of the $S = \frac{1}{2}$ $J_1 - J_2$ Heisenberg model on the triangular lattice. *Phys. Rev. B*, 92:041105, 2015.
- [32] A. Wietek and A. M. Läuchli. Chiral spin liquid and quantum criticality in extended $S = \frac{1}{2}$ Heisenberg models on the triangular lattice. *Phys. Rev. B*, 95:035141, 2017.
- [33] A. Szasz, J. Motruk, M. P. Zaletel, and J. E. Moore. Observation of a chiral spin liquid phase of the Hubbard model on the triangular lattice: a density matrix renormalization group study. *arXiv:1808.00463*, 2018.
- [34] K. P. Schmidt and G. S. Uhrig. Excitations in One-Dimensional $S = \frac{1}{2}$ Quantum Antiferromagnets. *Phys. Rev. Lett.*, 90:227204, 2003.
- [35] A. M. Läuchli. Numerical Simulations of Frustrated Systems. In F. Mila C. Lacroix, P. Mendels, editor, *Introduction to Frustrated Magnetism*. Springer Series in Solid-State Sciences, Springer Berlin Heidelberg, 2011.
- [36] C. K. Majumdar and D. K. Ghosh. On Next-Nearest-Neighbor Interaction in Linear Chain. I. *J. Math. Phys.*, 10(8):1388–1398, 1969.
- [37] F. Monti and A. Sütő. Spin-1/2 Heisenberg model on Δ trees. *Physics Letters A*, 156(3):197 – 200, 1991.
- [38] B. S. Shastry and B. Sutherland. Exact ground state of a quantum mechanical antiferromagnet. *Physica B+C*, 108(1):1069 – 1070, 1981.
- [39] K. Ueda and S. Miyahara. A class of Heisenberg models with orthogonal dimer ground states. *J. Phys. Condens. Matter*, 11(17):L175–L178, 1999.
- [40] S. Chen and H. Büttner. Exact ground state of the generalized three-dimensional Shastry-Sutherland model. *Eur. Phys. J. B*, 29(1):15–18, 2002.
- [41] A. V. Chubukov and D. I. Golosov. Quantum theory of an antiferromagnet on a triangular lattice in a magnetic field. *J. Phys. Condens. Matter*, 3(1):69–82, 1991.
- [42] K. Hida. Magnetic Properties of the Spin-1/2 Ferromagnetic-Ferromagnetic-Antiferromagnetic Trimerized Heisenberg Chain. *J. Phys. Soc. Jpn.*, 63(6):2359–2364, 1994.
- [43] M. Oshikawa, M. Yamanaka, and I. Affleck. Magnetization Plateaus in Spin Chains: “Haldane Gap” for Half-Integer Spins. *Phys. Rev. Lett.*, 78:1984–1987, 1997.
- [44] S. Miyahara and K. Ueda. Exact Dimer Ground State of the Two Dimensional Heisenberg Spin System $\text{SrCu}_2(\text{BO}_3)_2$. *Phys. Rev. Lett.*, 82:3701–3704, 1999.

- [45] E. Müller-Hartmann, R. R. P. Singh, C. Knetter, and G. S. Uhrig. Exact Demonstration of Magnetization Plateaus and First-Order Dimer-Néel Phase Transitions in a Modified Shastry-Sutherland Model for $\text{SrCu}_2(\text{BO}_3)_2$. *Phys. Rev. Lett.*, 84:1808–1811, 2000.
- [46] D. A. Schneider, K. Coester, F. Mila, and K. P. Schmidt. Pressure dependence of the magnetization plateaus of $\text{SrCu}_2(\text{BO}_3)_2$. *Phys. Rev. B*, 93:241107, 2016.
- [47] P. Corboz and F. Mila. Crystals of Bound States in the Magnetization Plateaus of the Shastry-Sutherland Model. *Phys. Rev. Lett.*, 112:147203, 2014.
- [48] K. Totsuka. Magnetization plateau in the $S = \frac{1}{2}$ Heisenberg spin chain with next-nearest-neighbor and alternating nearest-neighbor interactions. *Phys. Rev. B*, 57:3454–3465, 1998.
- [49] F. Mila. Ladders in a magnetic field: a strong coupling approach. *Eur. Phys. J. B*, 6(2):201–205, 1998.
- [50] Y. Iqbal, F. Becca, S. Sorella, and D. Poilblanc. Gapless spin-liquid phase in the kagome spin-1/2 Heisenberg antiferromagnet. *Phys. Rev. B*, 87(6), 2013.
- [51] Y.-C. He, M. P. Zaletel, M. Oshikawa, and F. Pollmann. Signatures of Dirac Cones in a DMRG Study of the Kagome Heisenberg Model. *Phys. Rev. X*, 7:031020, 2017.
- [52] M. Hermele, V. Gurarie, and A. M. Rey. Mott Insulators of Ultracold Fermionic Alkaline Earth Atoms: Underconstrained Magnetism and Chiral Spin Liquid. *Phys. Rev. Lett.*, 103:135301, 2009.
- [53] M. Hermele and V. Gurarie. Topological liquids and valence cluster states in two-dimensional $\text{SU}(N)$ magnets. *Phys. Rev. B*, 84:174441, 2011.
- [54] M. A. Cazalilla, A. F. Ho, and M. Ueda. Ultracold gases of ytterbium: ferromagnetism and Mott states in an $\text{SU}(6)$ Fermi system. *New Journal of Physics*, 11(10):103033, 2009.
- [55] A. V. Gorshkov, M. Hermele, V. Gurarie, C. Xu, P. S. Julienne, J. Ye, P. Zoller, E. Demler, M. D. Lukin, and A. M. Rey. Two-orbital $\text{SU}(N)$ magnetism with ultracold alkaline-earth atoms. *Nature Physics*, 6:289–295, 2010.
- [56] S. Taie, R. Yamazaki, S. Sugawa, and Y. Takahashi. An $\text{SU}(6)$ Mott insulator of an atomic Fermi gas realized by large-spin Pomeranchuk cooling. *Nature Physics*, 8:825–830, 2012.
- [57] F. Scazza, C. Hofrichter, M. Höfer, P. C. De Groot, I. Bloch, and S. Fölling. Observation of two-orbital spin-exchange interactions with ultracold $\text{SU}(N)$ -symmetric fermions. *Nature Physics*, 10:779–784, 2014.
- [58] X. Zhang, M. Bishof, S. L. Bromley, C. V. Kraus, M. S. Safronova, P. Zoller, A. M. Rey, and J. Ye. Spectroscopic observation of $\text{SU}(N)$ -symmetric interactions in Sr orbital magnetism. *Science*, 345(6203):1467–1473, 2014.

-
- [59] M. A. Cazalilla and A. M. Rey. Ultracold Fermi gases with emergent $SU(N)$ symmetry. *Reports on Progress in Physics*, 77(12):124401, 2014.
- [60] G. Pagano, M. Mancini, G. Cappellini, P. Lombardi, F. Schäfer, H. Hu, X.-J. Liu, J. Catani, C. Sias, M. Inguscio, and L. Fallani. A one-dimensional liquid of fermions with tunable spin. *Nature Physics*, 10:198–201, 2014.
- [61] C. Hofrichter, L. Riegger, F. Scazza, M. Höfer, D. R. Fernandes, I. Bloch, and S. Fölling. Direct Probing of the Mott Crossover in the $SU(N)$ Fermi-Hubbard Model. *Phys. Rev. X*, 6:021030, 2016.
- [62] P. Nataf, M. Lajkó, A. Wietek, K. Penc, F. Mila, and A. M. Läuchli. Chiral Spin Liquids in Triangular-Lattice $SU(N)$ Fermionic Mott Insulators with Artificial Gauge Fields. *Phys. Rev. Lett.*, 117:167202, 2016.
- [63] S. Bieri, M. Serbyn, T. Senthil, and P. A. Lee. Paired chiral spin liquid with a Fermi surface in $S = 1$ model on the triangular lattice. *Phys. Rev. B*, 86:224409, 2012.
- [64] H.-H. Lai. Possible uniform-flux chiral spin liquid states in the $SU(3)$ ring-exchange model on the triangular lattice. *Phys. Rev. B*, 87:205111, 2013.
- [65] H.-H. Lai. Possible spin liquid states with parton Fermi surfaces in the $SU(3)$ ring-exchange model on the triangular lattice. *Phys. Rev. B*, 87:205131, 2013.
- [66] C. Boos. Mott physics of $SU(N)$ -Hubbard models from the strong-coupling perspective. Master’s thesis, Technische Universität Dortmund, 2016.
- [67] B. S. Shastry and B. Kumar. $SrCu_2(BO_3)_2$: A Unique Mott Hubbard Insulator. *Progress of Theoretical Physics Supplement*, 145:1–16, 2002.
- [68] H. Kageyama, K. Yoshimura, R. Stern, N. V. Mushnikov, K. Onizuka, M. Kato, K. Kosuge, C. P. Slichter, T. Goto, and Y. Ueda. Exact Dimer Ground State and Quantized Magnetization Plateaus in the Two-Dimensional Spin System $SrCu_2(BO_3)_2$. *Phys. Rev. Lett.*, 82:3168–3171, 1999.
- [69] M. Albrecht and F. Mila. First-order transition between magnetic order and valence bond order in a 2D frustrated Heisenberg model. *Europhysics Letters*, 34(2):145–150, 1996.
- [70] A. Koga and N. Kawakami. Quantum Phase Transitions in the Shastry-Sutherland Model for $SrCu_2(BO_3)_2$. *Phys. Rev. Lett.*, 84:4461–4464, 2000.
- [71] A. Läuchli, S. Wessel, and M. Sigrist. Phase diagram of the quadrumerized Shastry-Sutherland model. *Phys. Rev. B*, 66:014401, 2002.
- [72] W. Zheng, J. Oitmaa, and C. J. Hamer. Phase diagram of the Shastry-Sutherland antiferromagnet. *Phys. Rev. B*, 65:014408, 2001.
- [73] Y. Takushima, A. Koga, and N. Kawakami. Competing Spin-Gap Phases in a Frustrated Quantum Spin System in Two Dimensions. *J. Phys. Soc. Jpn.*, 70(5):1369–1374, 2001.

- [74] P. Corboz and F. Mila. Tensor network study of the Shastry-Sutherland model in zero magnetic field. *Phys. Rev. B*, 87:115144, 2013.
- [75] T. Waki, K. Arai, M. Takigawa, Y. Saiga, Y. Uwatoko, H. Kageyama, and Y. Ueda. A Novel Ordered Phase in $\text{SrCu}_2(\text{BO}_3)_2$ under High Pressure. *J. Phys. Soc. Jpn.*, 76(7):073710, 2007.
- [76] M. E. Zayed, Ch. Rüegg, J. Larrea J., A. M. Läuchli, C. Panagopoulos, S. S. Saxena, M. Ellerby, D. F. McMorrow, T. Strässle, S. Klotz, G. Hamel, R. A. Sadykov, V. Pomjakushin, M. Boehm, M. Jiménez-Ruiz, A. Schneidewind, E. Pomjakushina, M. Stingaciu, K. Conder, and H. M. Rønnow. 4-spin plaquette singlet state in the Shastry-Sutherland compound $\text{SrCu}_2(\text{BO}_3)_2$. *Nature Physics*, 13:962, 2017.
- [77] T. Sakurai, Y. Hirao, K. Hijii, S. Okubo, H. Ohta, Y. Uwatoko, K. Kudo, and Y. Koike. Direct Observation of the Quantum Phase Transition of $\text{SrCu}_2(\text{BO}_3)_2$ by High-Pressure and Terahertz Electron Spin Resonance. *J. Phys. Soc. Jpn.*, 87(3):033701, 2018.
- [78] J. Guo, G. Sun, B. Zhao, L. Wang, W. Hong, V. A. Sidorov, N. Ma, Q. Wu, S. Li, Z. Y. Meng, A. W. Sandvik, and L. Sun. Quantum phases of $\text{SrCu}_2(\text{BO}_3)_2$ from high-pressure thermodynamics. *arXiv:1904.09927*, 2019.
- [79] C. Boos, S. P. G. Crone, I. A. Niesen, P. Corboz, K. P. Schmidt, and F. Mila. Competition between intermediate plaquette phases in $\text{SrCu}_2(\text{BO}_3)_2$ under pressure. *Phys. Rev. B*, 100:140413, 2019.
- [80] S. Bettler, L. Stoppel, Z. Yan, S. Gvasaliya, and A. Zheludev. Sign switching of dimer correlations in $\text{SrCu}_2(\text{BO}_3)_2$ under hydrostatic pressure. *Phys. Rev. Research*, 2:012010, 2020.
- [81] I. Affleck, T. Kennedy, E. H. Lieb, and H. Tasaki. Rigorous results on valence-bond ground states in antiferromagnets. *Phys. Rev. Lett.*, 59:799–802, 1987.
- [82] I. Bose and S. Gayen. Hole motion in a coupled-chain model: Some exact results. *Phys. Rev. B*, 48:10653–10656, 1993.
- [83] A. K. Kolezhuk and H.-J. Mikeska. Models with exact ground states connecting smoothly the $S = \frac{1}{2}$ dimer and $S = 1$ Haldane phases of one-dimensional spin chains. *Phys. Rev. B*, 56:R11380–R11383, 1997.
- [84] A. A. Nersesyan and A. M. Tsvelik. One-Dimensional Spin-Liquid without Magnon Excitations. *Phys. Rev. Lett.*, 78:3939–3942, 1997.
- [85] A. K. Kolezhuk and H.-J. Mikeska. Non-Haldane Spin-Liquid Models with Exact Ground States. *Phys. Rev. Lett.*, 80:2709–2712, 1998.
- [86] A. K. Kolezhuk and H.-J. Mikeska. Finitely Correlated Generalized Spin Ladders. *International Journal of Modern Physics B*, 12(23):2325–2348, 1998.

-
- [87] V. Gritsev, B. Normand, and D. Baeriswyl. Phase diagram of the Heisenberg spin ladder with ring exchange. *Phys. Rev. B*, 69:094431, 2004.
- [88] C. D. Batista and S. A. Trugman. Exact Ground States of a Frustrated 2D Magnet: Deconfined Fractional Excitations at a First-Order Quantum Phase Transition. *Phys. Rev. Lett.*, 93:217202, 2004.
- [89] A. Gellé, A. M. Läuchli, B. Kumar, and F. Mila. Two-dimensional quantum antiferromagnet with a fourfold degenerate dimer ground state. *Phys. Rev. B*, 77:014419, 2008.
- [90] K. P. Schmidt and M. Laad. Family of Exactly Solvable Models with an Ultimate Quantum Paramagnetic Ground State. *Phys. Rev. Lett.*, 104:237201, 2010.
- [91] T. Hikihara, T. Tonegawa, K. Okamoto, and T. Sakai. Exact Ground States of Frustrated Quantum Spin Systems Consisting of Spin-Dimer Units. *J. Phys. Soc. Jpn.*, 86(5):054709, 2017.
- [92] E. Schrödinger. Quantisierung als Eigenwertproblem. *Annalen der Physik*, 385(13):437–490, 1926.
- [93] M. P. Gelfand and R. R. P. Singh. High-order convergent expansions for quantum many particle systems. *Advances in Physics*, 49(1):93–140, 2000.
- [94] A. L. Chernyshev, D. Galanakis, P. Phillips, A. V. Rozhkov, and A.-M. S. Tremblay. Higher order corrections to effective low-energy theories for strongly correlated electron systems. *Phys. Rev. B*, 70:235111, 2004.
- [95] T. Kato. Upper and Lower Bounds of Eigenvalues. *Phys. Rev.*, 77:413–413, 1950.
- [96] M. Takahashi. Half-filled Hubbard model at low temperature. *Journal of Physics C: Solid State Physics*, 10(8):1289, 1977.
- [97] P.-O. Löwdin. Studies in Perturbation Theory. IV. Solution of Eigenvalue Problem by Projection Operator Formalism. *Journal of Mathematical Physics*, 3(5):969–982, 1962.
- [98] C. Knetter and G. Uhrig. Perturbation theory by flow equations: dimerized and frustrated $S=1/2$ chain. *Eur. Phys. J. B*, 13(2):209–225, 2000.
- [99] D. Klagges. Effektive Zweispinmodelle für Cluster-State-Hamilton-Operatoren, Diplomarbeit, Technische Universität Dortmund. 2011.
- [100] C. Boos, C. J. Ganahl, M. Lajkó, P. Nataf, A. M. Läuchli, K. Penc, K. P. Schmidt, and F. Mila. Time-reversal symmetry breaking Abelian chiral spin liquid in Mott phases of three-component fermions on the triangular lattice. *Phys. Rev. Research*, 2:023098, 2020.
- [101] L. G. Marland. Series expansions for the zero-temperature transverse Ising model. *J. Phys. A*, 14(8):2047–2057, 1981.

-
- [102] M. P. Gelfand. Series expansions for excited states of quantum lattice models. *Solid State Communications*, 98(1):11 – 14, 1996.
- [103] S. Trebst, H. Monien, C. J. Hamer, Z. Weihong, and R. R. P. Singh. Strong-Coupling Expansions for Multiparticle Excitations: Continuum and Bound States. *Phys. Rev. Lett.*, 85:4373–4376, 2000.
- [104] W. Zheng, C. J. Hamer, R. R. P. Singh, S. Trebst, and H. Monien. Linked cluster series expansions for two-particle bound states. *Phys. Rev. B*, 63:144410, 2001.
- [105] J. Oitmaa, C. Hamer, and W. Zheng. *Series Expansion Methods for Strongly Interacting Lattice Models*. Cambridge University Press, 2006.
- [106] C. Knetter, K. P. Schmidt, and G. S. Uhrig. The structure of operators in effective particle-conserving models. *J. Phys. A*, 36(29):7889, 2003.
- [107] B. Tang, E. Khatami, and M. Rigol. A short introduction to numerical linked-cluster expansions. *Computer Physics Communications*, 184(3):557 – 564, 2013.
- [108] K. Coester and K. P. Schmidt. Optimizing linked-cluster expansions by white graphs. *Phys. Rev. E*, 92:022118, 2015.
- [109] D. Ixert. Nichtperturbative Linked-Cluster Entwicklungen für unkonventionelle Mottisolatoren. Dissertation, Technische Universität Dortmund. 2016.
- [110] Y. Yang H, A. F. Albuquerque, S. Capponi, A. M. Läuchli, and K. P. Schmidt. Effective spin couplings in the Mott insulator of the honeycomb lattice Hubbard model. *New Journal of Physics*, 14(11):115027, 2012.
- [111] F. Mila and K. P. Schmidt. Strong-Coupling Expansion and Effective Hamiltonians. In F. Mila C. Lacroix, P. Mendels, editor, *Introduction to Frustrated Magnetism*, volume 164, chapter 20, pages 537–559. Springer Series in Solid-State Sciences, Springer Berlin Heidelberg, 2011.
- [112] D. Yao and J. Shi. Projection operator approach to time-independent perturbation theory in quantum mechanics. *American Journal of Physics*, 68(3):278–281, 2000.
- [113] C. Knetter. Perturbative Continuous Unitary Transformations: Spectral Properties of Low Dimensional Spin Systems. PhD thesis, Cologne. 2003.
- [114] K. P. Schmidt. Spectral Properties of Quasi One-dimensional Quantum Antiferromagnets: Perturbative Continuous Unitary Transformations. PhD thesis, Cologne, 2004.
- [115] F. Wegner. Flow-equations for Hamiltonians. *Annalen der Physik*, 506(2):77–91.
- [116] S. D. Glazek and K. G. Wilson. Perturbative renormalization group for Hamiltonians. *Phys. Rev. D*, 49:4214–4218, 1994.
- [117] S. D. Glazek and K. G. Wilson. Renormalization of Hamiltonians. *Phys. Rev. D*, 48:5863–5872, 1993.

-
- [118] S. Dusuel and G. S. Uhrig. The quartic oscillator: a non-perturbative study by continuous unitary transformations. *J. Phys. A*, 37(39):9275–9294, 2004.
- [119] F. J. Wegner. Flow equations for Hamiltonians. *Nuclear Physics B - Proceedings Supplements*, 90:141 – 146, 2000.
- [120] A. Mielke. Flow equations for band-matrices. *Eur. Phys. J. B*, 5(3):605–611, 1998.
- [121] S. K. Kehrein, A. Mielke, and P. Neu. Flow equations for the spin-boson problem. *Zeitschrift für Physik B Condensed Matter*, 99(2):269–280, 1995.
- [122] C. P. Heidbrink and G. S. Uhrig. Landau’s Quasiparticle Mapping: Fermi Liquid Approach and Luttinger Liquid Behavior. *Phys. Rev. Lett.*, 88:146401, 2002.
- [123] A. C. Guttman. *Phase Transitions and Critical Phenomena*, volume 13. Academic Press, New York, 1989.
- [124] A. Weiße and H. Fehske. Exact Diagonalization Techniques. In H. Fehske, R. Schneider, and A. Weiße, editors, *Computational Many-Particle Physics*, volume 739, page 529–544. Lecture Notes in Physics, Springer Berlin Heidelberg, 2008.
- [125] C. Lanczos. An iteration method for the solution of the eigenvalue problem of linear differential and integral operators. *J. Res. Natl. Bur. Std.*, 45:225–282, 1950.
- [126] P. Nataf and F. Mila. Exact diagonalization of Heisenberg $SU(N)$ chains in the fully symmetric and antisymmetric representations. *Phys. Rev. B*, 93:155134, 2016.
- [127] B. Bernu, C. Lhuillier, and L. Pierre. Signature of Néel order in exact spectra of quantum antiferromagnets on finite lattices. *Phys. Rev. Lett.*, 69:2590–2593, 1992.
- [128] B. Bernu, P. Lecheminant, C. Lhuillier, and L. Pierre. Exact spectra, spin susceptibilities, and order parameter of the quantum Heisenberg antiferromagnet on the triangular lattice. *Phys. Rev. B*, 50:10048–10062, 1994.
- [129] B. Sutherland. Model for a multicomponent quantum system. *Phys. Rev. B*, 12:3795–3805, 1975.
- [130] I. Affleck. Critical behaviour of $SU(N)$ quantum chains and topological non-linear σ -models. *Nuclear Physics B*, 305(4):582 – 596, 1988.
- [131] I. Affleck and J. B. Marston. Large- n limit of the Heisenberg-Hubbard model: Implications for high- T_c superconductors. *Phys. Rev. B*, 37:3774–3777, 1988.
- [132] J. B. Marston and I. Affleck. Large- n limit of the Hubbard-Heisenberg model. *Phys. Rev. B*, 39:11538–11558, 1989.
- [133] N. Read and S. Sachdev. Some features of the phase diagram of the square lattice $SU(N)$ antiferromagnet. *Nuclear Physics B*, 316(3):609 – 640, 1989.

- [134] I. Affleck, D. P. Arovas, J. B. Marston, and D. A. Rabson. SU($2n$) quantum anti-ferromagnets with exact C-breaking ground states. *Nuclear Physics B*, 366(3):467 – 506, 1991.
- [135] B. Frischmuth, F. Mila, and M. Troyer. Thermodynamics of the One-Dimensional SU(4) Symmetric Spin-Orbital Model. *Phys. Rev. Lett.*, 82:835–838, 1999.
- [136] F. F. Assaad. Phase diagram of the half-filled two-dimensional SU(N) Hubbard-Heisenberg model: A quantum Monte Carlo study. *Phys. Rev. B*, 71:075103, 2005.
- [137] P. Corboz, A. M. Läuchli, K. Penc, M. Troyer, and F. Mila. Simultaneous Dimerization and SU(4) Symmetry Breaking of 4-Color Fermions on the Square Lattice. *Phys. Rev. Lett.*, 107:215301, 2011.
- [138] T. C. Lang, Z. Y. Meng, A. Muramatsu, S. Wessel, and F. F. Assaad. Dimerized Solids and Resonating Plaquette Order in SU(N)-Dirac Fermions. *Phys. Rev. Lett.*, 111:066401, 2013.
- [139] P. Nataf and F. Mila. Exact Diagonalization of Heisenberg SU(N) Models. *Phys. Rev. Lett.*, 113:127204, 2014.
- [140] J. Dufour and F. Mila. Stabilization of the chiral phase of the SU($6m$) Heisenberg model on the honeycomb lattice with m particles per site for m larger than 1. *Phys. Rev. A*, 94:033617, 2016.
- [141] M. Lajkó, K. Wamer, F. Mila, and I. Affleck. Generalization of the Haldane conjecture to SU(3) chains. *Nuclear Physics B*, 924:508 – 577, 2017.
- [142] M. A. Perlin and A. M. Rey. Effective multi-body SU(N)-symmetric interactions of ultracold fermionic atoms on a 3D lattice. *New Journal of Physics*, 21(4):043039, 2019.
- [143] A. Läuchli, F. Mila, and K. Penc. Quadrupolar Phases of the $S = 1$ Bilinear-Biquadratic Heisenberg Model on the Triangular Lattice. *Phys. Rev. Lett.*, 97:087205, 2006.
- [144] A. Young. On Quantitative Substitutional Analysis I. *Proceedings of the London Mathematical Society*, 33:97–146, 1901.
- [145] A. Young. On Quantitative Substitutional Analysis. *Proceedings of the London Mathematical Society*, s2-34(1):196–230, 1932.
- [146] D. Jaksch and P. Zoller. The cold atom Hubbard toolbox. *Annals of Physics*, 315(1):52 – 79, 2005. Special Issue.
- [147] I. Bloch. Quantum gases in optical lattices. *Physics World*, 17(4):25–29, 2004.
- [148] I. Bloch. Ultracold quantum gases in optical lattices. *Nature Physics*, 1:23–30, 2005.

-
- [149] P. Soltan-Panahi, J. Struck, P. Hauke, A. Bick, W. Plenkers, G. Meineke, C. Becker, P. Windpassinger, M. Lewenstein, and K. Sengstock. Multi-component quantum gases in spin-dependent hexagonal lattices. *Nature Physics*, 7:434 EP, 2011.
- [150] L. Tarruell, D. Greif, T. Uehlinger, G. Jotzu, and T. Esslinger. Creating, moving and merging Dirac points with a Fermi gas in a tunable honeycomb lattice. *Nature*, 483:302 EP, 2012.
- [151] J. Struck, C. Ölschläger, R. Le Targat, P. Soltan-Panahi, A. Eckardt, M. Lewenstein, P. Windpassinger, and K. Sengstock. Quantum Simulation of Frustrated Classical Magnetism in Triangular Optical Lattices. *Science*, 333(6045):996–999, 2011.
- [152] D. Jaksch, C. Bruder, J. I. Cirac, C. W. Gardiner, and P. Zoller. Cold Bosonic Atoms in Optical Lattices. *Phys. Rev. Lett.*, 81:3108–3111, 1998.
- [153] W. Hofstetter, J. I. Cirac, P. Zoller, E. Demler, and M. D. Lukin. High-Temperature Superfluidity of Fermionic Atoms in Optical Lattices. *Phys. Rev. Lett.*, 89:220407, 2002.
- [154] I. Bloch, J. Dalibard, and W. Zwerger. Many-body physics with ultracold gases. *Rev. Mod. Phys.*, 80:885–964, 2008.
- [155] D. Jaksch, H.-J. Briegel, J. I. Cirac, C. W. Gardiner, and P. Zoller. Entanglement of Atoms via Cold Controlled Collisions. *Phys. Rev. Lett.*, 82:1975–1978, 1999.
- [156] M. Greiner, O. Mandel, T. Esslinger, T. W. Hänsch, and I. Bloch. Quantum phase transition from a superfluid to a Mott insulator in a gas of ultracold atoms. *Nature*, 415(6867):39–44, 2002.
- [157] R. Jördens, N. Strohmaier, K. Günter, H. Moritz, and T. Esslinger. A Mott insulator of fermionic atoms in an optical lattice. *Nature*, 455:204 EP, 2008.
- [158] U. Schneider, L. Hackermüller, S. Will, Th. Best, I. Bloch, T. A. Costi, R. W. Helmes, D. Rasch, and A. Rosch. Metallic and Insulating Phases of Repulsively Interacting Fermions in a 3D Optical Lattice. *Science*, 322(5907):1520–1525, 2008.
- [159] J. Dalibard, F. Gerbier, G. Juzeliūnas, and P. Öhberg. Colloquium: Artificial gauge potentials for neutral atoms. *Rev. Mod. Phys.*, 83:1523–1543, 2011.
- [160] S. Stellmer, R. Grimm, and F. Schreck. Detection and manipulation of nuclear spin states in fermionic strontium. *Phys. Rev. A*, 84:043611, 2011.
- [161] N. Papanicolaou. Unusual phases in quantum spin-1 systems. *Nuclear Physics B*, 305(3):367 – 395, 1988.
- [162] A. H. MacDonald, S. M. Girvin, and D. Yoshioka. $\frac{t}{U}$ expansion for the Hubbard model. *Phys. Rev. B*, 37:9753–9756, 1988.
- [163] E. Müller-Hartmann and A. Reischl. Derivation of effective spin models from a three band model for CuO -planes. *Eur. Phys. J. B*, 28(2):173–183, 2002.

- [164] G. Szirmai, E. Szirmai, A. Zamora, and M. Lewenstein. Gauge fields emerging from time-reversal symmetry breaking for spin-5/2 fermions in a honeycomb lattice. *Phys. Rev. A*, 84:011611, 2011.
- [165] P. Sinkovicz, A. Zamora, E. Szirmai, M. Lewenstein, and G. Szirmai. Spin liquid phases of alkaline-earth-metal atoms at finite temperature. *Phys. Rev. A*, 88:043619, 2013.
- [166] P. Nataf, M. Lajkó, P. Corboz, A. M. Läuchli, K. Penc, and F. Mila. Plaquette order in the SU(6) Heisenberg model on the honeycomb lattice. *Phys. Rev. B*, 93:201113, 2016.
- [167] S. S. Chung and P. Corboz. SU(3) fermions on the honeycomb lattice at $\frac{1}{3}$ filling. *Phys. Rev. B*, 100:035134, 2019.
- [168] M. Hafez-Torbati and W. Hofstetter. Artificial SU(3) spin-orbit coupling and exotic Mott insulators. *Phys. Rev. B*, 98:245131, 2018.
- [169] M. Capone, L. Capriotti, F. Becca, and S. Caprara. Mott metal-insulator transition in the half-filled Hubbard model on the triangular lattice. *Phys. Rev. B*, 63:085104, 2001.
- [170] B. Bauer, P. Corboz, A. M. Läuchli, L. Messio, K. Penc, M. Troyer, and F. Mila. Three-sublattice order in the SU(3) Heisenberg model on the square and triangular lattice. *Phys. Rev. B*, 85:125116, 2012.
- [171] K. Penc and A. M. Läuchli. Spin Nematic Phases in Quantum Spin Systems. In C. Lacroix, P. Mendels, and F. Mila, editors, *Introduction to Frustrated Magnetism*, volume 164 of *Springer Series in Solid-State Sciences*, chapter 13. Springer, Berlin, Heidelberg, 2010.
- [172] H. Tsunetsugu and M. Arikawa. Spin Nematic Phase in S=1 Triangular Antiferromagnets. *J. Phys. Soc. Jpn.*, 75(8):083701, 2006.
- [173] M. Takigawa and F. Mila. Strong-Coupling Expansion and Effective Hamiltonians. In F. Mila C. Lacroix, P. Mendels, editor, *Introduction to Frustrated Magnetism*, volume 164, chapter 10, pages 241–264. Springer Series in Solid-State Sciences, Springer Berlin Heidelberg, 2011.
- [174] H.-D. Liu, Y.-H. Chen, H.-F. Lin, H.-S. Tao, and W.-M. Liu. Antiferromagnetic Metal and Mott Transition on Shastry-Sutherland Lattice. *Scientific Reports*, 4:4829 EP, 2014.
- [175] S. Miyahara. Exact Results in Frustrated Quantum Magnetism. In F. Mila C. Lacroix, P. Mendels, editor, *Introduction to Frustrated Magnetism*, volume 164, chapter 19, pages 513–537. Springer Series in Solid-State Sciences, Springer Berlin Heidelberg, 2011.
- [176] M. Moliner, I. Rousochatzakis, and F. Mila. Emergence of one-dimensional physics from the distorted Shastry-Sutherland lattice. *Phys. Rev. B*, 83:140414, 2011.

- [177] J. Y. Lee, Y.-Z. You, S. Sachdev, and A. Vishwanath. Signatures of a Deconfined Phase Transition on the Shastry-Sutherland Lattice: Applications to Quantum Critical $\text{SrCu}_2(\text{BO}_3)_2$. *Phys. Rev. X*, 9(4), 2019.
- [178] H. Nakano and T. Sakai. Third Boundary of the Shastry–Sutherland Model by Numerical Diagonalization. *J. Phys. Soc. Jpn.*, 87(12):123702, 2018.
- [179] Z. Wang and C. D. Batista. Dynamics and Instabilities of the Shastry-Sutherland Model. *Phys. Rev. Lett.*, 120:247201, 2018.
- [180] S. Wessel, I. Niesen, J. Stapmanns, B. Normand, F. Mila, P. Corboz, and A. Honecker. Thermodynamic properties of the Shastry-Sutherland model from quantum Monte Carlo simulations. *Phys. Rev. B*, 98:174432, 2018.
- [181] A. Wietek, P. Corboz, S. Wessel, B. Normand, F. Mila, and A. Honecker. Thermodynamic properties of the Shastry-Sutherland model throughout the dimer-product phase. *Phys. Rev. Research*, 1(3), 2019.
- [182] J. Dorier. Exotic phases of quantum frustrated magnets: Magnetization plateaus, nematic order and supersolid phases. PhD thesis, École Polytechnique Fédérale de Lausanne. 2008.
- [183] R. W. Smith and D. A. Keszler. Synthesis, structure, and properties of the orthoborate $\text{SrCu}_2(\text{BO}_3)_2$. *J. Solid State Chem.*, 93(2):430 – 435, 1991.
- [184] S. Miyahara and K. Ueda. Theory of the orthogonal dimer Heisenberg spin model for $\text{SrCu}_2(\text{BO}_3)_2$. *J. Phys. Condens. Matter*, 15(9):R327–R366, 2003.
- [185] H. Kageyama, K. Onizuka, T. Yamauchi, Y. Ueda, S. Hane, H. Mitamura, T. Goto, K. Yoshimura, and K. Kosuge. Anomalous Magnetizations in Single Crystalline $\text{SrCu}_2(\text{BO}_3)_2$. *J. Phys. Soc. Jpn.*, 68(6):1821–1823, 1999.
- [186] H. Kageyama, K. Onizuka, Y. Ueda, M. Nohara, H. Suzuki, and H. Takagi. Low-temperature specific heat study of $\text{SrCu}_2(\text{BO}_3)_2$ with an exactly solvable ground state. *J. Exp. Theor. Phys.*, 90(1):129–132, 2000.
- [187] K. Onizuka, H. Kageyama, Y. Narumi, K. Kindo, Y. Ueda, and T. Goto. $1/3$ Magnetization Plateau in $\text{SrCu}_2(\text{BO}_3)_2$ - Stripe Order of Excited Triplets -. *J. Phys. Soc. Jpn.*, 69(4):1016–1018, 2000.
- [188] Y. H. Matsuda, N. Abe, S. Takeyama, H. Kageyama, P. Corboz, A. Honecker, S. R. Manmana, G. R. Foltin, K. P. Schmidt, and F. Mila. Magnetization of $\text{SrCu}_2(\text{BO}_3)_2$ in Ultrahigh Magnetic Fields up to 118 T. *Phys. Rev. Lett.*, 111:137204, 2013.
- [189] J. Dorier, K. P. Schmidt, and F. Mila. Theory of Magnetization Plateaux in the Shastry-Sutherland Model. *Phys. Rev. Lett.*, 101:250402, 2008.
- [190] M. Nemeč, G. R. Foltin, and K. P. Schmidt. Microscopic mechanism for the $\frac{1}{8}$ magnetization plateau in $\text{SrCu}_2(\text{BO}_3)_2$. *Phys. Rev. B*, 86:174425, 2012.

- [191] Z. Weihong, C. J. Hamer, and J. Oitmaa. Series expansions for a Heisenberg antiferromagnetic model for $\text{SrCu}_2(\text{BO}_3)_2$. *Phys. Rev. B*, 60:6608–6616, 1999.
- [192] H. Kageyama, M. Nishi, N. Aso, K. Onizuka, T. Yosihama, K. Nukui, K. Kodama, K. Kakurai, and Y. Ueda. Direct Evidence for the Localized Single-Triplet Excitations and the Dispersive Multitriplet Excitations in $\text{SrCu}_2(\text{BO}_3)_2$. *Phys. Rev. Lett.*, 84:5876–5879, 2000.
- [193] K. Sparta, G. J. Redhammer, P. Roussel, G. Heger, G. Roth, P. Lemmens, A. Ionescu, M. Grove, G. Güntherodt, F. Hüning, H. Lueken, H. Kageyama, K. Onizuka, and Y. Ueda. Structural phase transition in the 2D spin dimer compound $\text{SrCu}_2(\text{BO}_3)_2$. *Eur. Phys. J. B*, 19(4):507–516, 2001.
- [194] C. Vecchini, O. Adamopoulos, L. C. Chapon, A. Lappas, H. Kageyama, Y. Ueda, and A. Zorko. Structural distortions in the spin-gap regime of the quantum antiferromagnet $\text{SrCu}_2(\text{BO}_3)_2$. *J. Solid State Chem.*, 182(12):3275 – 3281, 2009.
- [195] V. V. Mazurenko, S. L. Skornyakov, V. I. Anisimov, and F. Mila. First-principles investigation of symmetric and antisymmetric exchange interactions of $\text{SrCu}_2(\text{BO}_3)_2$. *Phys. Rev. B*, 78:195110, 2008.
- [196] C. Knetter, A. Bühler, E. Müller-Hartmann, and G. S. Uhrig. Dispersion and Symmetry of Bound States in the Shastry-Sutherland Model. *Phys. Rev. Lett.*, 85:3958–3961, 2000.
- [197] S. Haravifard, A. Banerjee, J. C. Lang, G. Srajer, D. M. Silevitch, B. D. Gaulin, H. A. Dabkowska, and T. F. Rosenbaum. Continuous and discontinuous quantum phase transitions in a model two-dimensional magnet. *Proceedings of the National Academy of Sciences*, 109(7):2286–2289, 2012.
- [198] G. Radtke, A. Saúl, H. A. Dabkowska, M. B. Salamon, and M. Jaime. Magnetic nanopantograph in the $\text{SrCu}_2(\text{BO}_3)_2$ Shastry-Sutherland lattice. *Proceedings of the National Academy of Sciences of the United States of America*, 112(7):1971–1976, 2015.
- [199] M. E. Zayed, C. Rüegg, E. Pomjakushina, M. Stingaciu, K. Conder, M. Hanfland, M. Merlini, and H. M. Rønnow. Temperature dependence of the pressure induced monoclinic distortion in the spin $S=1/2$ Shastry–Sutherland compound $\text{SrCu}_2(\text{BO}_3)_2$. *Solid State Communications*, 186:13 – 17, 2014.
- [200] P. Carretta and A. Keren. NMR and μSR in Highly Frustrated Magnets. In F. Mila C. Lacroix, P. Mendels, editor, *Introduction to Frustrated Magnetism*, volume 164, chapter 4, pages 79–106. Springer Series in Solid-State Sciences, Springer Berlin Heidelberg, 2011.
- [201] C. Berthier, M. Horvatić, M.-H. Julien, H. M., and S. Krämer. Nuclear magnetic resonance in high magnetic field: Application to condensed matter physics. *Comptes Rendus Physique*, 18(5):331 – 348, 2017.

- [202] S. T. Bramwell. Neutron Scattering and Highly Frustrated Magnetism. In F. Mila C. Lacroix, P. Mendels, editor, *Introduction to Frustrated Magnetism*, volume 164, chapter 3, pages 45–78. Springer Series in Solid-State Sciences, Springer Berlin Heidelberg, 2011.
- [203] M. Zayed. Novel States in Magnetic Materials under Extreme Conditions. A High Pressure Neutron Scattering Study of the Shastry-Sutherland Compound $\text{SrCu}_2(\text{BO}_3)_2$. PhD thesis, ETH Zurich. 2010.
- [204] C. Knetter and G. S. Uhrig. Dynamic Structure Factor of the Two-Dimensional Shastry-Sutherland Model. *Phys. Rev. Lett.*, 92:027204, 2004.
- [205] T. Sakurai, M. Tomoo, S. Okubo, H. Ohta, K. Kudo, and Y. Koike. High-field and high-pressure ESR measurements of $\text{SrCu}_2(\text{BO}_3)_2$. *Journal of Physics: Conference Series*, 150(4):042171, 2009.
- [206] H. Ohta, T. Sakurai, R. Matsui, K. Kawasaki, Y. Hirao, S. Okubo, K. Matsumabayashi, Y. Uwatoko, K. Kudo, and Y. Koike. Frequency Extension to the THz Range in the High Pressure ESR System and Its Application to the Shastry-Sutherland Model Compound $\text{SrCu}_2(\text{BO}_3)_2$. *The Journal of Physical Chemistry B*, 119(43):13755–13761, 2015.
- [207] H. Kageyama, H. Suzuki, M. Nohara, K. Onizuka, H. Takagi, and Y. Ueda. Specific heat study of $\text{SrCu}_2(\text{BO}_3)_2$. *Physica B: Condensed Matter*, 281-282:667–668, 2000.
- [208] A. Koga, K. Okunishi, and N. Kawakami. First-order quantum phase transition in the orthogonal-dimer spin chain. *Phys. Rev. B*, 62:5558–5563, 2000.
- [209] S. R. White and D. A. Huse. Numerical renormalization-group study of low-lying eigenstates of the antiferromagnetic $S=1$ Heisenberg chain. *Phys. Rev. B*, 48:3844–3852, 1993.
- [210] T. D. Kühner and S. R. White. Dynamical correlation functions using the density matrix renormalization group. *Phys. Rev. B*, 60:335–343, 1999.
- [211] S. R. White and I. Affleck. Spectral function for the $S = 1$ Heisenberg antiferromagnetic chain. *Phys. Rev. B*, 77:134437, 2008.
- [212] J. Haegeman, B. Pirvu, D. J. Weir, J. I. Cirac, T. J. Osborne, H. Verschelde, and F. Verstraete. Variational matrix product ansatz for dispersion relations. *Phys. Rev. B*, 85:100408, 2012.
- [213] J. Richter, N. B. Ivanov, and J. Schulenburg. The antiferromagnetic spin-chain with competing dimers and plaquettes: numerical versus exact results. *J. Phys. Condens. Matter*, 10(16):3635, 1998.
- [214] J. Röchner, L. Balents, and K. P. Schmidt. Spin liquid and quantum phase transition without symmetry breaking in a frustrated three-dimensional Ising model. *Phys. Rev. B*, 94:201111, 2016.

-
- [215] M. Arlego and W. Brenig. Plaquette order in the $J_1-J_2-J_3$ model: Series expansion analysis. *Phys. Rev. B*, 78:224415, 2008.
- [216] M. Arlego and W. Brenig. Series expansion analysis of a frustrated four-spin tube. *Phys. Rev. B*, 84:134426, 2011.
- [217] N. B. Ivanov and J. Richter. Competition between plaquette and dimer phases in Heisenberg chains. *Physics Letters A*, 232(3):308 – 312, 1997.
- [218] A. Honecker, S. Wessel, R. Kerkdyk, T. Pruschke, F. Mila, and B. Normand. Thermodynamic properties of highly frustrated quantum spin ladders: Influence of many-particle bound states. *Phys. Rev. B*, 93:054408, 2016.
- [219] S. Wessel, B. Normand, F. Mila, and A. Honecker. Efficient Quantum Monte Carlo simulations of highly frustrated magnets: the frustrated spin-1/2 ladder. *SciPost Phys.*, 3:005, 2017.
- [220] O. Golinelli, Th. Jolicoeur, and R. Lacaze. Finite-lattice extrapolations for a Haldane-gap antiferromagnet. *Phys. Rev. B*, 50:3037–3044, 1994.
- [221] H.-Y. Yang. private communication.
- [222] C. Boos and K. P. Schmidt. Exact plaquette singlet phases in an orthogonal-plaquette model. *Phys. Rev. B*, 101:144428, 2020.
- [223] S. Miyahara and K. Ueda. Superstructures at magnetization plateaus in $\text{SrCu}_2(\text{BO}_3)_2$. *Phys. Rev. B*, 61:3417–3424, 2000.
- [224] K. Kodama, M. Takigawa, M. Horvatić, C. Berthier, H. Kageyama, Y. Ueda, S. Miyahara, F. Becca, and F. Mila. Magnetic Superstructure in the Two-Dimensional Quantum Antiferromagnet $\text{SrCu}_2(\text{BO}_3)_2$. *Science*, 298(5592):395–399, 2002.
- [225] R. R. P. Singh. Thermodynamic parameters of the $T=0$, spin-1/2 square-lattice Heisenberg antiferromagnet. *Phys. Rev. B*, 39:9760–9763, 1989.

List of publications

Some of the results presented in this thesis were published in or submitted to scientific journals in the following articles.

[79] C. Boos, S. P. G. Crone, I. A. Niesen, P. Corboz, K. P. Schmidt, and F. Mila, Competition between intermediate plaquette phases in $\text{SrCu}_2(\text{BO}_3)_2$ under pressure, *Phys. Rev. B*, 100:140413, 2019.

Copyright (2019) by The American Physical Society.

[100] C. Boos, C. J. Ganahl, M. Lajkó, P. Nataf, K. Penc, A. M. Läuchli, K. P. Schmidt, and F. Mila, Time-reversal symmetry breaking Abelian chiral spin liquid in Mott phases of three-component fermions on the triangular lattice, *Phys. Rev. Research*, 2:023098, 2020.

Copyright (2020) by The American Physical Society.

[222] C. Boos and K. P. Schmidt, Exact plaquette singlet phases in orthogonal-plaquette model, *Phys. Rev. B*, 100:144428, 2020.

Copyright (2020) by The American Physical Society.

Reference [79] was developed in cooperation between all authors C. Boos, S. P. G. Crone, I. A. Niesen, P. Corboz, K. P. Schmidt, and F. Mila. I derived all series. The series expansions approaches were designed together with my supervisor K. P. Schmidt. S. P. G. Crone, I. A. Niesen, and P. Corboz performed all iPEPS calculations. The insight that the FPP and the Haldane phase are identical arose in a discussion between P. Corboz and F. Mila. K. P. Schmidt, F. Mila, and I chose the possible distortions of the Shastry-Sutherland model and mainly resolved the connections with the experiments. The paper was mostly written between K. P. Schmidt, F. Mila, and me. S. P. G. Crone, I. A. Niesen, and P. Corboz added further improvements and the parts on iPEPS.

Reference [100] also contains results from my Master thesis [66], where the effective model for the triangular lattice was derived, and first studied in order five (only) with ED on 12 and 21 sites. The extrapolation of the coupling constants was done by me under supervision of K. P. Schmidt. The effective model in third-, fourth-, and fifth-order was at first investigated for eigenvalues, degeneracies, and symmetries by me with guidance from P. Nataf, K. P. Schmidt, and F. Mila. P. Nataf performed some ED on the 27-site cluster for the J - K model. The ED part was then taken over by C. J. Ganahl and A. M. Läuchli, who further determined chiralities, structure factors, and energy spectra for the effective model, and the energy spectrum of the Hubbard model on 12 sites. M. Lajkó carried out all VMC calculations. K. Penc contributed valuable insights in particular on the charge gap. The article was written as a joint effort by all authors.

Reference [222] was initiated by me, and I carried out the calculations. The most

interesting points were extracted together with K. P. Schmidt, who also supervised me writing the paper.

List of abbreviations

AFM: antiferromagnetic phase
AFQ: antiferroquadrupolar phase
CFT: conformal field theory
CSL: chiral spin liquid
CUT: continuous unitary transformation
ED: exact diagonalisation
ep: empty plaquette
EPP: empty plaquette singlet phase
ESR: electron spin resonance
FPP: filled plaquette singlet phase
INS: inelastic neutron scattering
iPEPS: infinite projected entangled-pair states
irreps: irreducible representations
lbe: lower band edge
ln: lattice nematic
NMR: nuclear magnetic resonance
dp: different plaquettes
PBCs: periodic boundary conditions
pCUT: perturbative continuous unitary transformations
series expansions: series expansions
VMC: variational Monte-Carlo
WZNW: Wess-Zumino-Novikov-Witten

Acknowledgements

My major thanks goes to Kai P. Schmidt, who encouraged and helped me with my projects, and who I could easily motivate about new topics. To this end, he was available often by email or mostly with an open door. I'm especially grateful for his insistent encouragement to participate in the workshop in Cargèse.

This thesis was created within a network of collaboration. Our main collaborator and almost my second supervisor is Frédéric Mila, who I would like to thank for many good discussions, insights, and ideas! For the investigation of the $SU(3)$ Hubbard model, further, Miklós Lajkó, Clemens Ganahl, Pierre Nataf, Andreas Läuchli, and Karlo Penc contributed calculations and insights. Miklós Lajkó also did so for $SU(7)$. Without them the determination of the CSLs would have not been possible. The investigations of the extended Shastry-Sutherland model was supported by Schelto Crone, Ido Niesen, and Philippe Corboz. I thank all of my collaborators for their efforts and joint discussions.

I'm grateful to the Theoretische Physik I. I really enjoyed chatting about many interesting topics at lunch, and I would like to thank all of those who were happy to join in, and apologise to all of those who I forced in at times. Also, in "Kai's group" we had many fruitful discussions, which was really interesting. My thanks go to the administrators dealing with the computer infrastructure, as well as Ingrid resolving formal issues.

Thanks to Gregor for reading my introduction from the perspective of an experimental particle physicist, and to Francisco and his answers to my $SU(N)$ -related questions. Further, Sebastian, Matthias II, Max, and Wiebke gave some helpful feedback on parts of this thesis.

A massively big thanks goes to my family, just for being my family, and because its big, and because it got a lot bigger during my time as a PhD student! Thank you all for the very pleasant times we had away from work. I know that I can always count on your support.

I would also like to thank a couple of companions, which gave me warm and dark power in difficult phases, showing me how bitter and sweet the world can be. We had good times together, not only in the early morning hours, but also after lunch. Dear coffee, dear chocolates, without you, this thesis would have not been possible!

Finally, I get to thank two very important players. The mountains and Andy. They are both great and supportive, and often made me forget about physics or allowed me seeing things from a different perspective.